## ABSTRACT

## NOVEL MICRON- AND NANO-SCALE ENERGETIC MATERIALS FOR ADVANCED GUN PROPULSION, THEIR MATERIAL PROPERTIES, AND THEIR EFFECTS ON BALLISTIC PERFORMANCE

**by**
**Thelma Gatuz Manning**

This dissertation focused on the investigation of novel materials that are both energetic and inert in their micron- and nano-scale crystalline form. The characterization of the materials properties and its effects on the ballistic performance when incorporated into a composite material were evaluated as a gun propellant for application in a future weapon system for the US Army. Some of these materials may find dual use in civilian applications. Applications in small and medium arms, artillery, tank, aircraft, and shipboard gun systems will all benefit from these advancements. Not only will gun system performance be improved for greater stand-off range and accuracy, but the ability to perform consistently across a broad temperature range. Additionally, an improved performance and longer gun barrel life achievable by tailoring the combustion products, lowering the propellant flame temperature, minimum sensitivity of burning velocity to pressure, temperature and gas velocity (erosive burning) and with munitions that are insensitive to outside stimulus attack will give such systems a significant advantage during military use. In addition, "green" chemistry and lower lifecycle cost were taken into consideration during this research.

The approach to be taken was to incorporate these novel materials into a gun propellant formulation by using nitramine-based micron scale cyclotrimethylene

trinitramine (RDX) explosives in combination with synthesized novel ingredients in nanoscale crystalline form, characterize the material properties and predict the ballistic performance across the ballistic temperature range. The nano-scale crystalline materials evaluated consisted of polymeric nitrogen stabilized in single wall carbon nanotubes (SWNTs), nitrogenated boron nanotubes / nanofibers (BNNTs/BNNFs), nano-aluminum, and titanium dioxide. The polymeric nitrogen and the nitrogenated boron nanotubes / nanofibers (BNNTs/BNNFs), should provide an enhancement in the propellant burn rate by achieving the burn rate differential goal of 3:1 between the fast and the slow burning propellant and at the same time improve the gun propellant performance by lowering the $CO/CO_2$ ratio and raising the $N_2$ / CO ratio for mitigating gun bore wear and erosion, respectively.

For the synthesis approaches of polymeric nitrogen stabilized in carbon nanotubes, the following synthesis method were performed, optimized and compared: Electrochemical Reactions, Microwave Induced Electrochemical Chemical Reactions and Plasma Enhanced Chemical Vapor Deposition (PE-CVD). The Electrochemical Reaction process has proven to be the most efficient synthesis approach for the polymeric nitrogen based on analytical results obtained through Raman Spectroscopy, Laser Ablation Mass Spectroscopy, Scanning Electron Microscope, Fourier Transform Infrared-Attenuated Total Reflectance (FTIR-ATR) and Differential Scanning Calorimeter/Thermal Gravimetric Analysis (DSC/TGA). The PE-CVD is the second recommended synthesis approach to synthesize the polymeric nitrogen although a cost benefit economic analysis has to be performed which is beyond the objectives of this research work.

For the synthesis of the nitrogenated boron nanotubes, the use of the magnesium borohydride to initiate the reaction has proven to be the most optimized process due to a much lower reaction temperature which is approximately 500 $^0$C when compared with the reaction temperature of 950 $^0$C when using Magnesium Boride (MgB2) in the thermally induced CVD process. The small scale synthesis of boron nanotubes /nanofibers carried out using $MgB_2$ powder, Nickel Boride ($Ni_2B$) powder catalysts and mesostructured hexagonal framework zeolite powder was successfully achieved at 950C. The quality of the nanotubes produced was checked by Raman spectroscopy and transmission electron microscope analysis. The TEM data shows the production of 10-20 nm boron nanotubes using the $MgB_2$, $Ni_2B$ and Mobile Crystalline Material (MCM-41) in the synthesis process.

# NOVEL MICRON- AND NANO-SCALE ENERGETIC MATERIALS FOR ADVANCED GUN PROPULSION, THEIR MATERIAL PROPERTIES, AND THEIR EFFECTS ON BALLISTIC PERFORMANCE

**by**
**Thelma Gatuz Manning**

**A Dissertation**
**Submitted to the Faculty of**
**New Jersey Institute of Technology**
**in Partial Fulfillment of the Requirements for the Degree of**
**Doctor of Philosophy in Materials Science and Engineering**

**Interdisciplinary Program in Materials Science and Engineering**

**May 2010**

**APPROVAL PAGE**

**NOVEL MICRON- AND NANO-SCALE ENERGETIC MATERIALS FOR ADVANCED GUN PROPULSION, THEIR MATERIAL PROPERTIES, AND THEIR EFFECTS ON BALLISTIC PERFORMANCE**

**Thelma Gatuz Manning**

4/29/10

Dr. Boris Khusid, Dissertation Co-Advisor — Date
Professor, Department of Chemical, Biological and Pharmaceutical Engineering, NJIT

4/29/2010

Dr. Zafar Iqbal, Dissertation Co-Advisor — Date
Research Professor, Department of Chemistry and Environmental Science, NJIT

4/29/10

Dr. Nuggehalli M. Ravindra, Dissertation Committee Member — Date
Department Chair and Professor, Department of Physics, NJIT

April 29, 2010

Dr. Marek Sosnowski, Dissertation Committee Member — Date
Professor, Department of Electrical and Computer Engineering, NJIT

May 3, 2010

Dr. Rao Surapaneni, Dissertation Committee Member — Date
Energetics Lead Technical Expert
US Army Armament Research, Development and Engineering Center, Picatinny, NJ

## BIOGRAPHICAL SKETCH

**Author:** Thelma G. Manning

**Degree:** Doctor of Philosophy

**Date of Birth** May 21, 1949

**Undergraduate and Graduate Education:**

- Doctor of Philosophy in Materials Science and Engineering,
  New Jersey Institute of Technology, Newark, NJ, 2010

- Master of Science in Mechanical Engineering,
  City College of New York, 1981

- Master of Science in Chemical Engineering,
  Polytechnic University of New York, 1977

- Master of Engineering in Chemical Engineering,
  University of the Philippines, Diliman, Metro Manila, Philippines 1973

- Bachelor of Science in Chemical Engineering,
  University of Santo Thomas, Manila, Philippines 1971

**Major:** Materials Science and Engineering

**Presentations and Publications:**

Thelma G. Manning and Zafar Iqbal, "Polymeric Nitrogen Stabilized on Carbon Nanotubes: A Highly Energetic, Green Explosive", Chemical Physics Letters, Manuscript Number CPLETT-10-596 for Peer Review, March 26, 2010.

Thelma G. Manning and Zafar Iqbal, "Polymeric Nitrogen Stabilized on Carbon Nanotubes: A Highly Energetic, Green Explosive", US Patent Provisional Application Serial Number 61/321,584 (UNCLASSIFIED), Picatinny Arsenal, NJ, April 7, 2010.

Thelma G. Manning and Zafar Iqbal, "Synthesis of Polymeric Nitrogen Stabilized on Carbon Nanotubes: A Highly Energetic, Green Explosive", 2010 Insensitive Munitions and Energetic Materials Technology Symposium, IMEMTS 2010, 11 - 14th October 2010, Munich, Germany.

Thelma G. Manning and Zafar Iqbal, "Polymeric Nitrogen Stabilized on Carbon Nanotubes: A Highly Energetic, Green Explosive", Proceedings of the 41st International ICT-Conference, FRAUNHOFER-INSTITUT FÜR CHEMISCHE TECHNOLOGIE Fraunhofer ICT, Joseph-von-Fraunhofer-Straße 7 , 76327 Pfinztal (Berghausen), Karlsruhe, Germany, accepted June 29 – July 2, 2010.

Thelma G. Manning and Zafar Iqbal, "Polymeric Nitrogen Stabilized on Carbon Nanotubes: A Highly Energetic, Green Explosive", Proceedings of the 57th Joint Army-Navy-NASA-Air Force (JANNAF) Propulsion Meeting / 7th Modeling and Simulation Subcommittee (MSS) / 5th Liquid Propulsion Subcommittee (LPS) / 4th Spacecraft Propulsion Subcommittee (SPS) Joint Meeting, Cheyenne, Colorado Springs, Colorado, accepted May 3-7, 2010.

Thelma G. Manning and Dr. Zafar Iqbal," Polymeric Nitrogen Stabilized on Carbon Nanotubes: A Highly Energetic, Green Explosive", National Capital Region Energetics Symposium, College of Southern Maryland, La Plata Campus, MD, April 27-29, 2009.

Thelma Manning, Eugene Rozumov, Duncan Park Sam Moy, and Donald Chiu, ARMY Advanced Gun Propellant Formulations, Proceedings of the 55th JANNAF Propulsion Meeting / 42nd Combustion Subcommittee / 30th Airbreathing Propulsion Subcommittee / 30th Exhaust Plume Technology Subcommittee / 24th Propulsion Systems Hazards Subcommittee / 12th Spectral and In-band Radiometric Imaging of Targets and Scenes User Group Joint Meeting, U.S. Army RDECOM-ARDEC, Boston, MA, May 12-16, 2008.

Thelma G. Manning, D. Chiu and D. Park," Characterization and Ballistic Properties of High Energy High Performance ETPE Gun Propellant for Future Large Caliber Applications", Proceedings of the 2005 JANNAF 40th Combustion Sub-Committee/28th APS/22nd PSHS/ 4th MSS Joint Meeting at Charleston Convention Center & Charleston AFB, Charleston, S. Carolina, 13-17 Jun 2005.

*Dedicated to my beloved father and mother for their love and support throughout all these years.*

## ACKNOWLEDGMENT

My sincerest thanks go to Professor Zafar Iqbal for his commitment, encouragement, and selfless contribution toward my academic development. I am fortunate to have him as my mentor and co-advisor. I would like to express my deepest appreciation to Professor Boris Khusid as my co-advisor and for his guidance in the characterization instrument in his class. I am very thankful to Professor Marek Sosnowski for his helpful advice on the design of experiments and operation of the plasma enhanced chemical vapor deposition equipment in his laboratory. I would also like to thank Dr Rao Surapaneni from the US Army RDECOM ARDEC for his advice, suggestions and encouragement during the experimental design of the synthesis experiments. I greatly appreciate Professor Nuggehalli Ravindra for his kind help, understanding, considerations and time for serving on my dissertation committee.

I would like to thank Anitha Patlolla for showing me how to make the nanopapers and other routine laboratory work, for example, running the galvanostat–potentiometer. I would like to thank Anna Zarow for meticulously showing me the proper use and calibration of the EAZY Raman and the Mesophotonics Raman instruments. I would like to thank Jinwen Liu for annealing the nanopapers and help in the Scanning Electron Microscope. I would like to thank also Dr Shiunchin Chris Wang for helping me with the electrochemistry experiments. I would like to thank Abhinav Sharma for helping me run the PE-CVD including the design of experiments. But most of all, I would like to thank all of them, Anitha , Anna, Abhinav, Jinwen and Dr Chris for their warm friendship during my residence requirements at NJIT. Additionally, I would like to thank Drs. Ming Wang Young, Subhash Patel and John Herman Suwardie from the Polymer Processing

Institute for their help in the DSC analysis. I would like to thank Henry Grau for his help in the FTIR-ATR and Electron Density Spectrometer analysis at ARDEC. I would like to thank Dr. Amer Lahamer from Berea College, Berea, Kentucky for the laser ablation mass spectroscopy analysis. I would like to thank Joseph Prezelski for his help in the English language and suggestions during the editing of the manuscript.

Finally, I gratefully acknowledge the US Army RDECOM ARDEC Science Fellowship program and committee members for their financial support in achieving this goal.

## TABLE OF CONTENTS

## TABLE OF CONTENTS
## (Continued)

**TABLE OF CONTENTS**
**(Continued)**

## LIST OF TABLES

## LIST OF FIGURES

## LIST OF FIGURES
## (Continued)

**Figures** **Page**

## LIST OF FIGURES
## (Continued)

**Figures** **Page**

## LIST OF FIGURES
## (Continued)

## LIST OF FIGURES
## (Continued)

**Figures** **Page**

## LIST OF FIGURES
## (Continued)

**Figures** **Page**

## LIST OF FIGURES
## (Continued)

## LIST OF SYMBOLS

| | |
|---|---|
| RDX | cyclotrimethylene trinitramine or 1,3,5-Trinitro-1,3,5-triazacyclohexane |
| CL-20 | 2,4,6,8,10,12-hexanitro-2,4,6,8,10,12-hexaazaisowurtzitane |
| HMX | Cyclotetramethylene-tetranitramine, tetra hexamine tetranitramine, or octahydro-1, 3, 5, 7-tetranitro-1, 3, 5, 7-tetrazocane |
| MCM-41 | Mobile Crystalline Material |
| BAMO | Bis-azido methyl oxetane copolymer of 3, 3-bis (azidomethyl) oxetane and 3-azidomethyl-3-methyloxetane (BAMO/AMMO), a copolymer of 3, 3-bis (azidomethyl) oxetane and tetrahydrofuran (BAMO/THF), and a copolymer of 3, 3-bis (azidomethyl) oxetane and 3-nitratomethyl-3-methyloxetane (BAMO/NMMO). |

# CHAPTER 1

# INTRODUCTION

## 1.1 Objective

Two key objectives of this dissertation are to achieve an optimized synthesis approach to stabilized polymeric nitrogen in single wall carbon nanotubes and a process to synthesize pure nitrogenated boron nanotubes/nanofibers.

The polymeric nitrogen and nitrogenated boron nanotubes/nanofibers (BNNTs/BNNFs), should provide an enhancement in the propellant burn rate by achieving the burn rate differential goal of 3:1 between the fast and the slow burning propellant in fast core propellant configurations and at the same time improve the gun propellant performance by lowering the $CO/CO_2$ ratio and raising the $N_2$ / CO ratio for mitigating gun bore wear and erosion, respectively.

For synthesis approaches to polymeric nitrogen, the following synthesis methodwere performed, optimized and compared: Electrochemical Reaction, Microwave Induced Chemical Reaction and Plasma Enhanced Chemical Vapor Deposition (CVD). Electrochemical Reaction process proved to be the most effective synthesis approach for polymeric nitrogen based on results obtained using Raman Spectroscopy and Laser Ablation Mass Spectroscopy. The results obtained were also consistent with Fourier Transform Infrared Attenuated Total Reflection (FTIR-ATR) and Scanning Electron Microscope (SEM) results. The Plasma Enhanced CVD is the second recommended approach to synthesize polymeric nitrogen based on similar characterization results.

Cost analysis that is beyond the scope of this dissertation, needs to be performed to determine which process is most cost effective.

For the nitrogenated boron nanotubes/nanofibers (BNNTs/BNNFs), the use of the magnesium borohydride ($Mg(BH_4)_2$) to initiate the reaction has proven to be the most scaleable process. The smaller scale synthesis of boron nanotubes/nanofibers carried out using Magnesium Boride ($MgB_2$) as the boron precursor instead of Magnesium Borohydride ($Mg(BH_4)_2$), Nickel Boride ($Ni_2B$) powder as catalyst and the mesostructured hexagonal framework of Mobile Crystalline Material (MCM-41) zeolite powder as template, was successfully achieved. The quality of the nanotubes produced was checked by Raman spectroscopy and transmission electron microscope and Electron Energy Loss Spectroscopy (EELS). The TEM data shows high quality 10-20 nm diameter pristine boron nanotubes prepared as described above.

The other key objectives of this dissertation is the use of nano-scale crystalline materials, such as nano-aluminum, titanium dioxide, nano-boron, and nano-carbon incorporated in micron-scale hexahydro-1,3,5-trinitro-1,3,5-triazine (RDX)-based propellant formulations to enhance propellant performance, have demonstrated burn rate increase resulting in a burn rate differential between the slow and the fast burning propellant of 1.7:1. The predicted muzzle velocity using the IBHVG2 code was a 6% increase with the 1.7:1 burn rate differential.

## 1.2 Background Information

The US Army has currently fielded high performance ammunition systems for large caliber guns to meet the needs of achieving longer-range munitions. As a result, gun propellants with more energy and higher flame temperatures have been introduced.

These propellants generate combustion products containing elements and compounds that can reduce the life of a gun barrel. Additionally, to achieve increased gun performance, high energy propellants with high flame temperatures and erosive combustion products are often utilized, the undesirable consequences of which are often increased gun bore wear and erosion, blast and flash. These characteristics are dependent on the propellant formulation thermochemistry and can be tailored to a certain extent by adjusting component compositions and incorporating specific additives. In order to achieve high performance with these currently produced gun propellant ingredients, propellant developers are forced to use ingredients that raise the flame temperatures of these propellants by several hundreds of degrees over the current legacy propellant systems. As seen in the Figure 1.1 below, calculations of barrel wear due solely to thermal effects using the Smith-O'Brasky [1,2] model, propellants that have higher flame temperatures and higher impetus values, barrel wear values increase dramatically.

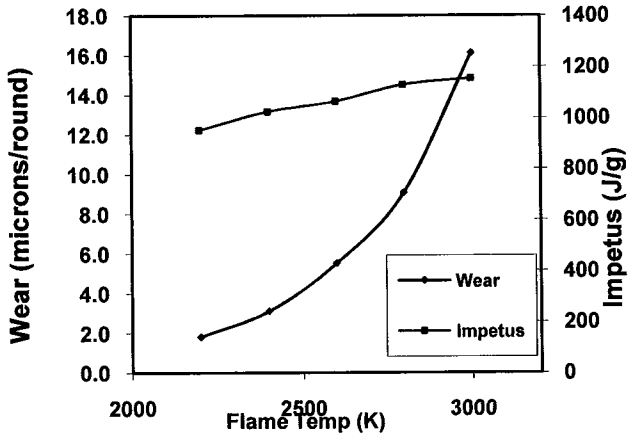


**Figure 1.1** Barrel wear and impetus as a function of propellant flame temperature [2,3 ].

Source: C. Leveritt, P. Conroy and A. Johson, "Characterization of the Erosivity of Advanced Solid Gun Propellants", Proceedings of the 37th JANNAF Combustion Subcommittee Meeting, Monterey, CA, November 2000

Walsh, C. and Knott, C., "Gun Propellant Formulations with High Nitrogen Modifiers", Proceedings of the 31st JANNAF Propellant Development and Characterization Subcommittee Meeting, Charlottesville, VA, March 2003.

Based on his model, we can conclude, gun wear and erosion can be minimized if the propellant flame temperature can be lowered while increasing the energy density of the propellant.

Over the years, the Army has funded research and development programs dedicated either to improve the performance of existing weapon systems or to develop higher performance weapon systems. Recent Army studies have shown that the chemistry of the propellant combustion products plays an important role in wear and erosion as well as shown in table 1. The primary driving reaction of the chemical mechanism is the dissociation of the carbon monoxide and subsequent adsorption/absorption of the carbon into the steel [4, 5, 6].

**Table 1.1** Examples of erosion related chemical reactions

| | |
|---|---|
| Major propellant gas Products | $CO$, $CO_2$, $H_2$, $H_2O$, and $N_2$, $H_2S$ from additives ( e.g., $K_2SO_4$ ) |
| Water gas reaction | $CO_2 + H_2 = CO + H_2O$ |
| Carbon deposition | $2CO = C + CO_2$ |
| Iron Oxide formation | $Fe + CO_2 = FeO + CO$ |
| Carbide formation | $3Fe + 2\ CO = Fe_3C + CO$ |
| Iron sulfide formation | $Fe + H_2S = FeS + H_2$ |

Sources: S. Sopok, C. Rickard, G. Pflegl, P. Vottis, P. O'Hara, S. Dunn, and D. Coats, "Erosion Predictions for the Final Configuration of the M829E3 Round, Technical Report ARAEW-TR-04001, U.S. Army ARDEC, Armaments Engineering & Technology Center, Weapon Systems & Technology, Benet Laboratories, Jan 2004.
S. Sopok, P. Vottis, P. O'Hara, G, Pflegl and C. Rickard, " Comprehensive Erosion Model for the 120-mm M256/M829A2 Gun System, Technical Report ARCCB-TR-98018, U.S. Army ARDEC, Armaments Engineering & Technology Center, Weapon Systems & Technology, Benet Laboratories, Oct

Methods to mitigate erosion would include methods to suppress this dissociation

or suppress the production of carbon monoxide. Ponec and Barneveld [7] suggest that the surface dissociation of CO on an iron surface is spoiled by nitrogen intrusion on the surface. This leads to the possibility that increasing the nitrogen content of the propellant products may diminish the CO dissociation and thereby the wear/erosion.

Leveritt et al [2, 8 ] has discovered that some advanced propellants that contain large amounts of nitrogen in the combustion products, but with even higher flame temperatures than older double base propellants such as JA2, are not as erosive as those propellants. Complicating matters is the fact that these advanced propellants have a much higher $CO/CO_2$ ratio in the combustion products than that of the double base propellants. One would expect these higher ratios to exacerbate the carburization mechanism. Ponec and Barnevelkd explanation may be applied to these new propellants because their nitrogen content is approximately three times that of conventional propellants. Studies by Leveritt have indicated that reducing CO and increasing $N_2$ in the combustion products can be beneficial in reducing erosivity. The current high performance guns have operating peak pressures as high as 414 MPa (60,000 psi) for 155 -mm guns and 690 MPa (100,000 psi) for 120-mm guns. In the high pressure regime, the heating rates from the high flame temperature of the propellant is also high, and as a result, there is insufficient time for heat to be conducted away from the bore surface. Propellant flame temperatures range from 2500 to 3600K with the 155-mm propellants and 120-mm propellants, respectively. In this case, the bore surface temperature can exceed the melting point of gun steel (1400-1900$^0$C). The action of high-pressure hot combustion gases flowing across the surface wipes away any molten steel. The major contributors to wear/erosion damage are thermal effects and chemical attack by

propellant gases. Gas –metal reactions from combustion products with high flame temperatures are major factors in erosion. As was listed in table 1.1, steel oxidation is a common high temperature reaction in erosion. Nitrocellulose (NC) is the major ingredient in most conventional gun propellants with Nitroglycerine and Nitroguanidine added for higher energy formulations. Other additives may be used such as potassium sulfate as a flash suppressant, magnesium oxide as an extrusion processing aid and other minor ingredients added to improve the propellant ballistics properties. The combustion products consist of CO, $CO_2$, $H_2O$, $H_2$, and $N_2$. Other gases that are highly reactive such as $H_2S$, are generated from the potassium sulfate flash suppressants, primers and igniters. The white layers on the bore surfaces, Figure 1.2, are known to represent fine grained retained austenite stabilized by carbon and nitrogen with precipitates, primarily carbides, distributed throughout the retained austenite [ 9, 10, 11 ]. Their universal occurrence, mostly in greatly eroded areas, indicates that carbon is another important chemical factor in gun bore erosion. The formation, melting, and removal of low melting temperature carbide are known as the most erosive mechanism in carbon attack because of the low melting point of $Fe_3C$ (2075K).

Recent gun firings of M31 type propellants have caused major spiral wear and erosion damages downbore of the M777 howitzer resulting in the comdemnation of 12 gun tubes. Large amount of ceramic type particulates/grits like residues were found at the downbore surface of the M777 tube. The obturator rotating band was found to be 60% worn down and contaminated with ceramic type residues that felt like rough sand. It is still unkown what the chemical composition of the residues found on the M77 bore surface were. During the firing of rounds, the gun bore surfaces are usually subjected to

short (5-10 ms) pulses of high thermal energy. These include among the harmful thermal effects, melting, metallurgical transformations, thermal and transformational stresses, and surface cracking. Figure 1.2 shows a typical macro-photo of the peak-eroded bore area of the latest condemned M256 cannon that fired a final configuration of M829E3 rounds and a firing mix of less erosive rounds. The cannon was condemned on numerous pits as shown in Figure 1.2. It is common to see hundreds of pits condemnation, attributable to the M829E3 round resulting in condemnation.

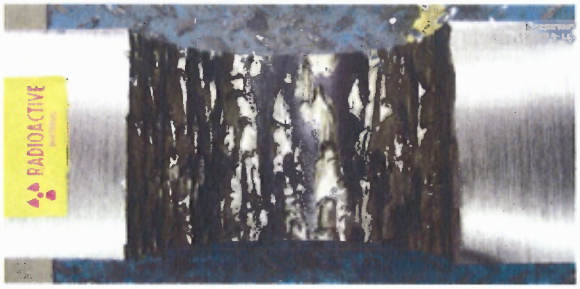


**Figure 1.2** Typical M829E3 macro-photo. Typical M829E3 M256 substrate exposure; some damaging slug and HEAT erosion rounds.

Source: S. Sopok, P. Vottis, P. O'Hara, G, Pflegl and C. Rickard, " Comprehensive Erosion Model for the 120-mm M256/M829A2 Gun System, Technical Report ARCCB-TR-98018, U.S. Army ARDEC, Armaments Engineering & Technology Center, Weapon Systems & Technology, Benet Laboratories, Oct 1998.

Figure 1.3 shows a typical $360^0$C macro-photo of the latest peak– eroded bore area that was taken from the same gun shown in figure 1.2. The bore region shown in figure 1.2 fired M829E3 rounds. This peak eroded bore area is the 1.4- to 1.6-m (57- to 63-in) RFT region and it was condemned on erosion based on numerous pits shown in this photo.

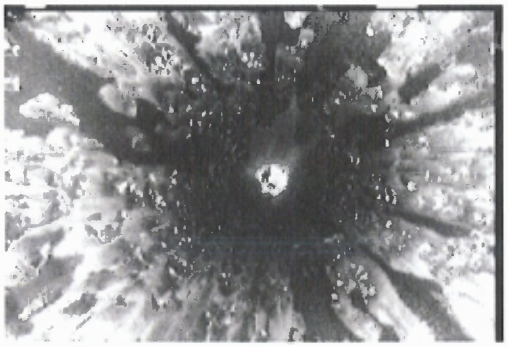

**Figure 1.3** Typical M829E3 M256 macro-photo; $360^0$ view of 0.9-to 2.0-m erosion band.

Source: S. Sopok, C. Rickard, G. Pflegl, P. Vottis, P. O'Hara, S. Dunn, and D. Coats, "Erosion Predictions for the Final Configuration of the M829E3 Round, Technical Report ARAEW-TR-04001, U.S. Army ARDEC, Armaments Engineering & Technology Center, Weapon Systems & Technology, Benet Laboratories, Jan 2004.

The first contribution of the proposed dissertation effort to the Army's mission will be to enable the use of high energy and high flame temperature propellant while concurrently lowering the barrel wear and erosion of the gun. During gun firing, the mircocracks grow, and the surface micro cracks, especially propagate through the chromium to the steel substrate. The original chromium deposit becomes, in effect, an assembly of individual, isolated islands as shown in Figure 1.4. By Fick's law of diffusion, a nano additive such as boronized ( BNNT /BNNF sublimate) chrome plated steel would result after every gun firing of each round. This phenomena is brought about by the propellant high flame temperatures. In addition, the nitrogenated BNNT/BNNF additives lower the bore temperature and heat transfer. Boronizing is a diffusion process which causes boron to strongly adhere to base metals. Boronizing can offer improved wear and erosion resistance, high-temperature use and lower friction values than many traditional coatings.

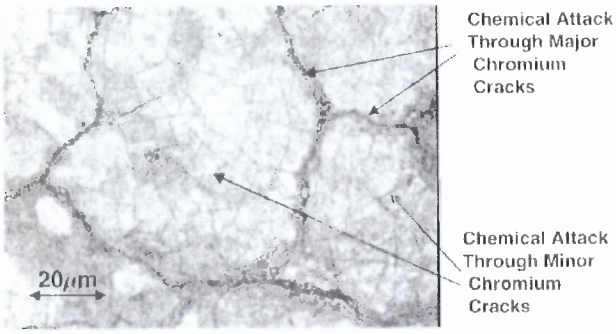


**Figure 1.4** Chemical Attack Through Major Chromium and Minor Chromium Cracks.

Source: S. Sopok, C. Rickard, G. Pflegl, P. Vottis, P. O'Hara, S. Dunn, and D. Coats, "Erosion Predictions for the Final Configuration of the M829E3 Round, Technical Report ARAEW-TR-04001, U.S. Army ARDEC, Armaments Engineering & Technology Center, Weapon Systems & Technology, Benet Laboratories, Jan 2004.

As described above, the Army is interested in reducing the barrel erosion, blast and flash characteristics of ammunition in large caliber gun systems by incorporating selected nano-size additives in propellant formulations. These characteristics are dependent on the propellant formulation thermochemistry and can be tailored to a certain extent by adjusting component compositions and incorporating specific additives. A great deal of work has been devoted to developing the class of materials known as nano-materials. A number of propellant formulations with new nano-scale crystalline form additives will be designed to reduce gun barrel wear and erosion through both decreased flame temperature and favorable propellant chemistry. Characterized by extremely small particle size, these materials have been found to exhibit interesting *unique* properties that are beneficial for many applications.

The second contribution of the proposed dissertation to the Army's mission will be to enchance the concept of high performance high energy density gun propellant through the use of the co-layered configuration. ARDEC developed a gun propellant that would meet future high performance ballistic requirements of a 120 mm direct fire

armament system. A layered propellant consisting of a fast inner burning layer and a slower outer burning layer, as shown in figure 1.5, was selected to achieve the requirements.

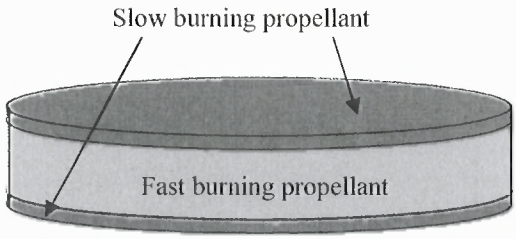


**Figure 1.5** Schematic Diagram of a Typical Layered Propellant Geometry

Specific technical goals included the following: impetus levels, of 1250 J/g and 1075 J/g for the fast layer and slower layer, respectively; a burning rate ratio of 3:1; an average flame temperature of 3450K or less; vulnerability and sensitivity characteristic similar to or better than those of JA2 and mechanical properties similar to or better than those of JA2 from -32C to 63C. The advantage of utilizing co-layered propellant is its progressive burning relative to pressure generation. A well designed and fabricated co-layered propellants can impart a "double hump" in the ballistic pressure-time plot, as shown in Figures 1.6 and 1.7, consequently increasing the muzzle velocity without significantly increasing the maximum pressure in the chamber. As the slow burning layer burns first the pressure in the chamber rises slowly and moves the projectile forward. The increasing volume in the chamber due to moving projectile decreases the pressure in the gun. However, when the slow layers are burnt out the fast burning inner layer begins to burn more quickly. Therefore, the pressure in the gun can be built for the second time transferring more kinetic energy to the projectile as shown Figure 1.6. The area under the

curve translates to the velocity of the projectile. So, by inducing the second hump, the area under curve can be increased. The shaded region in Figure 1.6 depicts that larger area under the curve, which can in turn increase the projectile velocity[12].

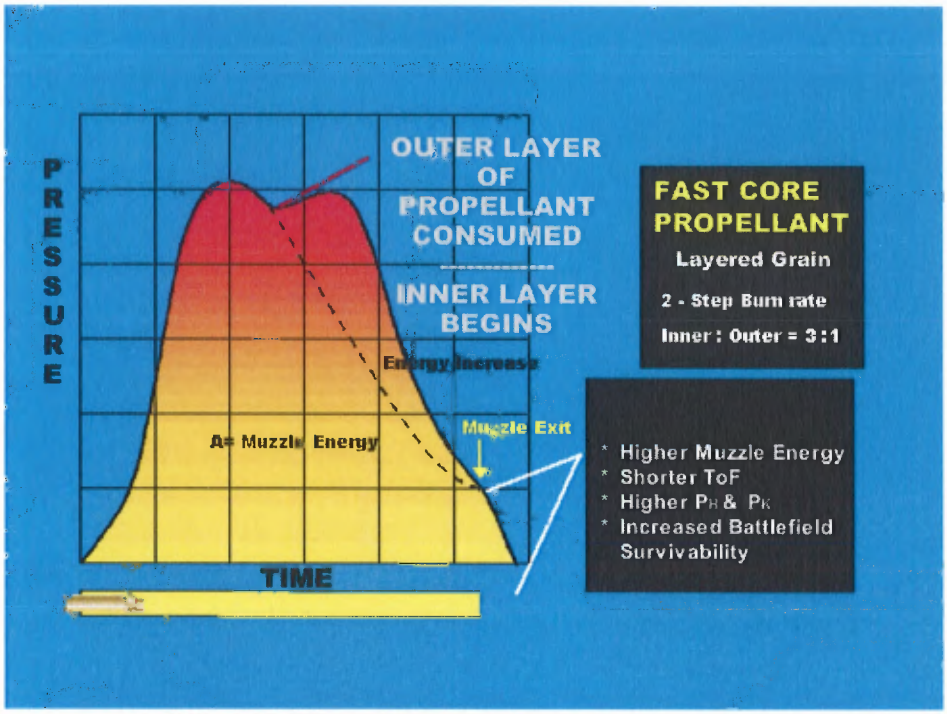


**Figure 1.6** Double Hump in the Ballistic Pressure-Time Plot.

Source: T.G. Manning, D. Chiu and D. Park, Characterization and Ballistic Properties of High Energy High Performance ETPE Gun Propellant for Future Large Caliber Applications" , Proceedings of the 2005 JANNAF 40th Combustion Sub-Committee/28th APS/22nd PSHS/ 4th MSS Joint Meeting at Charleston Convention Center & Charleston AFB, Charleston, S.Carolina, 13-17 Jun 2005.

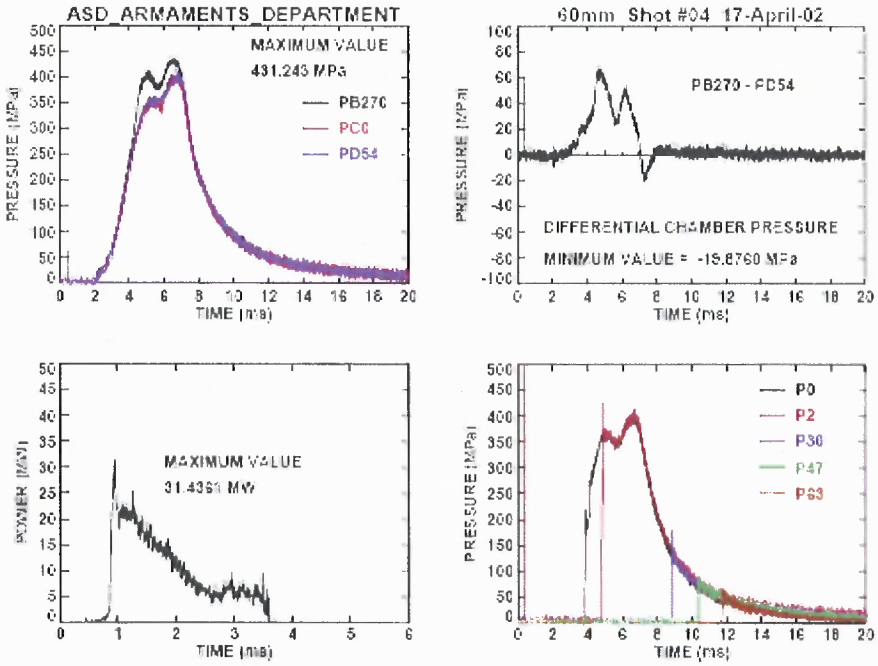


**Figure 1.7** A sample of pressure –time date. Typical P-t curves from 60mm ETC firings.

Source: T.G. Manning, D. Chiu and D. Park, Characterization and Ballistic Properties of High Energy High Performance ETPE Gun Propellant for Future Large Caliber Applications" , Proceedings of the 2005 JANNAF 40th Combustion Sub-Committee/28th APS/22nd PSHS/ 4th MSS Joint Meeting at Charleston Convention Center & Charleston AFB, Charleston, S.Carolina, 13-17 Jun 2005.

When designing a co-layered propellant, several parameters must be considered such as the burn rate ratio of fast to slow burning layers, thickness of individual layers, the configurations, and the manufacturability of the propellants. Usually the increasing burn rate ratio will yield better gun performance, and the ratio of 3:1 is desired [12]. Several configurations such as disc, cord, scroll, concentric wrap, and radial strip have been studied. Figure 1.8 shows a co-layered disks configuration. The purple layer is the slow burning propellant formulation and the inner white layer is the fast burning propellant formulation.

**Figure 1.8** Embossed 2" co-layered disks.

Source: T.G. Manning, D. Chiu and D. Park, Characterization and Ballistic Properties of High Energy High Performance ETPE Gun Propellant for Future Large Caliber Applications" , Proceedings of the 2005 JANNAF 40th Combustion Sub-Committee/28th APS/22nd PSHS/ 4th MSS Joint Meeting at Charleston Convention Center & Charleston AFB, Charleston, S.Carolina, 13-17 Jun 2005.

T.G. Manning, E. Rozumov, D. Park, S.Moy, and D. Chiu, Army Advanced Gun Propellant Formulations, Proceedings of the 55th JANNAF Propulsion Meeting/42nd Combustion Subcomittee/30th Airbreathing Propulsion Subcommittee/30th Exhaust Plume Technology Subcommittee /24th Propulsion Systems Hazards Subcommittee/12th Spectral and In-band Radiometric Imaging of Targets and Scenes User Group Joint Meeting, U.S. Army RDECOM-ARDEC, Boston Marriott Newton Hotel, MA, May 12-16, 2008.

The fastcore configuration through the use of micron–scale crystalline energetic materials such as 2,4,6,8,10,12-hexanitro-2,4,6,8,10,12-hexaazaisowurtzitane (CL-20) and RDX in the fast burning formulation and Nitroguanidine in the slow burning formulation, respectively provided a burn rate differential of 1.7:1 which is well below the 3:1 goal. In order to achieve high performance high energy density muzzle energy of 45% increase from the 3:1 burn rate differential, an investigation of nano-scale crystalline materials were conducted. The nanoscale crystalline materials investigated consisted of nano-aluminum, nitrogenated boron nanotubes/nanofibers, and polymeric nitrogen stabilized in single wall carbon nanotubes with the hope of achieving the 3:1 burn rate differential goal for high performance high energy density gun propellant. A great deal of work has been devoted to developing the class of materials known as nano-scale crystalline materials, e.g. nano-aluminum, functionalized carbon nanotubes, and nitrogenated boron nanotubes/ nanofibers. Characterized by extremely small particle size, these materials have been found to exhibit interesting *unique* properties that are

beneficial for many applications. Recent advances in novel energetic materials and formulations have allowed the development of high performing propellants that are also less sensitive with lower flame temperature and less erosive combustion products. Therefore, new propelling charges for these systems can be developed that would achieve compliance with Insensitive Munitions (IM) requirements and can also meet ballistic performance requirements, lower life cycle cost and green ammunitions that will be environmentally friendly.

# CHAPTER 2

# LITERATURE REVIEW

## 2.1 Solid Propellants

A solid propellant is a combustible solid that is capable of self-deflagration (or burning). A solid propellant consists of a binder, fuel and an oxidizer. Propellant burning is a propagating chemical process where the initial constituent substances near the propellant surface decompose and the fuel species are oxidized releasing heat. Some of the released heat is transferred back into the unburned propellant further decomposing the unburned propellant continuing the combustion front. The remainder of heat elevates the generated combustion products.

The ingredients and types of solid propellants vary greatly. The products of combustion depend on the type of solid propellant formulations but in most cases are predominantly $H_2O$, CO, $CO_2$, $H_2$ and $N_2$. For rocket propellants, combustion products include significant quantities of $Al_2O_3$ (or other oxidized metals), HCl and in rare cases HF. Combustion temperatures range from several hundred degrees for gas generating propellants up to 3,800 K or more.

Most solid propellants burn as a function of pressure that is as pressure increases so does the propellant's burning rate ($r_b$). Generally, propellants follow Saint Robert's Law:

$$r_b = a * P^n \tag{2.1}$$

Since the burning rate is an exponential function of pressure, generally burn rate is plotted as a dependent variable against pressure on a log-log graph. This type of curve plots is a straight line on a log-log set of axis.

## 2.2 Types of Solid Propellants

There are two types of solid propellants: homogeneous and heterogeneous (also known as double and triple base and composite propellants). In homogeneous propellants fuel and oxidizer are chemically joined by mixing with a solvent and a binder. Nitroglycerin/nitrocellulose (NG/NC) propellants are the classic homogeneous propellants. Homogeneous propellant are processed with and without solvents and ram extruded into granular propellants either as a chord, single, seven or 19 perforated grains. In heterogeneous propellants such as rockets, fuel and oxidizer species are physically distinct. In a heterogeneous propellant, a crystalline oxidizer, such as ammonium perchlorate (AP), is cast and cured into a polymer binder matrix that acts as the fuel species.

### 2.2.1 Double and Triple Base Propellants

A double base propellant consists of a nitrocellulose binder and a plasticizer processed with and without solvents and finally ram extruded for a chord, single, seven or nineteen perforated granular shapes. Conventionally, a nitrocellulose binder is colloided by using a solvent while plasticized with nitroglycerin or other nitrate esters such as triethylene glycol dinitrate (TEGDN), trimethylolethane trinitrate (TMETN) orbutanetriol trinitrate (BTTN) plasticizers. Nitrocellulose is nitrated to contain a 12.6 % nitrogen or 13.15 %

nitrogen depending on the applications. A double base propellant is modified by adding a nitroguanidine which makes it a triple base propellant. A triple base propellant had been used for indirect fire applications such as the artillery. A double base propellant is commonly used for direct fire applications such as tanks.

### 2.2.2 JA2 and M30 Propellant

JA2 Propellant is a modified double base propellant consisting of three major ingredients nitroglycerin (NG), nitrocellulose (NG) and diethylene glycol dinitrate (DEGDN). JA2 has found extensive use in gun propulsion applications because it

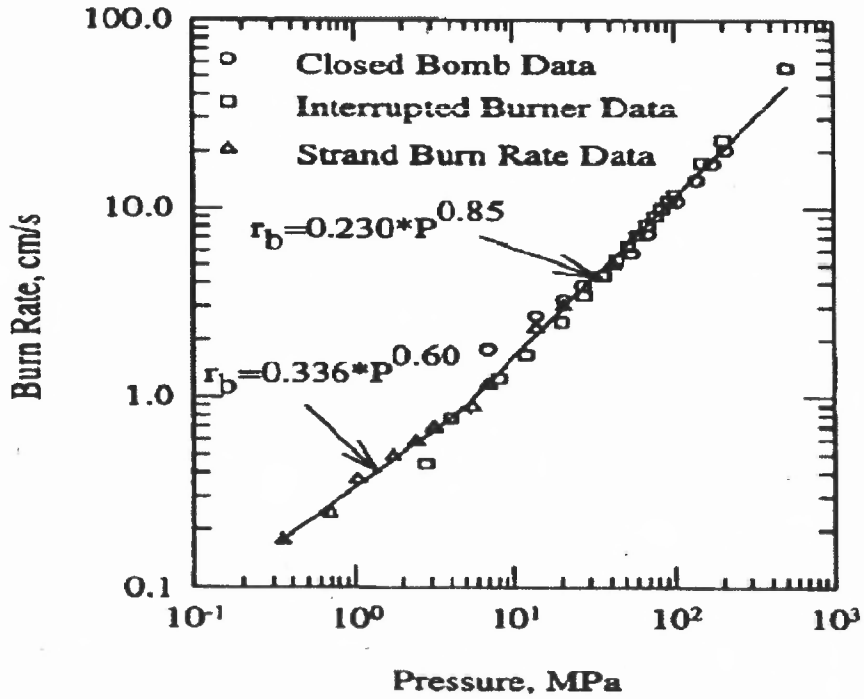


**Figure 2.1** Burning Rate of JA2 as a function of pressure[9].

Source: Mench, M.M., Yeh, C.L., Kuo, K.K., "Propellant Burning Rate Enhancement and Thermal Behavior of Ultra-Fine Aluminum Powders (ALEX)" Energetic Materials Materials Production, Processing and Characterization, 29th International ICT Conference, June 30–July 3, 1998, 301-305.

provides a fairly high impetus for propulsion without causing barrel erosion and because the propellant grains have a high resistance to fracture especially at extremely cold temperatures. Due to its wide use as a gun propellant, the burning rate of JA2 is shown in Figure 2.1. The burn rate at low pressure shows a slope break[13].

M30 and M31A2 are triple base propellants currently used for the 155mm M232A1 howitzer. The ingredients consist of the Nitrocellulose, Nitroglycerine, Nitroguanidine plus some additives. It is processed using the solvent as a processing aid, ram extruded into seven perforated grains and forced air dried.

### 2.2.3 Nitramine Based Composite Propellants

Different types of solid ingredients are held together by a polymer binder. M43 propellant is an example of a composite propellant manufactured by a solvent process. It is highly filled with an RDX crystalline material held together by a nitrocellulose and cellulose acetate butyrate binders after the process solvents had been air dried. Other energetic binders are quickly becoming viable binder alternatives for nitrocellulose. Such binders include Glycidyl Azide Polymer (GAP), PolyGlynn (PGN), Bis-azido methyl oxetane copolymer of 3,3-bis(azidomethyl) oxetane and 3-azidomethyl-3-methyloxetane (BAMO/AMMO), copolymer of 3,3-bis(azidomethyl) oxetane and 3-nitratomethyl-3-methyloxetane (BAMO/NMMO), and others. Energetic binders contain some oxidizing species that add some additional energy resulting in increased performance.

More recently, composite propellants based on nitramine organic oxidizers RDX and HMX have become increasingly attractive. Originally these compounds were developed for blasting. Their multiple nitro ($-NO_2$) groups balance the molecule's decomposition products almost ideally for gun propulsion. The physical structure of RDX

and cyclotetramethylene-tetranitramine (HMX) based propellants is very similar to that of Ammonium Perchlorate (AP) based composite propellants. However, like double base propellants the burning is homogeneous and there exists a dark zone between the propellant surface and the luminous flame. This dark zone decreases in size with increasing pressure and increased burning rate.

## 2.3 Ingredients Investigated

In this dissertation, several nano-scale crystalline materials were investigated for possible utilization in the current military ammunition systems. Many of the ingredients utilized are new or not fully understood yet. Some of these, nano-scale crystalline form of materials such as nano-aluminum, titanium dioxide, nitrogenated boron nanotubes/ nanofibers and polymeric nitrogen in single wall carbon nanotubes.

### 2.3.1 Aluminum/Nano Aluminum

Aluminum particles have been added to solid rocket propellants since the mid 1950s when it was found that aluminum combustion could raise the temperature of combustion and by consequence, the specific impulse of solid propulsion systems. It was also found that aluminum particles incorporated into a solid propellant motor can also improve combustion instabilities. Aluminum utilization also increases the propellant density. Since first utilized in the 1950s single aluminum particle combustion and aluminized propellant combustion have been studied extensively.

Research has primarily been limited to micron-sized particle combustion as nano-sized aluminum particles are still in the infancy of development. Many of the principles of micron-sized particle combustion apply to nano-sized particle combustion. It is found

that every aluminum particle has an impervious oxide shell. The melting point of the solid aluminum core is 933 K. As the particle is heated, the aluminum core is melted and induces egg-like stresses on the still solid oxide shell. Full-fledged ignition is thought to occur when the aluminum oxide shell is damaged exposing the molten aluminum core to the oxidizing environment.

Exposure of the aluminum core can happen by one of two mechanisms; the oxide shell can be ruptured by the phase changing process occurring in the aluminum core, otherwise, the shell itself may melt at 2,300 K. In either case, as the temperature reaches the oxide melting point, surface tension draws the molten oxide to a lobe to one side of the aluminum particle. The aluminum is found to evaporate readily above 2,000 K, well below its boiling point of 2,737 K. Figure 2.2, adopted from Mench [14] depicts the mechanism of aluminum ignition. As depicted in the figure, the aluminum particle core is first melted; next, either by rupture or by melting, the oxide skin forms an oxide lobe; finally the evaporating aluminum forms a combustion envelope around the burning particle. Mench aluminum particle combustion model describes the existence of aluminum sub- oxides occurring beneath the primary diffusion flame. The final product of aluminum combustion is alumina, $Al_2O_3$. The flame has been characterized at approximately 3,800 K, the saturation temperature of alumina.

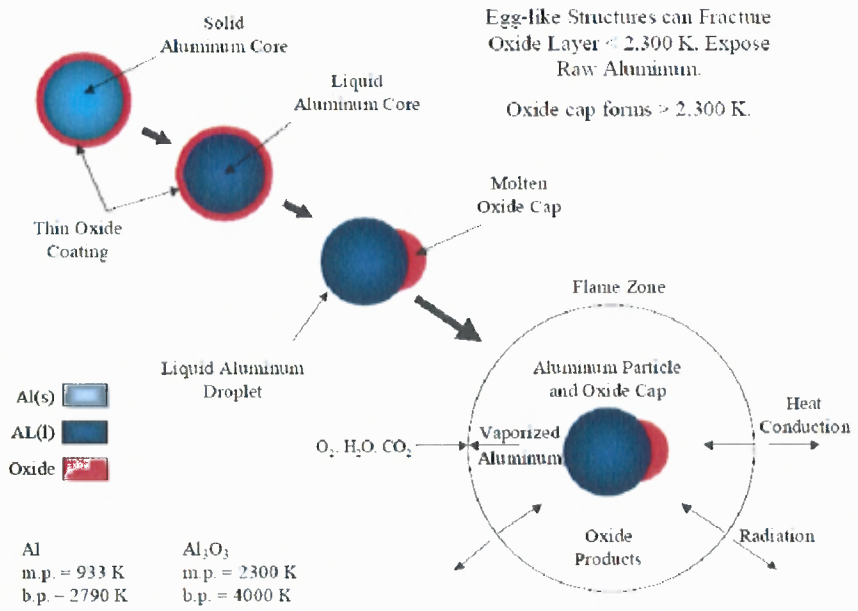


**Figure 2.2** Aluminum combustion mechanism.

Source: Mench, M.M., Yeh, C.L., Kuo, K.K., "Propellant Burning Rate Enhancement and Thermal Behavior of Ultra-Fine Aluminum Powders (ALEX)" Energetic Materials Production, Processing and Characterization, 29th International ICT Conference, June 30–July 3, 1998, 301-305.

Mench compared aluminum particle combustion times from a host of experimental investigations. He correlated particle combustion time to aluminum particle diameter and found good agreement. His presentation of others' data is shown in Figure 2.3. Figure 2.3 also shows that an extrapolation of the wealth of data implies very short combustion times for 300-400 nm particles (one of the several reported sizes for ALEX® aluminum). The extrapolated combustion times are three orders of magnitude smaller than any previously observed combustion times.

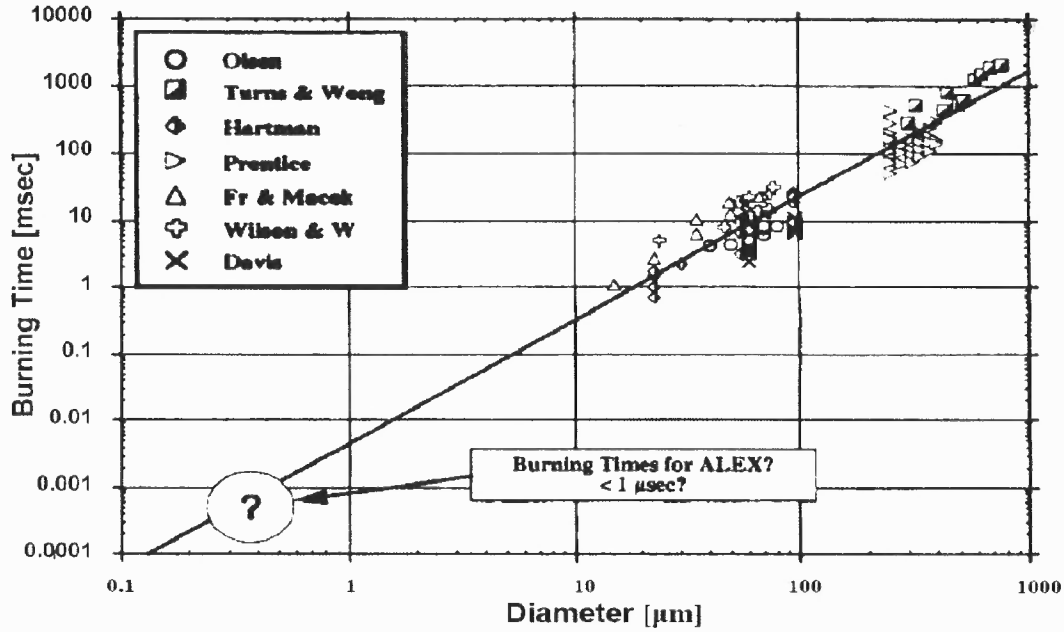


**Figure 2.3** Aluminum burning times as a function of particle diameter.

Source: Mench, M.M., Yeh, C.L., Kuo, K.K., "Propellant Burning Rate Enhancment and Thermal Behavior of Ultra-Fine Aluminum Powders (ALEX)" Energetic Materials Production, Processing and Characterization, 29th International ICT Conference, June 30–July 3, 1998, 301-305.

### 2.3.2 Boron/Nano-Boron

Boron has also been utilized as a metallic additive to composite propellants. Boron is attractive as a propellant fuel because of its extremely high gravimetric and volumetric heat of oxidation. Like aluminum particle combustion, most studies to date have focused on micron-sized particles rather than nano-sized particles. Also like the aluminum particles, each boron particle is surrounded by a thin oxide layer. Ulas and Kuo[15] found that the combustion of boron takes place in a two-stage process. The first stage of combustion is an oxide layer stripping process, as the oxide layer melts at the relatively low temperature 722 K. This process is slow and is kinetic or diffusion- limited process and constitutes a significant portion of the boron combustion time. Above this time the liquid boria forms islands on the neat boron surface. Boron melts at ~2,300 K, availing

the boron for combustion. However, boron combustion is slow due to the low vapor pressure of boron below its boiling point of 4,000 K. Boron combustion is further hampered by the thermodynamic preference to form HOBO below 2,400 K. This preference prevents the boron from achieving full heat release by oxidation. The conversion to form $B_2O_3$ from HOBO is slow in an oxygen/hydrogen environment again limiting the success of boron combustion [15]. It is expected that the utilization of nano-sized boron will assist boron combustion by addressing slow evaporation with significant increase in surface area. As described in the previous section 1, by Fick's law of diffusion, a nano additive such as boronized (BNNT/BNNF sublimate[16]) chrome plated steel would result after gun firing of each rounds. This phenomena is brought about by the propellant high flame temperatures. In addition, the nitrogenated BNNT/BNNF additives would lower the bore temperature because of high thermal conductivity and provide sufficient heat transfer. Boronizing is a diffusion process which causes boron to strongly adhere to base metals Boronizing can offer improved wear-resistance, high-temperature operation and lower friction values than many traditional coatings. Additionally, as has been described previously in Chapter1 section 1.2, increasing the $N_2/CO$ ratio and lowering the $CO/CO_2$ ratio in a gun propellant formulation, wear and erosion can be mitigated as shown in table 2.1.

**Table 2.1** Nitrogen Doped Boron Nanotubes in a Propellant

| **Formulation** | **Temp (K)** | **Impetus (J/g)** | **$N_2/CO$** | **Wear (mg)** |
|---|---|---|---|---|
| JA-2/RPD351 | 3743 | 1172 | 0.487 | 251[3] |
| IHGP-300 | 3723 | 1332 | 0.893 | 114[3] |
| M43 | 3004 | 1155 | 0.662 | 27[3] |
| M30 | 3022 | 1078 | 0.996 | 21[3] |
| TGD-009 | 2570 | 1070 | 0.668 | 21[3] |

| | | | | |
|---|---|---|---|---|
| M30 with Nitrogenated Boron Nanotubes/ Nitride (calculated using Cheetah 5 code) | 2976 | 1064 | 0.7751 | <21 |

Source: Walsh, C. and Knott, C., Gun Propellant Formulations with High Nitrogen Modifiers, Proceedings of the 31st JANNAF Propellant Development and Characterization Subcommittee Meeting, Charlottesville, VA, March 2003.

### 2.3.3 Polymeric Nitrogen Stabilized on Carbon Nanotubes: A Highly Energetic High Density Green Energetic Material

This section will discuss the different synthesis method of single wall carbon nanotubes with $N_8$ and $N_4$. For synthesis approaches to polymeric nitrogen, the following synthesis method were performed, optimized and compared: Electrochemical Reaction, Microwave Induced Chemical Reaction and Plasma Enhanced Chemical Vapor Deposition (CVD).

Nitrogen, the major constituent of air, consists of inert molecule nitrogen where two atoms are strongly triple-bonded. Now, Eremets et al [17, 18] have synthesized a polymeric cubic form of nitrogen where all atoms are connected with single covalent bonds, similar to carbon atoms in diamond. This cubic phase has not been observed previously in any element. It possesses unique properties such as energy capacity: more than five times that of the most powerful explosives.

Single-bonded nitrogen was postulated theoretically two decades ago. It was predicted that at high pressure, solid molecular nitrogen would transform to an atomic solid with a single-bonded cubic gauche (cg-N) structure.

There have been extensive experimental searches for this polymeric form of nitrogen at high pressures and various temperature ranges. Several new nitrogen phases

have been found, including a non-molecular semi-conducting phase, but production of polymeric nitrogen has failed until now. The *cg*-polymeric nitrogen structure has been formed in minute quantities by compression of azide ions in sodium azide. Attempts to recover the solid polymeric nitrogen phase at ambient conditions from high pressure experiments were unsuccessful, but catalytically forming the polymeric nitrogen phase at high pressures on a platinum substrate produced a Pt-N material which is stable at low pressures and temperatures, with a Raman line that can be assigned to a N-N vibration corresponding to that of the pure polymeric nitrogen phase extrapolated to low pressures . Initial theoretical simulations by Abou-Rachid showed that a poly-nitrogen $N_8$ cluster and a polymeric nitrogen structure can be formed and stabilized on the sidewalls of carbon nanotubes [19, 20]. More detailed ab-initio molecular dynamic simulations by Abou-Rachid et al further confirmed that a polymeric nitrogen $N_8$ cluster and a polymeric nitrogen structure can be formed and stabilized at ambient conditions inside a carbon nanotube.

Researchers of the High Pressure Group at the Max Planck Institute for Chemistry in Mainz have now been successful: they synthesized polymeric nitrogen directly from its molecular form at temperatures above 2000 K and pressures above 110 GPa ( 1.1x106 atm using a novel arrangement of the laser-heated diamond cell (Figure 2.4). X-ray diffraction measurements and Raman spectra of a transparent crystal confirm the formation of polymeric nitrogen with the theoretically predicted cubic gauche structure (cg-N) shown in Figure 2.5 (a) and (b). The phase is a stiff substance with a bulk modulus above 300 GPa, characteristic of strong covalent solids. Therefore, it is called

" nitrogen diamond", says Mikhail Eremets [17].

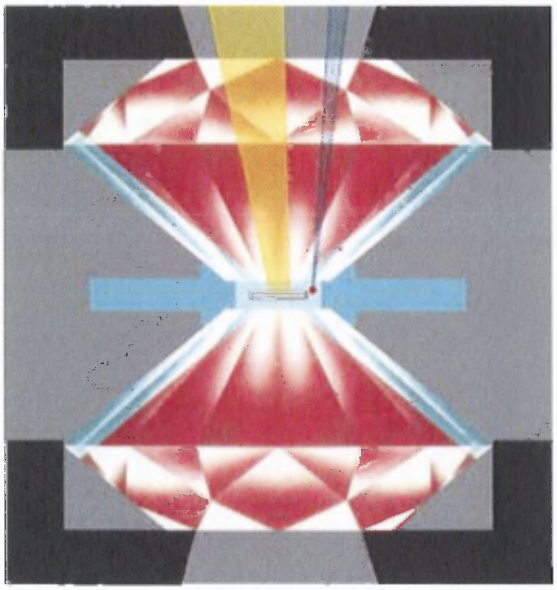

**Figure 2.4** Schematic view of a diamond anvil press. The sample in the centre is contained by a metallic gasket and an inert gas pressure medium. The sample is heated with high power IR laser (yellow) and the pressure is measured using the shift of the ruby fluorescence line which is excited with a blue argon-ion laser.

Source: Eremets, M.I., Gavriliuk, A.G., Trojan, I.A., Dzivenko, D.A., Boehler, R., Single-bonded form of nitrogen, *Nature Materials*, **3** (2004) 558.

a

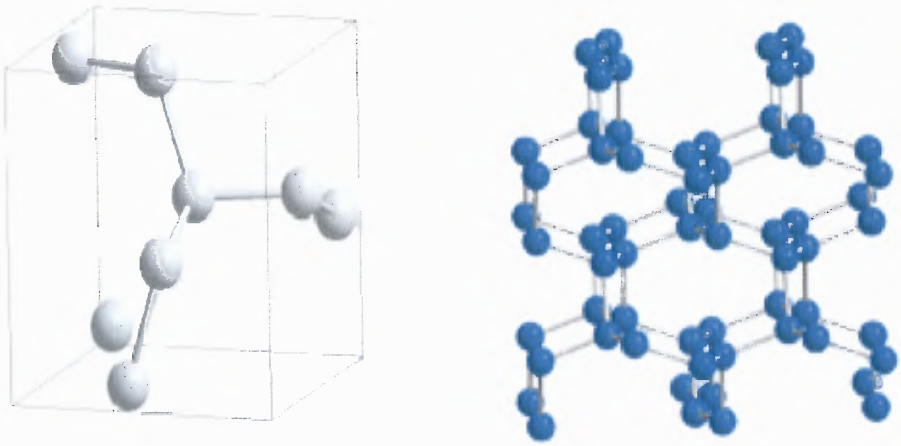

b

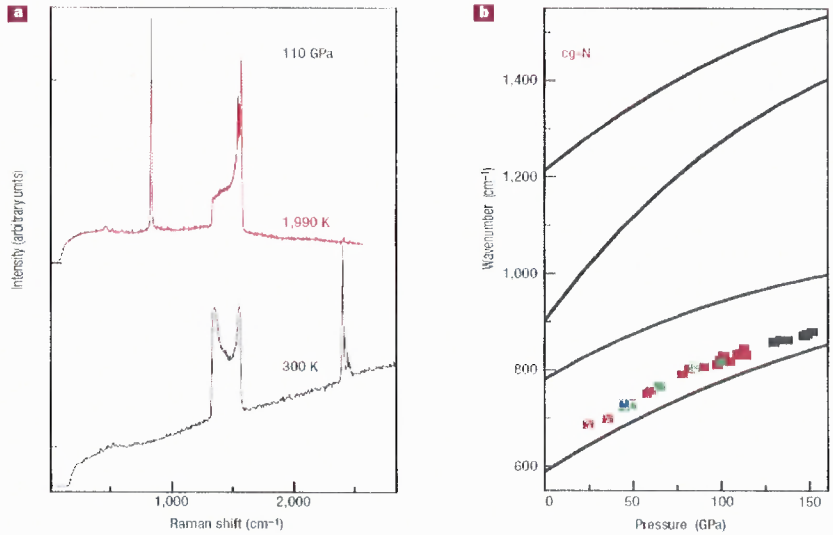


**Figure 2.5** (a) Theoretically predicted cubic gauche structure (cg-N);(b) Raman scattering from cg-N. a. Raman spectra of nitrogen before and after heating at 110 GPa. The starting sample (at 300 K) is in the molecular phase as evident from the vibron peaks at 2,400 $cm^{-1}$.The band at 1,300 $cm^{-1}$–1,550 $cm^{-1}$ is Raman signal from the stressed diamond adjacent to the sample. As a result of laser heating to 1,990 K, the sample transformed to a new phase: the vibron peaks disappeared while a pronounced peak at 840 $cm^{-1}$ appeared. Small peaks at 470 $cm^{-1}$ and 2,400 $cm^{-1}$ are from the untransformed molecular phase. Note that heating also improved hydrostatic conditions in the sample resulting in sharpening of the high-frequency edge of the diamond Raman band. b, Comparison of the pressure dependence of the Raman peak from the new phase (color points from four different runs) with calculations of zone-centre phonon modes for cg-N shown by solid lines.

Source: Eremets, M.I., Gavriliuk, A.G., Trojan, I.A., Dzivenko, D.A., Boehler, R., Single-bonded form of nitrogen, *Nature Materials*, **3** (2004) 558.

A lot more energy is stored in the single-bonded polymeric nitrogen than in the known stable form of triple-bonded molecular nitrogen. Therefore, a large amount of energy would be released under the transformation from the single-bonded to the molecular form, much more than that of the most powerful energetic materials. Since the only product of this transformation would be just common non-polluting molecular

nitrogen, the new polymeric nitrogen could be used as an explosive replacement for Trinitrotoluene (TNT) or HMX.

The nanostructured polynitrogen systems of $N_8$ and $N_4$ promise a factor of 10 theoretical increase performance when compared to TNT [21,22]. The thermochemical properties are tabulated in table 2.3. The research work will create a TNT replacement that can provide a factor of 10 theoretical increase in several performance metrics; (a) Nitrogen is unique in that diatomic molecule is bound by triple bond ( 954 kJ/mole) as shown in Figure 2.5. (a) The decomposition of single bonded (160 kJ/mole) polymeric nitrogen into $N_2$ is highly exothermic. As shown in table 2.3, CNT- $N_4/N_8$ is much more powerful as compared to TNT. High energetic materials made of pure nitrogen, are not only environmentally friendly but also have the highest power and energy release rates of monomolecular energetic materials.

The synthesized CNT -$N_8$ and $N_4$ will be compared with TNT performance characteristics as listed in table 2.3.

**Table 2.3** Theoretical Performance Values for TNT versus $N_4/N_8$

| Thermochemical Properties | TNT | $N_4/N_8$ (FCC) |
|---|---|---|
| ΔHd( cal/g) | 1100 | 6673 |
| ρ0 (g/ cc) | 1.63 | 3.1 |
| DCJ (km/s) | 6.93 | 19.74 |
| PCJ (Mbar) | 0.210 | 3.14 |

Source: Kuhl, A. L., Ullrich, G.W., Gurtman, G., McFarland, C., "Disruptive Energetics", 4th Advanced Energetics Technical Exchange, Jan 22-25, 2008, Fort Belvoir, VA

Kuhl, A.L., Fried, L.E. Howard, Michael W. and Seisew, M.R., et al, Detonation of Meta-stable Clusters, 39th ICT Conference on Energetic Materials, 24-27, 2008, Karlsruhe, Germany

Kuhl and coworkers have performed theoretical work and was able to determine the detonation properties of $N_4/N_8$[20,21] using the equation of state –JWL fit. The $N_4/N_8$ [21] has single-bonded polymeric phase (cubic gauche) of nitrogen with diamond like structure as described by Eremets, previously shown in Figure 2.5. Most of his work to date has been theoretical. Furthermore, a modelling and simulation performed by Ullrich et al on the $N_4/N_8$ molecule using targets such as a two story vented bunker and an open tunnel have demonstrated a bunker pressure of 200 bars from CNT-$N_4/N_8$ as compared to 2 bars from TNT in 7 msec.

The introduction of $N_4/N_8$ species into carbon nanotubes ( CNT) has been studied theoretically [23, 24,25,26,27] using molecular simulations based on first principles. The electronic structures, thermodynamics properties and chemical stability have been studied. It was also predicted that doped $N_4$ and encapsulated $N_8$ in CNTs should be stable as shown in Figures 2.6.

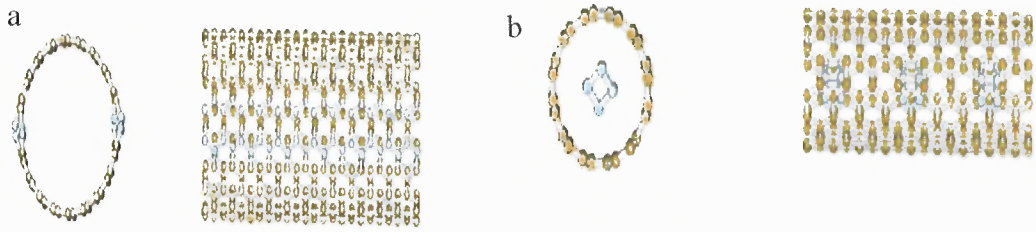


**Figure 2.6** (a) $N_4$ polynitrogen doped CNT (10,10) (b) Cubane nitrogen compound encapsulated in (6,6) carbon nanotube

Source: Abou-Rachid, H., Hu, A., Timoshevskii, V., Song, Y., Lussier, L-S., Nanoscale High Energetic Materials: A Polymeric Nitrogen Chain N8 Confined inside a Carbon Nanotube *Phys. Rev. Lett.* 100 (2008)196401.

A novel approach to the isolation of a polymeric nitrogen phase that would be stable at ambient conditions is suggested by the work of Abou-Rachid *et a l*[27]. They showed by *ab initio* molecular dynamics simulations that such a polymeric nitrogen phase can be stabilized at ambient conditions inside a carbon nanotube, as shown schematically in Figure 2.7 (a)-(b). Figure 2.7 (c) shows the calculated electron density of a N8 cluster of a polymeric nitrogen phase inside a (5,5) single wall carbon nanotube (SWNT). Bonding between the carbon atoms on the SWNT framework and nitrogen is also likely to occur and may further stabilize the cluster structure.

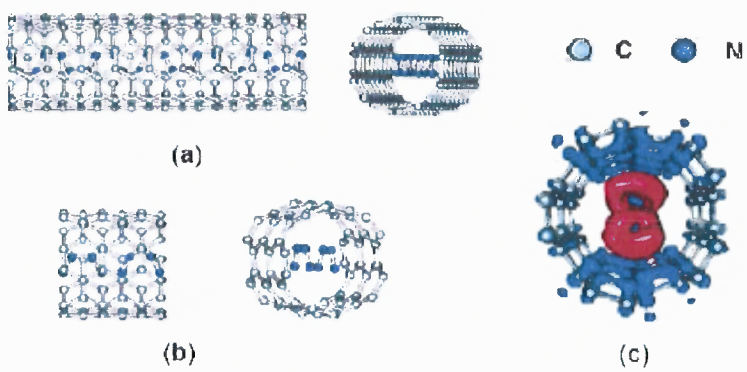


**Figure 2.7** (a) $N_{24}$ cluster inside a (5,5) single wall carbon nanotube ( SWNT) with 9 unit cells, (b) $N_8$ cluster inside a (5.5) SWNT with 3 unit cells, and (c) The electronic density of a $N_8$ cluster indise a (5,5) SWNT ,system, minus the electron densities of a stand alone carbon nanotube and nitrogen chain. The red (inside the SWNT) and blue colors denote the effective positive and negative charges, respectively.

Source: Abou-Rachid, H., Hu, A., Timoshevskii, V., Song, Y., Lussier, L-S., Nanoscale High Energetic Materials: A Polymeric Nitrogen Chain N8 Confined inside a Carbon Nanotube *Phys. Rev. Lett.* 100 (2008)196401.

Experimental synthesis confirmed nitrogen doping onto carbon nanotubes as shown in Figure 2.8, but details of doping sites and structures are not clear from the

experimental point of view. Therefore, further experimental studies on synthesis to encapsulate and dope into and onto carbon nanotubes are necessary at this time.

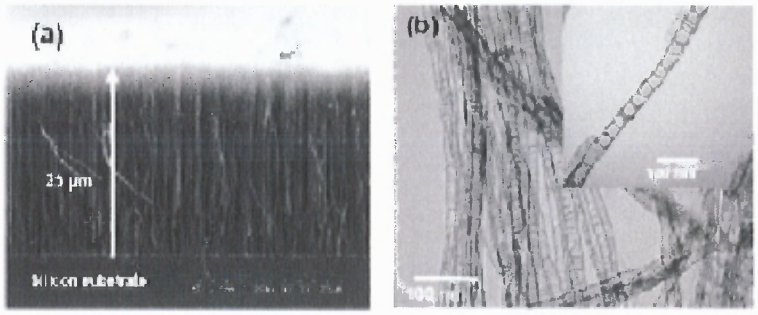


**Figure 2.8** N-doped CNTs (a) SEM image of aligned N-doped nanotubes (b) TEM image of N-doped nanotubes.

Source: Abou-Rachid, H., Hu, A., Timoshevskii, V., Song, Y., Lussier, L-S., Nanoscale High Energetic Materials: A Polymeric Nitrogen Chain N8 Confined inside a Carbon Nanotube *Phys. Rev. Lett.* 100 (2008)196401.

### 2.3.4 Nitrogenated Boron Nanotubes and Nanofibers

Boron and its compounds occupy a unique place within chemistry and physics because of the complexity of their uncommon structures associated with their unusual three-center electron –deficient bonds[28]. The existence of quasiplanar sheets boron clusters suggests that boron nanotubes and /or boron fullerenes can be formed. Experimental studies to synthesize the boron nanotubes (BNT) were therefore undertaken. Boron has a low density but a high melting point of around $2300^0$ C, as well as hardness close to that of a diamond. The Boron nanotubes (BNT) have been synthesized using similar methods to those used to grow carbon nanotubes (CNT). CNT synthesized primarily by methods such as arc-discharge[29], laser ablation[30] and chemical vapor deposition (CVD)[$^{31}$] are also applicable for the BNT synthesis. One of the objective of this dissertation is to

synthesize a novel BNT by using thermal CVD process. The synthesis of BNT nanotubes are desired and have attracted intense research interest[28].

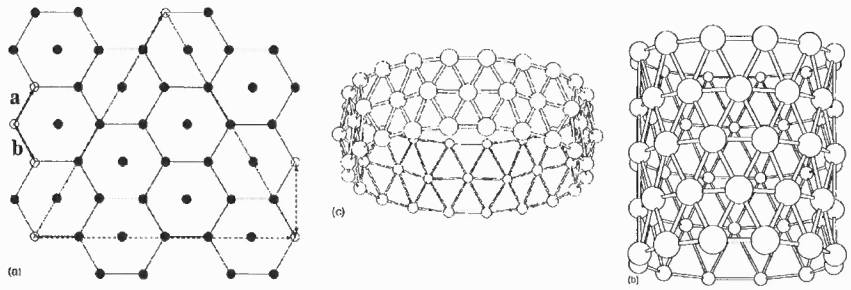


**Figure 2.9** (a) Construction of boron tubes from 2D hexagonal boron layers. The fat dashed lines mark the direction of the finite horizontal cut, as well as the direction of the infinite vertical cuts. (b) tubular $B_{60}$ cluster composed of five 12 membered rings. (c) $B_{60}$ cluster composed of three 20 membered rings and characterized by a buckled surface.

Because of the similarity of the chiral structure of carbon nanotubes and boron nitride (BN), it is just as convenient to discuss the properties and formation mechanism of BN nanotubes in terms of carbon nanotube models. The BNT clusters can be constructed via cut and paste procedure using the basic building 2D honeycomb lattice shown in Figure 2.9(a). It follows the same procedure used in constructing a CNT from graphene sheets. Two tubular segments of $B_{60}$ are shown in Figures 2.9(b) and 2.9(c). Both figures show remarkable structural stability. This type of structure indicates low strain energy, which is defined as the difference in energy per atom in a tube of a given diameter and that of the corresponding flat sheet. This fact is an indication that a BNT can be grown experimentally. The carbon nanotubes are known to be either metallic or semiconducting, depending on the tube diameter, wrapping angle, twisting and topological defects while BN nanotubes have a wide band gap that is insensitive to tube

diameter and chirality that can be controlled by chemical composition. This phenomenon is due to the ionic origin of the band gap. The strong ionic B-N bonding has an influence on the formation of BN nanotubes. Furthermore, the existence of quasiplanar boron clusters implies the formation of boron nanotubes and boron fullerenes, because during synthesis, a growing quasi-planar cluster tends to remove dangling bonds by forming closed tubular or polyhedral modifications[32].

## 2.4 Gun Propellant Formulation Optimization

Gun propellant formulation optimization is performed by using the thermochemical code, Cheetah version 5, developed by Lawrence Livermore National Laboratory. This code solves thermodynamic equations between product species to find chemical equilibrium. Cheetah solves the equilibrium of the reaction at a specified pressure and temperature. The gun propellant formulations impetus, flame temperature and theoretical maximum density are determined to be used in the interior nballistic code determination of the theoretical muzzle velocity. The combustion products such as CO, CO, etc. are obtained and determined in the liquid, vapor or solid phase. The combustion products from the Cheetah run can also determine if the propellant formulation is erosive or not. Chapman – Jouget ( C-J) theory indicates that the detonation point is a state of thermodynamic and chemical equilibrium that predicts properties of state. From these come the detonation velocity and other performance indicators such as impetus, flame temperature and density.

## 2.5 Motivation

The novel energetic and nanoscale crystalline materials when incorporated into gun propellant formulations will clearly have the great potential of meeting the objectives of previously discussed above, for example, longer gun barrel life, high performance high energy density, insensitive munitions properties, low life cycle cost and green munitions properties.

# CHAPTER 3

# PREDICTIVE TOOLS

## 3.1 Modelling Tools

The purpose of this section is to briefly describe the modeling tools used that are related to the experimental studies and synthesis of nano-scale crystalline materials discussed in this thesis. The tools described facilitate understanding the theoretical energy content of advanced gun propellants with incorporated nanoscale energetic materials. For example, the thermochemical equilibrium computer code used to predict the composite propellant's energy content when nano-scale crystalline materials are incorporated.

### 3.1.1 Chemical Equilibrium Codes

Several chemical equilibrium codes were utilized to predict the energy content of propellant formulations. These codes, using thermodynamic properties (such as molecular weight and heat of formation) of ingredients as well as reactor conditions (constant volume, constant pressure, etc) as their inputs, output the state (temperature, pressure, etc) and chemical species of the products that would result from an infinite time for thermal equilibrium to be achieved. These codes rely on an internal library of product species and their corresponding molecular weight, heat of formation, specific heat capacity, and other properties to determine the products of the reactor. The constant volume of chemical equilibrium, while a simplification, is a suitable approximation to the final state that will be observed in a gun chamber for ballistic purposes. Many of the

major product species, $H_2O$, $N_2$ , $H_2$ , and CO form rapidly; the thermal equilibrium calculations can closely predict the energetics of the composition. The most significant deviation between equilibrium and reality will exist for metal combustion. Metal particles may have significant ignition delays or may agglomerate such that these materials may burn incompletely, failing to yield their expected heat release or predicted products. All the thermochemical equilibrium calculations results presented in this writing are performed under constant volume, constant internal energy conditions.. A discussion of the treatment of this phenomenon will be addressed later. All the thermochemical equilibrium calculations results presented in this thesis were performed under constant volume, constant internal energy conditions. The constant volume of chemical equilibrium, while a simplification, is a suitable approximation to the final state that will be observed in a gun chamber for ballistic purposes

#### 3.1.1.1 CHEETAH 5.0 Code

This analysis utilized Cheetah 5.0 developed by Energetic Materials Center of the Lawrence Livermore National Laboratory. CHEETAH has many functions and capabilities. It has built in gun propellant analysis and computes impetus directly. CHEETAH has many product libraries built in as well as several equations of state. These non-ideal equations of state accurately predict high-pressure results and combustion products. The chemical equilibrium results stated in this writing are computed using CHEETAH 5.0 unless otherwise specified. Since CHEETAH[34] is export-controlled software, no example inputs and output files are included here.

### 3.1.2 MCVECP Code

Propellant development began using the Hunter version 3.04 of the MCVECP[33] equilibrium code, developed by the US Navy. Work using this equilibrium code was very limited because it was found to be unstable when some elements such as boron were added into propellant formulation. Since MCVECP is also export controlled software, no inputs and output files are included here. The Heat of Explosion of the propellant formulation was determined by using this code.

### 3.1.3 Interior Ballistics Code

IBHVG2, which stands for Interior Ballistics of High Velocity Guns, version 2, is a lumped-parameter, interior ballistic computer code. The code, which was developed at the Ballistic Research Laboratory [see report 34]. is an updated version of the classic Baer Frankle interior ballistic code. IBHVG2 is used for calculation of interior ballistic trajectories, including gas pressure, projectile displacement and projectile velocity as a function of time. The code treats both regular and deterred propellants. It contains powerful variational and searching capabilities, so that it can, for example, search and find the best propellant dimensions, given the maximum allowable gas pressure. This report thoroughly documents IBHVG2, so that all of its many features can be used effectively. The report contains a detailed description of the range of possible user input and description of both the algorithms embodied along with the FORTRAN subroutines which implement them. There are also complete examples of input and output from the code. Although the code has been written to be as generally applicable as possible, the report has a short section describing modifications that are necessary to enable the code

to run on various computers and compiler combinations. A machine-readable copy of the code can be obtained by contacting the authors of this report [34].

### 3.2 Gun Propellant Formulation Optimization

Gun propellant formulation optimization is performed by using the thermochemical code, version 5, developed by Lawrence Livermore National Laboratory. This code solves thermodynamic equations between product species to find chemical equilibrium. Cheetah solves the equilibrium of the reaction at a specified pressure and temperature. The gun propellant formulations impetus, flame temperature and theoretical maximum density are determined to be used in the interior ballistic code determination of the theoretical muzzle velocity. The combustion products such as CO, CO, etc. are solved and determined in the liquid, vapor or solid phase. The combustion products from the Cheetah run can also determine if the propellant formulation is erosive or not. Chapman – Jouget ( C-J) theory indicates that the detonation point is a state of thermodynamic and chemical equilibrium that predicts properties of state. From these come the detonation velocity and other performance indicators such as impetus, flame temperature and density can be determined.

# CHAPTER 4

# SAMPLE PREPARATION

## 4.1 Propellant Preparation

The RDX based propellant formulations incorporated with nano-scale materials such as nano-aluminum, nano-titanium dioxide, nano-boron and carbon nanotubes were prepared using the conventional solvent process. The energetic ingredients, solvents and additives are weighed out individually following the propellant composition optimized using the Cheetah Code version 5. These ingredients are mixed in a horizontal sigma blade mixer until the mix becomes homogeneous followed by evaporation of the solvents to approximately 30% by weight. The propellant mix is then extruded into shapes that were determined by using the interior ballistic code, IBHVG2.

## 4.2 Preparation of Carbon Nanopaper

A new processing method to produce self-assembled reinforced nanopaper by using single-wall nanotubes (SWNT) was utilized. The electrochemical and PECVD synthesis experiments used SWNT nanopaper as electrodes and substrates placed on quartz boat, respectively. Highly SWNTs obtained from Southwest Nanotechnologies Inc (SWeNT) and Cheap Tubes Incorporated were used in these experiments. The Cheap Tubes SWNTs have an outer diameter of 1-2 nm and fiber length of 5-30 μm. SWNTs from SWeNT Inc have an outer diameter of 1.12 nm and average fiber length of about 1.02 μm. The SWNT nano paper is an entangled mat of SWNTs, which is a highly

porous mesh structure. To successfully produce SWNT nano paper, it important toprepare a uniform SWNT dispersion. This was done as follows. The powders of SWNTs were mixed with the deionized water , and then about two drops of a surfactant Triton-X100 was added. The suspension was subsequently dispersed using an ultrasonic horn sonicator (FISHER SCIENTIFIC Sonicator 3000) at 300 W to achieve a uniform dispersion of SWNTs. The high-energy sonication times ranged from 15 to 60 min. Finally, the suspension was vacuum filtrated through a 10 LC-MILLIPORE MITEX™ membrane filter to produce the final nano paper. The preliminary nano paper was further cut into ¼ inch x ½ inch small sheets for used as substrate for the polymeric nitrogen synthesis. Figure 4.1 shows the ambient room temperature dried SWNT nanopaper after vacuum filtration.

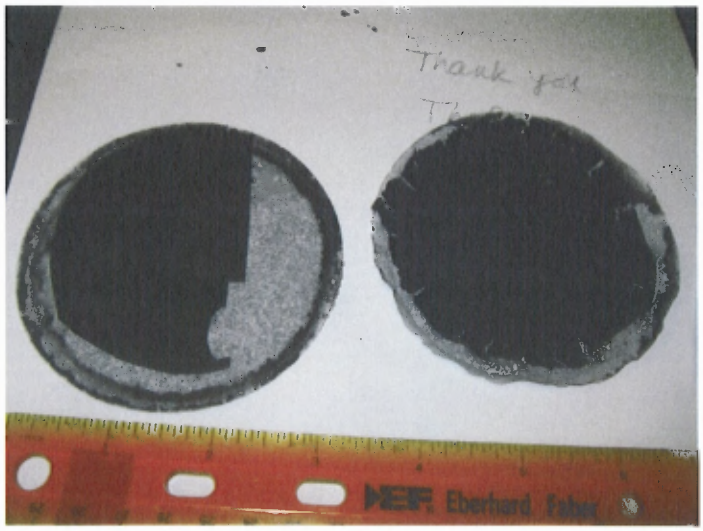


**Figure 4.1** Ambient temperature dried SWNT nanopaper.

Realization of the applications potential of SWNT paper has been hindered by the many difficulties associated with their processing. Fabricating low-density carbon

nanotube powder into functional macroscale structures has been a major challenge. Some progress has been made recently with the fabrication of one-, two-, and three dimensional bulk nanotube material in the form of fibers, sheets, and Bucky Pearls™ pellets. However, while individual SWNTs display impressive Young's moduli and strengths of approximately 640 and 40 GPa, respectively, the mechanical properties of the bulk materials remain disappointing. These low bulk mechanical properties are in part because the individual SWNT usually forms 10–50nm-diameter bundles that are only weakly bound by van der Waals interactions at junction points. Both carbon multiwalled nanotubes (MWNTs) and SWNTs have been used as reinforcing agents in polymer and epoxy composites [35]. Ideally, any load applied to the polymer matrix is transferred to the nanotubes. This load transfer relies on effective interfacial stress transfer at the polymer–nanotube interface, which tends to be polymer dependent. This reinforcement technique has met with some success, providing increases in Young's modulus by a factor of 1.8 for 1 wt% loading of MWNTs in polyvinyl alcohol, and increases in hardness by a factor of 3.5 for 2 wt% loading of SWNTs in epoxy [36]. In this work, we showed that the reverse procedure of polymer intercalation can be used to reinforce bulk nanotube SWNT materials. Binding agents such as polystyrene were intercalated into the porous internal structure of nanotube SWNT sheets ~Buckypaper[37]. Intercalation was performed by simply washing the nanotube sheets in 1% to 5% polystyrene polymer in toluene solutions at the end of the vacuum filtration process. The resulting polymer-intercalated sheets display improvements in Young's modulus and tensile strength[38].

The nanotube sheets, referred to as Buckypaper or nanopaper, used in this work were prepared by filtration of SWNTs dispersed in water and Triton X-100, as previously

described. The SWNTs containing small amount of metal catalyst were obtained from CHEAP Tubes Inc. The carbon nanotube sheets were annealed under flowing ammonia or nitrogen at up to 1000 °C before use, in order to remove residual surfactant, solvents, and contaminants. Under these conditions the metal particle impurities are also vaporized. These sheets were then cut into rectangular strips (40 mm x 2 mm x 2 cm). Buckypaper strips were washed in polystyrene (PS) solution once, and then dried in ambient conditions for 8 hours.

Raman spectroscopy was used study the nature of the insertion or infiltration of the polymer into the SWNT bundles. In the low-frequency region of the Raman spectrum, a number of features associated with the radial breathing modes of the SWNT are observed for all the nanopaper sheets. These features are slightly downshifted by approximately 2 $cm^{-1}$ for all polymer coated sheets compared to the pristine sheets as shown in figures 4.2 and 4.3. The small frequency shift suggests the environment of the individual SWNT has not dramatically changed. However, the presence of a downshift may suggest a weakening of the intertube van der Waals interaction, indicating that polymer chains are beginning to diffuse into the ropes, hence debundling the nanotubes [39]. The DSC data found in Appendix A, Figure A.4-A.6 for unanealed from Cheap Tubes SWNT show changes in the melt transition consistent with crystallization of the polymer chains onto the nanotube ropes on infiltration. This is in good agreement with previous studies showing nanotubes acting as nucleation sites for polymer crystal growth[40].

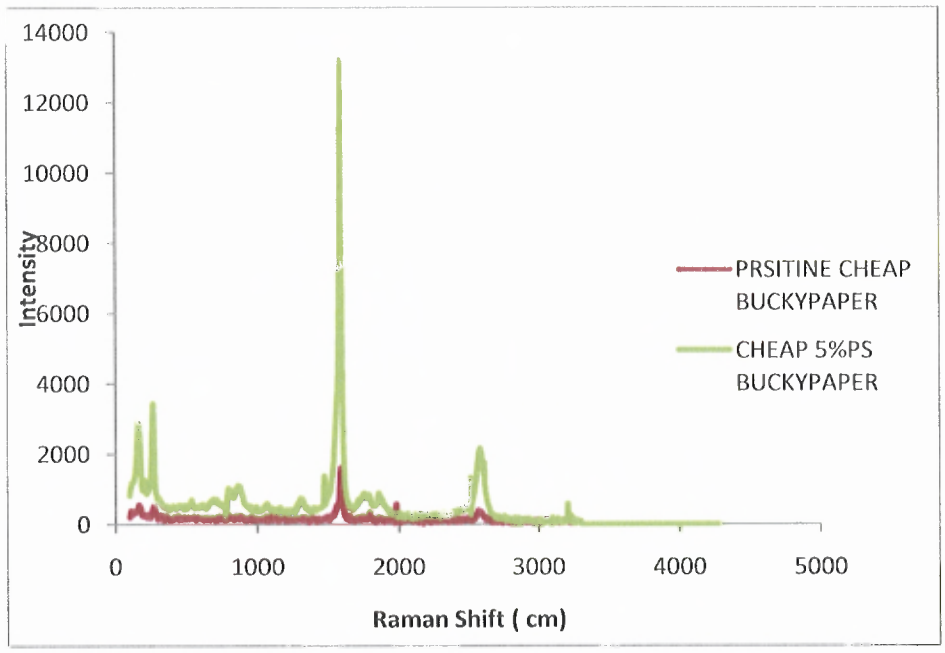


**Figure 4.2** Raman spectra using 735 nm laser excitation for pristine SWNT nanopaper and 5% polystyrene coated nanopaper.

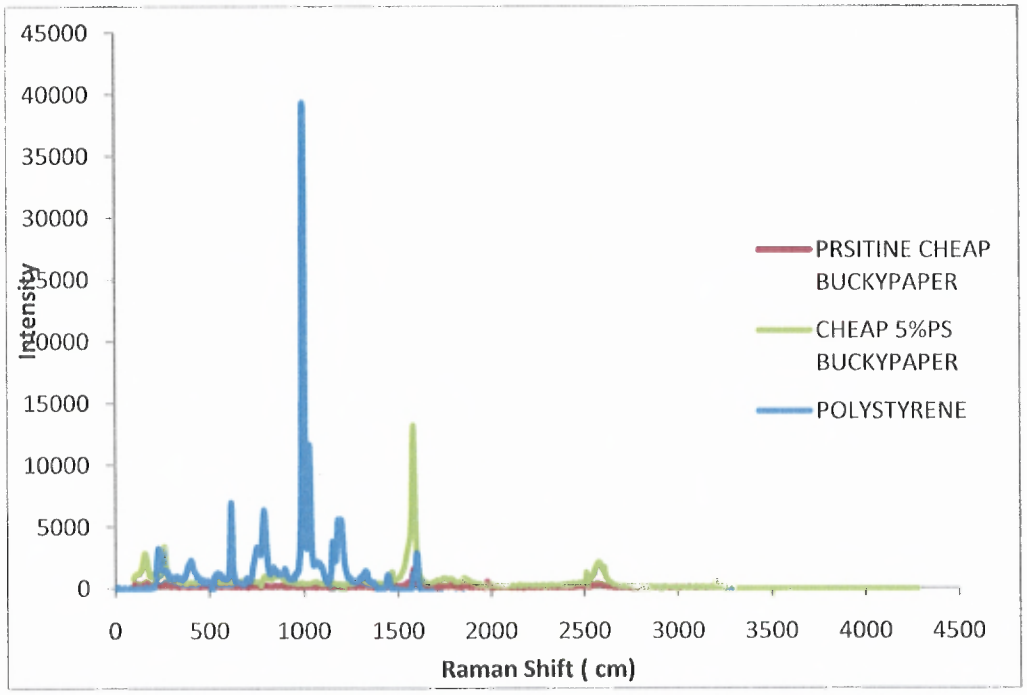


**Figure 4.3** Raman spectra using 735 nm laser excitation for pristine SWNT (red), 5% polystyrene coated nanopaper ( green) and polystyrene ( blue).

SEM images are shown in Figures 4.4 (a) and (b) from the surface of a pristine nanopaper sheet and a PS coated SWNT sheet, respectively. For the pristine sheet, a porous mat of SWNT ropes is seen on the surface shown on Figure 4.4 (a). For the PS coated sheet, however, it is clear on Figure 4.4 (b), that the surface has been coated with polymer, although this coating is relatively thin as pores can still be seen. More importantly, Figure 4.4(c) shows that not just the outer region, but the entire surface of the nanotube sheet, has been coated with a thin layer of polystyrene suggesting extensive intercalation. that sizable infiltration of PS between the individual SWNTs may have occurred.

In conclusion, polymer chains can be infiltrated into porous nanotube sheets in near equilibrium conditions by soaking in polymer solutions. SEM measurements show that the infiltrated polymer adsorbs onto the internal surface of existing free volume within the sheets. In all cases, Raman spectroscopy shows that polymer strands have partially diffused between individual nanotubes within the ropes. Overall, infiltration results in the enhancement of inter-rope stress transfer, which strongly modifies the mechanical properties, providing increases in Young's modulus, strength, and toughness by factors of 3, 9, and 28, respectively[ 41].

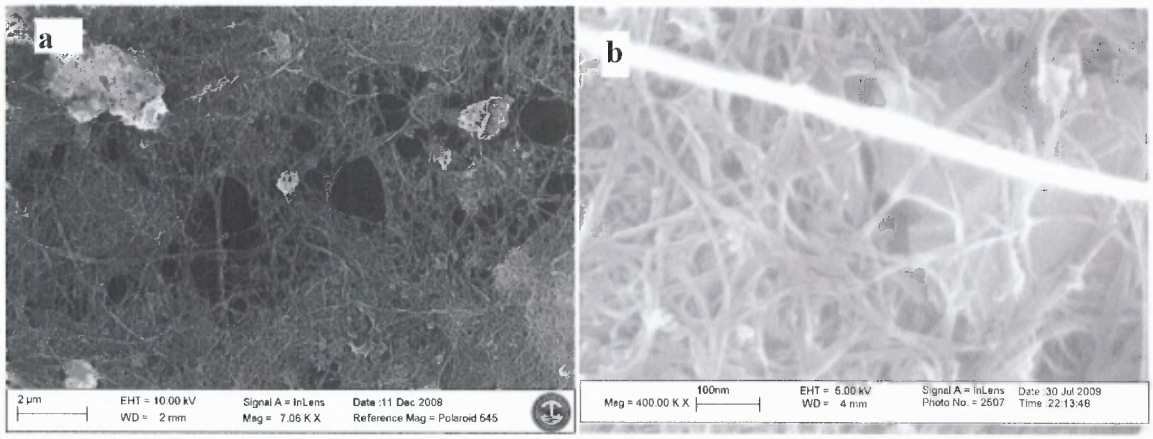

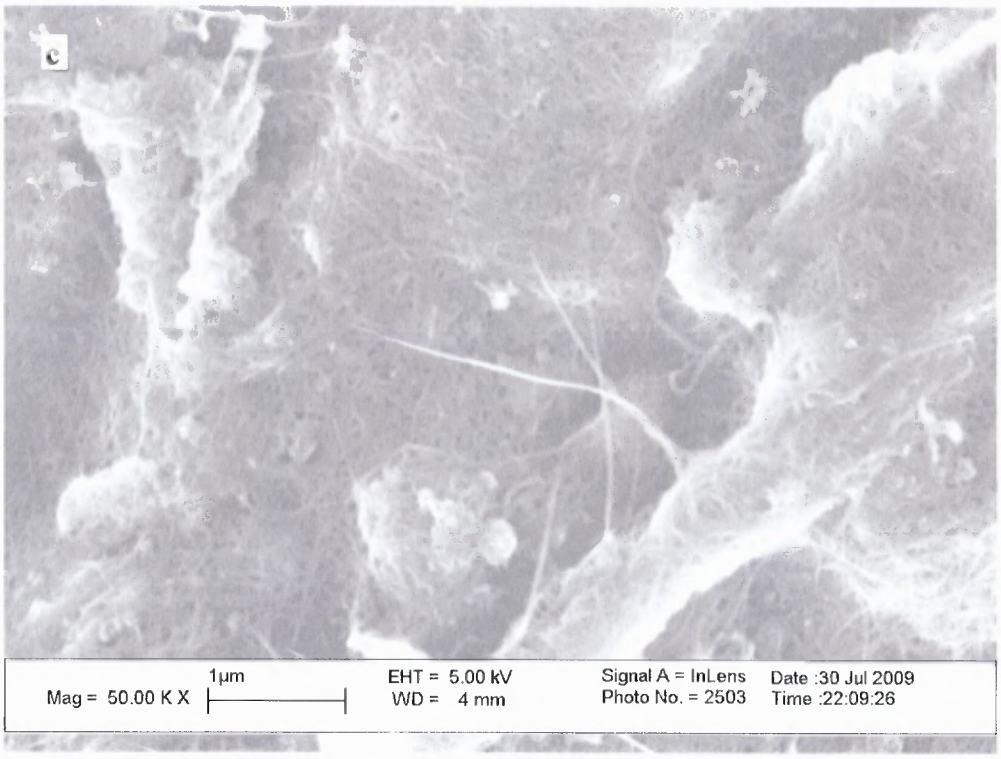


**Figure 4.4** SEM images of some of the CHEAP SWNT bundles from sample obtained from Cheap Tubes Inc used in this study. (a) Surface of pristine nanotube sheet. Prepared from these SWNT , (b) Surface of polystyrene infiltrated nanotube sheet (c) Surface of nanotube sheet, showing a thin coating of PS polymer indicating sizable infiltration had occurred.

### 4.3 Synthesis of Polymeric Nitrogen and Boron/Nitrogenated Boron Nanotubes

As previously discussed in section 2.3.3, there were four different synthesis methods of single wall carbon nanotubes encapsulated and doped with $N_8$ and $N_4$ investigated. Novel nanoscale synthesis performed by thermal and plasma enhanced chemical vapor deposition methods followed by ultraviolet light induced electrochemical and microwave induced electrochemical reactions.

#### 4.3.1 Thermal Chemical Vapor Deposition Method (T-CVD)

Encapsulation and doping of $N_4$ and $N_8$ and related clusters into and on the sidewalls of carbon nanotubes involves the initial synthesis of carbon nanotubes followed by

deposition of $N_4$ and $N_8$ and polymeric nitrogen clusters using either thermal enhanced chemical vapor deposition. Ethanol and acetylene mixed with argon were used as carbon sources, while melamine was used as the source for nitrogen doping and ferrocene as the precursor compound for the floating iron catalyst needed for carbon nanotube growth. Melamine has a chemical structure with nitrogen atoms arranged in the 2,4,6-triamino-1,3,5-triazine nitrogen conformation. The thermal enhanced methods ( schematic of apparatus is shown in Figure 4.5) was initially evaluated for synthesis and eventual scale up because of its relatively low cost. However, this synthesis method was not pursued due to extensive work already performed by Abou-Raschid et al [24,25] using thermal chemical vapor deposition to form bamboo-shaped multiwall carbon nanotubes where nitrogen doping was observed but no evidence for polymeric nitrogen clusters was found.

A plasma chemical vapor deposition approach using pre-synthesized SWNT with high surface areas was considered to a better approach to forming polymeric nitrogen clusters on and inside the nanotube sidewalls. Plasma are also known to provide a non-equilibrium environment for the synthesis of metastable species.

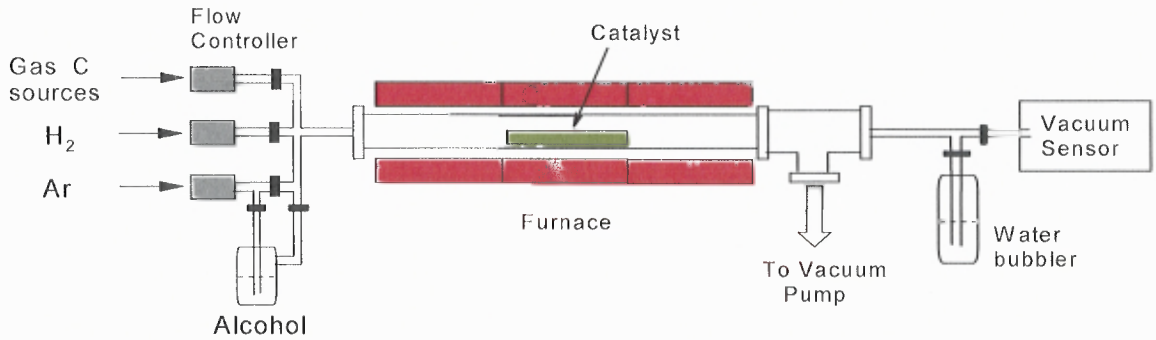


**Figure 4.5** Experimental Set-Up: Schematic for Thermal Chemical Vapor Deposition Process.

### 4.3.2 Plasma Enhanced Chemical Vapor Deposition Method ( PECVD)

Synthesis apparatus for plasma-enhanced Chemical Vapor Deposition (PECVD) shown in figure 4.6, set up by Yu *et al* [45]. was used in this investigation. PECVD synthesis shows distinct advantages in nitrogen doping of the nanotubes[42, 43. 44, 45, 46 ]. Conventionally, melamine is a nitrogen-containing organic compound which will evaporate in the plasma to nitrogen radicals that will then dope, carbon nanotubes being formed or nanotubes used as a substrate, with nitrogen groups [47, 48, 49, 50].

The deposition chamber in the PECVD system is a quartz tube 78 cm in length with an inner diameter of 3.8 cm for deposition carried out under radio frequency (RF) plasma conditions. Heating of the SWNT nanopaper substrate, which was placed in a quartz glass boat, was accomplished by placing the deposition/reaction tube in a temperature-controlled tube furnace. Argon or hydrogen carrier gas mixed with the nitrogen precursor gas were used at a flow rate of 25-50 standard cubic centimeters per minute (sccm). Three SWNT nanopaper substrates were placed in boats located in the front, middle and back of the reaction zone about 40 mm apart. A thermocouple that was isolated from the grounded anode was kept in contact with only the middle substrate during plasma reaction with nitrogen on the nanopaper substrate.

a

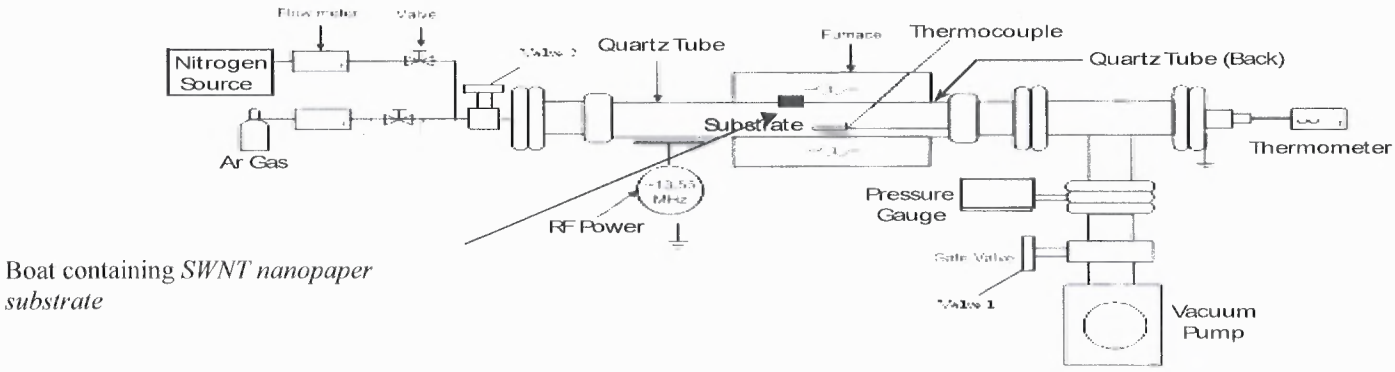


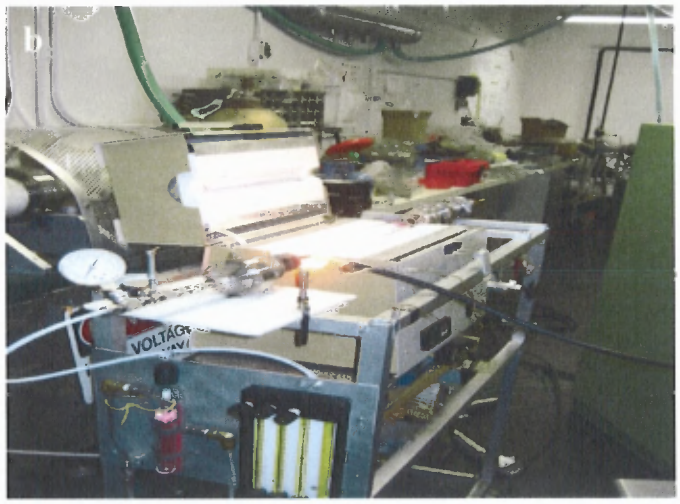

**Figure 4.6** Experimental set-up for plasma-assisted synthesis: a) Schematic of Plasma-Enhanced Chemical Vapor Deposition ( PECVD) apparatus, and b) Photograph of the PECVD set-up used in this work.

### 4.3.3 Electrochemical Method

Prior to reaction by the electrochemical method, a chemical vapor deposition process with ammonia was used to dope the SWNT nanopaper used as the working electrode. As discussed previously in section 4.2, the SWNT nanopapers were prepared as follows: The SWNT powder was de-agglomerated and suspended in water by sonication in the

presence of Triton X-100 surfactant. The suspension was vacuum-filtered through 0.5-5 micron pore size Teflon coated membranes. After washing with de-ionized water, a self-assembled, free-standing sheet of nanopaper consisting entirely of SWNT bundles was peeled off the filtration membrane. The nanopaper sheets were annealed for 1 hour at $800^0$ C in flowing argon, to remove water, remnants of surfactant and functional groups formed during the acid reflux before doping with ammonia.

An electrochemical cell filled with 0.50M, 1M, and 2M aqueous solution of sodium azide, $NaN_3$, as electrolyte was used for the electrochemical nitrogenation experiments. A free standing SWNT nanopaper was used as the working electrode, platinum foil was used as the counter electrode, and a saturated calomel electrode (SCE) as the standard electrode. Experiments for cyclic voltammetry were carried out for approximately 3 hours under cyclic voltammetric conditions using an Elchema computer-controlled potentiostat-galvanostat unit.

Cyclic Voltammetry (CV) is one of the most effective and versatile electroanalytical techniques for the mechanistic study of redox systems [51, 52, 53 ]. It enables the electrode potential to be rapidly scanned in search of redox couples. Once located, a couple can then be characterized from the potentials of peaks on the cyclic voltammogram and from changes caused by variation of the scan rate. CV is often one of the first experiments used in an electrochemical study[ 54, 55, 56].

The repetitive triangular potential excitation signal for CV (Figure 4.7) causes the potential of the working electrode to sweep back and forth between two designated values (the switching potentials). To obtain a cyclic voltammogram, the current at the working electrode is measured during the potential scan as shown in Figure. 4.8.

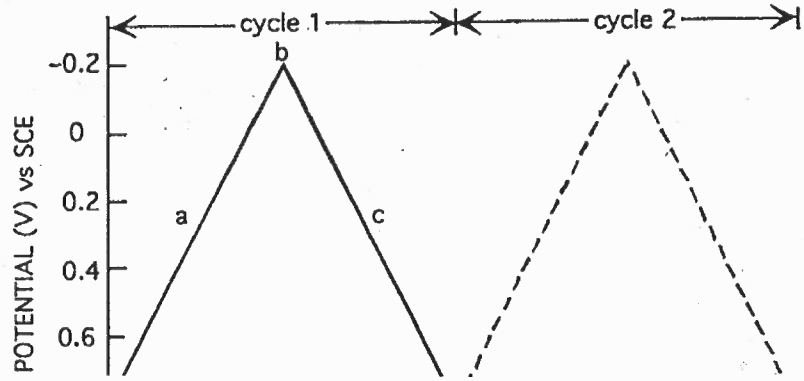


**Figure 4.7** Typical excitation signal for cyclic voltammetry.

Source: http://www.chem.uic.edu/chem421/cv.PDF viewed Feb 25, 2010.

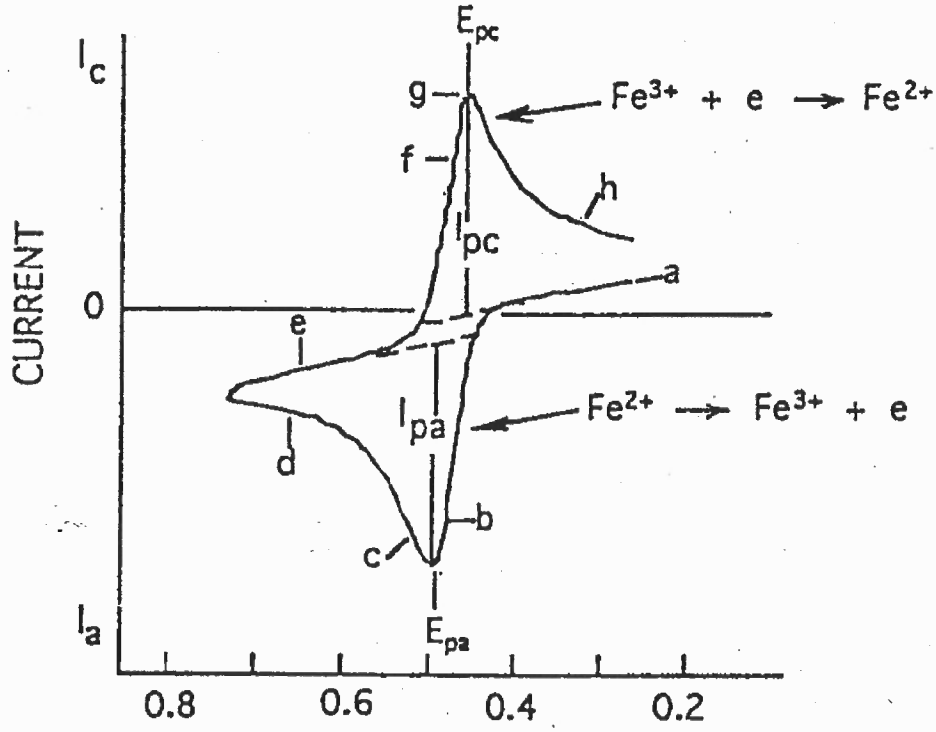

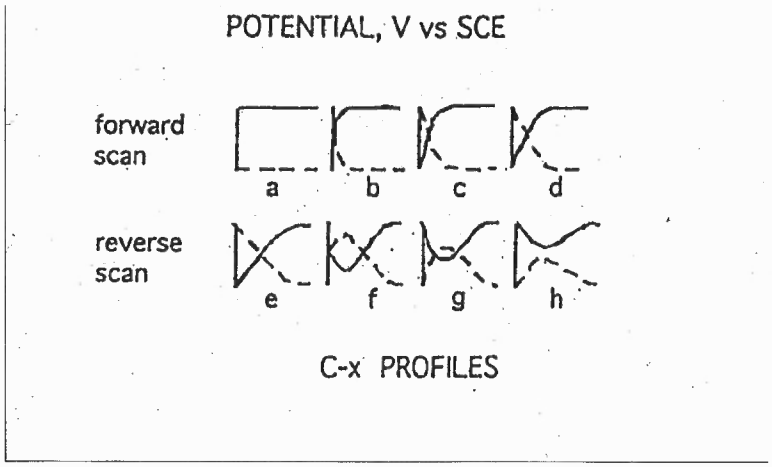


**Figure 4.8** (Top)Cyclic voltammogram of $Fe^{2+}$ in 1M $H_2SO_4$. (Bottom) Concentration profiles C-x discussed in the text.

Source: http://www.chem.uic.edu/chem421/cv.PDF, accessed Feb 28, 2010.

During the scan +250 to +750 mV, the applied potential becomes sufficiently positive at 400 mV to cause oxidation of $Fe^{2+}$ to occur at the electrode surface. This oxidation is accompanied by an anodic current, which increases rapidly until the surface concentration of $Fe^{2+}$ approaches zero, as indicated by a peak in the current at point c in Figure 4.8. The current then decays (after c) as the solution surrounding the electrode is depleted of $Fe^{2+}$ due to its oxidation to $Fe^{3+}$. This depletion of $Fe^{2+}$ and accumulation of $Fe^{3+}$ near the electrode is depicted by concentration-distance profiles a-e as shown in Figure 4.8. The magnitude of the current is related to the slope of the c-x profile for $Fe^{2+}$, as described by where:

$$I_t = nFAD_o(\frac{\partial C_o}{\partial X})_x = 0, t \qquad (4.1)$$

It = Current at time t, (Amperes).

n = Number of electrons, eq/mole.

F = Faraday's constant, 96,485 e/eq.

A = Electrode area, $cm^2$.

C = Concentration of oxidized species, $mol/cm^3$. (not mol/L!)

Do = Diffusion coefficient of oxidized species, $cm^2/s$.

t = Time (s).

X = Distance from the electrode (cm).

The product Do ($\partial Co/\partial X$) at x = 0, t is the flux or the number of moles of oxidized species diffusing per unit time to unit area of the electrode in units of $mol/cm^2 s$. During the positive scan in which $Fe^{2+}$ is oxidized to $Fe^{3+}$, the depletion of $Fe^{2+}$ in the vicinity of the electrode is accompanied by an accumulation of $Fe^{3+}$. This can be seen by the concentration distance profiles at various potentials in the shown figure. After the direction of the potential scan is switched at 750 mV to a negative scan, oxidation continues (as is evident by the anodic current and the C-x profile, (e), as seen in Figure 4.8, until the applied potential becomes sufficiently negative to cause reduction of the accumulated $Fe^{3+}$. Reduction of $Fe^{3+}$ is signaled by the appearance of cathodic current. Once again, the current increases as the potential becomes increasingly negative until all of the $Fe^{3+}$ near the electrode is reduced. When the concentration of $Fe^{3+}$ is significantly depleted, the current peaks, and then decreases. See f, g, and h in Figure 4.8. Thus the physical phenomena that caused a current peak during an oxidation cycle also cause a

current peak during the reduction cycle. This can be seen by comparing the concentration-distance profiles for the two scans.

Simply stated, in the forward scan $Fe^{3+}$ is electrochemically generated, as indicated by the anodic current. In the reverse scan, this $Fe^{3+}$ is reduced back to $Fe^{2+}$, as indicated by the cathodic current. Thus, CV is capable of rapidly generating a new species during the forward scan and then probingits fate on the reverse scan. The important parameters of cyclic voltammetry are the magnitude of the peak currents, Ipa and Ipc, and the potentials at which peaks occur, $E_{pa}$ and $E_{pc}$. Difficulty in obtaining accurate peak currents is perhaps the biggest liability of CV.

A redox couple in which both species rapidly exchange electrons with the working electrode is termed an electrochemically reversible couple. The following equation applies to a system that is both electrochemically and chemically reversible:

$$\Delta E_p = E_{pa} - E_{pc} \sim 0.059/n \text{ (at } 25^{o}C) \qquad (4.2)$$

where n = number of electrons transferred.

The values of $I_{pa}$ and $I_{pc}$ are similar in magnitude for a reversible couple with no kinetic complications. In most CV experiments there is little advantage to be gained by carrying on the potential scan for more than two to three cycles (Note: The first voltammogram is not always quite the same as the reproducible curves obtained after several cycles.)

### 4.3.4 Synthesis of Nitrogenated Boron Nanotubes

A schematic view of the structures involved in the synthesis of boron nanotubes using a CVD-type decomposition process is shown in Figure 4.9. First boron nanotubes (BNTs) are grown by this new process and the BNTs are then doped with nitrogen using ammonia or melamine as dopant precursors to form nitrogenated boron nanotubes (BNNTs).

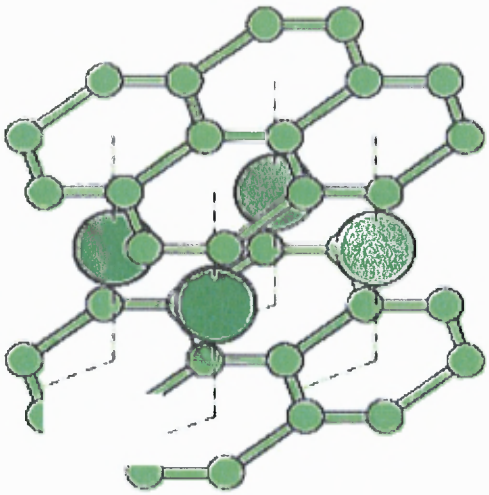

(a)

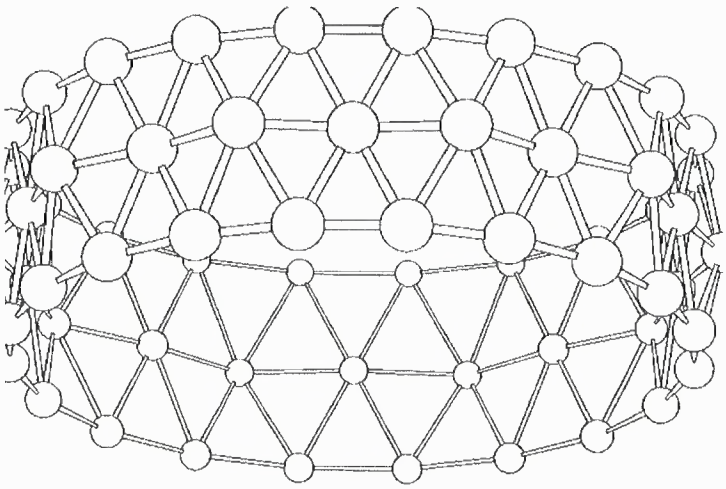

(b)

**Figure 4.9** (a) Structure of MgB2 from which magnesium would de-intercalate due to decomposition; (b) Model of a tubular structure of boron leading to boron nanotubes.

During the thermal CVD-type process, $MgB_2$ is decomposed to its elements: magnesium and boron (reaction 4.3):

$$MgB_2 \Rightarrow Mg + 2B \qquad (4.3)$$

at a temperature of 900 - 950°C

The magnesium ions then intercalate between the initially formed boron sheets to catalyze the formation of tubular BNTs without being substantially incorporated into the final product. While carbon nanotubes permit each carbon to be bound to three other carbons, in BNT, each boron can bind to six other borons. However, BNT formed freely in this fashion are highly irregular in diameter, and the main product is actually boron nanowires.

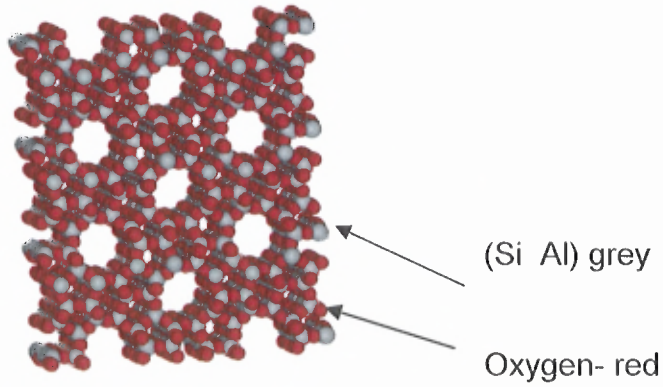


**Figure 4.10** The micro-porous molecular structure of a zeolite, ZSM-5 with the chemical formula $Na_2Al_2Si_3O_{10}$-$2H_2O$. The maximum size of the molecular or ionic species that can enter the pores of a zeolite is controlled by the diameters of the tunnels. These are defined by the ring size of the aperture, where a "8 or 10 ring" refers to a closed loop that

is built from 8 or 10 tetrahedrally coordinated silicon (or aluminum) atoms and 8 or 10 oxygen atoms.

However, to generate BNTs of a near-constant diameter, a template is necessary to guide the growth of tubes and minimize defect formation. Zeolites, with their arrays of constant pore size (as depicted in figure 4.10 ) have proven to be excellent templates for producing BNTs. The CVD method of Pfefferle and Ciuparu[57] uses a highly reactive $BCl_3$ gas mixed with hydrogen as the boron source, and the BNTs are grown in a Mg-derivatized MCM-41, a zeolite with pores of 3-4 nm in diameter. However, the BNTs produced appeared to have many defects. MCM-41 was also used in this work, but $MgB_2$ alone or mixed with $Ni_2B$ as co-catalyst was employed to provide both the boron and catalyst source. Intimate mixing of $MgB_2$ alone or mixed with $Ni_2B$ in different atomic ratios with MCM-41 modifies the zeolite to contain the Mg catalyst without the need for chloride atoms present in Pfefferle and Ciuparu's method, thus limiting the number of chemical species and contaminants. The reaction is carried out at 950°C under flowing argon to keep the reaction atmosphere weakly reducing or neutral to propagate the formation of BNTs as shown in Figure 4.11. The BNTs produced via this method were smooth and defect free as evident from Figure 4.12.

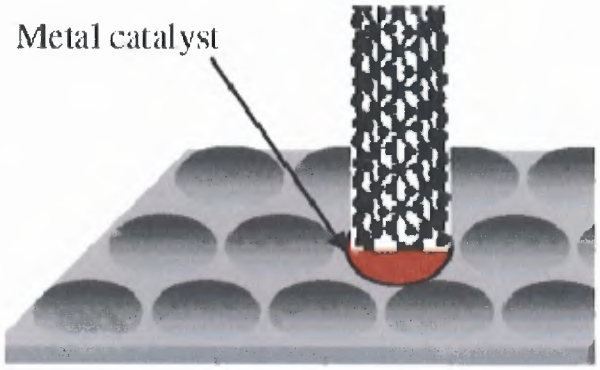


**Figure 4.11** Schematic representation of a nanotube aided by Mg catalyst growing out of the pores of a zeolite.

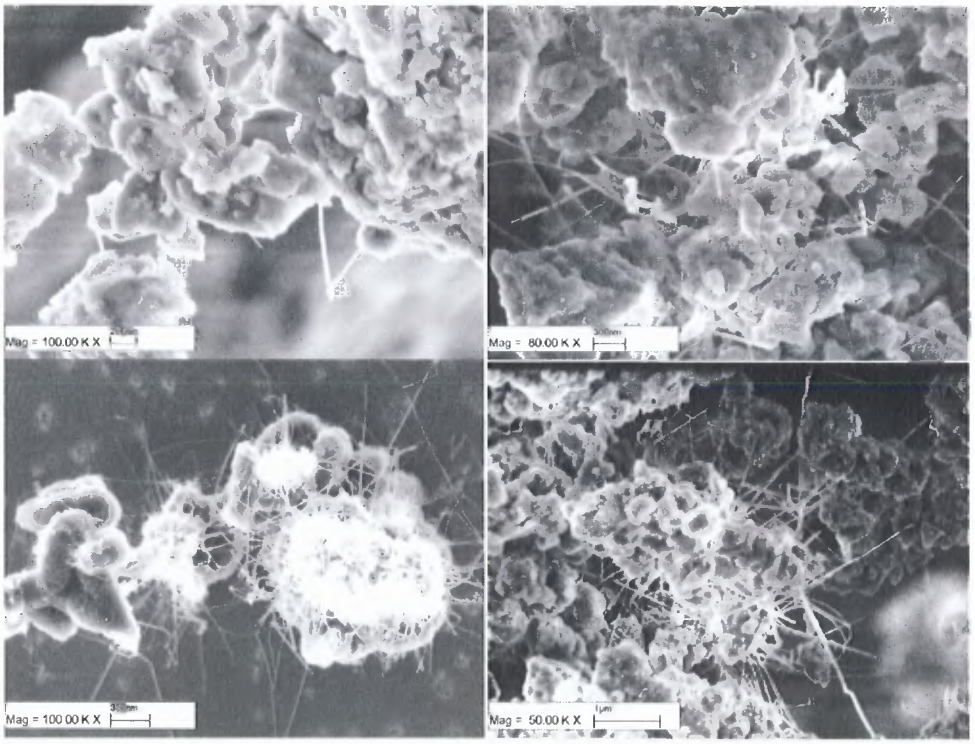


**Figure 4.12** SEM images of boron nanotubes growing on the zeolite pores by the CVD method used in this work.

As seen in Figure 4.12, not all of the pores had BNTs growing out of them. This is surprising, since all of the pores contained the catalyst and some boron to initiate growth. The effect of temperature, pressure, catalyst type (as mentioned earlier, the use of $Ni_2B$ may be better), and zeolite pore diameter on the BNT growth process will be

examined. Furthermore, upon closer examination it may be determined that there exists an optimal BNT diameter, whereby deviation from this diameter could prohibit growth of the BNTs and/or cause defects. Another variable to consider is the boron source added to the mixture, which in our case also contains magnesium. An alternative would be to use diborane ($B_2H_6$) gas as the boron source but use a magnesium modified MCM-41. Yet another alternative would involve the use of $Mg(BH_4)_2$ which decomposes more efficiently and at lower temperature to Mg and boron can be used in a scaled up process as discussed below.

With the success of the templated CVD method the formation of nitrogenated BNTs or BNNTs was explored. This could readily be achieved by annealing the previously synthesized BNTs in flowing partial pressure of ammonia. As shown in equation 4.4, ammonia readily decomposes to nitrogen radicals. These would react with the BNTs formed in equation 4.3 to form nitrogenated BNTs or BNNTs (equation 4. 5).

$$2NH_3 \Rightarrow 2N^{\cdot} \text{ (radicals)} + 3H_2 \text{ at a temperature of } 900^{\circ}C \qquad (4.4)$$

$$2N^{\cdot} \text{ (radicals)} + 2\,B \Rightarrow B(N) \text{ nanotubes} \qquad (4.5)$$

The effect of nitrogen incorporation into the BNTs is examined for the effects of temperature, pressure, gas flow rate, catalyst type, and zeolite pore diameter using other zeolites with both larger and smaller pore sizes, to obtain the optimal template conditions for producing BNNT of constant diameter. Finally, the zeolite is rapidly removed by dissolution in dilute sodium hydroxide to give pristine BNNTs.

A more cost-effective approach mentioned earlier was performed using a scaled-up CVD apparatus and using $Mg(BH_4)_2$ as the boron precursor. A small scale ball mill is used to mechanochemically (by milling) react $MgCl_2$ with $NaBH_4$ to form $Mg(BH_4)_2$ according to the following reaction.

$$MgCl_2 + 2NaBH_4 = 2NaCl + Mg(BH_4)_2 \tag{4.6}$$

The reaction is carried out in alcohol in which NaCl is partly soluble for removal or in diethyl ether in which $Mg(BH_4)_2$ is soluble. Grinding magnesium chloride with sodium borohydride up to 24 hrs is explored to ensure complete mechanochemical reaction.

## 4.4 Characterization of Functionalized SWNT Nanopaper Substrates

Characterization was performed using Scanning Electron Microscopy (SEM), Raman spectroscopy, attentuated total reflection-Fourier transform infrared (ATR-FTIR) spectroscopy, thermogravimetric analysis (TGA), differential scanning calorimetry (DSC) and laser ablation mass spectrometry to determine the presence of $N_4/N_8$ and other nitrogen clusters onto and in the SWNTs. Some details of the Raman, SEM and ATR-FTIR methods are described below.

### 4.4.1 Raman Spectroscopy

Two different Raman instruments at the New Jersey Institute of Technology were used to collect Raman spectra: (a) Mesophotonics SE 1000 Raman spectrometer with a 250 mW near-infrared laser operating at 785 nm, a 130 μm diameter spot size and calibrated to 2

$cm^{-1}$ ; and (b) EZRaman-LE Raman Analyzer System from Enwave Optronics with a HRP-8 high throughput fiber probe and a 250 mW 785 nm laser focused at a working distance of 6 mm. Raman scattering or the Raman effect is the inelastic scattering of a photon and were discovered by Sir Chandrasekhara Venkata Raman in liquids and by Grigory Landsberg and Leonid Mandelstam in crystals in the 1920's. When light is scattered from an atom or molecule, most photons are elastically scattered (Rayleigh scattering), such that the scattered photons have the same energy (frequency) and wavelength as the incident photons. However, a small fraction of the scattered light (approximately 1 in 10 million photons) is scattered by an excitation, with the scattered photons having a frequency different from, and usually lower than, the frequency of the incident photons. In a gas, Raman scattering can occur with a change in vibrational, rotational or electronic energy of a molecule as shown in Figure 4.13. For materials characterization purposes, chemists are concerned primarily with the vibrational Raman effect.

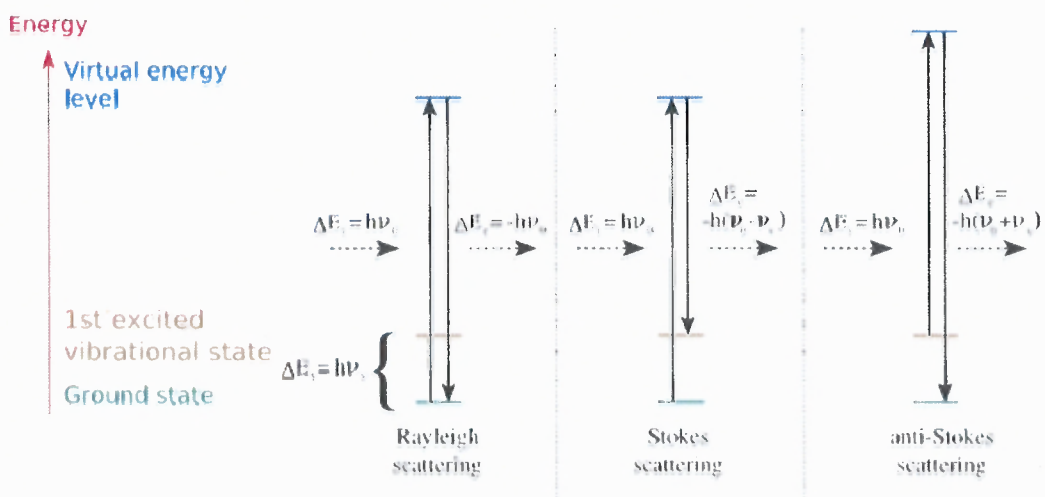


**Figure 4.13** Virtual energy level.

Source: Professor Z. Iqbal lecture, MtSE 748:Nanomaterial, NJIT, Fall 2009.

There are two components of conventional spontaneous Raman scattering, Stokes scattering and anti-Stokes scattering. The interaction of light with matter in a linear regime allows the absorption or simultaneous emission of light precisely matching the difference in energy levels of the interacting electrons. The Raman effect corresponds to the absorption and subsequent emission of a photon via an intermediate electronic state, having a virtual energy level shown in Figure 4.13. Following possibilities can occur:

- No energy exchange between the incident photons and the molecules (and hence no Raman effect)
- Energy exchanges occur between the incident photons and the molecules. The energy differences are equal to the differences of the vibrational and rotational energy-levels of the molecule. In crystals only specific phonons are allowed (solutions of the wave equations which do not cancel themselves) by the periodic structure, so Raman scattering can only appear at certain frequencies. In amorphous materials like glasses, more phonons are allowed and thereby the discrete spectral lines become broad.

- Molecule absorbs energy: Stokes scattering. The resulting photon of lower energy generates a Stokes line on the red side of the incident spectrum.

- Molecule loses energy: anti-Stokes scattering. Incident photons are shifted to the blue side of the spectrum, thus generating an anti-Stokes line.

These differences in energy are measured by subtracting the energy of the mono-energetic laser light from the energy of the scattered photons. The absolute value,

however, does not depend on the process (Stokes or anti-Stokes scattering), because only the energy of the different vibrational levels is of importance. Therefore, the Raman spectrum is symmetric relative to the Rayleigh band. In addition, the intensities of the Raman bands are only dependent on the number of molecules occupying the different vibrational states, when the process began. If the sample is in thermal equilibrium, the relative numbers of molecules in states of different energy will be given by the Boltzmann distribution equation 4.7:

$$\frac{N_1}{N_2} = \frac{g_1}{g_2} e^{-\frac{\Delta Ev}{kT}} \qquad (4.7)$$

$N_0$: number of atoms in the lower vibrational state

$N_1$: number of atoms in the higher vibrational state

$g_0$: degeneracy of the lower vibrational state (number of orbitals of the same energy)

$g_1$: degeneracy of the higher vibrational state

$\Delta E_v$: energy difference between these two vibrational states

$k$: Boltzmann's constant

$T$: temperature in kelvins

Thus lower energy states will have more molecules in them than will higher (excited) energy states. Therefore, the Stokes spectrum will be more intense than the anti-Stokes spectrum.

A typical Raman spectrum for SWNTs is shown in Figure 4.14. The spectrum has three important features namely, low frequency lines assigned to radial breathing modes ( RBM) of the nanotubes, intermediate frequency disorder-induced mode due to defects and/or amorphous carbon on the nanotube sidewalls ( D-peak), and a higher energy tangential mode (G-peak). One should note that in the G peak region there is shoulder also labeled as the $G^-$ peak due to the breakdown of the degeneracy of the G mode in graphite via roll-up of the graphene sheet. The Raman are Lorentzian except for the $G^-$ peak in metallic, which has a Breit-Wigner-Fano lineshape due to electron-phonon coupling.

The RBM lines usually appear in the low frequency region, between 120-280 $cm^{-1}$ and correspond to the atomic vibrations of the carbon atoms in the tube's radial direction. RBM line frequencies are diameter-dependent and can be use to determine the average individual SWNT diameters following the relationship in equation 4.8 [58].

$$d_t = \left({}^{238}/_{\omega_{RBM}}\right)^{1.075} \tag{4.8}$$

Where $\omega_{RBM}$ ($cm^{-1}$ ) indicates the RBM peak position and $d_t$ (nm) is the diameter of the nanotube. The D line is the second important feature. It indicates disorder-induced, defect bands at ~1300 $cm^{-1}$ for 785 nm laser excitation. Although it is usually referred to as disorder line no definitive studies have concluded that these features can be attributed to kinks, heptagons and other defects on the tube walls. However, by empirical observation between the D-peak and G-peak intensity ratio one can monitor the quality of

the SWNT sidewalls. The $G^+$ line similar in frequency to the main line in graphite is also referred to as tangential mode because it corresponds to the C-C stretching eigenvector parallel to the tube axis. As pointed out earlier, a second lower frequency $G^-$ component is observed in SWNT due to curvature-induced softening and removal of the degeneracy of the C-C graphene mode.

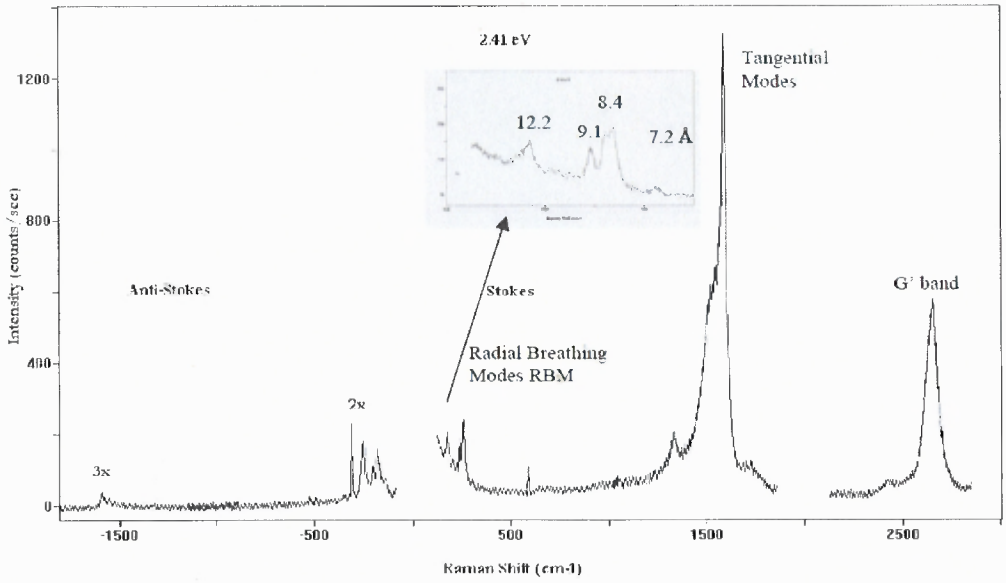


**Figure 4.14** Raman spectrum for SWNTs showing the RBM, D-peak and G-peaks discussed in the text.

Source: Professor Z. Iqbal lecture, MtSE 748:Nanomaterial, NJIT, Fall 2009.

### 4.4.2 Scanning Electron Microscope ( SEM )

Field emission Scanning Electron Microscopy is one of the most sophisticated techniques used in the characterization of SWNTs. In this work, a LEO (Carl Zeiss) 1530 VP microscope was used at the NJIT Material Characterization Laboratory. This SEM provides a three dimensional image of the SWNT bundles in nanopaper substrates, a

direct result of the larger depth of field, as well as the shadow relief effect of the secondary and backscattered electron contrast.

### 4.4.3 Fourier Transform Infrared Radiation-Attenuated Total Reflectance (FTIR-ATR)

Mid-Infrared spectroscopy is an extremely reliable and well recognized fingerprinting method. Many substances can be characterized, identified and also quantified. One of the strengths of IR spectroscopy is its ability as an analytical technique to obtain spectra from a very wide range of solids, liquids and gases. However, in many cases some form of sample preparation is required in order to obtain a good quality spectrum. Traditionally IR spectrometers have been used to analyze solids, liquids and gases by means of transmitting the infrared radiation directly through the sample. Where the sample is in a liquid or solid form the intensity of the spectral features is determined by the thickness of the sample and typically this sample thickness cannot be more than a few tens of microns. The technique of Attenuated Total Reflectance (ATR) has in recent years revolutionized solid and liquid sample analyses because it combats the most challenging aspects of infrared analyses, namely sample preparation and spectral reproducibility. The two most common forms of sample preparation for solids both involve grinding the material to a fine powder and dispersing it in a matrix. The ground material can be dispersed in a liquid to form a mull. The most commonly used liquid is mineral oil (nujol). Typically no more than 20 mg of solid is ground and then one or two drops of nujol are used to create a paste which is then spread between two mid-infrared transparent windows e.g. NaCl, KBr, $CaF_2$. The sample is now ready to be placed in the spectrometer for analysis by transmission.

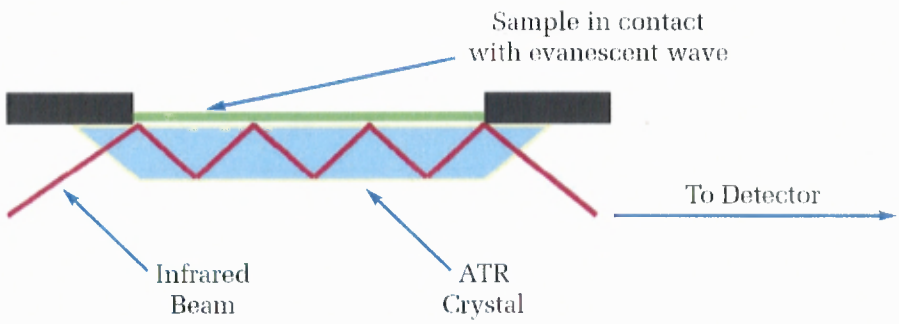


**Figure 4.15** Schematic of the optics involved in attentuated total reflection.

Source: [59]http://las.perkinelmer.com/content/TechnicalInfo/TCH_FTIRATR.pdf, February 28, 2010.

An attenuated total reflection accessory operates by measuring the changes that occur in a totally internally reflected infrared beam when the beam comes into contact with a sample (indicated in Figure 4.15 ). An infrared beam is directed onto an optically dense crystal with a high refractive index at a certain angle. This internal reflectance creates an evanescent wave that extends beyond the surface of the crystal into the sample held in contact with the crystal. It can be easier to think of this evanescent wave as a bubble of infrared that sits on the surface of the crystal. This evanescent wave protrudes only a few microns (0.5 μm - 5 μm) beyond the crystal surface and into the sample. Consequently, there must be good contact between the sample and the crystal surface. In regions of the infrared spectrum where the sample absorbs/energy, the evanescent wave will be attenuated or altered. The attenuated energy from each evanescent wave is passed back to the IR beam, which then exits the opposite end of the crystal and is passed to the detector in the IR spectrometer to generate an infrared spectrum. There are a number of crystal materials available for ATR. Zinc Selenide (ZnSe) and Germanium are by far the most common used for HATR sampling. Germanium has a much better working pH range and can be used to analyze weak acids and alkalis. Germanium has by far the

highest refractive index of all the ATR materials available which means that the effective depth of penetration is approximately 1 micron. For most samples this will result in a weak spectrum being produced, however, this is an advantage when analyzing highly absorbing materials, such as carbon black filled rubbers, which are typically analyzed using a Germanium ATR accessory. Diamond is by far the best ATR crystal material because of its robustness and durability.

# CHAPTER 5

# RESULTS AND DISCUSSIONS

## 5.1 Synthesis of Polymeric Nitrogen Stabilized on Single Wall carbon

**Nanotubes**Three different methods were used to synthesize polymeric nitrogen and its precursor clusters:

1. Electrochemical reaction of sodium azide aqueous solution with in-situ uv-irradiation.
2. Microwave-assisted reaction of sodium azide aqueous solution with and without uv pre-irradiation.
3. Radio-frequency plasma-assisted reaction of nitrogen mixed with argon or hydrogen.

### 5.1.1 Electrochemical Reaction

A modified version of a scalable electrochemical process that was used to nitrate the sidewalls of single wall carbon nanotubes is shown schematically in Figure 5.1. In the modified process, the carbon nanotubes employed as the working electrode were pre-doped with nitrogen via annealing in ammonia, and the reaction was carried out under ultraviolet irradiation in sodium azide solution in water at different concentrations and pH values. The nature of the chemistry taking place on the nanotube sidewalls and the nanotube morphology were characterized by *in-situ* cyclic voltammetry, Scanning Electron Microscopy (SEM), Raman spectroscopy, laser ablation mass spectroscopy, Fourier Transform Infrared-Attentuated Total Reflection (FTIR-ATR), and differential scanning calorimetry (DSC).

.

SWNT nanopaper was used as the working electrode. Nanopapers were prepared as discussed in Chapter 4 section 4.2. Prior to use, the nanopapers were heat-treated in argon to remove water, remnants of the surfactant and carbonize the polystyrene coating added to improve their mechanical strength by pouring a polystyrene solution in toluene during the final drying step using vacuum filtration (see chapter 4, section 4.2). The nanopaper shown in Figure 5.2 (top) was no longer brittle during handling. Nanopapers using nanotubes from both sources discussed in chapter 4 were electrochemically reacted in 1M and 2 M sodium azide solution in deionized (DI) water under ultraviolet irradiation. A photograph of the experimental set-up for electrochemical reaction where the SWNT nanopaper functions as the working electrode (WE) are shown in Figure 5.3(a) and (b), respectively. A platinum wire is used as the counter electrode (CE) with a standard calomel electrode as the reference electrode (RE) and in-situ computer controlled cyclic voltammetry data were collected during electro-functionalization of the nanopaper working electrode. SEM images of the working SWNT nanopaper electrode using SWNTs from Cheap Tubes prior to electrochemical reaction are shown in Figure 5.2 (bottom).

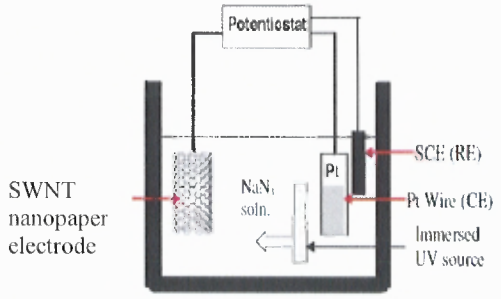


**Figure 5.1** Schematic of the 3-electrode electrochemical cell.

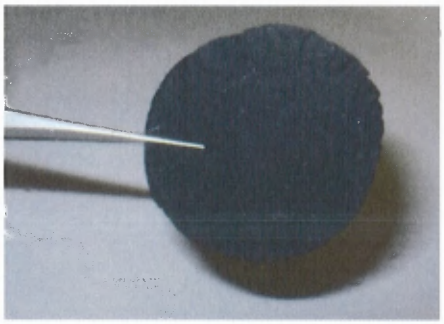

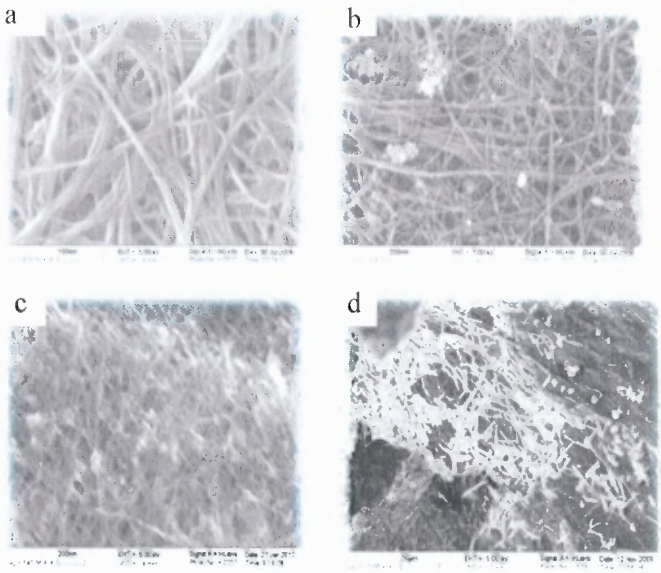


**Figure 5.2** At the top, peeled-off nanopaper mechanically improved by polystyrene infiltration; At the bottom, SEM images of as-prepared (a) and annealed (b) SWNT nanopaper prepared using SWNTs from Cheap Tubes Inc. Some contamination by particles from the reactor of the furnace is observed in the annealed sample. SEM images of as prepared (c) and annealed (d) nanopaper using SWNTs from SWeNT Inc.

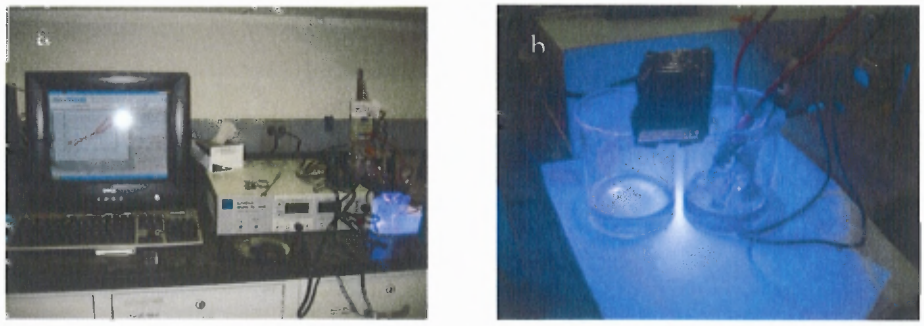

**Figure 5.3** Set-up for the electrochemical functionalization route to the synthesis of polymeric nitrogen in carbon nanotubes showing: (a) Galvanostat-potentiostat system, and (b) Beaker on the right containing 1M $NaN_3$ aqueous solution, SWeNT nanopaper as the working electrode, SCE as the reference electrode, and Platinum foil as the counter electrode.

The electrochemical oxidation reactions at the working electrode would occur as follows:

$$2N_3^- \rightarrow 2N_3^o \text{ (radicals)} + 2e \rightarrow 2N_3^o \rightarrow N_4^o + N_2^o \tag{5.1}$$

Oxidation would create radicals of the nitrogen cluster radicals and reduction would involve conversion of the radicals back to cations. If active sites are present on the nitrogen-doped SWNTs and excess radicals are present in solution, $N_4$ radicals will convert to $N_8$ and $N_2$ radicals will form $N_4$ and then $N_8$ clusters, which will be encapsulated on the SWNT sidewalls by covalent bonding between carbon on the SWNT sidewalls with the cluster nitrogen atoms. Oxidation reactions would then predominate. A secondary reaction is likely to involve oxidation of carbon on the SWNT sidewalls followed by bonding with the nitrogen clusters. Sodium formed during the reduction cycle will dissolve in water to increase the solution pH. In-situ ultraviolet radiation will

generate additional $N_3$ radicals to increase the production of $N_8$ clusters according to reaction (5.1) above. Cyclic voltammograms (CVs) using SWNTs from Cheap Tubes shown in Figure 5.4 indicate a 2 step oxidation process to form radicals according to equation (5.1) followed by oxidation of the nanotube sidewalls to bond the nitrogen clusters to the SWNT sidewalls.

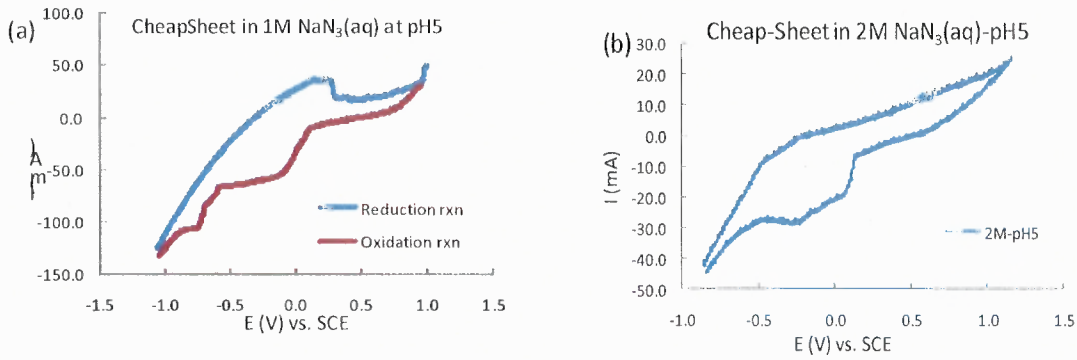


**Figure 5.4** Cyclic voltammetry scans recorded using nanopaper working electrodes using SWNTs from Cheap Tubes in 1M sodium azide aqueous solution (a) and 2M sodium azide aqueous solution (b).

Raman spectroscopy was used to check for $N_4$ and $N_8$ clusters and polymeric networks on the SWNT sidewalls, and FTIR-ATR spectroscopy was used to check for C-N bond vibrations. Micro-Raman experiments were carried out using an Enwave Optronic Lab Raman system, cooled CCD (charge coupled device) detection and 785 nm emitted wavelength. In order to verify proof of success, the micro-Raman data reported were checked at about 20 spots in different regions of the sample. FTIR-ATR spectra were measured directly on the pristine and functionalized SWNT nanopaper using a Perkin-Elmer/Nicolet Model 470 FTIR–ATR spectrometer equipped with a Pike Technologies single reflection ATR attachment. Thermogravimetric analysis (TGA) and

differential scanning calorimetry were performed with a Perkin Elmer Pyris Diamond TGA / DSC instrument. Continuous cyclic voltammogram (CV) sweeps were carried out from -1.0 to +1.5 V at a scan rate of 15 mV/s in 1 M $NaN_3$ with the pH held at 5.5 using a phosphate buffer. CVs shown in Figure 5.5 below for nanopaper using SWNTs from SWeNT are similar to the CVs shown in Figure 5.4 for nanopaper using SWNTs from Cheap Tubes. Two peaks are observed corresponding to the step-wise oxidation of $N_3^-$ anions followed by their chemisorption on defects and dangling bonds on the SWNT sidewalls and tube ends. At voltages above +1.0 V (versus SCE) decomposition resulting in oxygen evolution causes the CVs to become noisy.

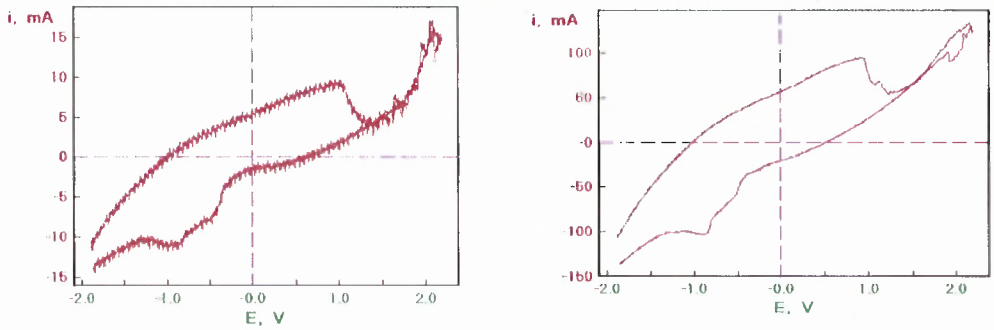


**Figure 5.5** The cyclic voltammogram from -600 to +1000 mV versus a saturated calomel electrode (SCE) of a SWNT nanopaper working electrode made using SWeNT nanopaper and Pt counter electrode in 1M $NaN_3$ aqueous solution with 0.1 M phosphate buffer (pH 7.4). The scan rate used is 15 mV/s.

CV experiments using nanopapers of single wall carbon nanotubes (SWNTs) from two sources – SWeNT and Cheap Tubes – were used for the experiments with and without polystyrene infiltration [60]. Both sets of nanopapers were annealed in ammonia mixed with argon at $500^0$ C for 30 minutes. Field emission scanning electron microscope (SEM) images [Figures 5.6 (a) and (b)] for the two types of nanopapers show that the

SWeNT sample has a distribution of much shorter nanotubes than the Cheap Tubes SWNT sample. This is likely to be the result of the greater sensitivity of the SWeNT nanotubes to sonication-induced dispersion in water required for nanopaper synthesis, resulting in a relatively higher density of tube-tip sites where functionalization with nitrogen can occur. The nanopapers were electrochemically reacted in 1M sodium azide solution under ultraviolet-irradiation.

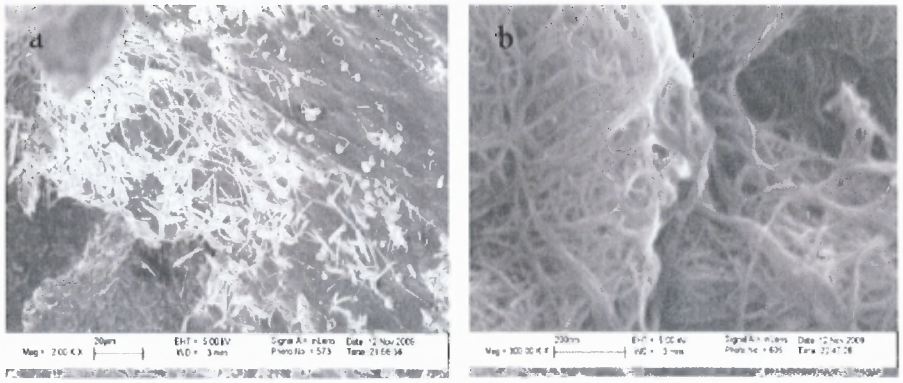


**Figure 5.6** Scanning electron microscope images of nanopapers from: (a-left) SWeNT single wall carbon nanotubes and (b-right) Cheap Tubes single wall carbon nanotubes.

A schematic of the experimental arrangement for electrochemical synthesis where the SWNT nanopaper functions as the working electrode is shown in Figure 5.7. A platinum wire is used as the counter electrode and in-situ computer controlled cyclic voltammetry data (referenced to a standard calomel electrode) were collected during electro-functionalization of the carbon nanopaper working electrode. Since electrochemical deposition is a widely used industrial process, the set up used can be readily scaled up for larger scale production. Key Raman and laser desorption mass spectrometry results is presented below which show that polymeric nitrogen clusters are being indeed produced by the electrochemical process. Details of the reaction

mechanism found in equation 5.1 of formation of the polymeric nitrogen inferred from the cyclic voltammetry data are shown in Figure 5.7 (a ) and (b).

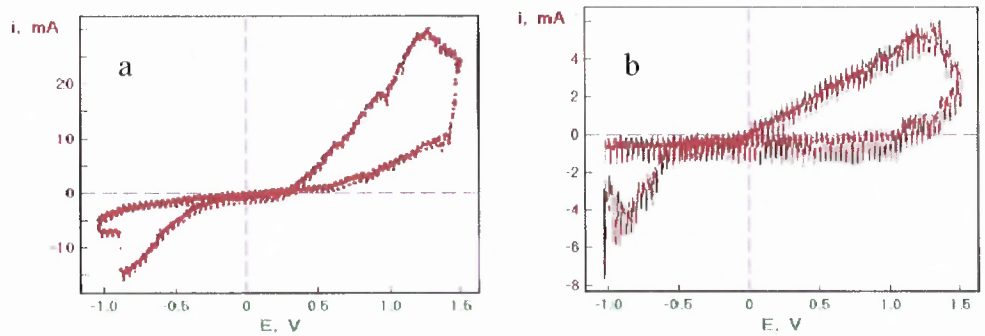


**Figure 5.7** Cyclic voltametry data for the (a-left) SWeNT nanopaper (b-right) CHEAP nanopaper.

A representative micro-Raman spectrum excited with 785 nm laser radiation of the charged nanopaper electrode displayed in Figure 5.8. The spectrum shown in Figure 5.8 (a) and (b) is closely similar to spectra taken from at least 20 spots across the sample. The overall intensity of the Raman spectrum after charging is reduced by a factor of 6–7, indicating a reduction in resonance enhancement due to the quasi-one dimensional structure of the SWNTs. The decrease in resonance-enhancement may result from an increase in structural dimensionality and disorder due to the formation of functional groups on the sidewalls and tube ends. Moreover, the intense line at 1580 cm–1 assigned to the C–C tangential mode after functionalization. The resulting downshift of the line at 1580 cm-1 relative to unfuntionalized nanotube may indicate electron donation to the tubes by nitrogen species.

Figure 5.8 (a) and (b) respectively show the Raman spectra excited with 785 nm laser radiation of the pristine nanopaper from Cheap Tubes and the same nanopaper after

electrochemical reaction in 1M sodium azide solution and under uv-irradiation. One clear feature is the dramatic enhancement of intensities of the SWNT nanopaper Raman lines relative to that of the pristine sample by an order of magnitude. In addition there is a small (of the order of 5 $cm^{-1}$) downshift of the main Raman lines which suggests electron-doping of the SWNT backbone as a result of functionalization by nitrogen-containing groups[61.

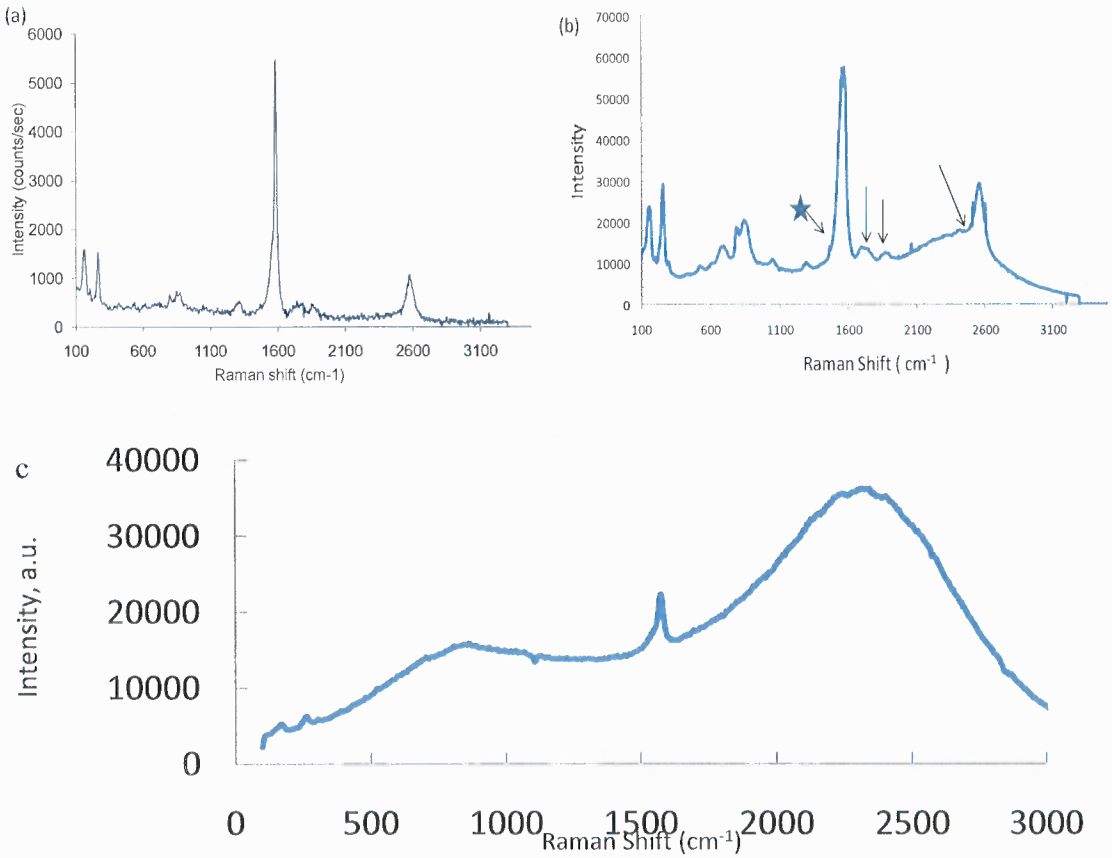


**Figure 5.8** Raman spectra excited with 785 nm laser from: (a) Pristine SWNT carbon nanopaper from Cheap Tubes Inc; and (b) Same nanopaper as (a) that was electrochemically functionalized in 1.0M sodium azide solution under uv-irradiation, and (c) in 2M sodium azide solution, at pH of 5, respectively.

The intensity enhancement can be tentatively attributed to electron doping-induced change in the electronic density-of-states which modulate the Raman cross-

section via the associated one-dimensional van Hove singularities. Other remarkable changes are also observed in the intrinsic G mode at 1590 $cm^{-1}$ (due to the tangential carbon-carbon stretching motion) and the G' mode near 2600 $cm^{-1}$ which has nothing to do with the G mode but is really the $2^{nd}$ harmonic of the disorder mode at 1300 $cm^{-1}$, and therefore more appropriately referred to as the 2D mode rather than its conventional notation as the G' mode. Most remarkably the 2D mode is enhanced in single layer graphene and is a factor of 4 stronger than the G line [62 , 63]. The G mode in SWNTs splits into so-called G+ and G- modes due to the curvature of the tubes and resulting quantum confinement that lifts the double degeneracy of the $E_{2g}$ symmetry of this mode in graphite. The 2D mode near 2600 $cm^{-1}$ is observed in Figure 58(a) in the pristine nanopaper and like the G modes is enhanced and downshifted. In addition, a broad feature (arrowed in Figure 5.8b) centered near 2460 $cm^{-1}$ and close to the 2D line emerges in the Raman spectrum of the electrochemically functionalized nanopaper sample. It is likely that it is due to a distribution of nitrogen cluster doped sites on the nanotube walls. It is worth noting however that the fundamental D mode itself, which senses overall disorder in the nanotubes, does not change in intensity as a result of electrochemical functionalization. This broad feature becomes particularly strong for a sample that was electrochemically functionalized in 2M sodium azide and shows a second broad feature centered at about 850 $cm^{-1}$ (Figure 5.8c). These broad lines are likely to be associated with the growth of a disordered polymeric nitrogen network on and inside the SWNT framework (see more detailed discussion below in sub-section on Plasma-assisted Reactions on Carbon Nanotubes). Two other relatively weak but important Raman lines appear in this sample at 1485 $cm^{-1}$ (shown with an asterisk in

Figure 5.8(b)) and at 1878 $cm^{-1}$. The former can be assigned to a C-N frequency based on a simple calculation based on the frequency expected on replacing carbon with the heavier nitrogen atom. The line at 1878 $cm^{-1}$ corresponds fairly closely to the calculated (using ab initio self consistent field, coupled cluster and many perturbation theory methods [64 ,65]) Raman frequency of a $C_{2v}$ Y-shaped $N_4$ cluster, which can link up to form $N_8$ and higher oligomers.

The laser desorption mass spectra taken from the nanopaper made using Cheap Tubes SWNTs depicted in Figure 5.9 clearly show the formation and cracking pattern of $C_x$-$N_8$ clusters consistent with the Raman data discussed above and the presence of a C-N Raman feature. Stabilization of the nitrogen cluster occurs via the bonding with carbon in agreement with the predictions of Abou-Rachid et al [66].

The corresponding Raman and laser desorption mass spectra for an electrochemically functionalized nanopaper made using SWeNT nanotubes are shown in Figures 5.10 and 5.11, respectively. The overall features in the Raman spectrum are similar to those for the nanopaper made using Cheap Tubes discussed above. However, relatively strong new peaks appear at 1752 and 1858 $cm^{-1}$ corresponding to weaker lines at 1754 and 1878 $cm^{-1}$ in the Cheap Tubes sample, and the broad scattering near the 2D line around is 2600 $cm^{-1}$ is about a factor of two weaker. The line at 1754 $cm^{-1}$ is a second order mode of the SWNT whereas the feature at 1878 $cm^{-1}$ is assigned to $N_4$. In the SWeNT sample the 1878 $cm^{-1}$ line is downshifted probably due to the formation of a larger cluster. The desorption mass spectra taken from the SWeNT sample shown in Figure 5.11 does indeed indicate the formation of larger $C_{25}N_{20}$ clusters with mass of 580 amu in addition to $C_x$-$N_8$ clusters. The relatively strong line at 1858 $cm^{-1}$ can therefore be

assigned to $C_x$-$N_{20}$ where $N_{20}$ can be considered to be comprised of five $N_4$ clusters or 1858 $cm^{-1}$ associated with $N_{20}$ which can be considered to be $(N_4)_5$.

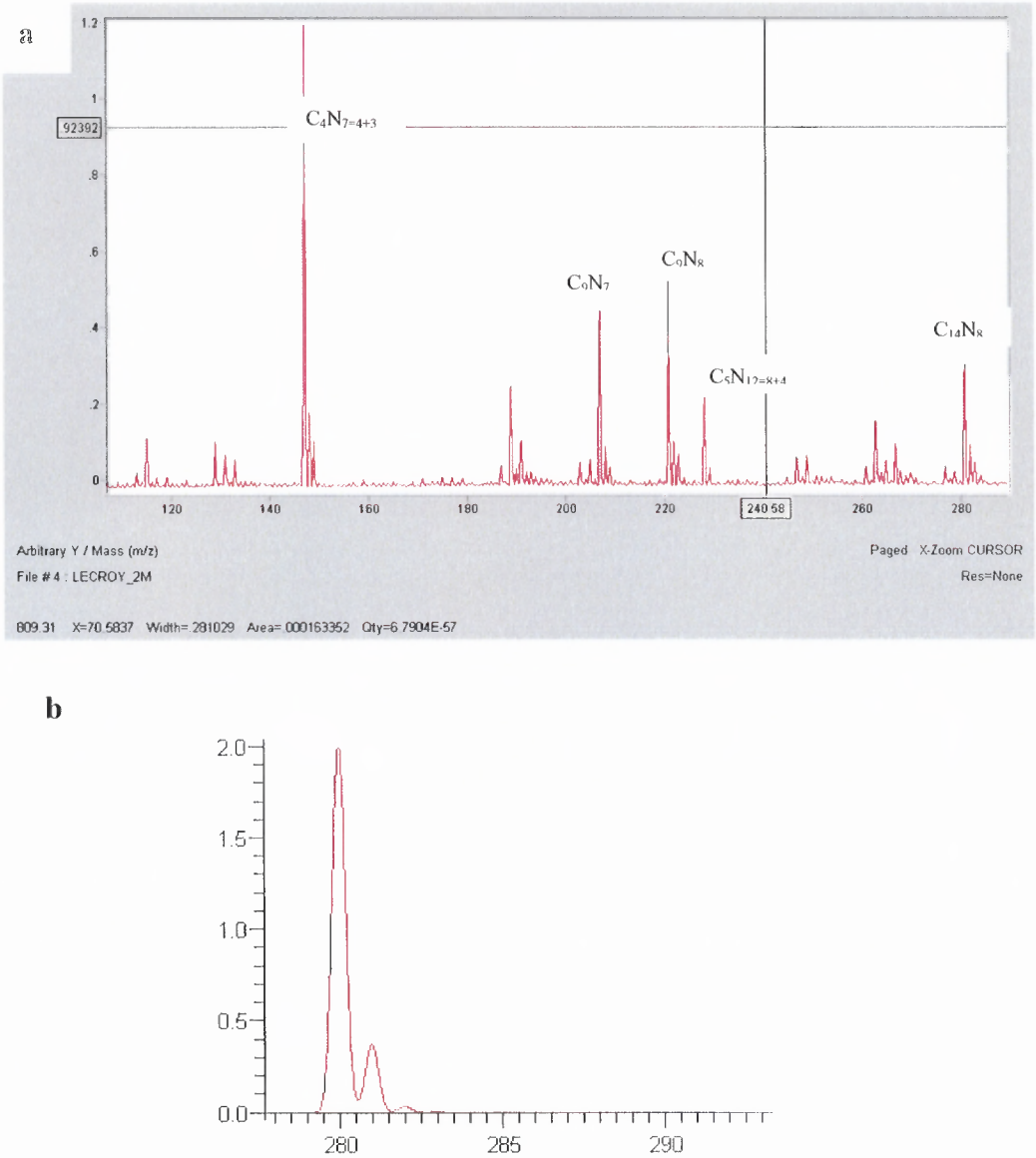


**Figure 5.9** Laser desorption time of flight mass spectrum in the (a) 100 to 300 amu and (b) 280 amu region region from the electrochemically functionalized SWNT nanopaper made from Cheap SWNTs.

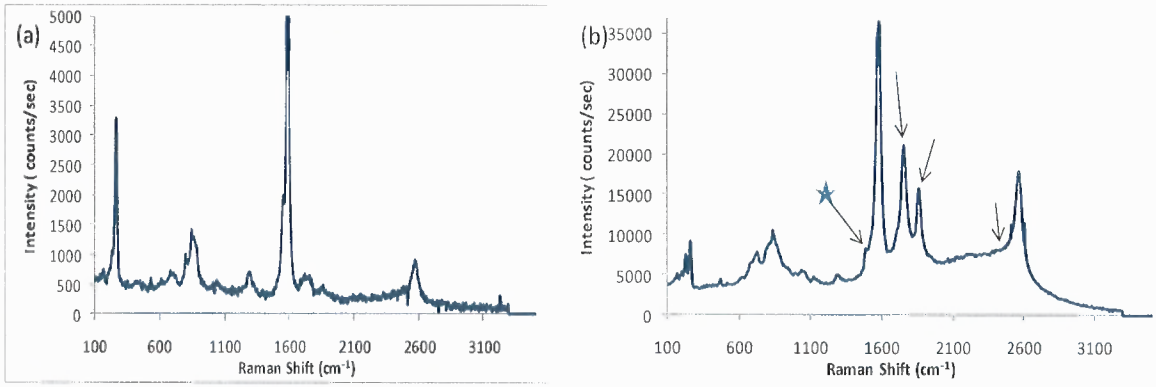


**Figure 5.10** Raman spectra excited with 786 nm laser from : (a) Pristine SWeNT SWNT nanopaper, and (b) Same bucky paper as (a) that was electrochemically functionalized in 1.0 M sodium azide solution under uv-irradiation.

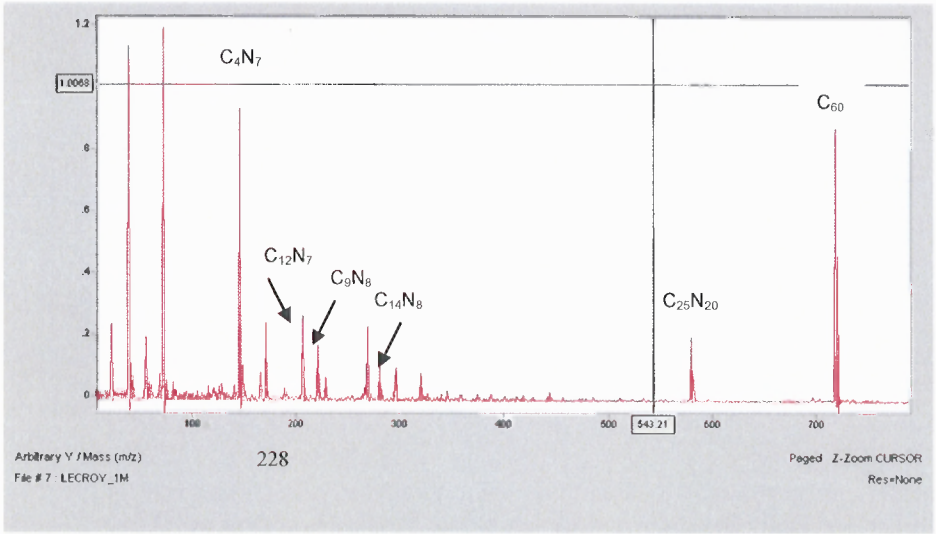


**Figure 5.11** Laser desorption time of flight mass spectrum in the (a) 200 to 450 amu region and (ab 580 amu region and from the electrochemically functionalized SWNT nanopaper made from SWeNT SWNTs. A drop of $C_{60}$ solution is added to calibrate the mass spectra.

### 5.1.2 Microwave Induced Electrochemical Reaction Synthesis Method

Carbon nanopapers were prepared using single-walled carbon nanotubes (SWNTs) from two sources–SWeNT and Cheap Tubes as described in Chapter 4. The SWNTs were

dispersed in deionized water in the presence of about 1% Triton X100 under horn sonication for 15 to 30 minutes. The suspension was then vacuum filtered at 0.2 atm pressure through 0.45 μm Teflon membrane filter paper from Millipore, washed successively with water and methanol, followed by successive washing with water and methanol again. The residue on the filter was dried in air for 24 hrs [67] and then peeled off as free-standing nanopaper. Both sets of nanopapers were used without further annealing in ammonia.

For the microwave synthesis experiments, the carbon nanopapers were pretreated by immersion in 5mM sodium tetrachloroplatinate II hydrate ($Na_2PtCl_4$) for 5 min to provide catalytic nanoparticles of platinum on the carbon nanotube sidewalls. The pretreated nanopapers were placed in 20ml glass vials each of 0.5M, 1M, and 2M sodium azide aqueous solutions and irradiated with ultra-violet radiation at 254 nm for 30 min and transferred to 100 ml capacity Teflon reaction vessels in a microwave oven (CEM Digestion System MDS-2100) shown in Figures 5.12.

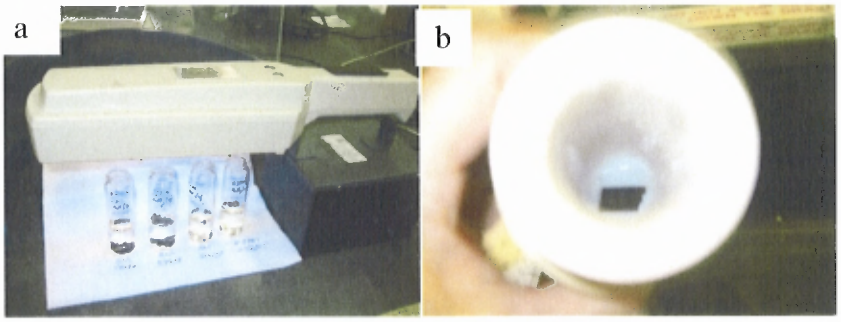

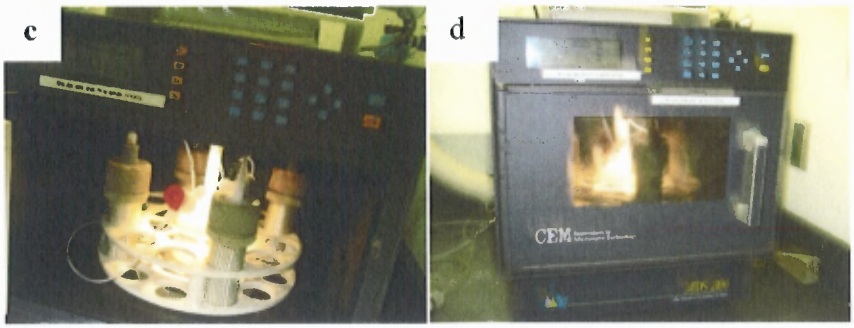


**Figure 5.12** Mircowave Assisted Synthesis (a) UV irradiation of SWNT in 20ml vials containing 0.5M, 1M, 2M aqueous solution of $NaN_3$.(b) SWNT nanopaper inside the reaction vessel prior to microwave reaction (c) SWNT in 2 reaction vessels, one vessel as control and 4$^{th}$ one that is part of the venting mechanism arrange in carousel for loading inside the microwave oven (d) Reaction vessels inside the microwave oven undergoing microwave assisted reactions.

Pure deionized water was used as the control in a separate vessel. Both reaction and control vessels were subjected to microwave radiation for 15 min under RAMP conditions and 5 min under HOLD to reach 150 °C, with approximately 950 watts of microwave energy at a frequency of 2450 MHz at full power and the pressure set at 200 psi. After completion of the reaction it was observed that the higher concentration, 2M, of the sodium azide solution has less volume of solution left inside the reactor. The nanopapers were carefully removed from the vessels, washed with deionized water and dried at room temperature and then characterized by Raman spectroscopy. Carbon nanopaper samples made of SWeNT nanotubes broke into many pieces under microwave irradiation in sodium azide solution. Most of the nanopapers made from SWeNT nanotubes did not have good mechanical properties and tended had to break apart even during handling. Characterization of these samples is therefore more time-consuming. Only nanopaper samples made from Cheap SWNT were analyzed using the Raman spectroscopy.

From Figures 5.13 and 5.14 it can be seen that there are no significant new peaks and decrease intensity after microwave reaction in 1M $NaN_3$ (aq) solution with and without uv-irradiation pre-treatment. However, when the concentration of sodium azide is doubled, the Raman spectrum (Figure 5.15) exhibits a substantial increase in intensity and appearance of new feature lines similar to observations depicted in Figure 5.8. for nanopaper samples that were electrochemically reacted with uv irradiation. The Raman features are however relatively weaker than those observed in the electrochemical reaction and are likely to be due to functionalization of the SWNT with polymeric nitrogen as discussed in the previous section.

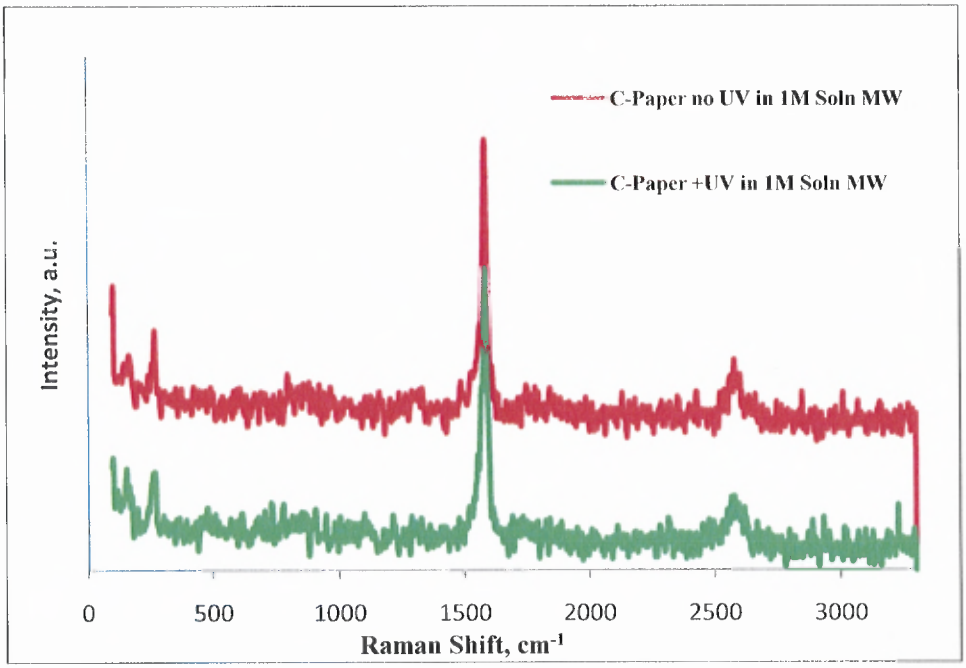


**Figure 5.13** Raman spectra of microwave reacted nanopaper from Cheap Tubes in 1M $NaN_3$(aq) solution with (green) and without (red) uv- pretreatment.

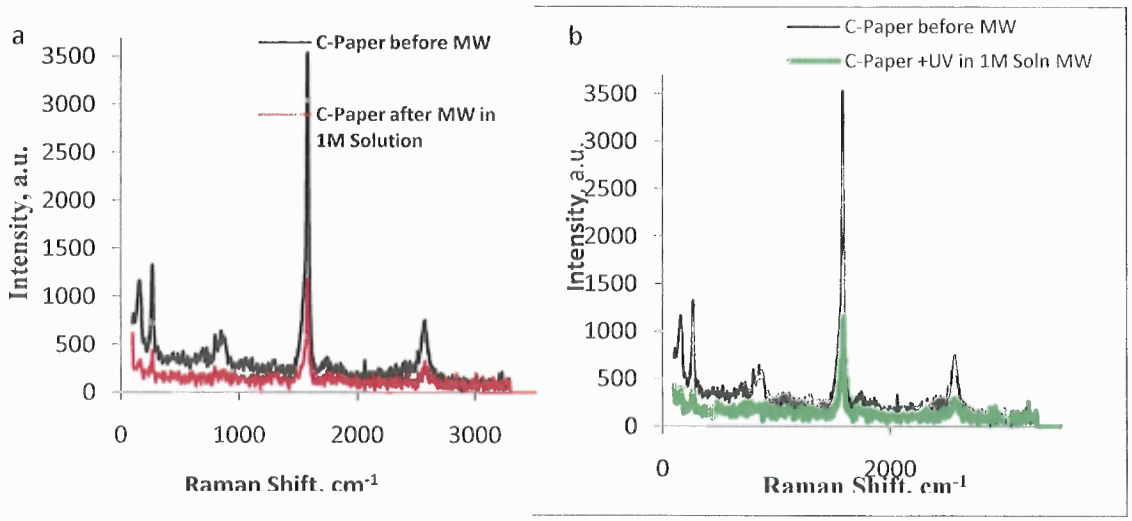


**Figure 5.14** (a) Raman spectra of pristine nanopaper from Cheap Tubes before (black) and after (red) microwave reaction in 1M $NaN_3$(aq) solution; and (b) Raman spectra of pristine nanopaper from Cheap Tubes before (black) and after (green) microwave and uv-irradiation in 1M $NaN_3$(aq) solution.

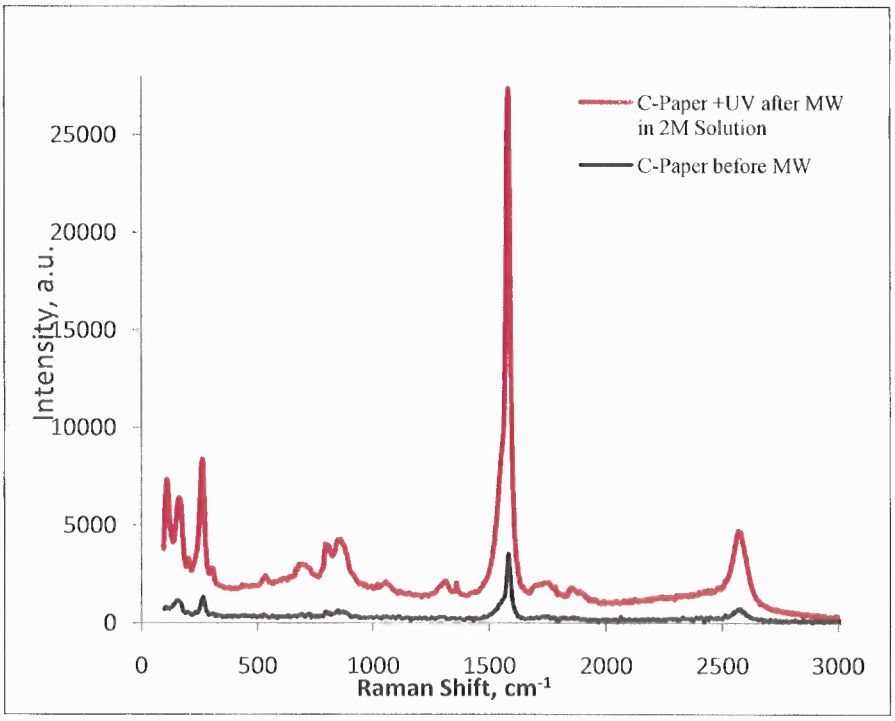


**Figure 5.15** Raman spectra of pristine nanopaper from Cheap Tubes before (black) and after (red) uv-treatment and microwave reaction in 2M $NaN_3$(aq) solution.

Prior work has shown that microwave synthesis of a carbon nanotube composite [68] can be achieved with decreased number of by-products. Moreover, rapid microwave-assisted purification of drugs using sodium azide has been achieved [69]. Microwave-assisted reaction has been shown to shorten the time to produce triazines (3 nitrogen hexagonal ring compounds) or tetrazoles (4 nitrogen pentagonal ring compounds) from sodium azide [70]. There are several reports in the literature indicating fast surface modification by sodium azide using low power (20-75W) microwave irradiation [71]. Most of the experiments performed in this research were performed using 100W microwave irradiation.

### 5.1.3 Plasma Enhanced Chemical vapor Deposition ( PECVD) Synthesis for the Polymeric Nitrogen

Carbon nanopapers were prepared using single-walled carbon nanotubes (SWNTs) from Cheap Tubes as described in Chapter 4. The Cheap Tubes SWNT powders were dispersed in deionized water in the presence of about 1% Triton X100 under horn sonication for 15 to 30 minutes. The suspension was then vacuum filtered at 0.2 atm pressure through 0.45 μm Teflon membrane filter paper from Millipore, washed successively with water and methanol, followed by successive washing with water and ethanol again. The residue on the filter was dried in air for 24 hrs [49 , 72, 73, 74] and then peeled off as free-standing nanopaper. The Cheap Tubes SWNT nanopapers were used without further annealing in ammonia.

The plasma enhanced chemical vapor deposition (PE-CVD) synthesis experiments were carried out on SWNT nanopaper substrates using SWNT from Cheap

Tubes in the plasma deposition system previously shown schematically in Figure 4.6. The reaction chamber of the plasma deposition system was a quartz tube 78cm in length with an inner diameter of 3.8 cm. Deposition was carried out with a radio frequency (rf) plasma at 50-70 watts power. Heating of the nanopaper substrate, which was placed in a quartz glass boat, was accomplished if required by placing the deposition tube in a temperature-controlled tube furnace. The experiments were run at a pressure of 1 Torr to 1.4 Torr. Argon and Hydrogen carrier gases were mixed with the precursor nitrogen at a flow rate of 25 to 50 standard cubic centimeters per minute (sccm) depending on the percentage of nitrogen and hydrogen or nitrogen and argon ratio utilized during the experiment. It was observed that at 50 sccm using 100% to 50% nitrogen, intensity of the broad Raman line centered near 2280 $cm^{-1}$ was much lower when compared to experiments ran at 25% nitrogen/75 % argon. In the latter sample however the broad line at 750 $cm^{-1}$ assigned to single bonded N-N stretching is more intense than the broad line at 2200 $cm^{-1}$ (shifted down from 2280 $cm^{-1}$) assigned to N=N and N≡N stretching modes. Three CHEAP nanopaper substrates were placed on boats located in the front, middle and back of the plasma in the reaction zone and approximately about 40mm apart from each other as shown in Figure 5.16. A thermocouple that was isolated from the grounded anode was kept in contact with the substrates during nitrogen deposition.

The PECVD experiments were run for one hour with 3 nanopaper substrates samples. The quartz boats containing the substrates were positioned on the front, middle and back position in the reaction tube as shown in Figure 5.16(b). The experimental runs consisted of 100%, 25% and 50% nitrogen with 0%, 75% and 50% argon gas as the carrier medium, respectively. The SWNT nanopaper treated in 100% nitrogen plasma

showed essentially no change in the Raman spectrum compared to the spectrum of the pristine material, indicating very little reaction. Samples that were placed in the back postion showed changes in in the Raman spectra due to plasma-induced reaction (Figure 5.17).

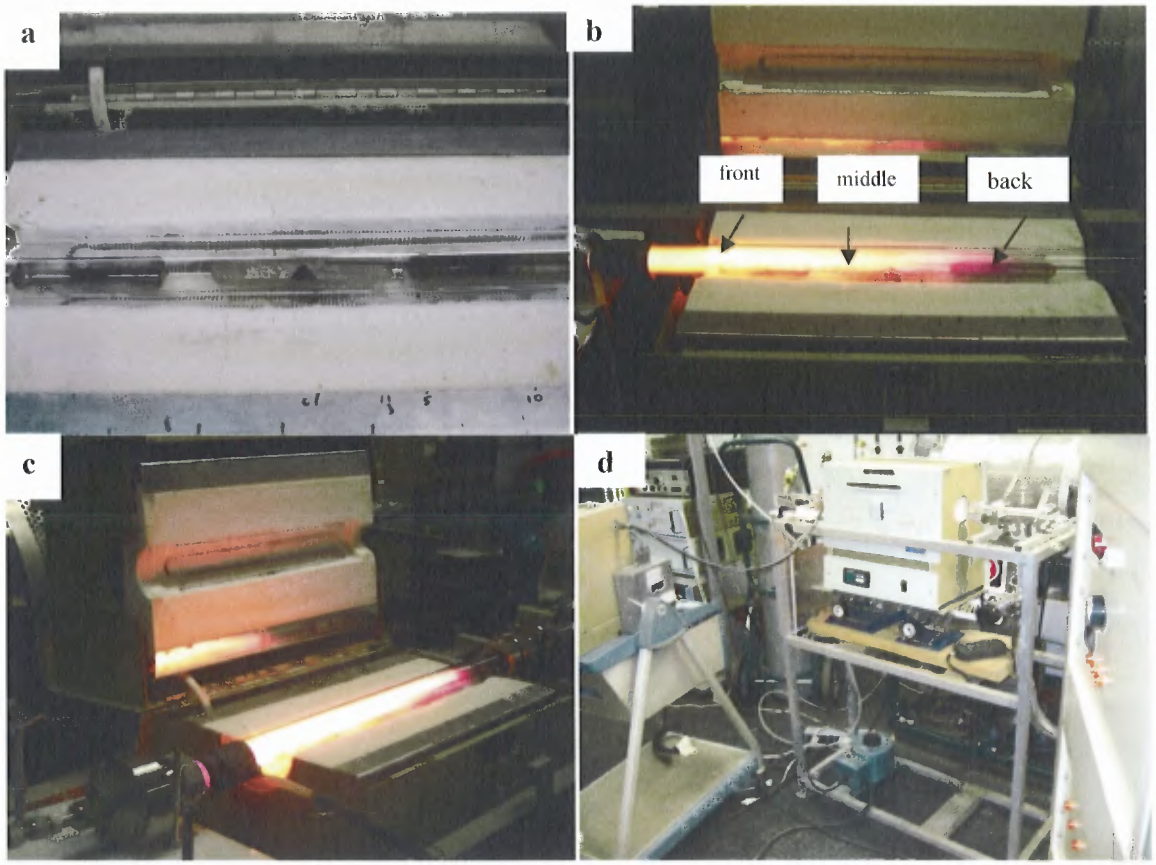


**Figure 5.16** Photographs of experimental PECVD set up used to carry out plasma-assisted reaction on SWNT nanopaper samples. Panel (a) shows three quartz boats containing nanopaper samples inside the PECVD quartz tube deposition chamber before the experiment; panel (b) shows on-going PECVD experiment with the location of the samples indicated; panel(c) shows a typical on-going plasma experiment; and panel (d) shows an overview of the laboratory scale PECVD set-up.

When the nitrogen was mixed with argon to raise the plasma temperature and hydrogen was added to induce catalytic effects, extensive reaction occurred as evident

from the Raman spectra shown in Figure 5.21 and the SEM images in Figure 5.27. The results shown in Figures 5.17.5.18 and 5.19 indicate that nanopapers treated in nitrogen/hydrogen plasma have more intense Raman spectra compared with those treated in a -nitrogen/argon plasma. Two broad Raman lines emerge on plasma treatment–one centered near 2250 $cm^{-1}$ and the other near 750 $cm^{-1}$. The former lies below the stretching frequency of triply bonded nitrogen in pure nitrogen and the latter near the stretching frequency of singly bonded nitrogen in *cg*-polymeric nitrogen at high pressure and temperature reported by Eremets *et al.* These broad features were also weakly evident, particularly in the Raman spectra of electrochemically reacted nanopaper shown in Figure 5.20 comparing the Raman spectra for electrochemically- and plasma- reacted nanopaper samples. The broad lines can therefore be assigned to a disordered network of polymeric nitrogen consisting of small and large clusters bonded to the carbon framework of the nanotube. The higher frequency line can be assigned to doubly bonded nitrogen and the lower frequency line to singly bonded nitrogen. SEM images in Figure 5.27 clearly show the formation of a coating on the sidewalls. In addition, ball-like dodecahedral structures of nitrogen inserted into the nanotubes would give rise to bulbous nanostructures that are clearly evident in Fig. 5.27 (a) and (f). The laser ablation mass spectrum depicted in Fig. 5.25 from a plasma-treated sample show the appearance of a strong signal assignable to $C_5N_{12}$ (where $N_{12}$ can be comprised of $N_8$ and $N_4$) and a clear signal due to $N_8$ clusters consistent with this picture of a polymeric nitrogen network built of nitrogen clusters bonded to the carbon framework. Advanced optimization of the plasma process to give ordered polymeric nitrogen would require *in-situ* annealing during reaction and nanopaper substrate pre-treatment. Such a material would have a Raman

spectrum similar but more intense than the spectrum shown in Figure 19 (b) for a sample treated in 25% nitrogen-75% argon plasma, where the line assigned to single bonded nitrogen is enhanced. Processing conditions to narrow the width of the Raman line centered near 750 $cm^{-1}$ as a result of ordering would be the next step in obtaining an ordered polymeric structure on the carbon nanotube sidewalls.

An attempt was made to duplicate the plasma-reaction experiments using nanopapers from Cheap Tubes SWNTs that were pre-annealed in a similar manner as the nanopaper working electrodes from Cheap Tubes SWNTs used in the electrochemical reaction experiments. The Raman spectra of the plasma-treated, pre-annealed nanopaper subtrates with nitrogen as precursor, and hydrogen and argon as the carrier gases are shown in Figures. 5.21 and 5.22, respectively. The Raman spectra are similar to those obtained for the plasma-treated unannealed nanopaper substrates shown in Figures 17 and 18 except that the relative intensity for the broad line centered at 750 $cm^{-1}$ does not exceed that of the line at 2250 $cm^{-1}$ as it does for unannealed nanopaper substrates treated in 25% nitrogen-75% argon plasma (shown in Figure 5.17 and 5.18). The spectra in Figure 5.21 and 5.22 are also similar to those observed for the electrochemically treated samples depicted in Figures 5.8 and 5.10. The FTIR-ATR spectra for annealed and unannealed nanopaper using SWNTs from Cheap Tubes that were plasma-treated in 25% nitrogen:75% hydrogen, are shown in Figs. 5.23(a) and (b), respectively. The spectra taken directly from the nanopaper surfaces are relatively weak but show clear lines. In the annealed sample, lines assignable to C=N (around 2000 $cm^{-1}$) and C-H stretching (around 3000 $cm^{-1}$) vibrations are observed, whereas lines associated with C-N and –C=OOH stretching vibrations between 1000 and 2000 $cm^{-1}$ are observed in the

unannealed sample. For the electrochemically treated sample, only a line assignable to the C=N vibration is observed. The observation of carbon-nitrogen stretching lines indicates bonding of the nitrogen atoms on the polymeric nitrogen with the carbon framework, consistent with the laser ablation mass spectral data. There are, however, differences between the infrared spectra for the annealed and unannealed nanopapers that would need further study (also see Appendices C-D).

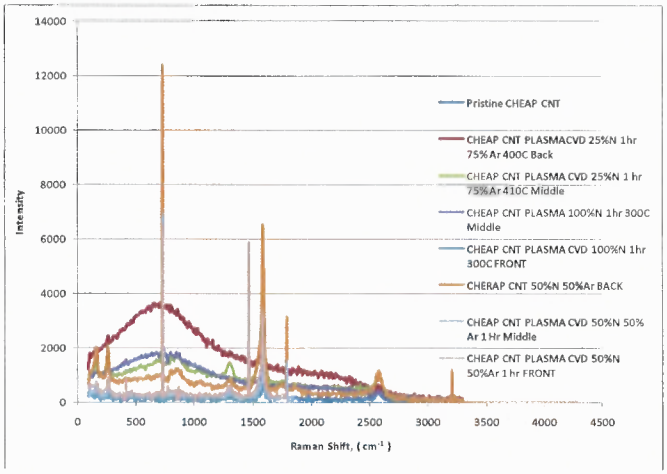


**Figure 5.17** Raman spectra of nanopaper using SWNTs from Cheap Tubes reacted in: 50% nitrogen and 50% argon and 50%nitrogen and 50% hydrogen and (B) 50% nitrogen and 50% hydrogen, 25% nitrogen and 75% hydrogen, 50% nitrogen and 50% argon and 25% nitrogen and 75% argon.

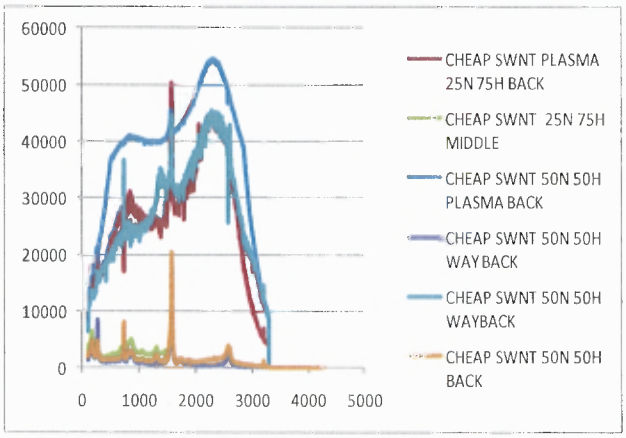


**Figure 5.18** Raman Spectra from nanopaers using SWNTs from Cheap Tubes reacted in nitrogen/ hydrogen plasma with composition indicated on the figure.

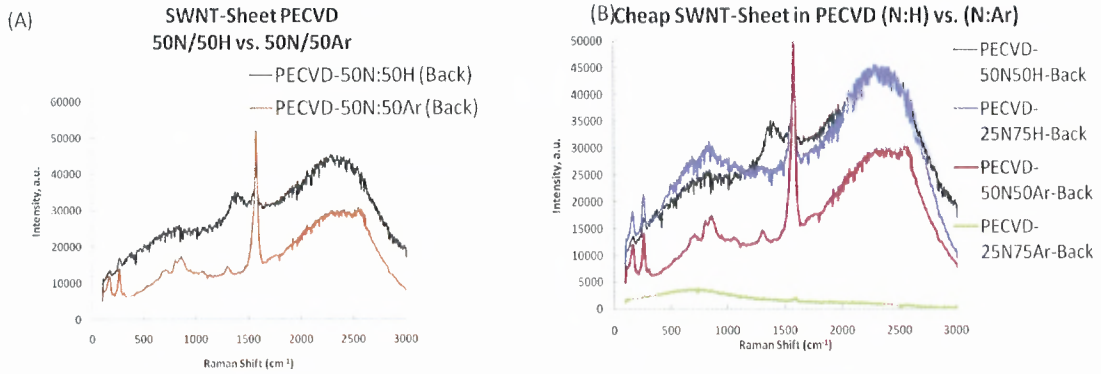


**Figure 5.19** Overlay of Raman spectra of plasma-treated unannealed Cheap Tubes nanopaper samples: (A) Raman spectra from nanopapers treated in 50% nitrogen/50% argon and hydrogen plasmas and placed at the back of the reaction zone, and (B) Raman spectra from nanopapers treated in: 50% nitrogen/50% hydrogen (black), 25% nitrogen/75% hydrogen (purple), 50% nitrogen/50% argon (red) and 25% nitrogen and 75% argon (green) plasmas.

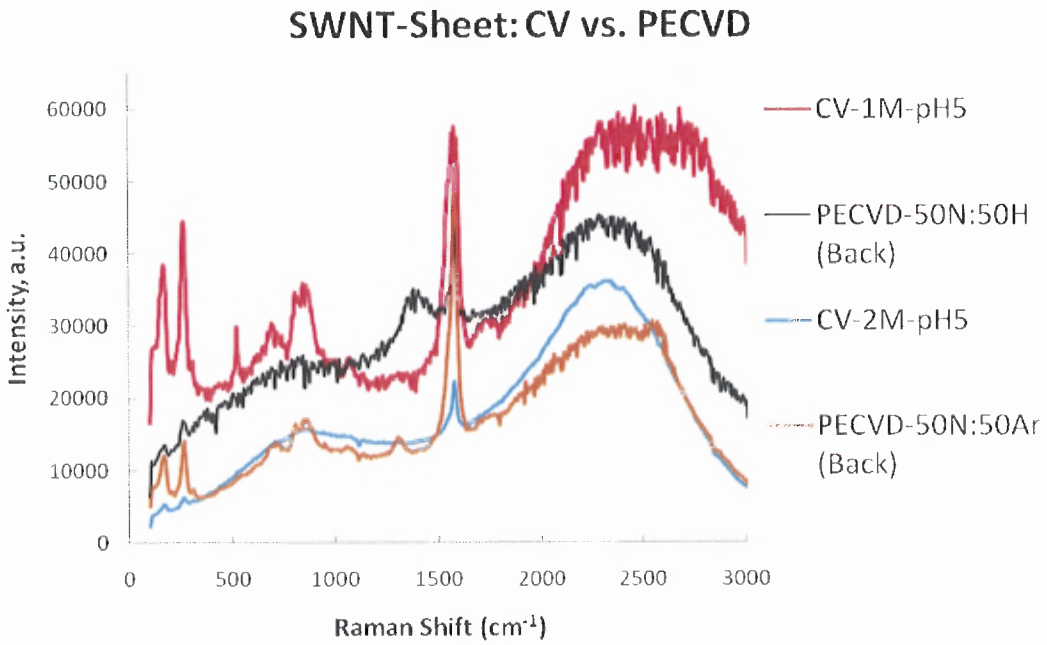


**Figure 5.20** Overlay of Raman spectra of plasma-treated (in PECVD reactor) nanopapers in 50% nitrogen-50% hydrogen (black) and 50% nitrogen-50% argon (orange) compared with spectra from electrochemically-reacted during cyclic voltammetry (CV) nanopapers in 1M sodium azide (red) and 2M sodium azide (blue).

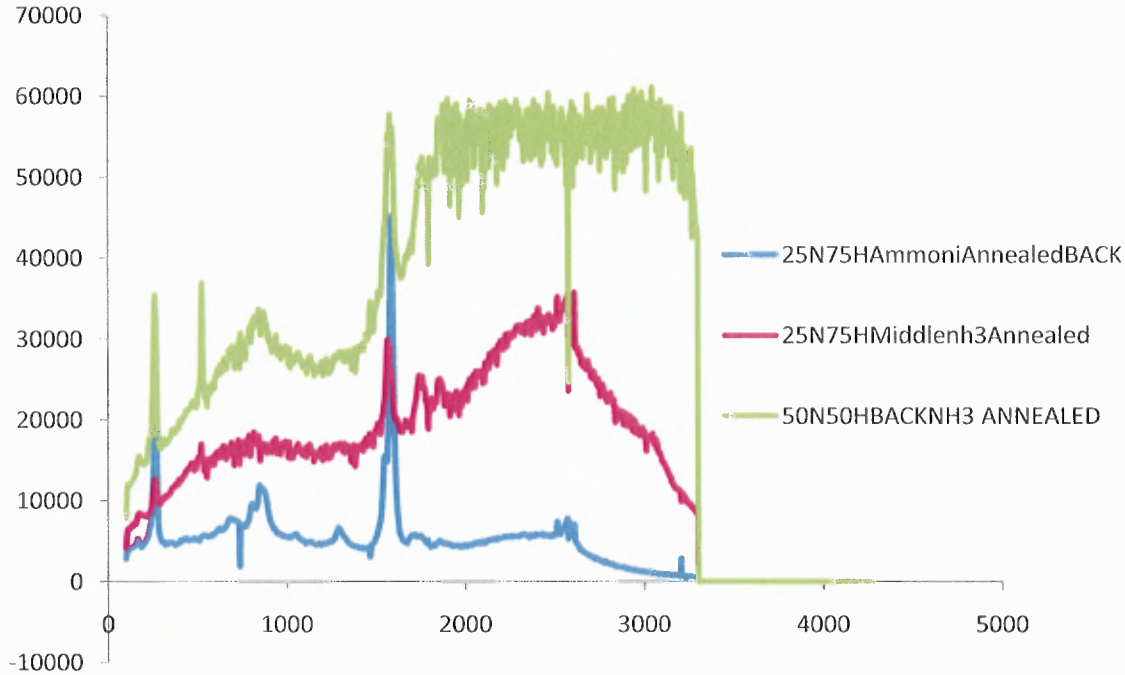


**Figure 5.21.** Raman spectra of annealed nanopaper from Cheap Tubes SWNTs in different reactor locations indicated in the figure reacted in 25% nitrogen/75% hydrogen and 50% nitrogen/50% hydrogen plasmas.

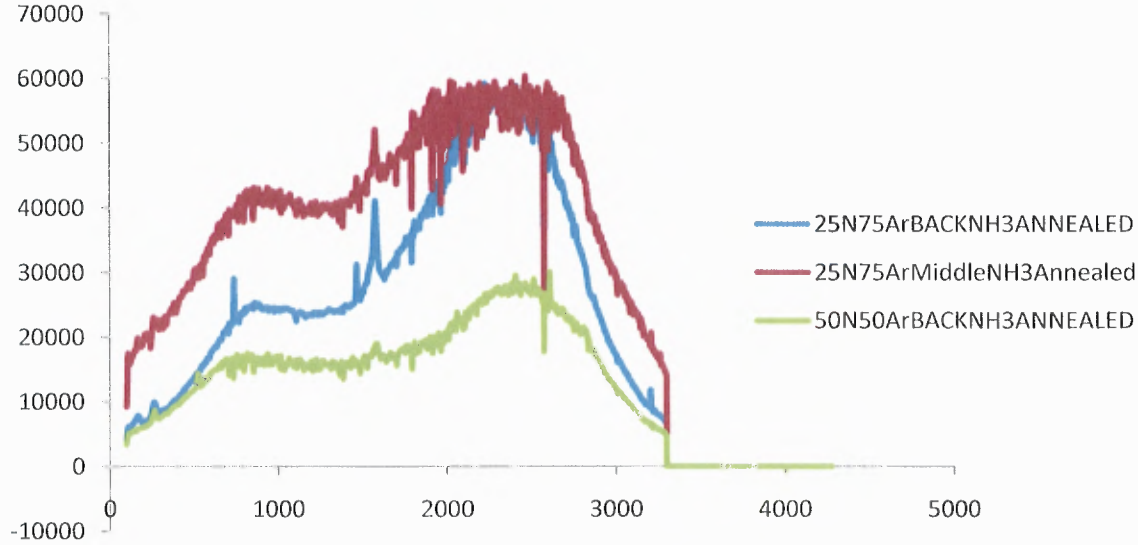


**Figure 5.22** Raman spectra of annealed nanopaper from Cheap Tubes in different reactor locations indicated in the figure reacted in 25% nitrogen/75% argon and 50% nitrogen/50% argon plasmas.

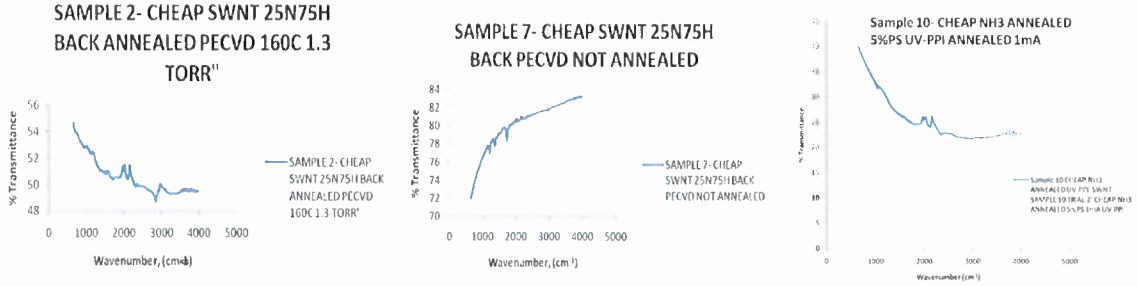


**Figure 5.23** FTIR-ATR of: (a) 25% nitrogen:75% hydrogen plasma-treated, annealed Cheap Tubes nanopaper, (b) 25% nitrogen:75% hydrogen plasma-treated unannealed Cheap Tubes nanopaper, (c) Electrochemically reacted annealed Cheap Tubes nanopaper.

The same experiments were performed using annealed nanopaper using Cheap Tube SWNTs. These nanopapers were annealed at 500$^{o}$ C in a CVD furnace for 1 hour in an inert atmosphere and then reacted in 25% nitrogen with 75% argon, and 50% nitrogen and 50% argon plasmas. A second set of experiments were performed using hydrogen as the carrier gas. The Raman spectra are shown in Figures 5.21 and 5.22. The intensity of the Raman spectra were five times stronger than from unannealed nanopaper made using SWNTs from Cheap Tubes. Substrates located in the back had more polymeric nitrogen than those in the middle location as shown in Figures 5.21 and 5.22. The key features of the spectra are the enhancement of the broad scattering previously seen at 2350 cm$^{-1}$ in Figures 5.8 and 5.10 for electrochemically reacted samples and the growth of a broad line centered at 800 cm$^{-1}$. Moreover, the broad line at 800 cm$^{-1}$ shows a further increase in relative intensity and shifts down to 700 cm$^{-1}$ for the sample treated in a 25% nitrogen/75% argon from the PE-CVD in Figure 5.22. It is worth noting that the center of the broad line at 2350 cm$^{-1}$ is close to the narrow line at 2328 cm$^{-1}$ of molecular nitrogen assigned to the stretching mode of the nitrogen-nitrogen triple bond [75, 76, 77],

whereas the center of the broad band at 700 $cm^{-1}$ is close to the frequency of the Raman line of single-bonded nitrogen in the cg-polymeric nitrogen phase reported by Eremets et al. The two broad Raman lines observed can therefore be assigned to a polymeric nitrogen network with bond order ranging from 1 (for ideal polymeric nitrogen) to between 2 (for nitrogen clusters) and 3 (for molecular nitrogen). The broadening of the line centered at 2350 $cm^{-1}$ extends to below 2000 $cm^{-1}$ where the double bonded nitrogen stretching mode frequencies of $N_4$ clusters occur. The broad lines are particularly enhanced in samples treated in the nitrogen/hydrogen plasma (where the plasma-induced temperature is measured to be $100^{o}$-150 °C and the relative intensities of the SWNT G modes are substantially masked. The Raman spectrum in Figure 5.17 for the sample treated in 25% nitrogen/75% hydrogen plasma with reaction temperature in the $400^{o}$-450°C range shows a reversal of the intensities of the two broad Raman lines, indicating the formation of a polymeric network with greater number of single N-N bonds. A similar plasma-synthesized amorphous phosphorous-nitrogen network has been previously reported by Veprek et al [78,79].

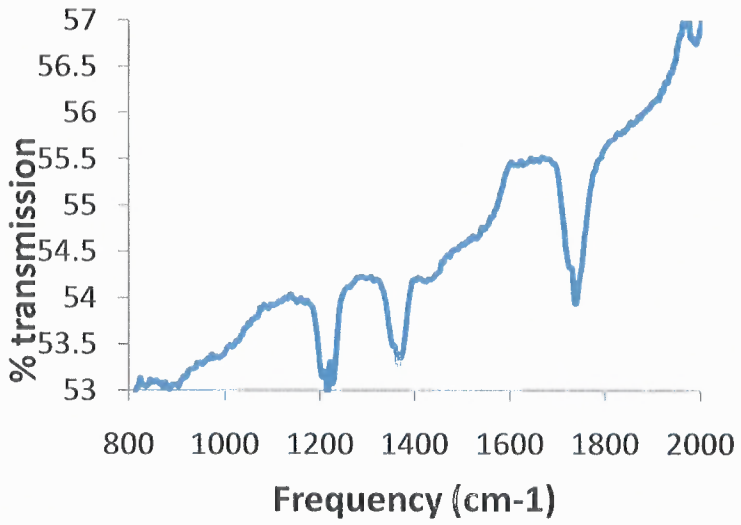


**Figure 5.24** FTIR-ATR spectrum of a 50% nitrogen-50% hydrogen plasma processed nanopaper prepared with Cheap Tubes SWNTs.

FTIR and laser ablation mass spectra shown in Figures 5.24 and 5.25 respectively, provide insights into the structure of the material produced on the SWNTs after plasma-treatment. The FTIR-ATR spectra (Figure 5.24) taken directly from the rough nanopaper surface shows relatively weak but well resolved lines centered at 1744 $cm^{-1}$, at 1372 $cm^{-1}$ and at 1220 $cm^{-1}$. The line at 1744 $cm^{-1}$ can be assigned to –COOH groups formed on the SWNTs sidewalls via oxygen adsorbed on the nanotube walls. The lines at 1372 $cm^{-1}$ and at 1220 $cm^{-1}$ can be assigned to the C-N stretching modes of $C_yN_x$ clusters [80]. Lastly, the line at 2000 $cm^{-1}$ can be assigned to C-N bond.

The laser ablation mass spectrum from a plasma-treated sample in Figure 5.25 and 5.26 shows $N_8$ clusters and a $C_5N_{12}$ cluster where $N_{12}$ is comprised of three $N_4$ clusters. Typical FE-SEM images for a 50%/50% nitrogen-hydrogen plasma-treated sample show a dramatic change in morphology and thickening of the nanotubes due to plasma-assisted deposition of the polymeric-nitrogen phase. The changes are associated

with coating of the SWNT sidewalls with the polymer network and in some regions formation of the polymer nitrogen within the nanotubes to form bulb-like structures and curved tubes.

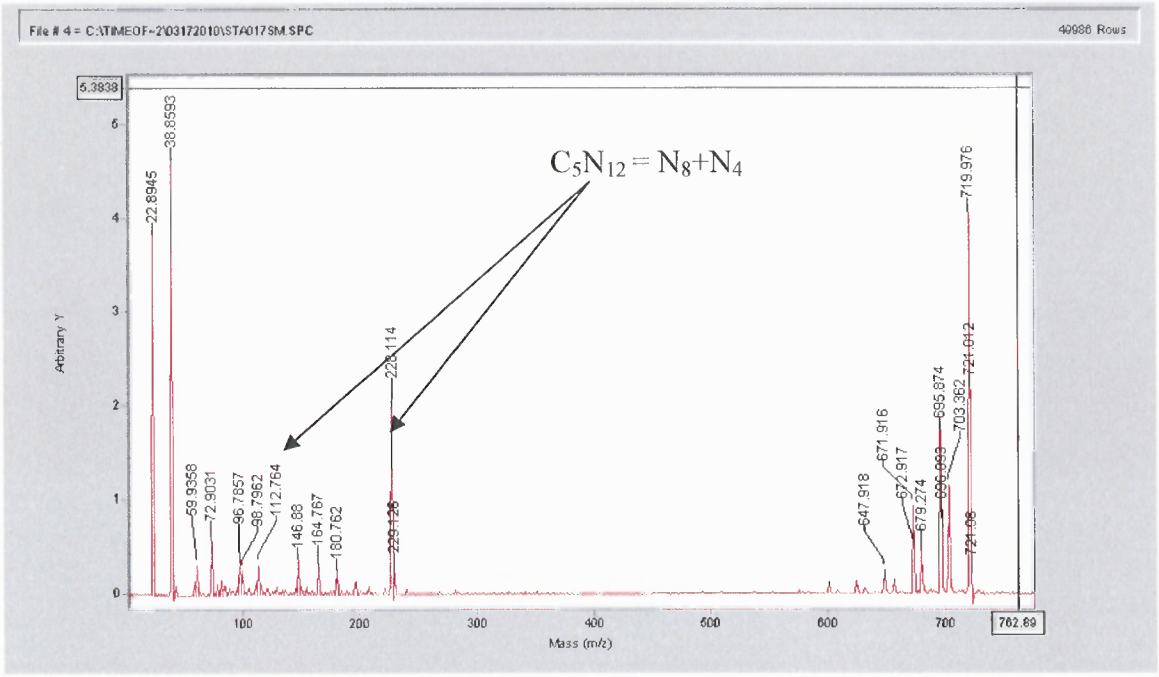


**Figure 5.25** Laser ablation mass spectrum from a nanopaper reacted in 50% nitrogen/50%hydrogen plasma.

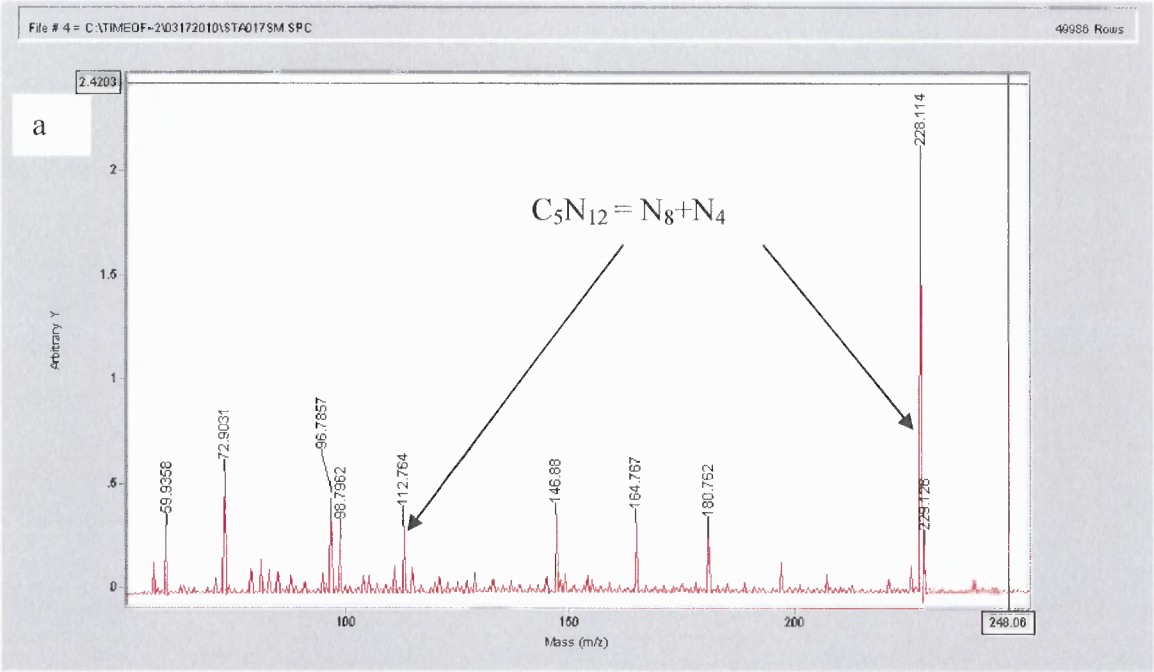


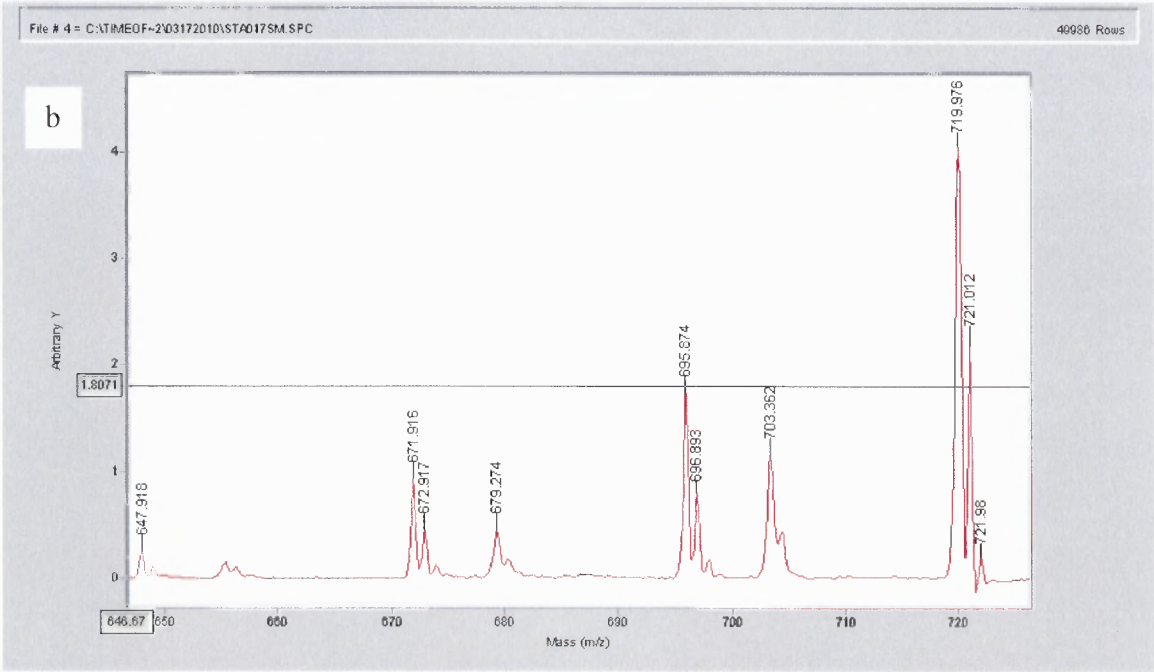


**Figure 5.26** **(a-b)** Laser ablation mass spectrum from a nanopaper reacted in a 50% nitrogen-50% argon plasma.

Further characterization of the PE-CVD samples by the FE-SEM images (Figure 5.27 (a),(b),(c),and (d) provide insights into how the three-dimensional architecture of the composite is formed. As indicated by Figure 5.27 (a) and (b), the nucleation of nitrogen followed by bonding to carbon occurs on the SWNT bundles at the onset of the reaction. Then, the polymeric nitrogen clusters randomly crosslink (Figures 5.27 (a)-(b) and grow into the macroscopic architecture shown in Fig. 5.27 (c). As shown in Figure 5.27 (d), in certain areas of the nanopaper, the SWNTs are completely covered by the polymeric nitrogen coating. The image shown in Figure 5.27 (d) is from the surface of SWNT fiber region, and the nanotubes that form the underlying framework of the structure are still embedded indicating strong interfacial binding of the SWNTs to the polymeric nitrogen.

A mechanism for the growth of the polymeric nitrogen-SWNT composite can be proposed based on the SEM images shown in Figure 5.27. More details will be provided by a future high resolution TEM study. The growth appears to be initiated by the reaction of –N at the–C sites on the SWNT sidewalls, locally forming $N_xC$. The $N_xC$ thus formed was further decomposed by the plasma to produce randomly growing $N_xC$ nanoparticles, which covered the nanotube surface and lead to the formation of a heterogeneous $N_xC$ – SWNT network with spherical growths (Figure 5.27(c)).

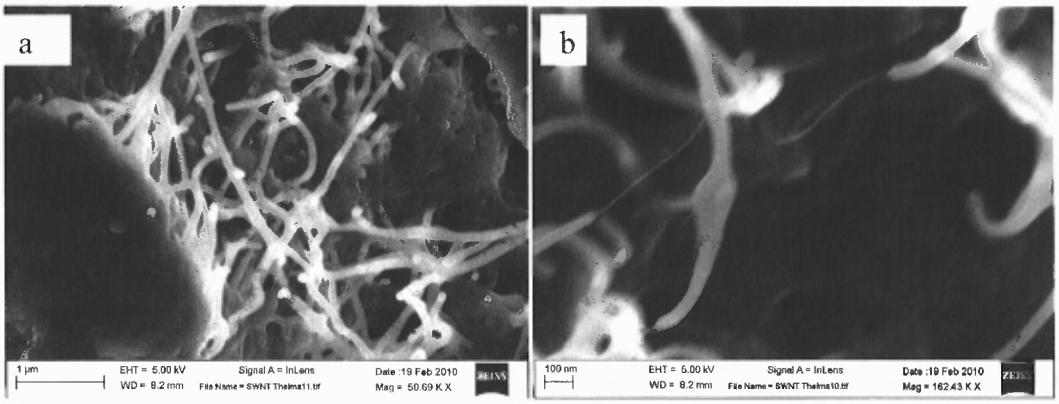

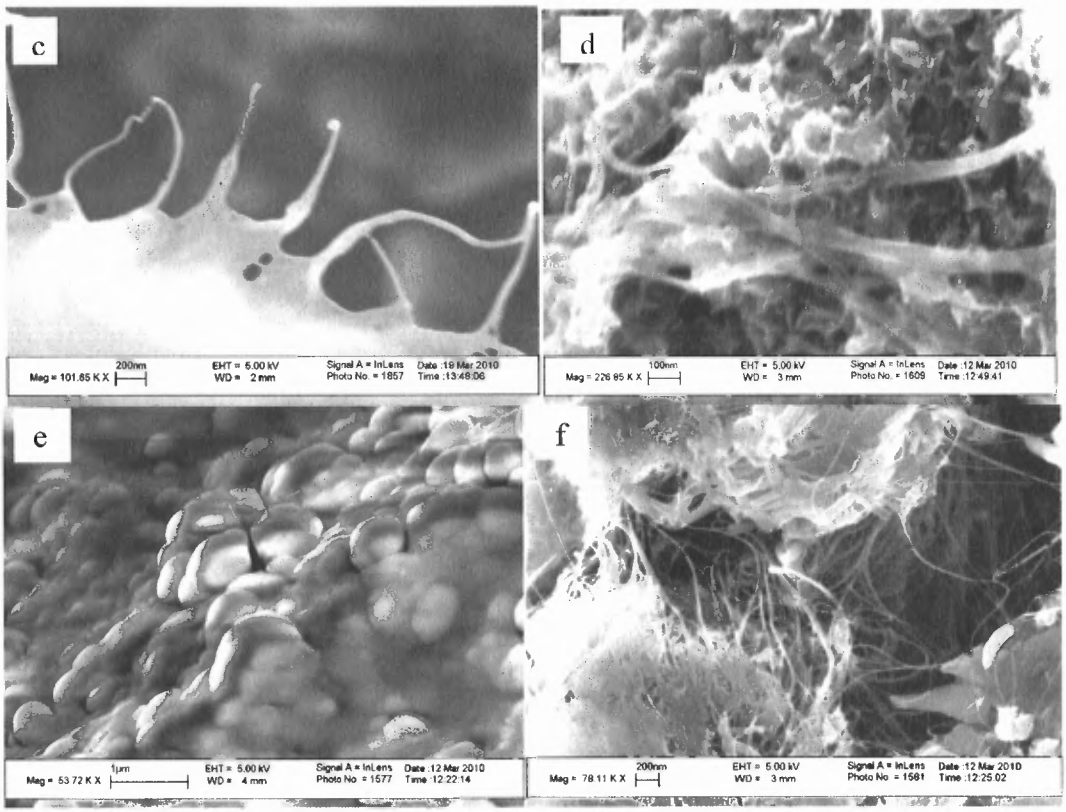


**Figure 5.27** Series of FE-SEM images of plasma-reacted SWNT nanopaper discussed in the text.

## 5.2 Thermal Properties of Nanopaper Samples from Electrochemical and Plasma Reactions

In order to determine if the polymeric nitrogen clusters and networks prepared on the carbon nanotubes are indeed energetic as predicted, differential scanning calorimetric (DSC) data were obtained to evaluate the thermal properties of the electrochemically functionalized nanopaper relative to that of a pristine nanopaper from the same batch[81]. For energetic materials, the guidelines taken from STANAG 4147[82] is stated as ," A decomposition peak temperature shift of 4 degrees Celsius or less is deemed compatible. Any shift towards a lower peak temperature of the explosive has some degree of incompatibility. The greater the shift towards lower temperatures, the greater the degree

of incompatibility. A peak temperature shift of more then 20 degrees indicates incompatibility. Peak temperatureshifts between 4 and 20 degrees indicate partial or potential incompatibility in which case Vacuum Stability testing is required to confirm. "

In this research work, we are not testing the CHEAP SWNT and the Polymeric Nitrogen, but actually what we are testing is a SWNT doped with N, an explosive material which is our baseline explosives. We are determining the endothermic onset and exothermic peaks of an explosive material to see how thermally stable it is. It is important to know the energetic polymeric nitrogen thermal stability and IM properties especially for response to hot spalls or hot conductive fragments ignition ( HCFI) stimuli. It is also important to know especially for the fast Cook-off or slow cook-off IM test requirements whether it will pass the IM standards before fielding to the soldiers. In our case, our control, baseline explosive is the energetic polymeric nitrogen not the CHEAP SWNT. The CHEAP SWNT does not cause a shift towards a lower temperature nor caused a temperature shift of more than 20 degrees to cause incompatibility on both cases as stated in the STANAG 4147. It was observed that a DSC scan at a heating rate of $20^0$ C per minute for a pristine nanopaper does not show an endothermic onset nor an exothermic peak [Figure 5.28(a)]. On the other hand, an electrochemically functionalized SWNT nanopaper exhibits an endothermic onset at $300^o$ C [Figure 5.28(b)] associated with endothermic dissociation similar to that seen by Wang et al in nitrated SWNTs [83,84]. This is followed by a exothermic peak at $350^oC$ similar to what is typically seen in an energetic material like cyclotetramethylene-tetranitramine (also referred to as HMX). The HMX weak endothermic onset (Tm=$185^0$ C) is due to the transformation of HMX from the low temperature phase (β) to the high temperature phase (δ) [85, 86]. The

sharp endothermic onset at 281.95$^0$ C corresponds to melting which is followed by a strong exothermic peak. The sharp peak (T=286.86$^0$ C) immediately after the melting is due to the self-decomposition of HMX. However, for HMX, the sharp endotherm onset is 281.3 $^o$C and the exotherm peak is 286.86 $^o$C as shown in Figure 5.29(b). This is an indication that the polymeric nitrogen is more thermally stable and less sensitive when compared to HMX [87,88,89]. Similar observations have been made by Lee *et al* in β-HMX where an endothermic melting process precedes the exothermic reaction [90].

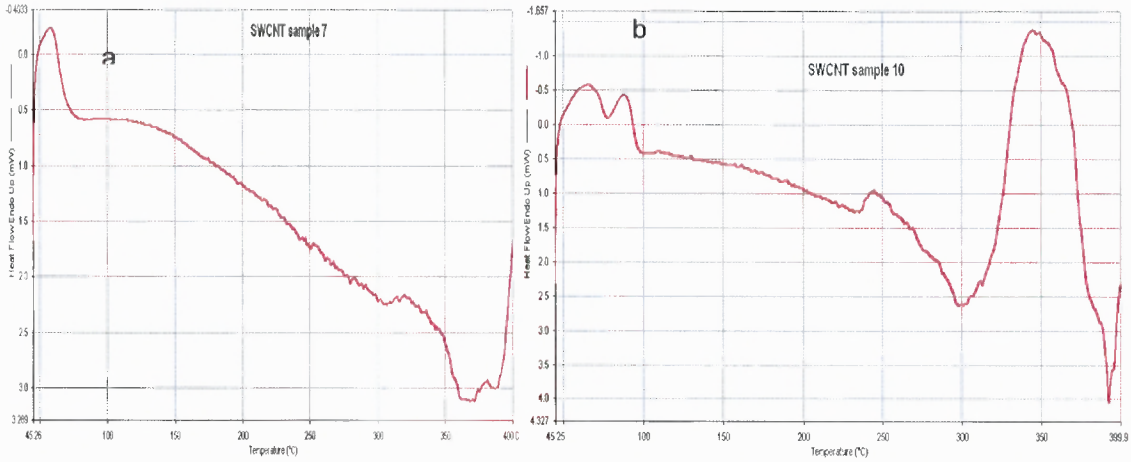


**Figure 5.28** (a) DSC scan for Cheap Tubes SWNT nanopaper before electrochemical reaction, and (b) DSC scan for electrochemically functionalized Cheap Tubes SWNT nanopaper.

Similar thermal behavior was observed for the CHEAP SWNT ammonia annealed prior to the Plasma-assisted synthesis using the PE-CVD process equipment. The DSC of the pre-annealed CHEAP SWNT nanopaper synthesize with 25% Nitrogen and 75% Hydrogen shown in Figure 5.28(a) exhibits endotherm onset at 250.79$^o$ C [Figure 5.28(b)] associated with endothermic dissociation similar to that seen by Wang et al in nitrated SWNTs [91,92]. This is followed by a rapid exothermic peak at 316.59$^o$C similar to what

is typically seen in an energetic material like cyclotetramethylene-tetranitramine (also referred to as HMX). HMX has an endotherm onset of 281.3C and an exotherm peak at 286.6 C [93, 94, 95, 96, 97]. The polymeric nitrogen substrate shows a broad endotherm onset and exotherm peak similar to the Reduced Sensitivity (RS) HMX, RDX and M30A1 propellant shown in Figures 5.29 (b), (c) and (d), respectively. As can be seen in Figure 5.29 (a), the functionalized SWNT have a higher exotherm onset of 316.59 $^{0}$C.

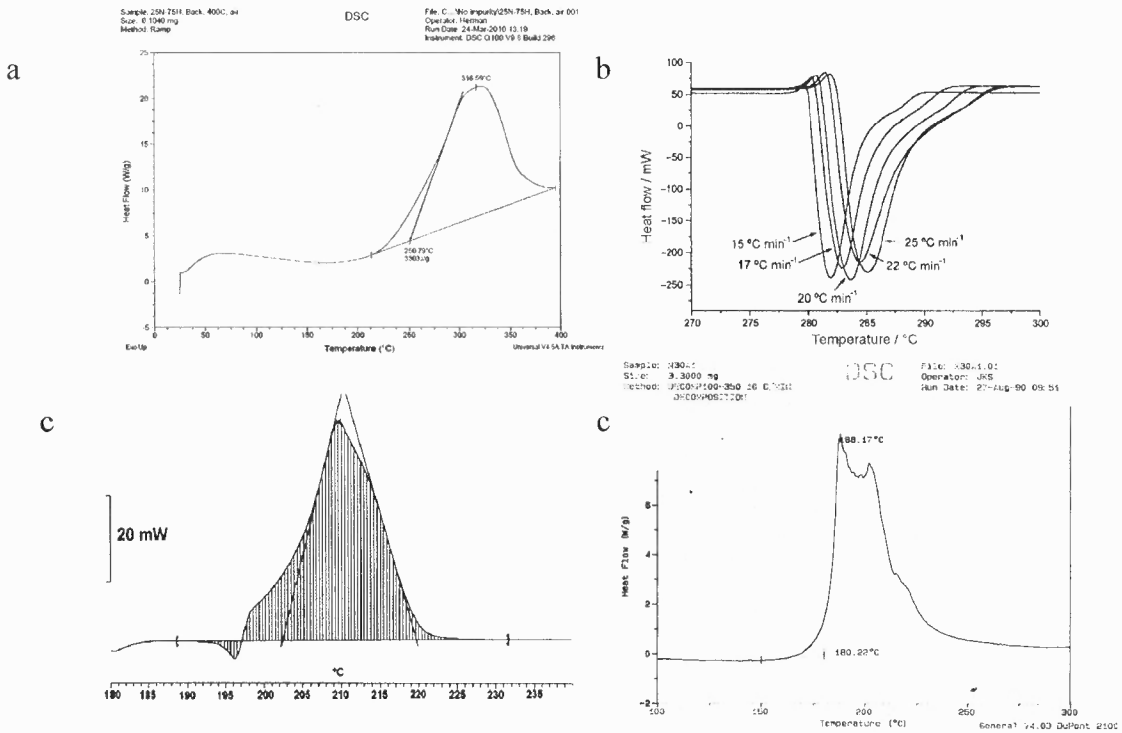


**Figure 5.29** (a) DSC scan for Cheap Tubes SWNT Back nanopaper after plasma enhance CVD with 25% nitrogen and 75% hydrogen at 20$^{0}$C min$^{-1}$and (b) DSC curves of HMX decomposition (15 to 25$^{o}$C min$^{-1}$ (c) Advanced DSC analysis of RS-RDX (IM behaviour) (d) DSC scan for M30A1 propellant.

Source: G.F.M. Pinheiro, V.L.Lowurenco and K.Iha, Influence of Heating Rate in the Thermal Decomposition of HMX, *Journal of Thermal Analysis and Calorimetry*, Vol. 67, (2002)445-452

Additional Differentail Scanning Calorimetry and Thermal Gravimetric Analysis (DSC and TGA ) analysis of the bukypaper substrates can be found in Appendix A and B for both the electrochemical and PE-CVD synthesized buckypapers, respectively. All the results are depicting a trend of thermally stable properties for the synthesizes polymeric nitrogen when compared to HMX and RDX explosives [98, 99,100, 101 ].

## 5.3 Fourier Transform Infrared Radiation-Attenuated Reflectance Transmission ( FTIR-ATR)

Electrochemical functionalization of the nanopapers prepared from Cheap Tubes and SWeNT nanotubes was further confirmed by FTIR-ATR spectroscopy. Representative examples of these spectra are shown in the Figures 5.30 and 5.31 FTIR-ATR spectral scans from the pristine nanopapers prepared from Cheap Tubes and SWeNT annealed in ammonia, respectively, are featureless consistent with the absence of strong infrared-active vibrations in SWNTs. Figure 5.30 (b) shows the spectrum of the electrochemically fuctionalized nanopaper made using SWNTs from Cheap Tubes. The infrared lines in the region around 2100 $cm^{-1}$ can be assigned to the C-N double bond stretching vibrations of $C_yN_x$ clusters linked to the SWNT sidewalls. In Fig. 5.30 (b) from functionalized nanopaper made using SWeNT nanotubes, only lines below 2000 $cm^{-1}$ are observed. The peak at 800 $cm^{-1}$ can be assigned to C–N single bond stretching vibrations associated with $C_yN_x$ clusters. The lines near 1500, 1600 and 1800 $cm^{-1}$ belong to the C=C stretching and C=O stretching of $C_yN_x$ clusters, respectively.

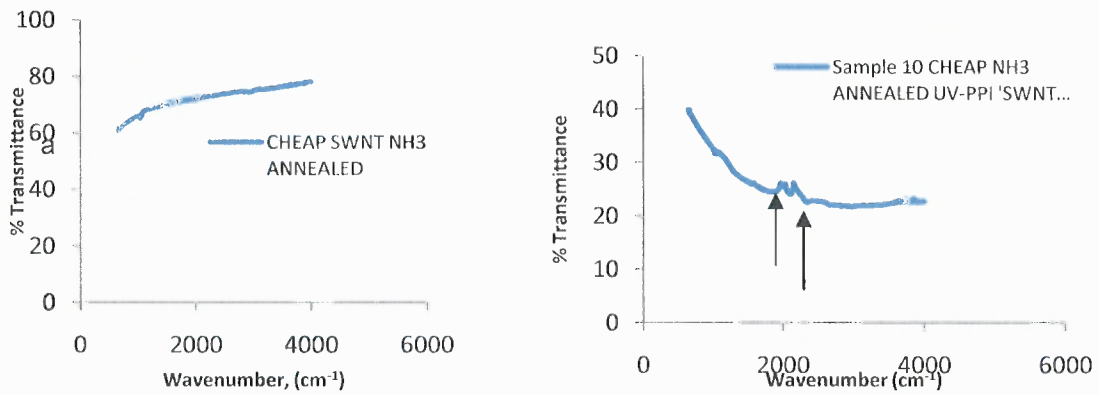


**Figure 5.30** (a) left shows the FTIR-ATR results for the pristine CHEAP SWNT after NH3 annealing (b) right shows the FTIR-ATR result for the electrochemically functionalized SWNT nanopaper made from CHEAP SWNTs.

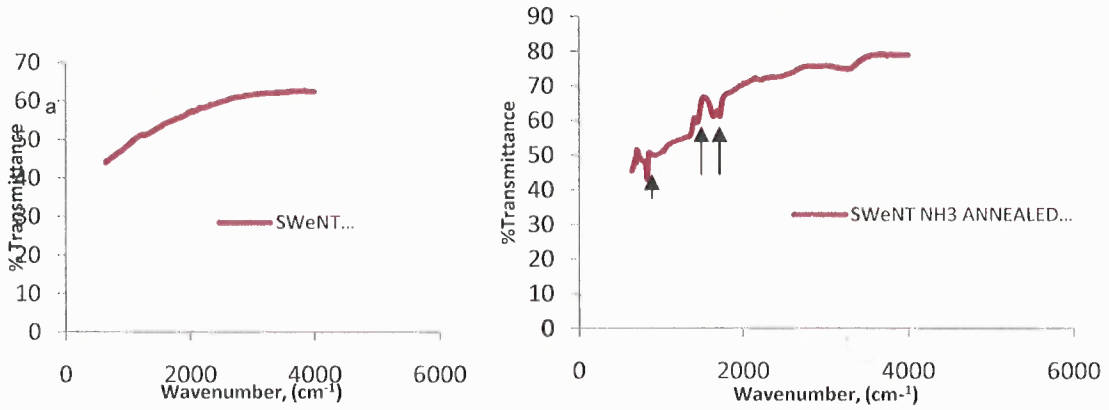


**Figure 5.31** (a) FTIR-ATR spectra for the pristine nanopaper made using SWeNT SWNTs after ammonia annealing, and (b) FTIR-ATR spectra for electrochemically reacted nanopaper using SWeNT SWNTs.

An FTIR-ATR analysis of the pre-annealed CHEAP SWNT annealed prior to PE-CVD using 25% Nitrogen with 75% Hydrogen carrier gas was perfomed. Figure 5.32 shows the spectrum of the PC-CVE functionalized nanopaper made using SWNTs from Cheap Tubes. The infrared lines in the region around 2000-2200 $cm^{-1}$ can be assigned to the C-N double bond stretching vibrations of $C_yN_x$ clusters linked to the SWNT sidewalls. The resulting line 2000-2200 $cm^{-1}$ shown in Figure 5.32 indicate a C-N

bond which is similar from Figures 5.30 and 5.31 for CHEAP SWNT and SWeNT synthesized by electrochemical reactions., respectively.

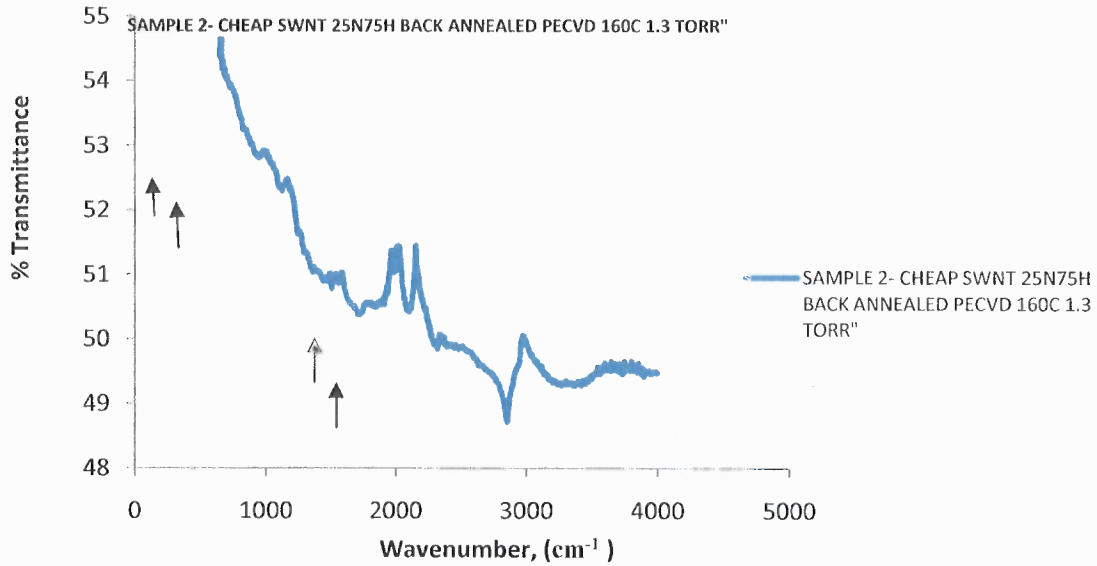


**Figure 5.32** CHEAP SWNT annealed prior to PE-CVD using 25% Nitrogen with 755 Hydrogen carrier gas.

Additional FTIR-ATR data for the electrochemically reacted, and annealed and unannealed nanopapers prior to PE-CVD can be found in Appendices C and D, respectively.

### 5.4 Effect of Nano-sized Aluminum, (4% and 8% Addition), Nano-Titanium Dioxide, Carbon Nanotubes and Boron Nanotubes Particle Addition

Addition of nano-sized aluminum particles as an energetic ingredient is highly desirable in propellant formulations because their small dimensions and high surface area-to-volume ratio enables the propellant to achieve the higher burning rates and impetus.

Aluminum has a relatively high gravimetric heat of oxidation (31.06 kJ/gm) and high volumetric heat of oxidation (83.86 kJ/cm$^3$). Aluminum also has a high density of 2.7 gm/cm$^3$. Mench[14] showed that by replacing 9 % of regular aluminum powder with nano-sized Alex® particles in an 18 % aluminized Ammonium Perchlorate (AP)-based propellant, the burning rate could be doubled. One advantage of utilizing Al particles in nanoscale dimension is that they have a short ignition delay and combustion time. If the particles burn close to the propellant surface, the heat feedback rate into the propellant surface can be increased, causing an increase in the burning rate as discussed by Mench. However, addition of nano-sized Al particles to the High Energy (HE) propellant did modify the burning rate as expected. Figure 5.33 shows a comparison between the burning rates of the HE and HE/Al propellants as a function of pressure. The addition of nano-sized Al particles increased the propellant burning rate by 20%.

It is well known that under hot-gas environments, the nano-sized Al particles have much shorter ignition delay and combustion time than the micron-sized particles. If nano-sized Al particles are contentiously supplied in an oxidizing environment, they could react to a high degree of completion in the close vicinity to the propellant surface. However, nitramine-based propellants have much less oxygen available for aluminum oxidation than do AP-based propellants. Both RDX and CL-20 have negative oxygen balance ($OB_{RDX}$= –21.61 % and $OB_{CL\text{-}20}$= –10.95 %) while AP has a positive oxygen balance of ($OB_{AP}$=+34.04 %). Also, the AP-based propellants decomposed to generate oxygen-rich species that diffuse into the fuel-rich region, while RDX decomposition does not generate an oxygen-rich region around the reacting particles. Thus, in the nitramine-

based propellant flame, the nano-sized Al particles combustion would be delayed until conventional aluminum oxidizing species, $H_2O$ and $CO_2$, are produced

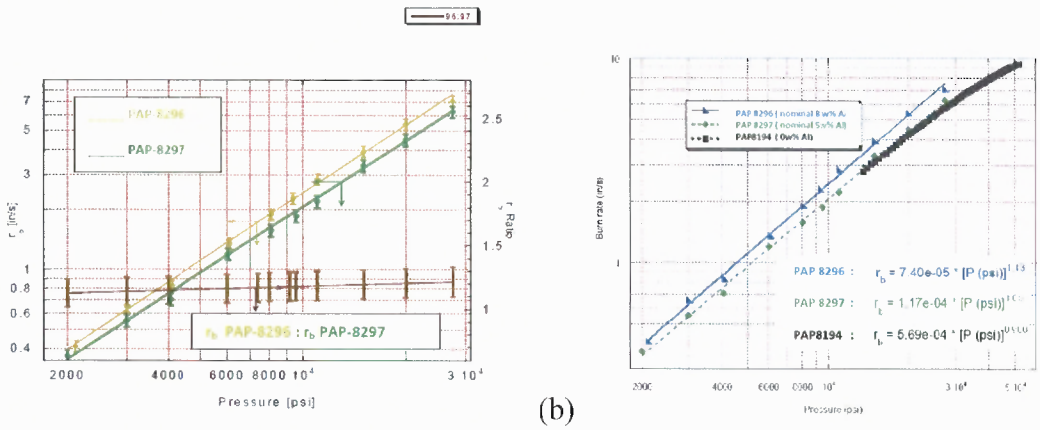


- $r_{b,8296} : r_{b,8297} = 1.2$, that is, a 20% burn rate enhancement was gained from a 3% increase of nano-Al.

**Figure 5.33** (a) and (b): Burn Rate of PAP-8297 and PAP -8296 Propellants with BAMO-NMMO binder and Nano-sized Aluminum Particles compared with the baseline PAP-8194.

Both nano sized $TiO_2$ and nano sized aluminum produced a slight increase in burning rate (2% to 4% at 40 ksi) when compared to the baseline propellant, TGD-035. As shown in Figure 5.34, the change in burning rate produced by the addition of $TiO_2$ was virtually identical to the change produced by the addition of nano sized aluminum. Examination of the vivacity plots for these tests indicated all propellants were burning in a reasonable fashion. Representative burning versus pressure plots for several mixes in this matrix are shown in Figures 5.34 (a-b) and 5.35(a-b). Closed bomb burning rate tests were conducted on lots TGD-041 and TGD-042 propellants and indicated that the higher levels of nano additive significantly increased propellant burning rate. The measured burning rate of both propellants was found to be approximately 25% higher than that of

the baseline propellant, lotTGD-035. These burning rates for the 0.5% and 1.0% nano aluminum and $TiO_2$ additive propellants are shown graphically in Figures 5.34, and 5.35.

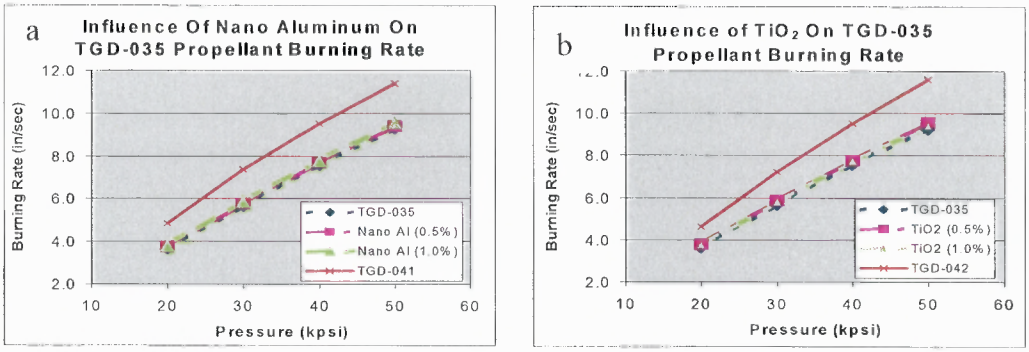


**Figure 5.34** Burn rates of propellant with BAMO AMMO binder with and without nano additives.

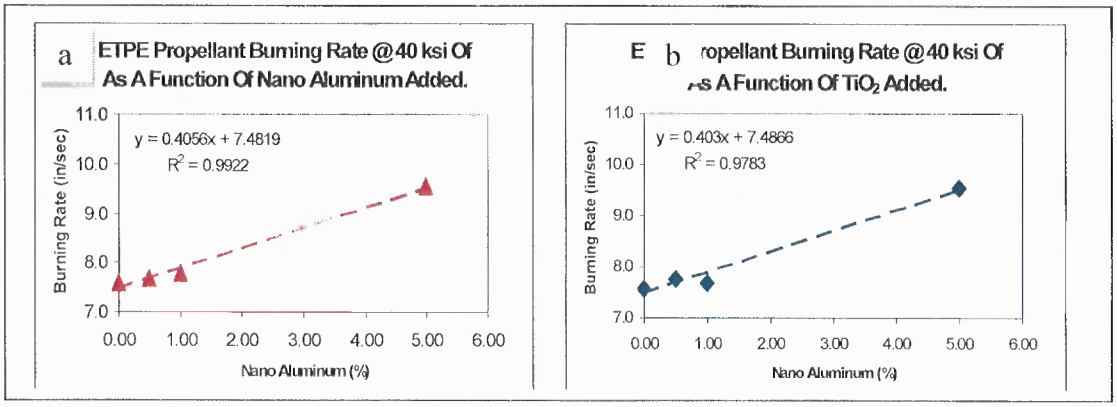


**Figure 5.35** Burning rates of propellant with BAMO AMMO binder with the % level of nano additives.

The effect of adding 2.3% carbon nanotubes did not show a significant increase in burn rates when compared to the 4.5% ( lot PAP-8297) and 7.8% ( lot PAP-8296) nano-aluminum added to the propellant., respectively. Figure 5.36 shows a comparison of the burn rates when 2.3% of carbon nano-tubes, 4.8% and 7.8% nano-aluminum were added to the propellant. Figures 5.37 and 5.38 shows the burning behavior of the carbon

nanotubes in the propellant formulation at a pressure of 5,000 psi.and 9,500 psi, respectively. The propellant was burning two times faster at higher pressure.

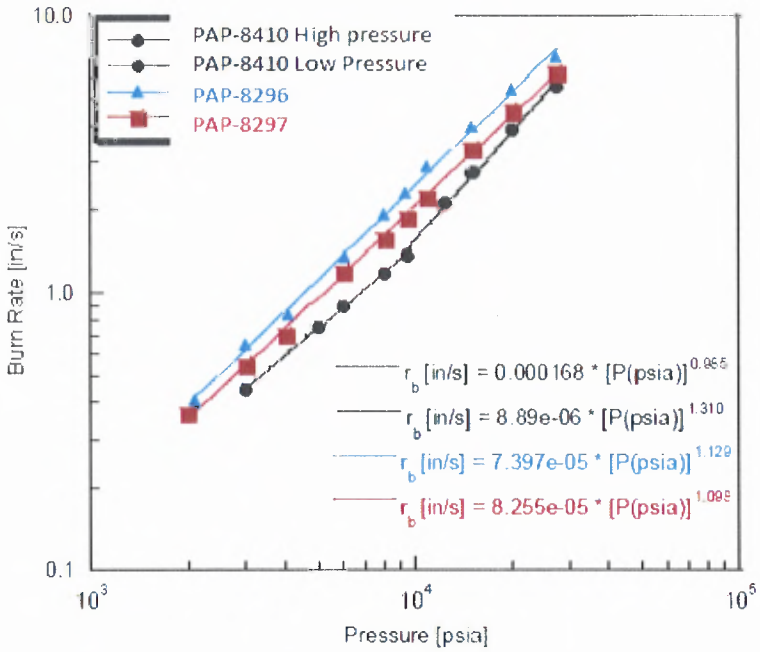


**Figure 5.36** Comparison of Burn Rates when nano-aluminum and carbon nanotubes were added.

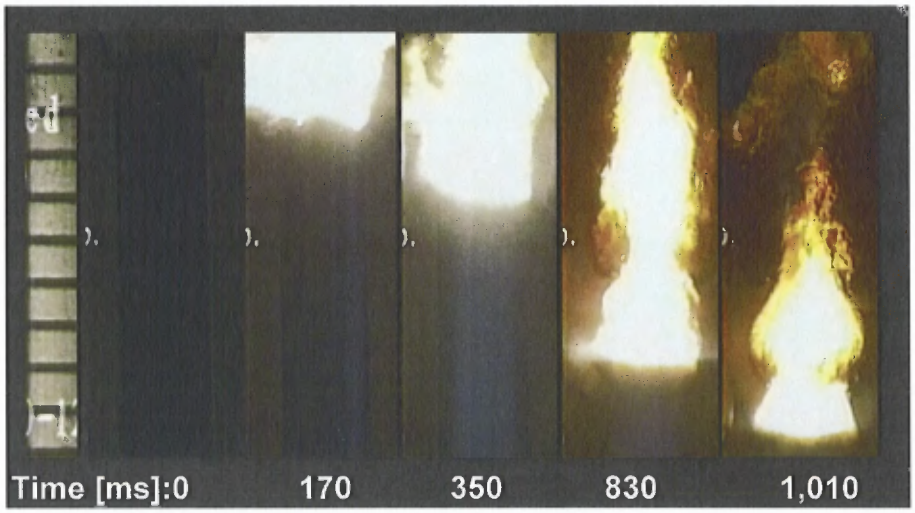


**Figure 5.37** Burning behavior of propellant with 2.3% carbon nanotubes at a pressure of 5,000 psi.

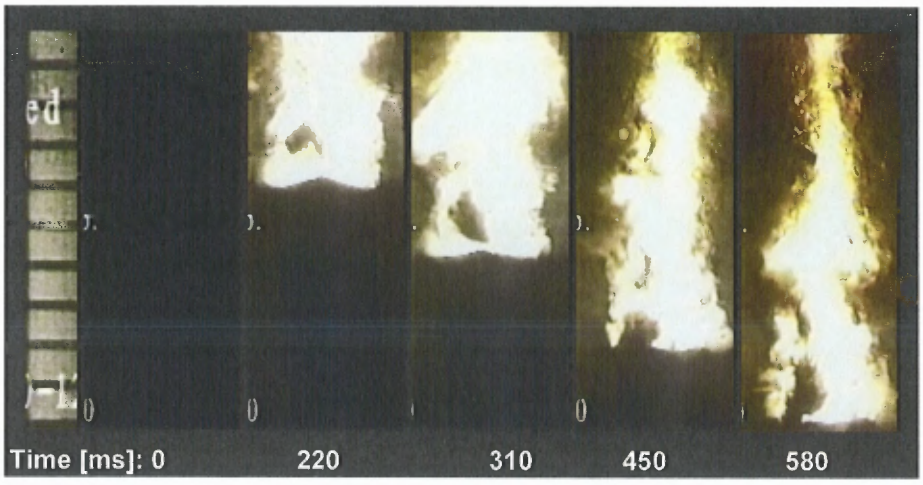


**Figure 5.38** Burning behavior of propellant with 2.3% carbon nanotubes at a pressure of 9,500 psi.

Boron has a high gravimetric heat of oxidation (58.74 kJ/gm) and high volumetric heat of oxidation (137.45 kJ/cm$^3$), the highest of all common fuels. Boron also has a density of 2.34 gm/cm$^3$, which is lower than aluminum and should increase the mass burning rate of the propellant. In a hybrid rocket motor, using 13 % of nano-boron particles in Hydroxy terminated polybutadiene (HTPB)-based solid fuels, Risha[102] observed an increase of mass burning rate of 44 % for nano-sized boron particles and 111 % for nano-sized $B_4C$ particles.

Figure 5.39 shows the burning rate of the HE/B propellant as a function of pressure. The effect of addition of boron nano-particles to the HE propellant is a noticeable decay of the burning rate rather than an enhancement of the burning rate. This can be expained by the "energy-sink" effects. Figure 5.39 reveals that boron particles have stronger effect on the reduction of the burning rate of the HE propellant. This can be attributed to three reasons. First, the specific heat capacity of boron is greater than that of

aluminum on a mass basis. Therefore, boron particles are a more effective thermal energy sink than aluminum particles. Second, the boron particles are harder to ignite than aluminum particles, thus the energy release due to their combustion occurs at even larger distances away from the propellant surface. Third, the HE/B propellant is more fuel-rich than the HE/Al propellant with the same weight percentage of B and Al in the propellant. This results in less oxidizing species for the boron oxidation reactions.

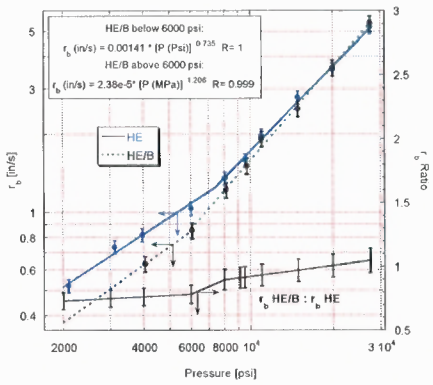


- At low P, the boron nano-sized particles reduce the burning rate of the HE propellant
- At higher P (>9,000 psi), $r_b$ converges with that of baseline HE propellant
- Large amount of ash observed
- Boron particles have long ignition delay, resulting in their energy release away from the burning surface
- On a molar basis, boron concentration is much higher than that of Al at similar wt.% due to much lighter molecular weight of B (wt.% may be too high for optimum combustion)

**Figure 5.39** Burn Rate of HE Propellant with 5% SB Boron Nano-sized Boron Particle

## 5.5 Characterization of Nano Particles

### 5.5.1 Atomic Force Microscopy (AFM)

The nano aluminum used for the propellant formulation was characrterized by AFM . As shown in Figure 5.40a the nano aluminum particle size varied from 5 nm to 130 nm but the average particle size distribution appears to be 70 nm. The AFM showed many 70 nm but associates into >300 nm clusters that look somewhat like "popcorn balls" which

are readily observed in the 3 $\mu^2$ height image shown in Figure 5.40(b) and somewhat reminiscent of the nano-boron shown in Figure 5.42. The 700 nm images of the nano-aluminum shows apparent "seams" about 10 nm wide that exist between quite a few of the particles that are fused together. Many of the particles appear "lumpy". The 1 $\mu^2$ image shows connected particles with < 10 nanometer pores between them as shown in Figure 5.41(a) and (b). A few are indicated but many more can be identified in this image.

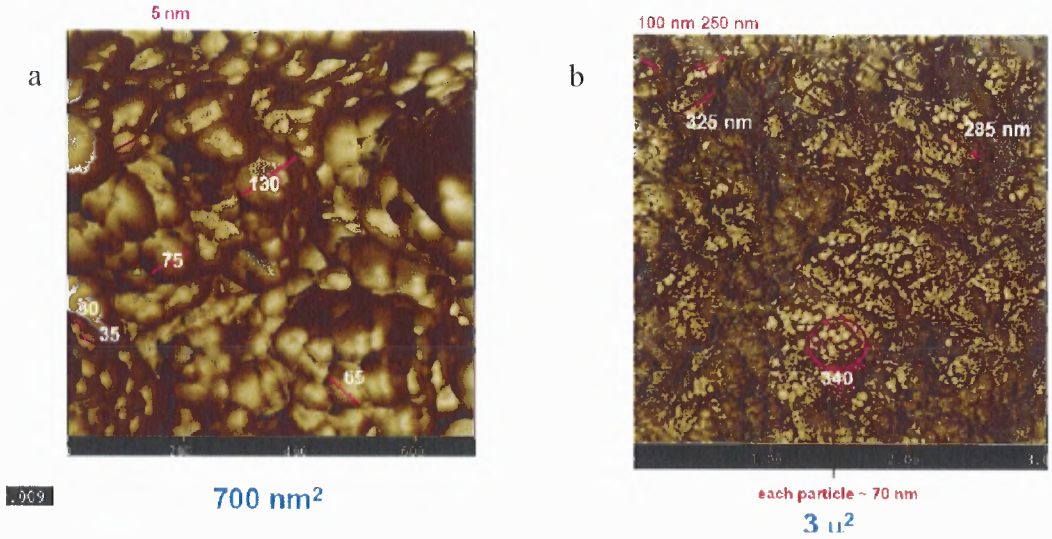


**Figure 5.40** (a)Nano –aluminum particle size. (b): Nano-aluminum clusters

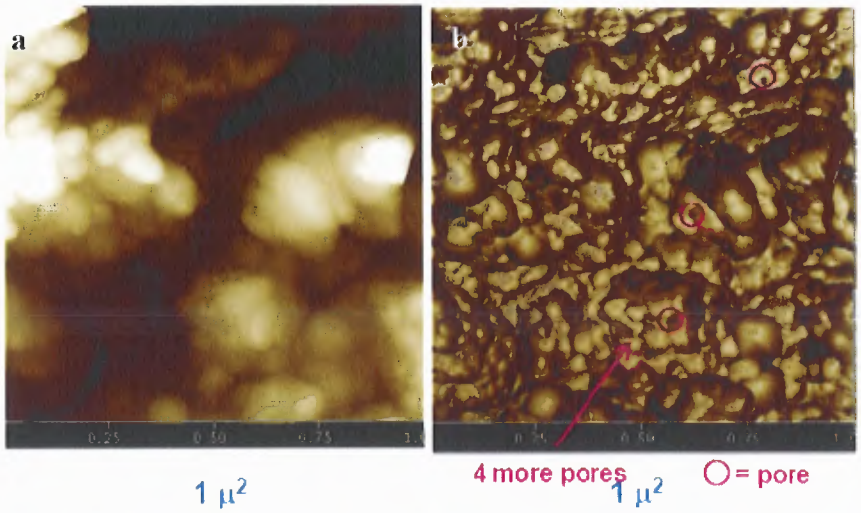


**Figure 5.41** Nano-aluminum pores in the 1 $\mu^2$ images.

The nano-boron AFM analysis used in the propellant is shown in Figure 5.42 (a) and (b). Most of the individual particles within the clusters are ~50-60 nm in diameter , but the clusters can be several hundreds nanometer in diameter.

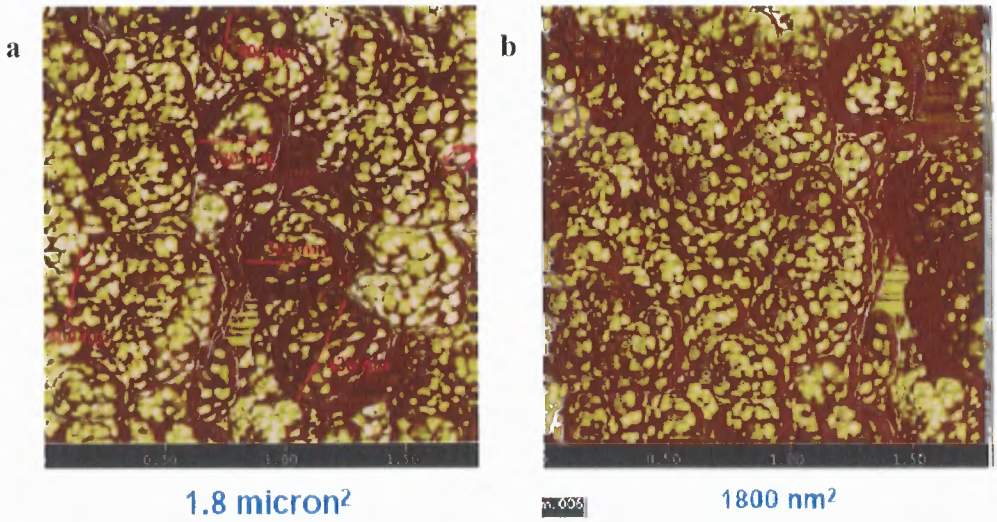


**Figure 5.42** Nano-Boron Particle size;(a) Nano–Boron arranged in clusters(b).

### 5.5.2 Scanning Electron Microscope (SEM) and Transmission Electron Microscopy (TEM) of Multi-Wall Carbon Nano-Tubes (MWCNT)

The SEM of the multi –wall carbon nanotubes is shown in Figure 5.43(a). The carbon nanotubes appear to be prevalent in hallow fiber shape. The MWCNT was used in the propellant lot PAP-8410. The SEM image is of 10,000X magnification, and 1 micron scale. The TEM image scale is 100 nm as shown in Figure 5.43(b).

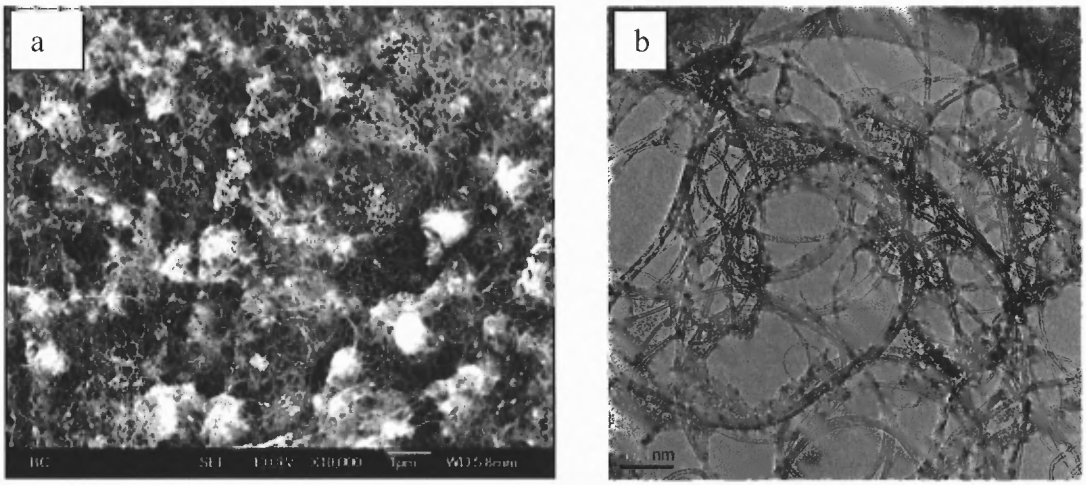


**Figure 5.43** Multi wall carbon nanotubes SEM, image is of 10,000X magnification, and 1 micron scale (a) MWCNT TEM Image, Scale: 100 nm(b) made at NJIT and used in the propellant lot PAP-8410.

### 5.6 Synthesis and Nitrogenation of Boron Nanotubes/Boron Nanofibers

Boron nanotubes (BNTs) and boron nanofibers (BNFs) were synthesized by thermal-treatment of $MgB_2$ or $Mg(BH_4)_2$ precursors with catalytic $Ni_2B$ in zeolite MCM-41 in a CVD reactor system. The Mg formed acts as a co-catalyst. The pristine nanotubes and nanofibers are then doped using ammonia or alternatively using melamine.

In order to optimize the synthesis temperature where the boron nanotubes (BNTs) and nanofibers (BNFs) are formed, several experiments were performed with temperatures from 875C° to 930C° with the same starting nominal composition by weight which was as follows:

30% $MgB_2$, 50% $Ni_2B$ (roughly 1:1 atomic ratio of $MgB_2$ to $Ni_2B$) and 20% MCM41 (5.2)

The samples prepared were evaluated by scanning electron microscopy (SEM). Very little BNT/BNF formation is observed below 900°C. BNTs and BNFs start growing at 910°C with large production occurring between 920°C and 930°C as shown by the SEM images in Figure 5.44(a) and (b).

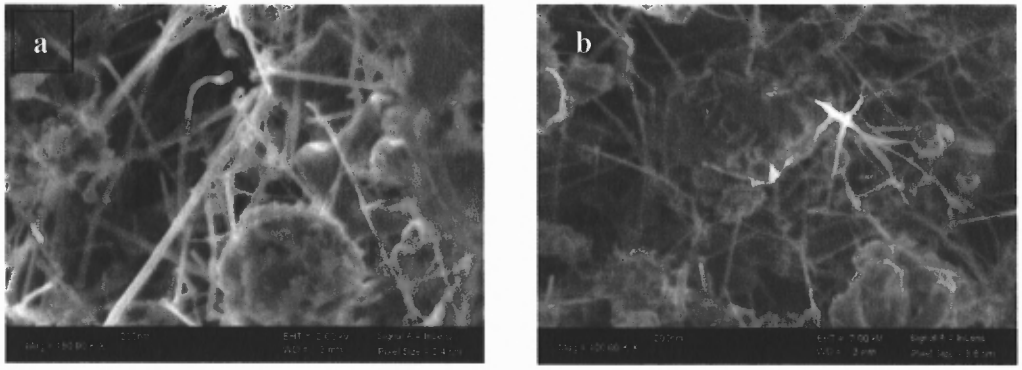


**Figure 5.44** SEM image of a sample of BNTs/BNFs prepared at 920°C (a) and at 930°C (b).

The detailed structural characterization of the highly purified BNT/BNF samples obtained after successful removal of MCM-41 used as template and catalyst support for the growth of the nanotubes and nanofiber were completed. The Raman spectra (typical one displayed in Figure 5.45 show a number of lines with frequencies of peaks at 274,

382, 538, 640, 1274 and 1379 $cm^{-1}$ in the 200-1500 $cm^{-1}$ region using 785 nm laser excitation. These lines correspond to those observed by the Yale University group of Pfefferle et al at 210, 450, 500, 580, 1080 and 1180 $cm^{-1}$ using 532 nm laser excitation and assigned by them to BNTs. The frequency differences are likely to be due to differences in the diameter and the fact that the nanotubes produced in this work are possibly multiwalled. The assignment of the lines at 274, 400 and 538 $cm^{-1}$ in our data to BNTs, while the features at 640 and 1274 $cm^{-1}$ can be assigned to BNFs. The strong feature at 1379 $cm^{-1}$ is due to a B-O mode resulting from the oxidation of the BNT surfaces by oxygen during purification. Due to the electron deficiency of boron, boron sidewall surfaces become susceptible to oxidation as they are released from MCM-41 pores during the purification process.

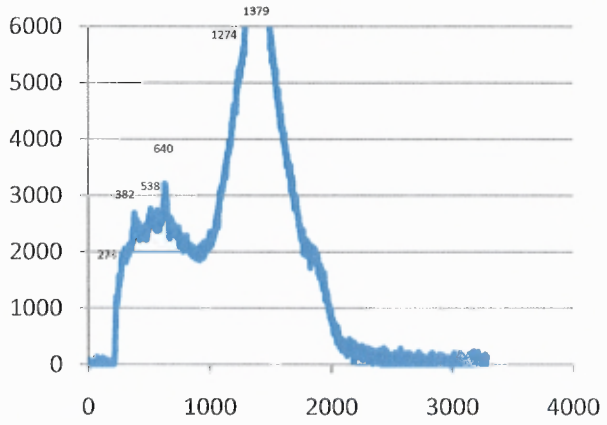


**Figure 5.45** Raman spectrum intensity (counts/sec) versus frequency in $cm^{-1}$ of purified BNT/BNF sample taken using Mesophotonics Raman system with 785 nm laser excitation. The peak at 1379 $cm^{-1}$ is due to the glass substrate on which the sample powder is placed.

The new boron nanotube CVD synthesis apparatus modified with a new temperature controller-microprocessor and improved vacuum system, has produced well-

grown, clearly visible nanotubes that are about 30 nm in diameter (and hence likely to be multiwalled), as is seen in the SEM images in Figures 5.44 (a) and (b). The samples were purified to remove the zeolite MCM-41 template by sonication in dilute sodium hydroxide. These samples were analyzed by transmission electron microscopy (TEM) and Electron Energy Loss Spectrum (EELS) measurements to determine how much Mg and Ni catalysts are incorporated into the nanotubes as shown in Figures 5.46 and 5.47. In addition, further detail on whether the tubes are single walled were determined by TEM and EELS although Raman data suggest that the nanotubes are single walled. In Figure 5.48, Boron nanotubes are shown lying on a holey carbon TEM grid obtained by process using MgB. Measured nanotube diameter is 10-20 nm. Nanotubes have larger diameter but are extremely straight compared with the more curvy boron nanotubes obtained by the Yale group[103].

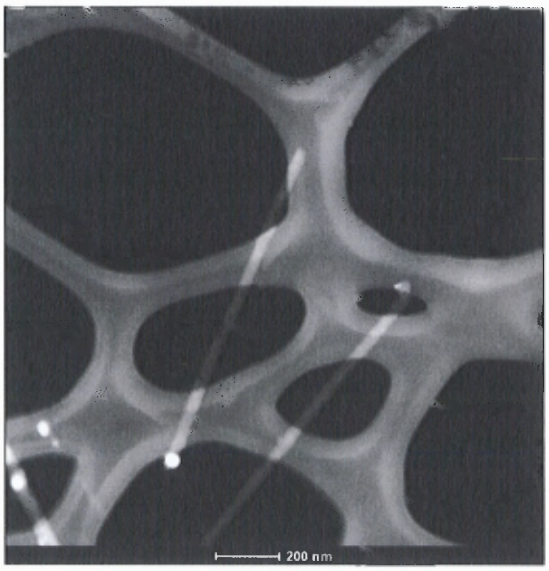


**Figure 5.46** TEM images of boron nanotubes are shown lying on a holey carbon TEM grid.

a

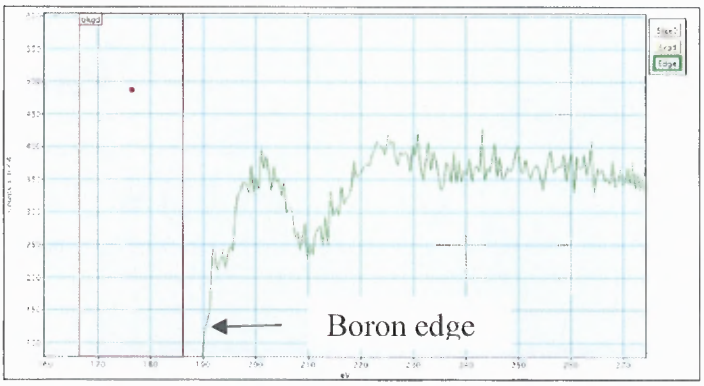


b

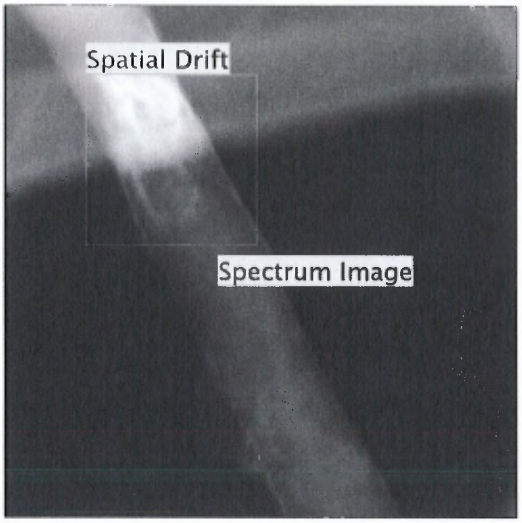


**Figure 5.47** Boron nanotubes (a) EELS-(b) TEM images from boron nanotube edges.

In Figure 5.47 b, the EELS scan clearly shows the boron edge proving that the nanotube comprises purely of boron.

The first synthesis of $MgBH_4$ was completed using the thermal reaction of $MgCl_2$ and $NaBH_4$ below the melting temperature of the borohydride near 500°C. The reaction, however, did not appear to go to completion based on initial chemical analysis by Raman spectroscopy. A chemical metathetical synthesis approach according to the following reaction in tetrahydrofuran (THF):

$$MgCl_2 + 2MBH_4 = Mg(BH_4)_2 + 2MCl \quad (5.3)$$
with M = Li, Na

In this reaction NaCl or LiCl will precipitate out and the Mg borohydride will remain in THF solution and will be recovered by solvent evaporation. A small ball milling system was used to conduct the mechano-chemical reaction which may be the most efficient method to produce $MgBH_4$ based on our results and survey of the literature.

Further experiments using the first level optimized process for producing BNTs and BNFs were conducted using the optimized process using $MgB_2$ as the primary precursor to refine the two key parameters; the reaction temperature and grinding of the constituents of the reaction. The reaction temperature is as determined in the first level optimization. However, a fine level of grinding of the constituents is necessary to obtaine the quality of BNTs/BNFs shown in Figure 5.48, a representative SEM image taken from these optimally ground samples. It is clear that the BNTs/BNFs grow out of the MCM-41 template particles.

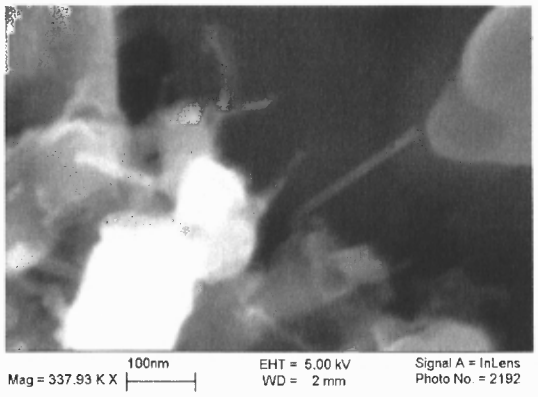


**Figure 5.48** BNTs/BNFs growing out of MCM-41 particles in optimally ground precursor mixture of $MgB_2$ and $Ni_2B$ with MCM-41.

Ball mill synthesis to prepare scaled up quantities of $Mg(BH_4)_2$ has been utilized. Ball milling will mechanochemically react $MgCl_2$ with $NaBH_4$ to form $Mg(BH_4)_2$ according to the following reaction:

$$MgCl_2 + 2NaBH_4 = 2NaCl + Mg(BH_4)_2 \qquad (5.4)$$

The reaction has been conducted in alcohol in which NaCl is partly soluble and can be therefore removed. However, the reaction product obtained has not been pure. Experiments was performed by the grinding in pure diethylether in which $Mg(BH_4)_2$ is completely soluble and can be extracted in pure form.

Synthesis of BNTs/BNFs using $Mg(BH_4)_2$ initially with Aldrich's newly commercialized material has been carried out successfully. In addition to its application in the production of BNTs/BNFs, magnesium borohydride will have major commercial potential as a lightweight hydrogen storage material for automotive fuel cells. Figure 5.50 shows an SEM image of BNTs/BNFs from $Mg(BH_4)_2$ prepared at 900°C. Lower temperature preparations was also successfully achieved at at 650 $^0$C as shown in Figure 5.49. The nanotubes appear to grow in spider web out of and on the MCM-41. For the higher temperature preparation of BNTs/BNFs, it is evident that some of the BNTs/BNFs produced have thinner diameters(down to a few nanometers) than BNTs/BNTs from samples prepared using $MgB_2$ (typically 10-20 nm ).. This could be due to the fact that magnesium borohydride decomposes more readily to create catalytic Mg particles in the

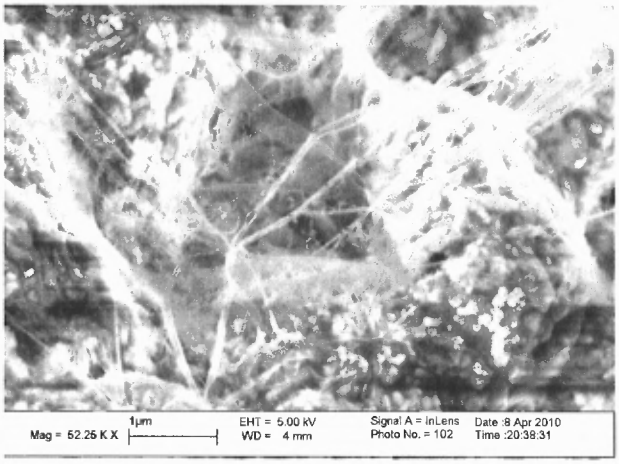


**Figure 5.49** Field-emission SEM images of BNTs/BNFs prepared at 650°C with $Mg(BH_4)_2$ prcursor. The nanotubes grow in spider web out of and on MCM-41.Arrows indicate a straight BNT growing on spherical particles which we believe to be Mg catalyst particles.

form of spheres in Figure 5.50 out of which boron nanotubes grow much as carbon nanotubes do out of transition metal catalyst particles. By optimizing the temperature to control the size of the magnesium particles it may now be possible to grow primarily single wall BNTs and very thin BNFs.

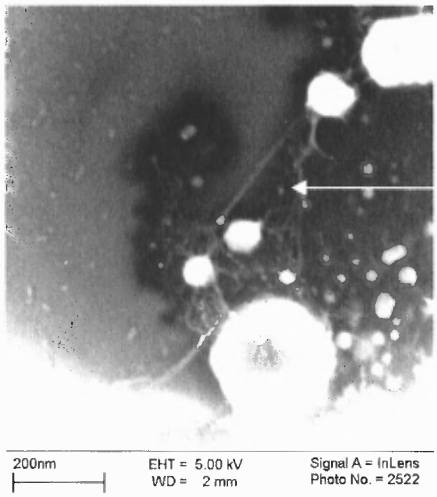


**Figure 5.50** Field-emission SEM images of BNTs/BNFs prepared at 900°C with $Mg(BH_4)_2$ prcursor. Arrows indicate a straight BNT growing on spherical particles which we believe to Mg catalyst particles.

# CHAPTER 6

## SUMMARY AND CONCLUSIONS, RECOMMENDATIONS FOR FUTURE WORK

We have used an electrochemical process to functionalize the inner and outer sidewalls of single wall carbon nanotubes with polymeric nitrogen clusters. In this process, the carbon nanotubes were employed as the working electrode and were pre-doped with nitrogen, and the reaction was carried out under ultraviolet irradiation in sodium azide solution at different pH values. The nature of the chemistry and changes in morphology taking place on the nanotube sidewalls were characterized by *in-situ* cyclic voltammetry. Raman spectroscopy, laser ablation mass spectroscopy, scanning electron microscopy (SEM), differential scanning calorimetry (DSC), and Fourier transform infrared-attenuated total reflectance (FTIR-ATR) spectroscopy. The results obtained have consistently shown the formation of $N_4$ to $N_{20}$ polymeric nitrogen clusters immobilized on the nanotube sidewalls. Differential scanning calorimetry on electrochemically functionalized SWNT nanopaper exhibits an endothermic onset at $300^{o}$ C associated with endothermic dissociation similar to that seen by Wang et al in nitrated SWNTs. This is followed by a rapid exothermic onset at $350^{o}$ C similar to what is typically seen in an energetic material like cyclotetramethylene-tetranitramine (also referred to as HMX). Similar results were also obtained using Raman spectroscopy, SEM, laser ablation mass spectrometry, DSC and FTIR-ATR for samples prepared by

the PE-CVD process using nitrogen gas as the precursor mixed with either argon or hydrogen. Although somewhat similar results were obtained using a microwave-assisted process on aqueous solutions of sodium azide, the reaction efficiency was much lower than using the electrochemical and plasma methods. Scale-up of both the electrochemical and plasma synthesis processes are recommended for near-future work.

Initial studies have been performed to evaluate the impact of adding nano-aluminum, nano-titanium dioxide ($TiO_2$), nano-boron and multiwall carbon nanotubes to propellant formulations. The results of this study indicate that the addition of both nano-sized additives to two different gun propellants produce an increase in propellant burning rate. The fact that the nano-sized additives produced identical burning rates at the 2.35% to 7.4% by weight level was somewhat surprising, especially when the predicted impetus and flame temperature of the subject propellants are markedly different. This ability to make significant changes in burning rate is important and provides the propellant formulator a powerful tool to use in achieving a desired burning rate.

For propellants with oxygen deficient oxidizers (such as RDX, CL20), the addition of nano-sized boron particles cannot increase the burning rate of the propellant because the reaction of these fuel particles can only occur at a distance away from the propellant burning surface. However, for propellants containing oxidizers with positive oxygen balance, the addition of nano-sized Al particles can greatly enhance the propellant burning rate because the reaction of the particles can occur in close proximity to the propellant's burning surface. Therefore, the addition of both carbon nanotubes and nano-sized aluminum particles can be used to substantially increase the propellant burningrate

The primary objectives of this dissertation to realize an optimized synthesis approach to a stable polymeric nitrogen on and in single wall carbon nanotubes, and to synthesize pure nitrogenated boron nanotubes/nanofibers (BNNTs/BNNFs), have been achieved. The polymeric nitrogen should improve the ballistic performance of guns by making it easier to achieve a burn rate differential of 3:1 between the fast and slow propellants in a fast core configuration. In addition, the polymeric nitrogen should be capable of increasing gun propellant performance by lowering the $CO/CO_2$ ratio of the combustion gases , and should reduce gun barrel wear and erosion by increasing the $N_2$ /CO ratio of these same combustion gases.

Future work recommended related to this research will be to scale up the synthesis methods developed and further enhance the properties of the high energy, high density energetic polymeric nitrogen and nitrogen-containing BNNT/BNNF through optimization.

## APPENDIX A

## DIFFERENTIAL SCANNING CALORIMETRY DATA FOR ELECTROCHEMICAL SYNTHESIS SAMPLES

Figure A1 to A10 show the DSC of CHEAP SWNT Pristine and Dope with Nitrogen

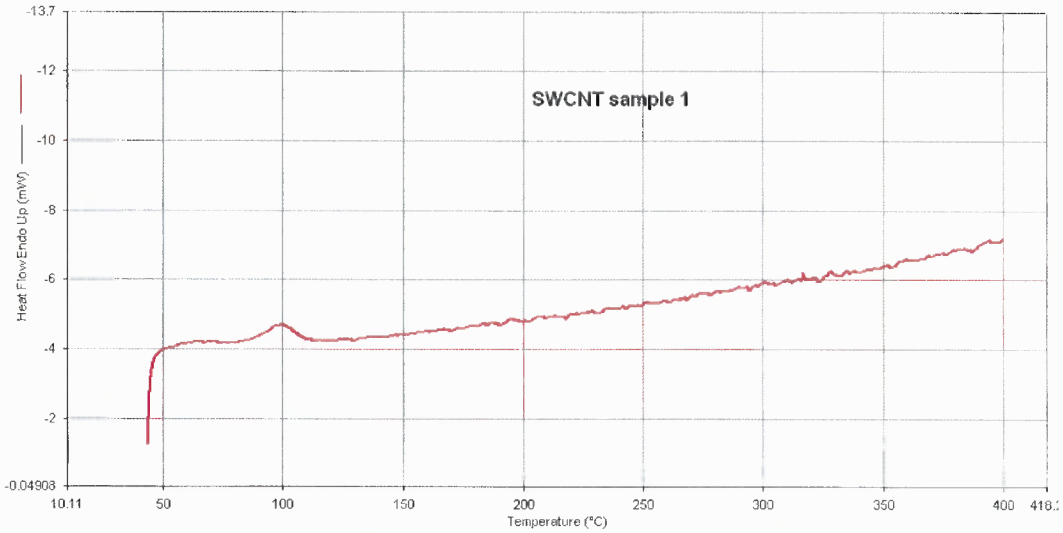


**Figure A.1** DSC for SWeNT SWNT, $NH_3$ annealed, 110mA, no PS.

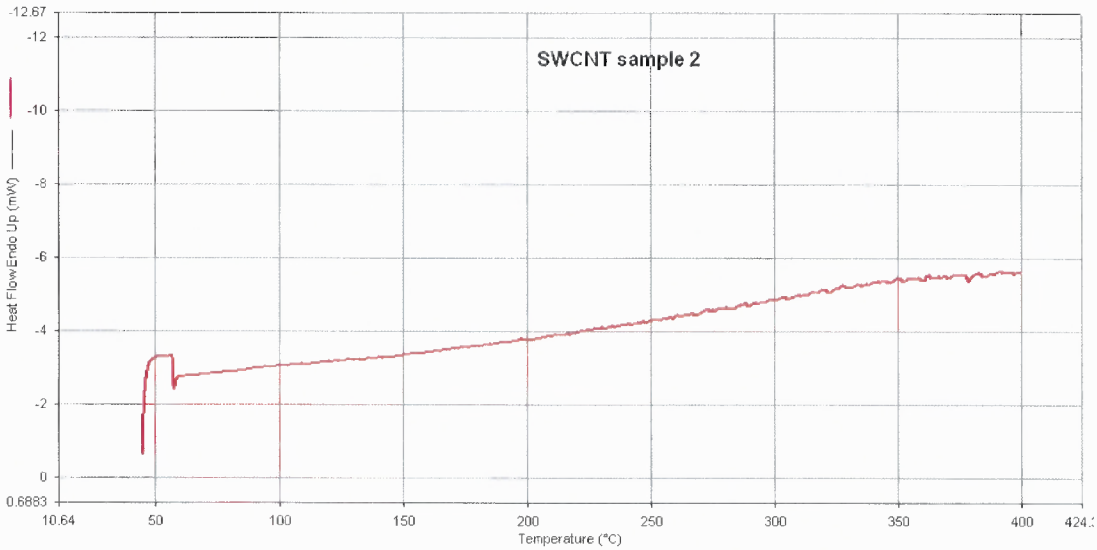


**Figure A.2** DSC for SWeNT, $NH_3$ annealeed, no PS, no electrochem.

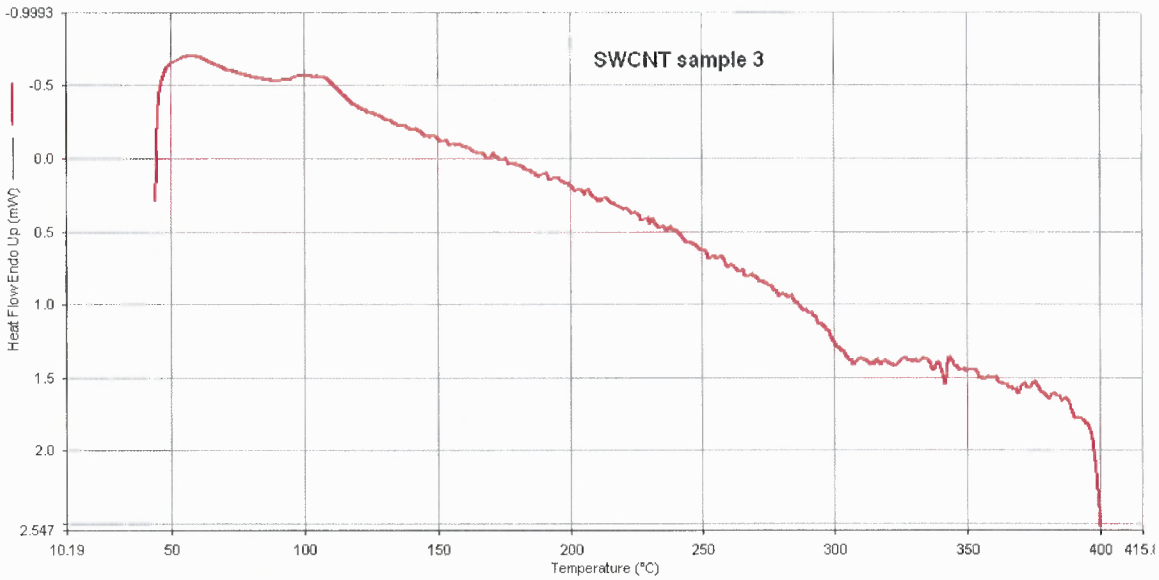


**Figure A.3** DSC for CHEAP SWNT , $NH_3$ annealed, 5%PS, 10mA.

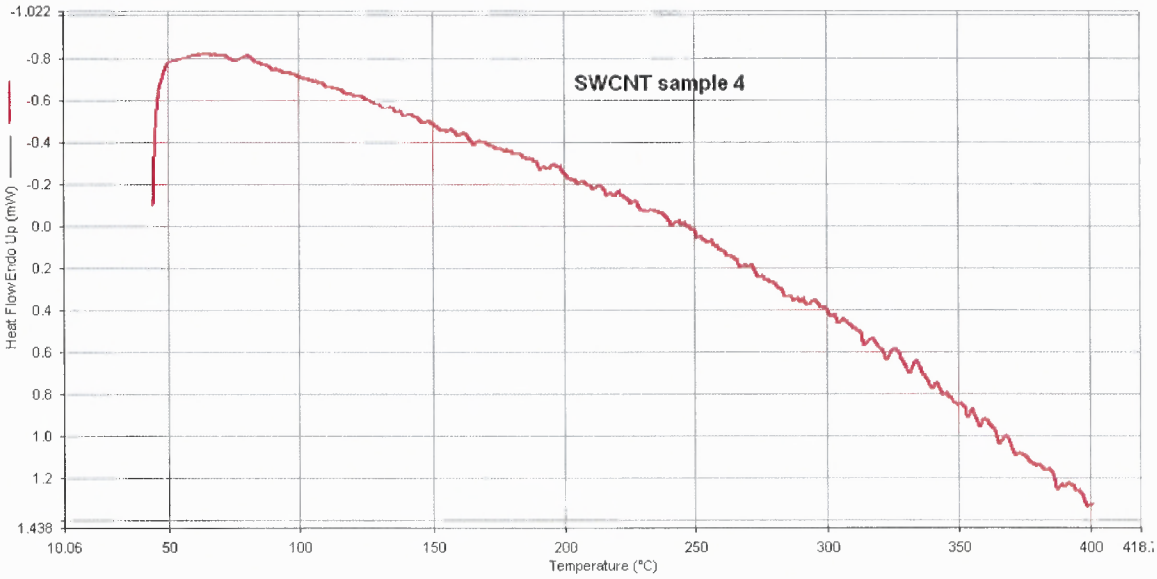


**Figure A.4** DSC CHEAP SWNT, $NH_3$ annealed, 5%PS, no electrochem.

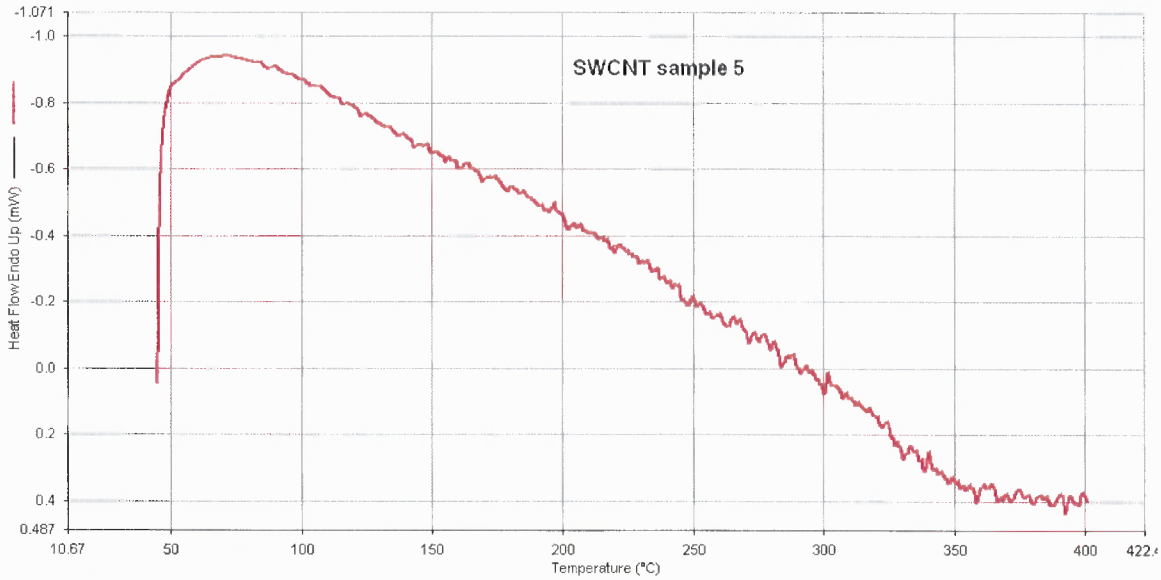


**Figure A.5** DSC CHEAP SWNT, 5%PS, No Electrochem.

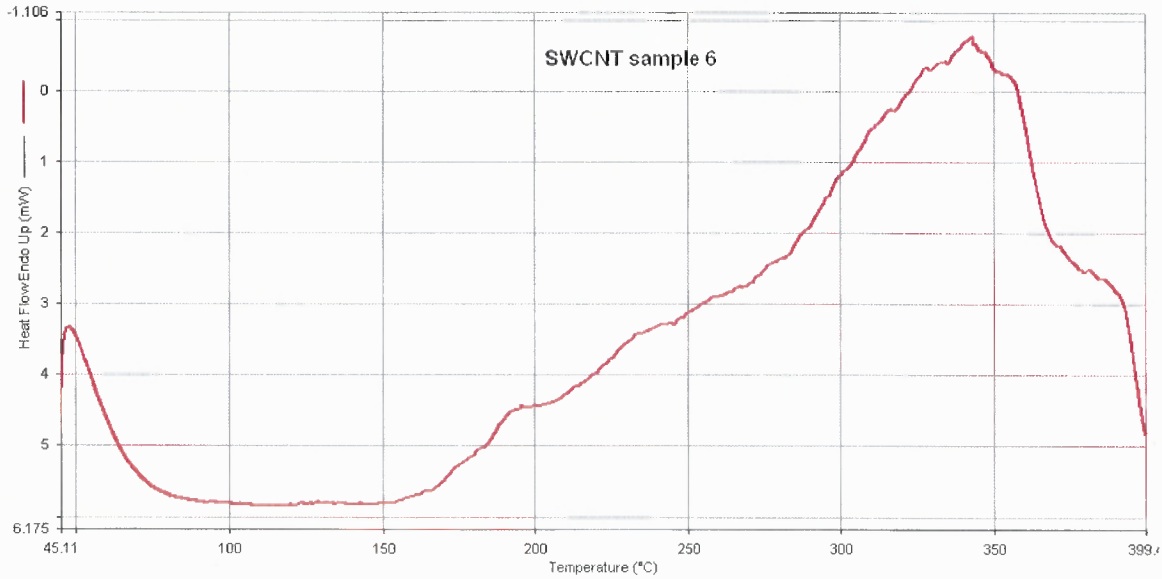


**Figure A.6** DSC SWeNT SWNT, $NH_3$ Annealed, No Electrochem.

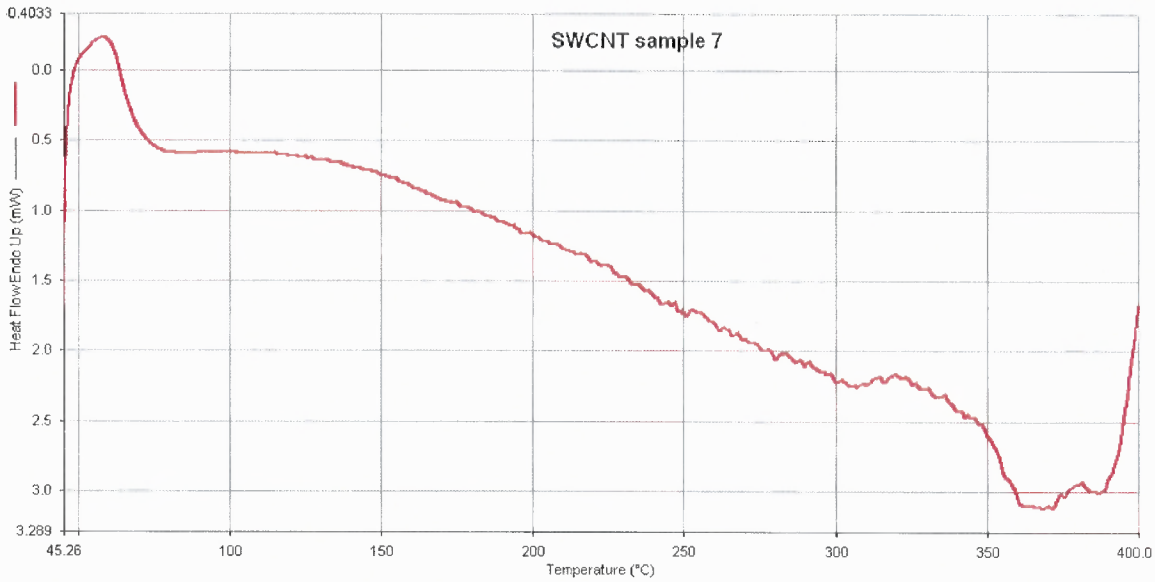


**Figure A.7** DSC of CHEAP SWNT, $NH_3$ annealed.

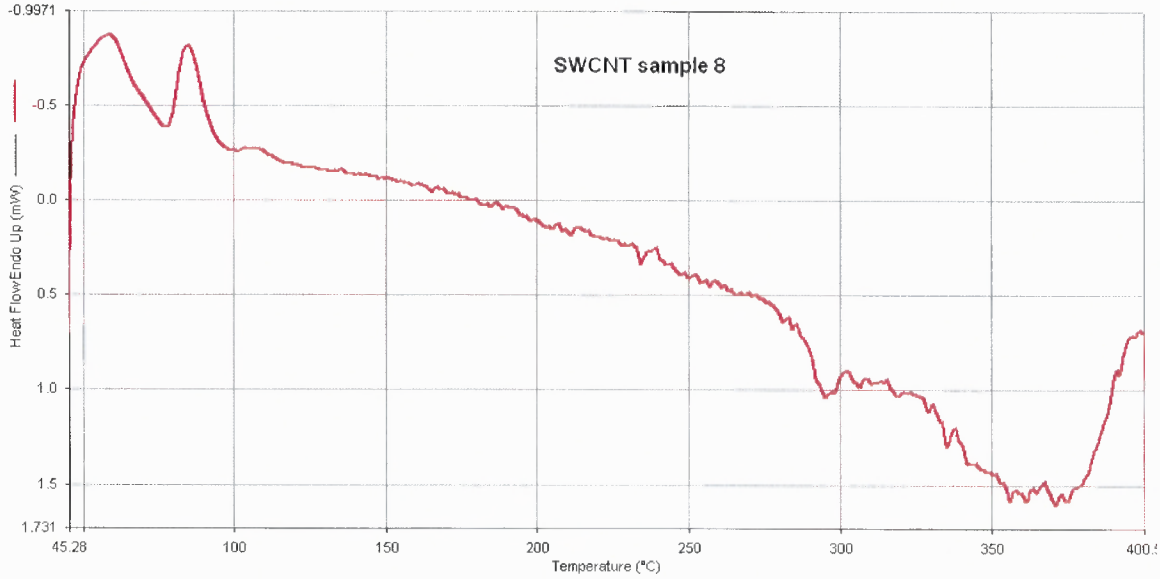


**Figure A.8** DSC of CHEAP SWNT, 5%PS, $NH_3$ Annealed, 1hr UV (Anitha's), 10mA.

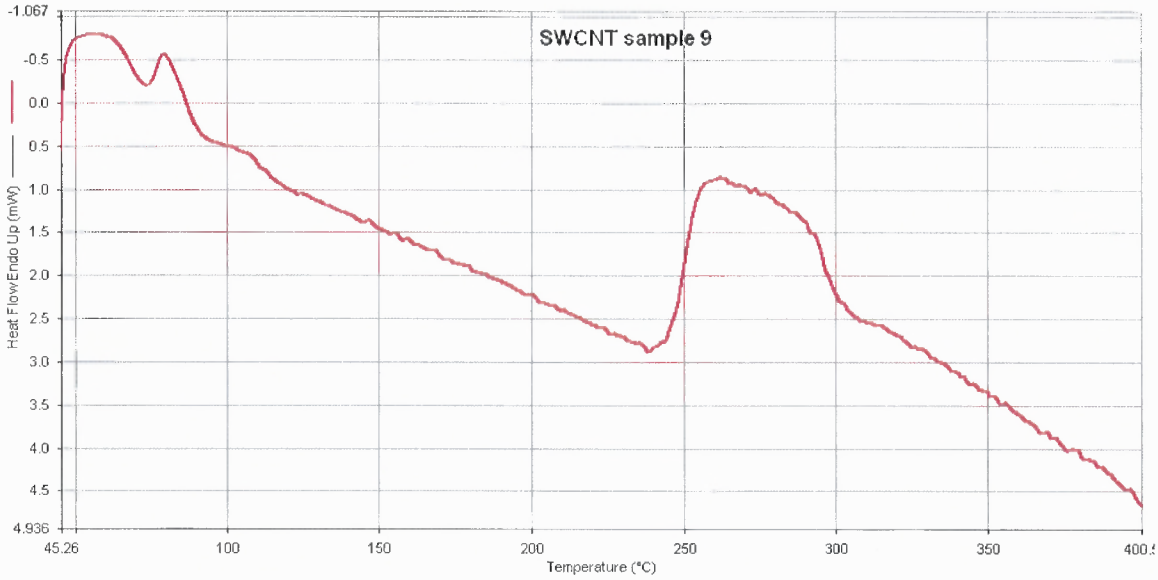


**Figure A.9** DSC of CHEAP SWNT, 5%PS, 1Ma, 1,495V, $NH_3$ Annealed.

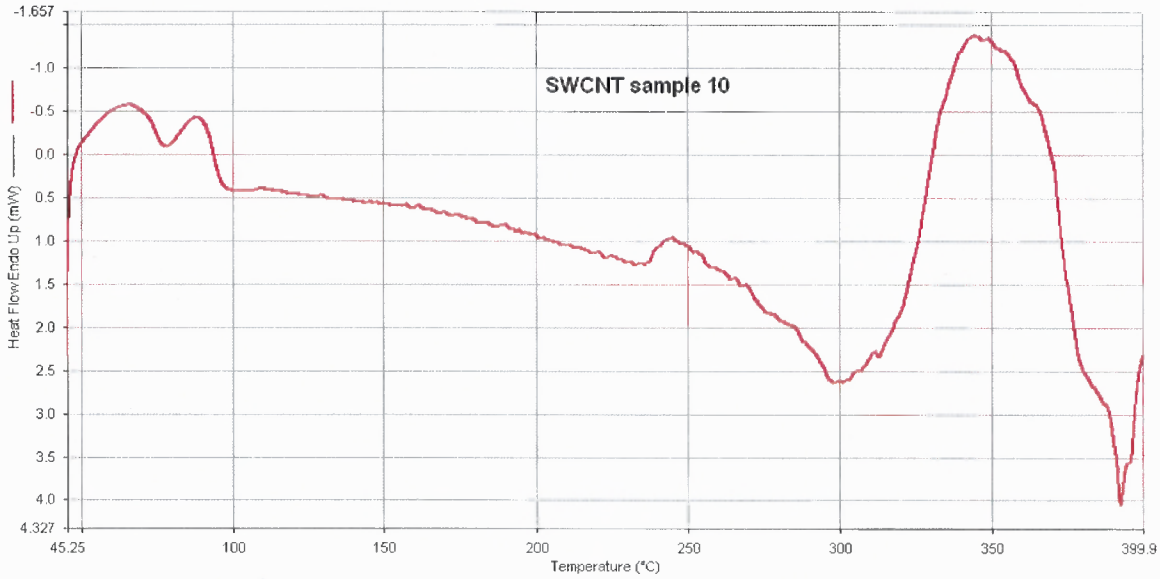


**Figure A.10** DSC of CHEAP SWNT, $NH_3$ Annealed, 1 Ma, 1597V, UV from PPI and no PS used.

## APPENDIX B

## DIFFERENTIAL SCANNING CALORIMETRY DATA FOR PE-CVD SAMPLES

Figures B1 to B23 DSC and TGA for Nitrogen :Argon and Hydrogen Treatment of Cheap SWNT that were not annealed and annealed.

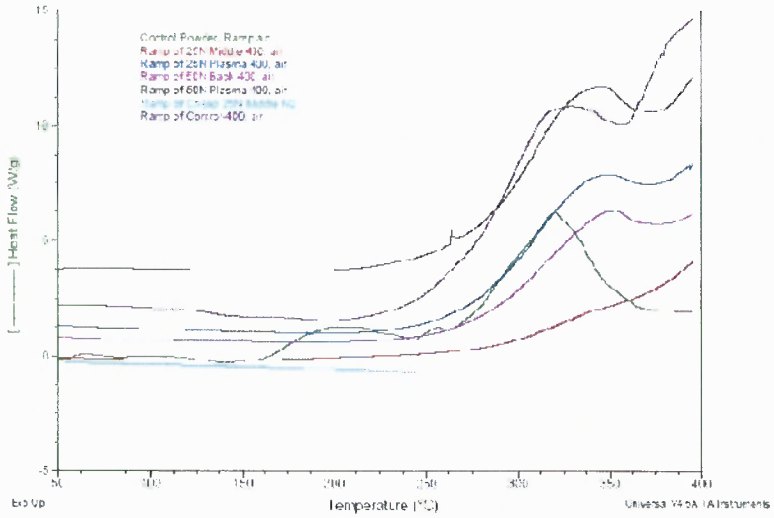


Figure B.1 Overlay of DSC for not annealed CHEAP SWNT substrate from the Nitrogen Argon PE-CVD process.

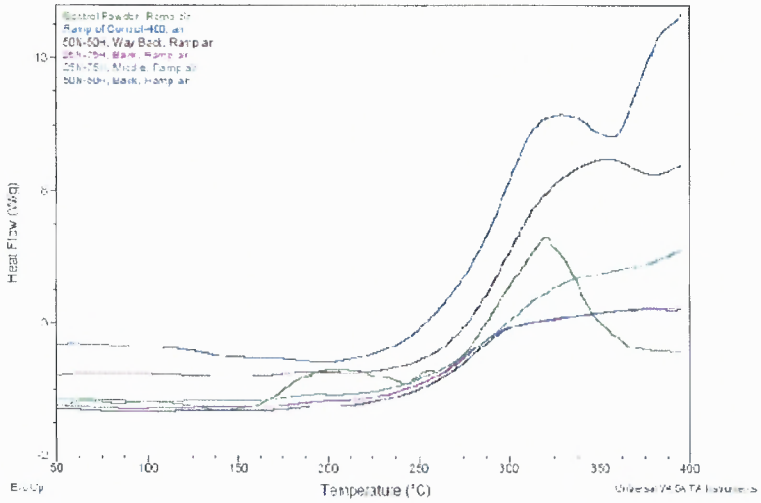


**Figure B.2** Overlay of DSC for not annealed CHEAP SWNT substrate treated with Nitrogen Hydrogen using the PE-CVD process.

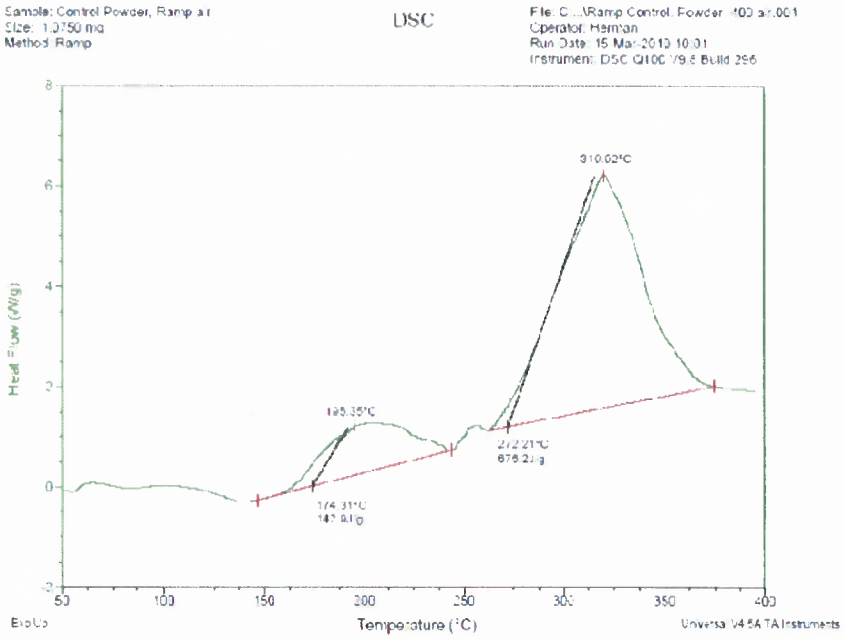


**Figure B.3** DSC for not annealed and pristine CHEAP SWNT powder.

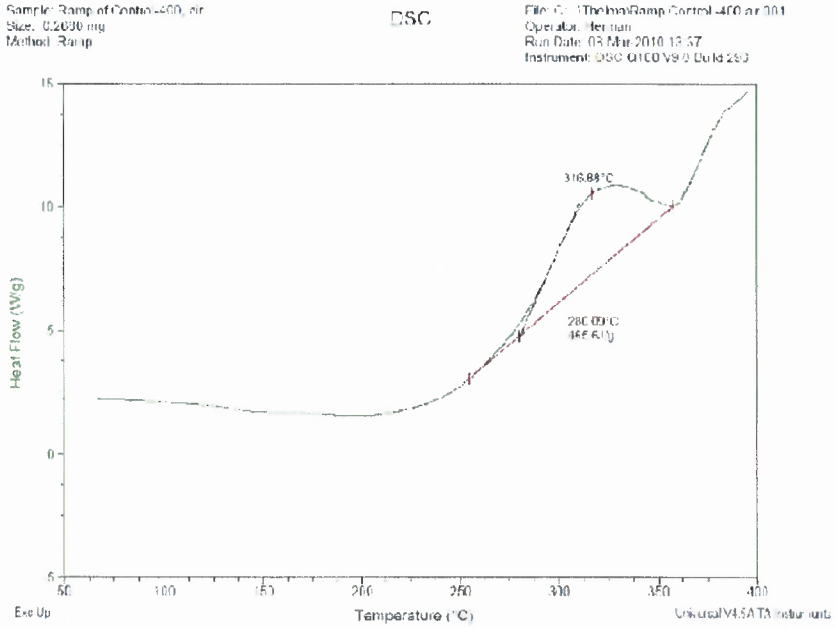


**Figure B.4** DSC for not annealed PRISTINE CHEAP SWNT BUCKYPAPER.

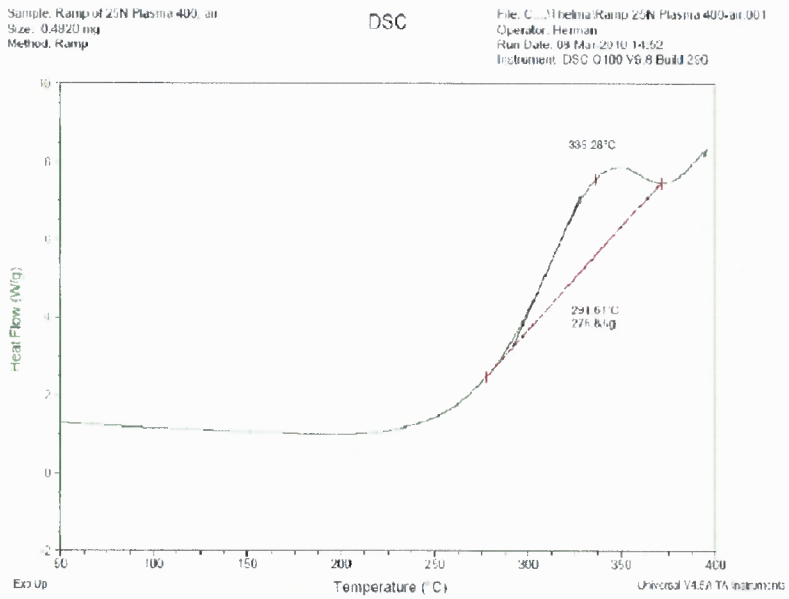


**Figure B.5** DSC for not annealed CHEAP SWNT substrate from 25%Nitrogen 75% Argon PE-CVD process.

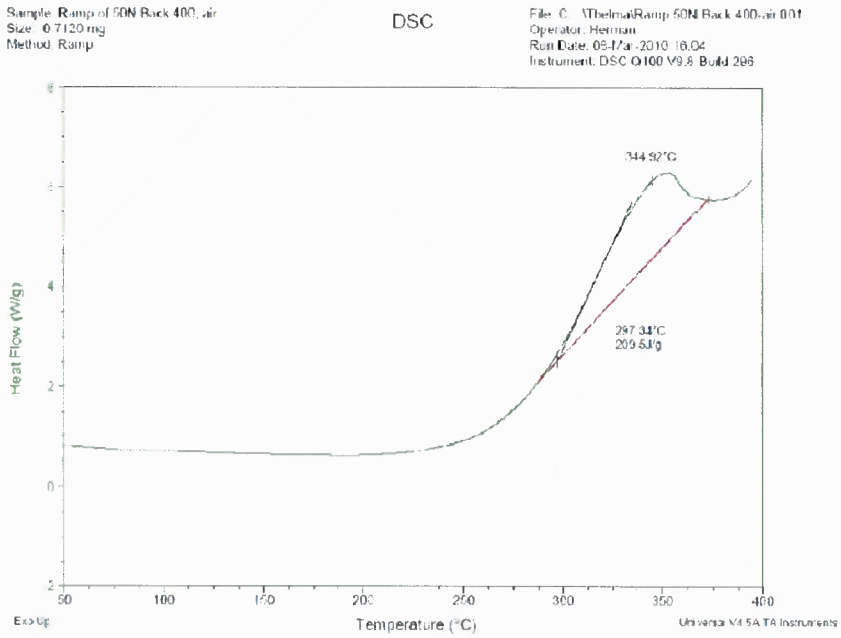


**Figure B.6** DSC for not annealed CHEAP SWNT substrate from 50%Nitrogen50% Argon PE-CVD process. Location at Back quartz boat.

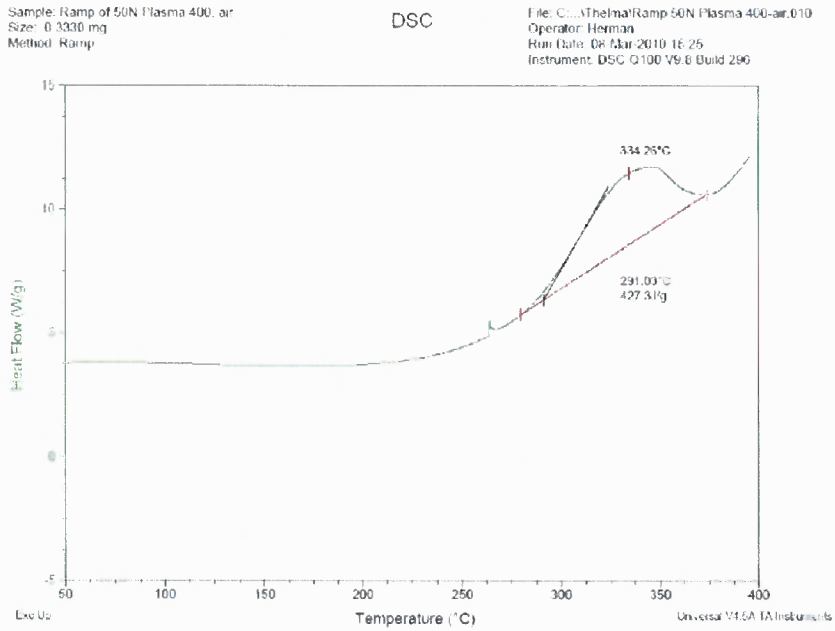


**Figure B.7** DSC for not annealed CHEAP SWNT substrate from 50%Nitrogen50% Argon PE-CVD process. Location at Back quartz boat.

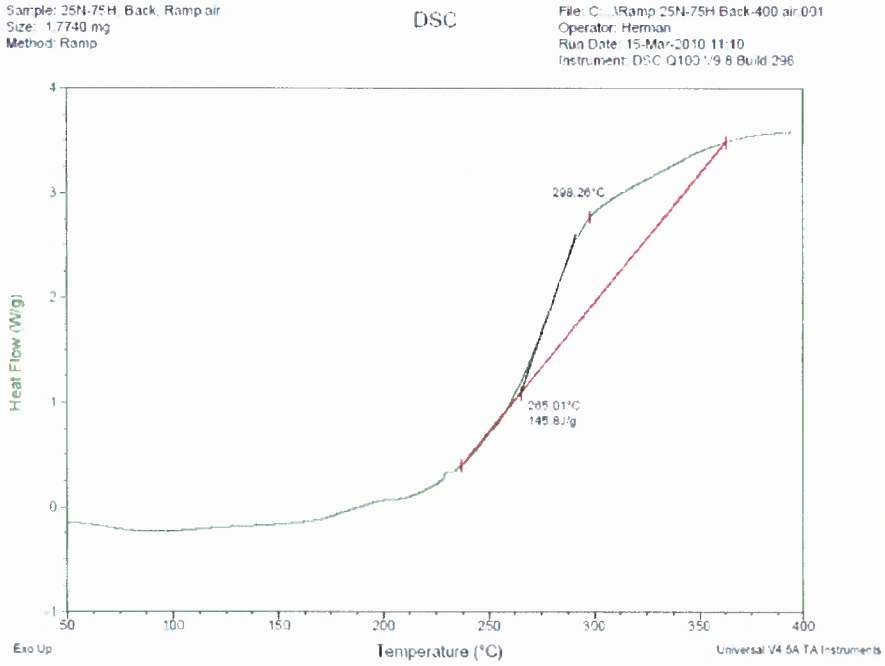


**Figure B.8** DSC for 25N75H treated by PECVD process not annealed, located at Back quartz boat.

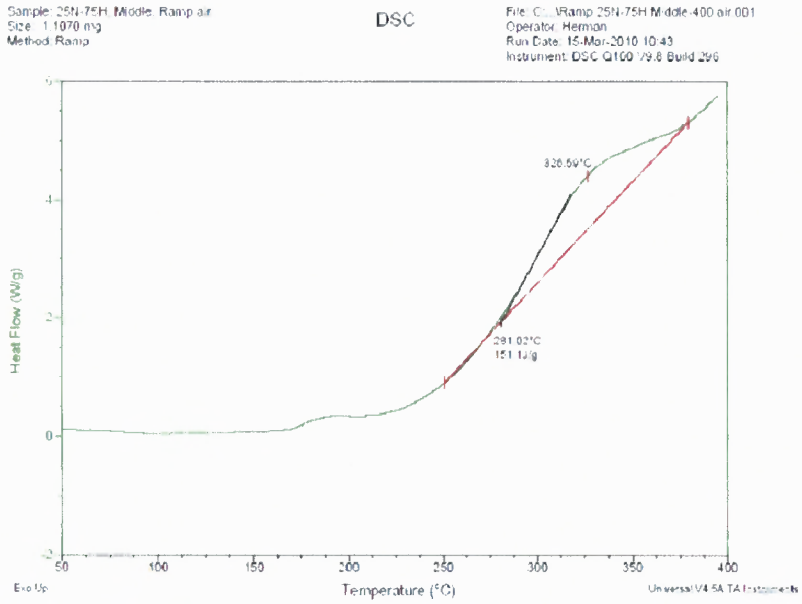


**Figure B.9** DSC for not annealed CHEAP SWNT substrate from 25%Nitrogen75% Hydrogen PE-CVD process. Location at Middle quartz boat.

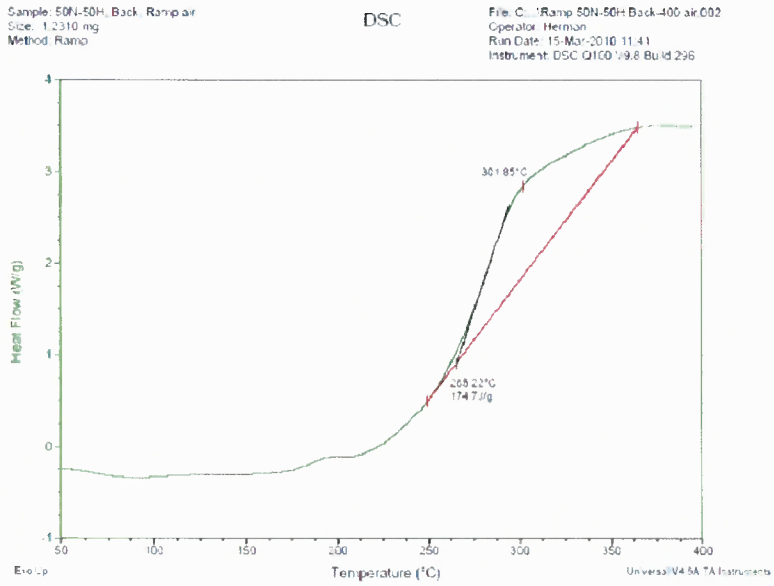


**Figure B.10** DSC for not annealed CHEAP SWNT substrate from 50%Nitrogen 50% Hydrogen PE-CVD process. Location at Back quartz boat

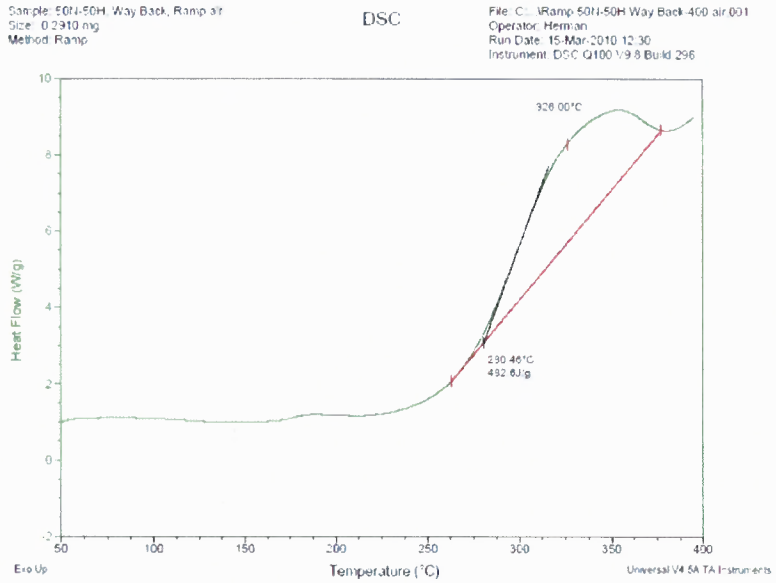


**Figure B.11** DSC for not annealed CHEAP SWNT substrate from 50%Nitrogen50% Hydrogen PE-CVD process. Location at Wayback quartz boat.

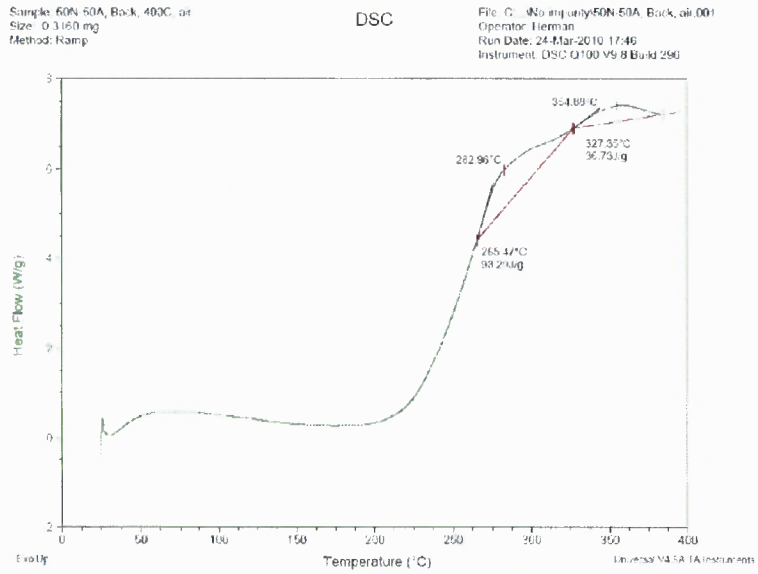


**Figure B.12** DSC for annealed CHEAP SWNT substrate from 50%Nitrogen50% Argon PE-CVD process. Location at Back quartz boat.

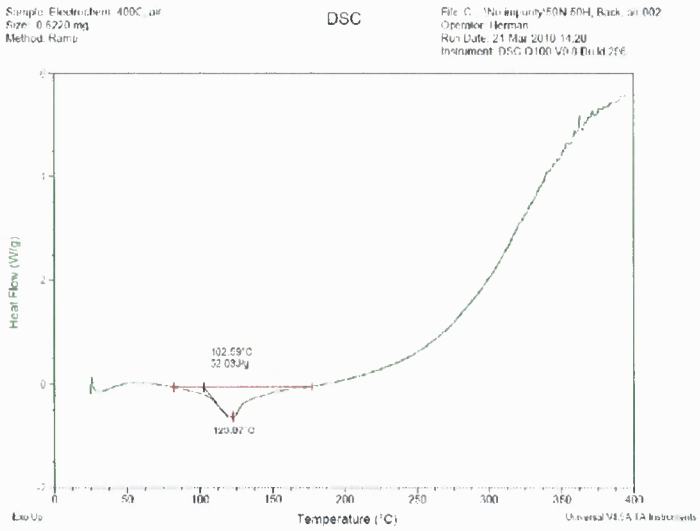


**Figure B.13** DSC for annealed CHEAP SWNT substrate from 50%Nitrogen50% Hydrogen PE-CVD process, Location at Back quartz boat.

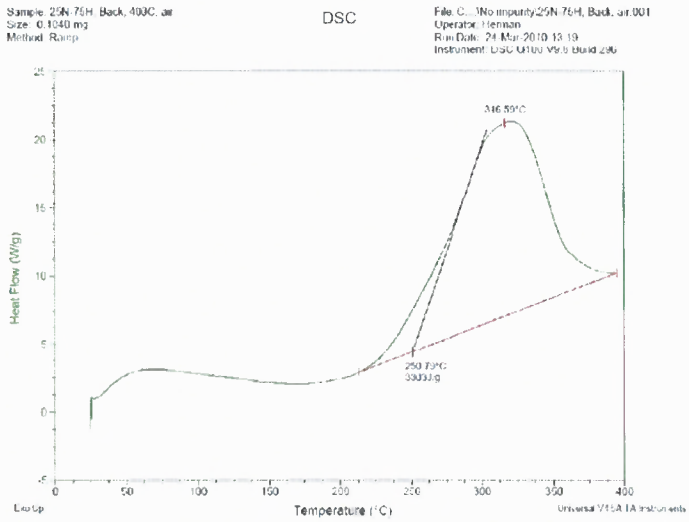


**Figure B.14** DSC for annealed CHEAP SWNT substrate from 25%Nitrogen75% Hydrogen PE-CVD process, Location at Back quartz boat.

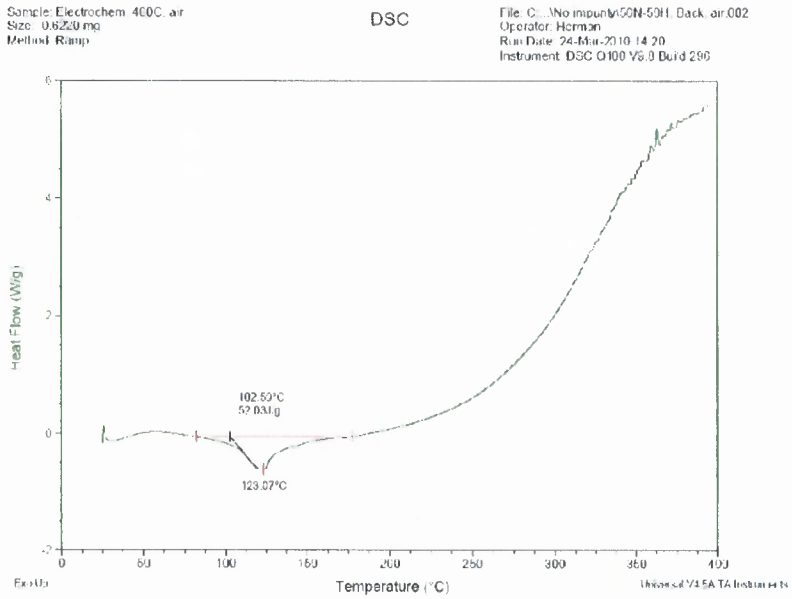


**Figure B.15** DSC for annealed CHEAP SWNT substrate from 50%Nitrogen50% Hydrogen PE-CVD process, Location at Back quartz boat.

t

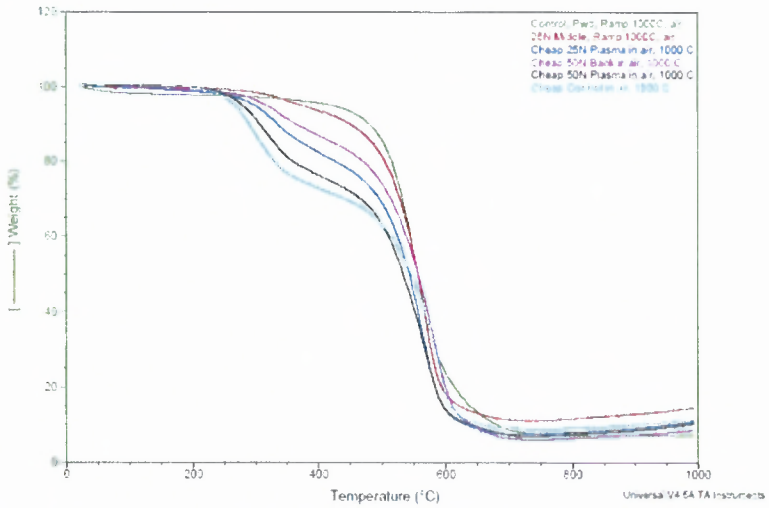


**Figure B.16** Overlay of TGA for not annealed CHEAP SWNT substrate from the Nitrogen Argon PE-CVD process.

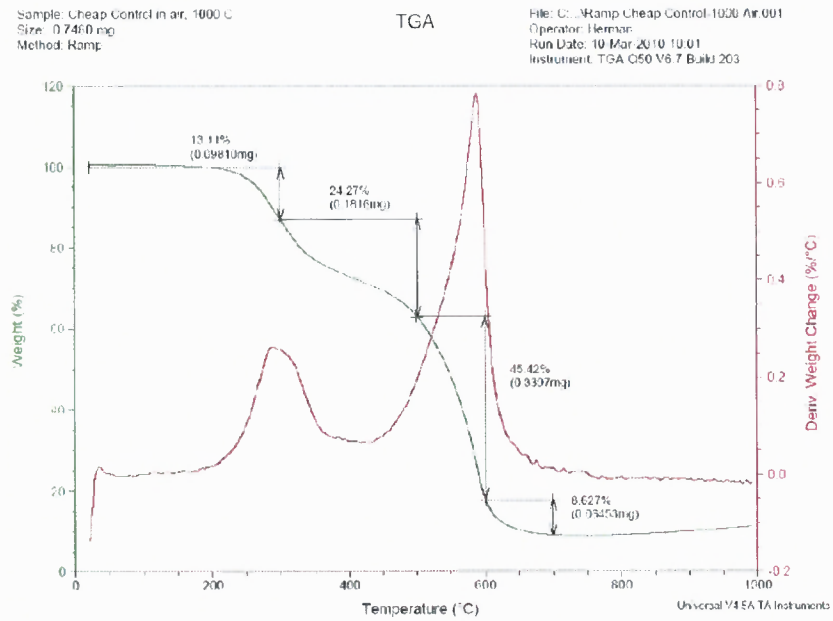


**Figure B.17** TGA for pristine CHEAP SWNT nanopaper.

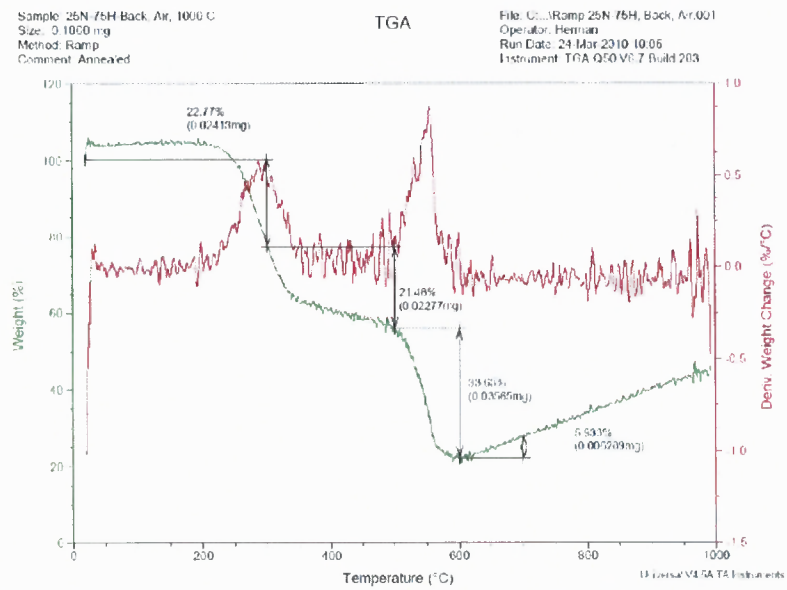


**Figure B.18** TGA for pristine CHEAP SWNT buckypaper substrate after the 25%N 75% H PECVD located at Back quartz boat from the plasma.

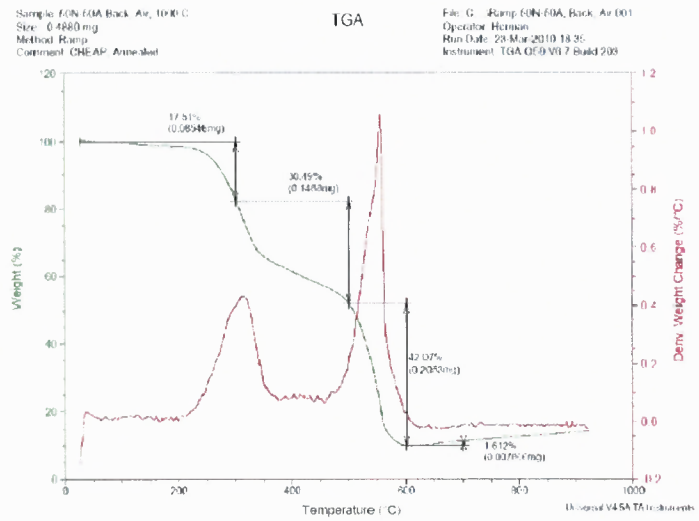


**Figure B.19** TGA for not annealed CHEAP SWNT buckypaper substrate after the 50%N 50% H PECVD located at back quartz boat.

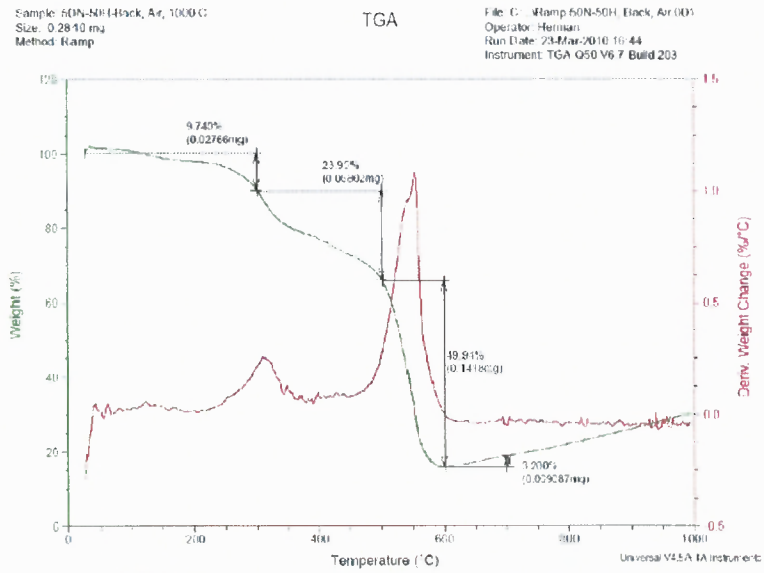


**Figure B.20** TGA for PRISTINE CHEAP SWNT nanopaper substrate after the 25%N 75% H PECVD located at back quartz boat from the plasma.

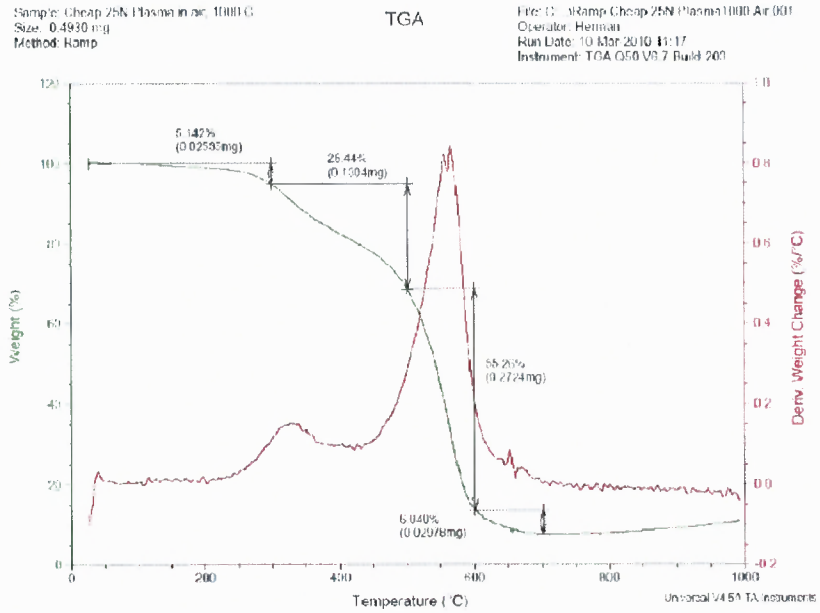


**Figure B.21** TGA for not annealed CHEAP SWNT substrate from 50%Nitrogen50% Argon PE-CVD process. Location at Back quartz boat.

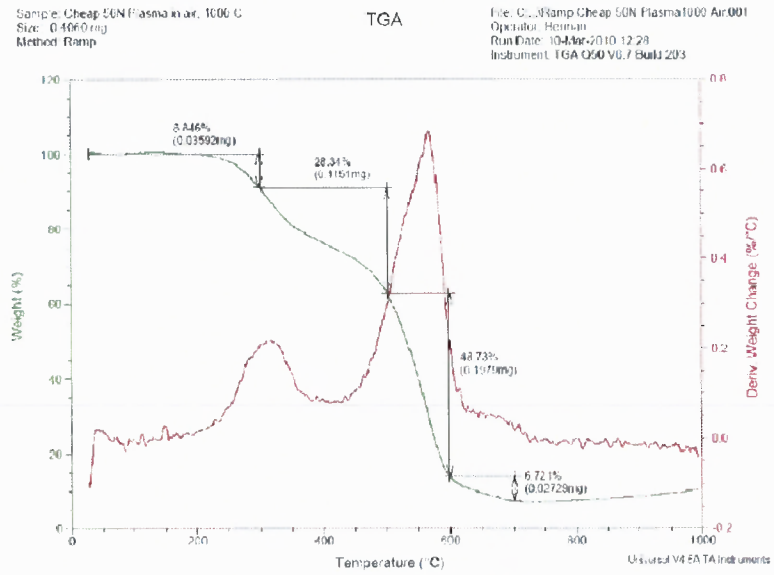


**Figure B.22** TGA for not annealed CHEAP SWNT substrate from 50%Nitrogen50% Argon PE-CVD process. Location at Back quartz boat.

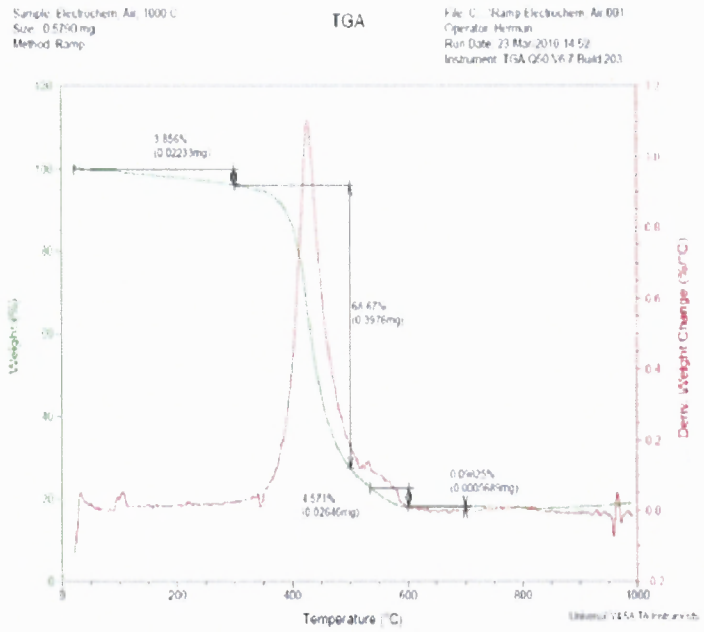


**Figure B.23** TGA for annealed CHEAP SWNT nanopaper prior to electrochem.

## APPENDIX C

## FTIR-ATR DATA FOR THE ELECTROCHEMICAL SYNTHESIS SAMPLES

Figure C.1 to C.11 show the FTIR-ATR analysis of SWeNT SWNT annealed .

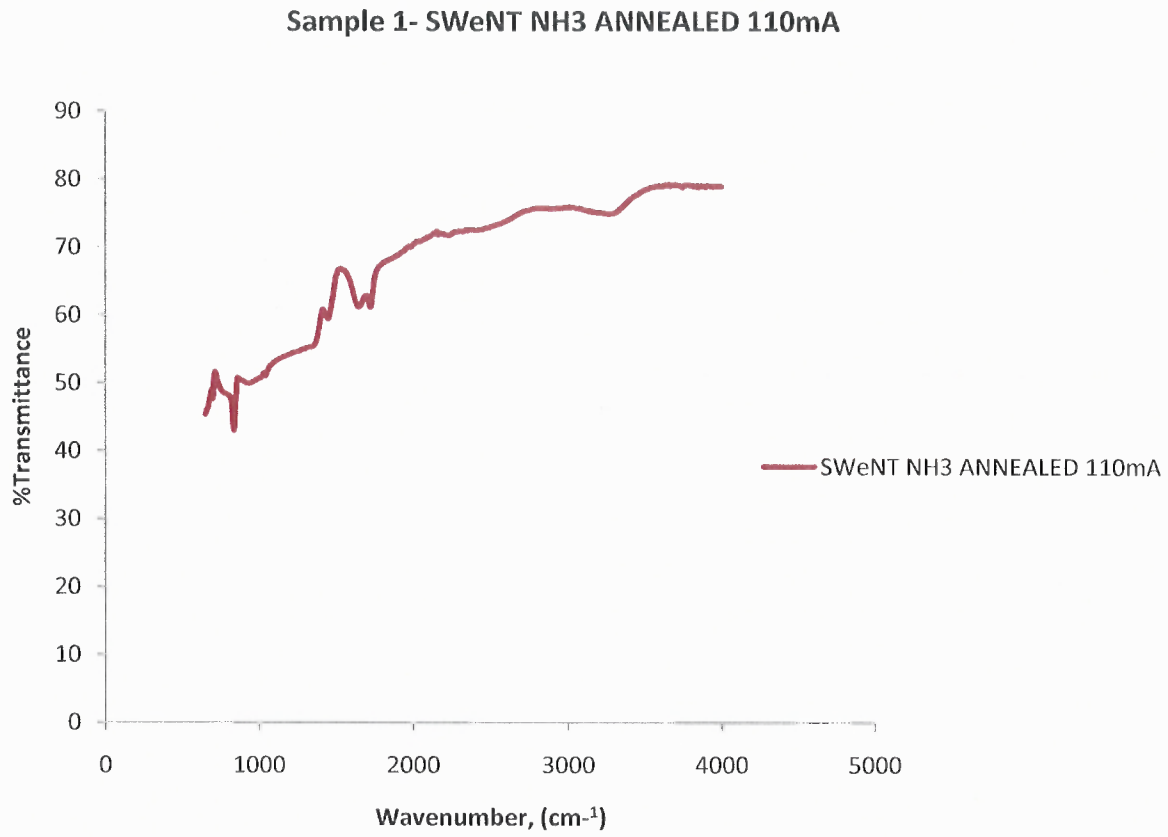


**Figure C.1** Sample number 1-SWeNT ammonia annealed , electrochem with 110mA.

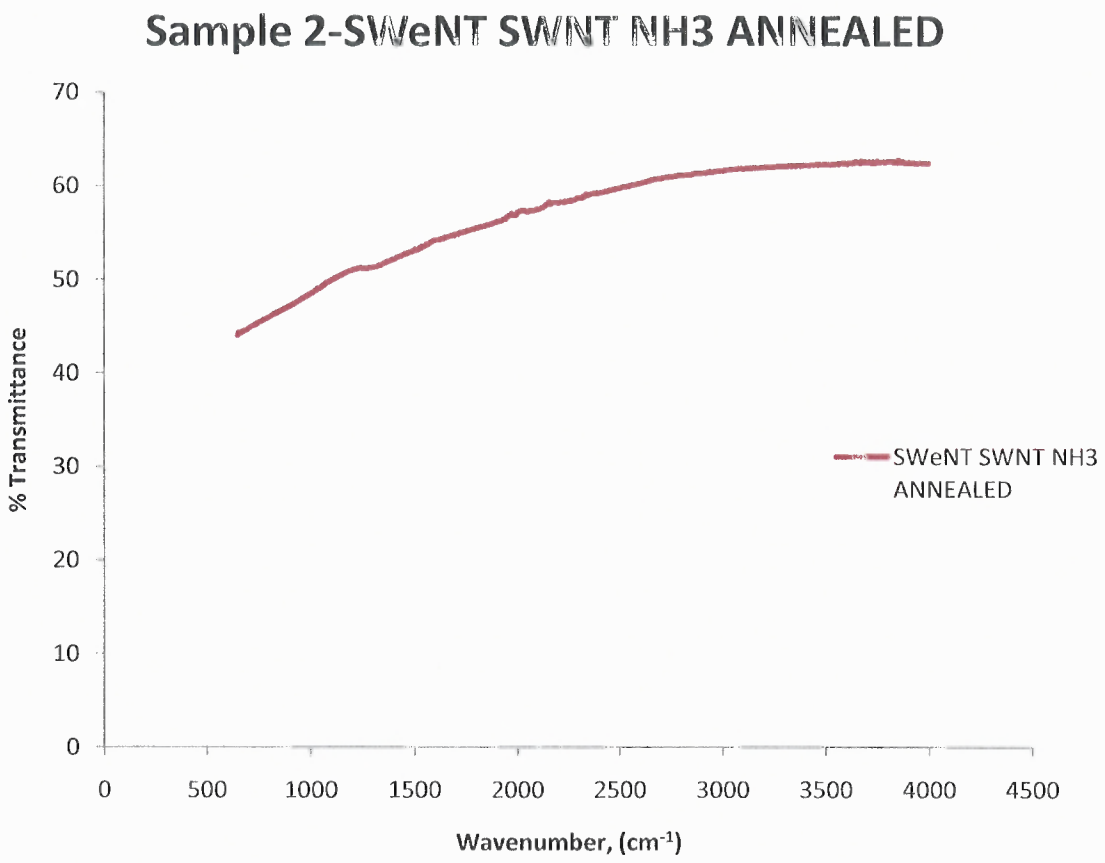


**Figure C.2** Sample number 2-SWeNT ammonia annealed, no electrochem.

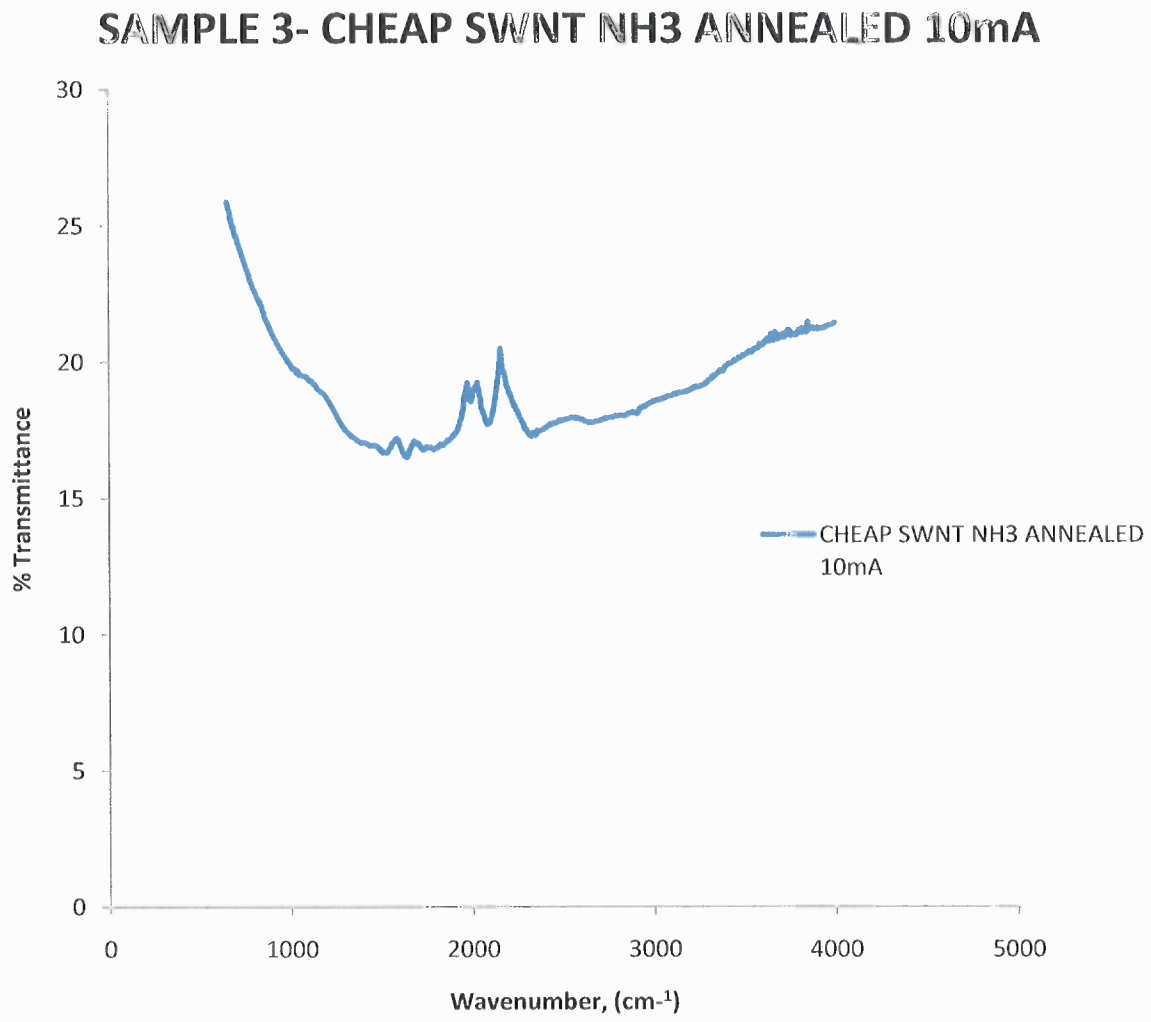


**Figure C.3** Sample number 3-CHEAP SWNT ammonia annealed , electrochem with 10mA.

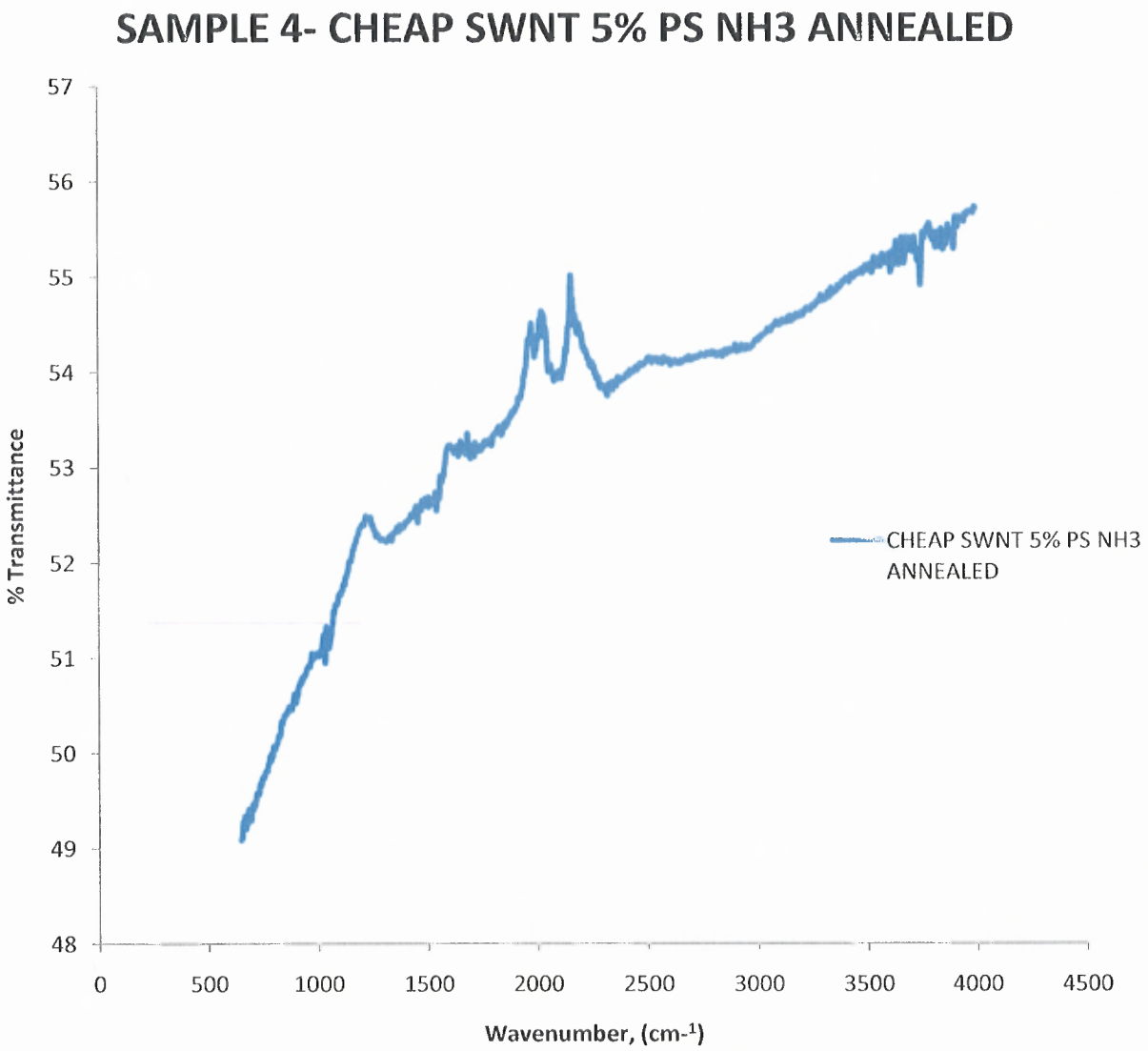


**Figure C.4** Sample number 4-CHEAP SWNT ammonia annealed , no electrochem.

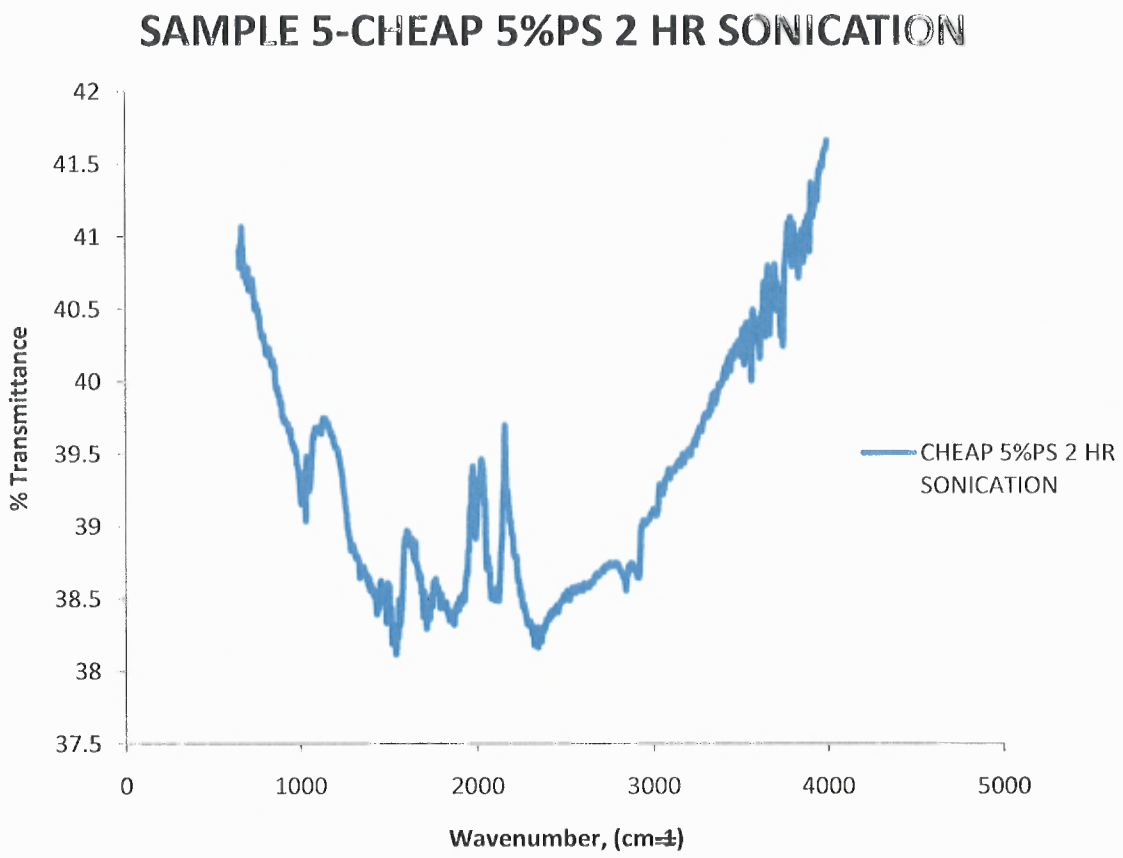


**Figure C.5** Sample number 5 - CHEAP SWNT with 5%polystyrene.

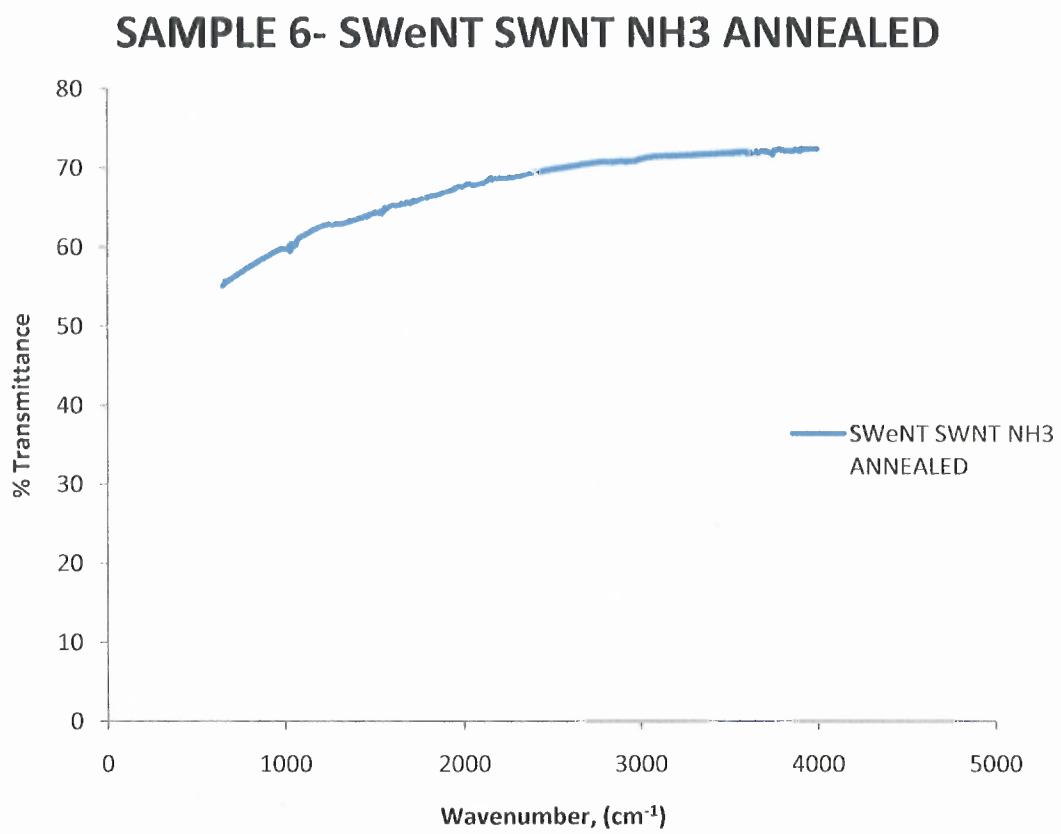


**Figure C.6** Sample number 6 - SWeNT SWNT ammonia annealed.

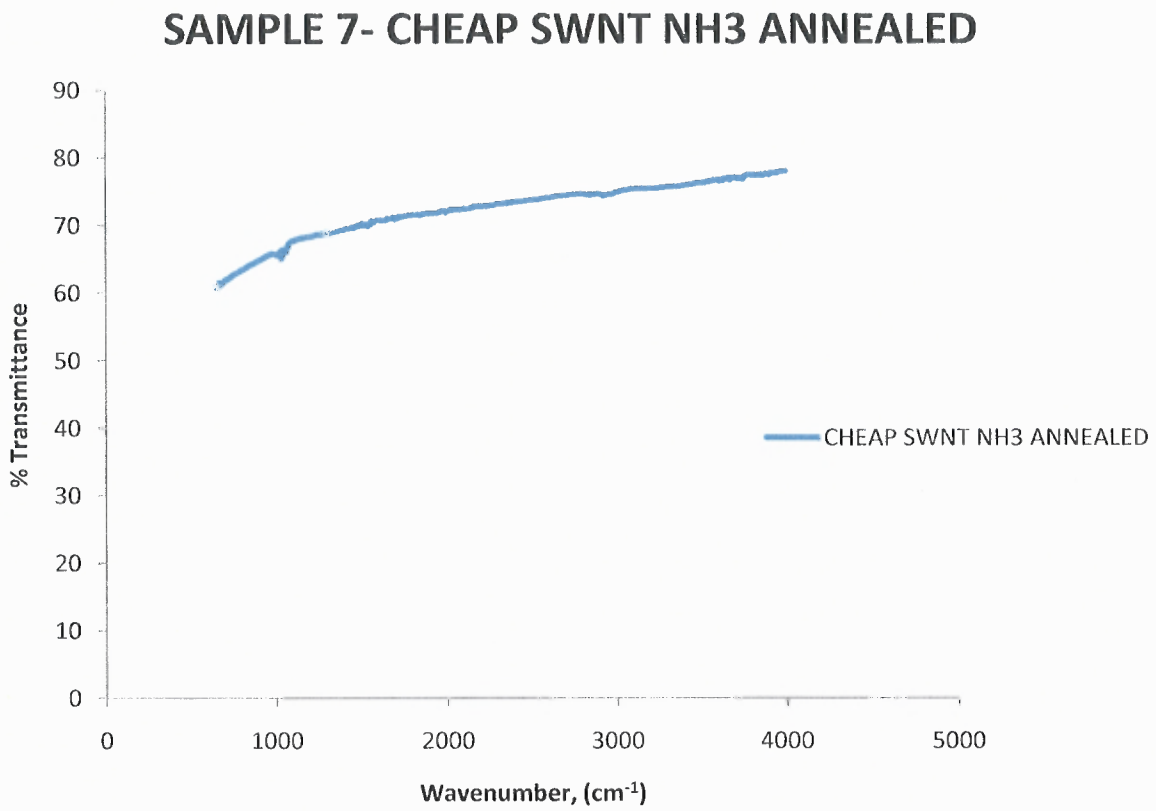


**Figure C.7** Sample number 7 - CHEAP SWNT ammonia annealed.

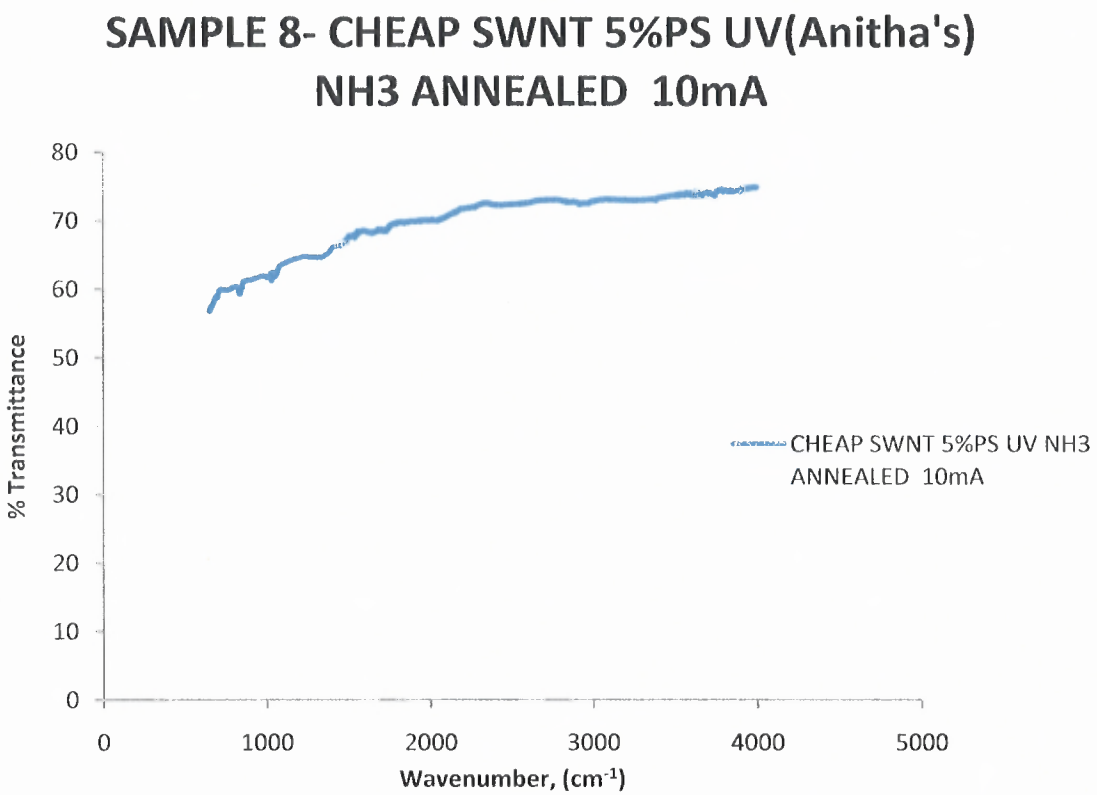


**Figure C.8** Sample number 8 CHEAP SWNT with 5% polystyrene, ammonia annealed and UV treated.at 10mA current.

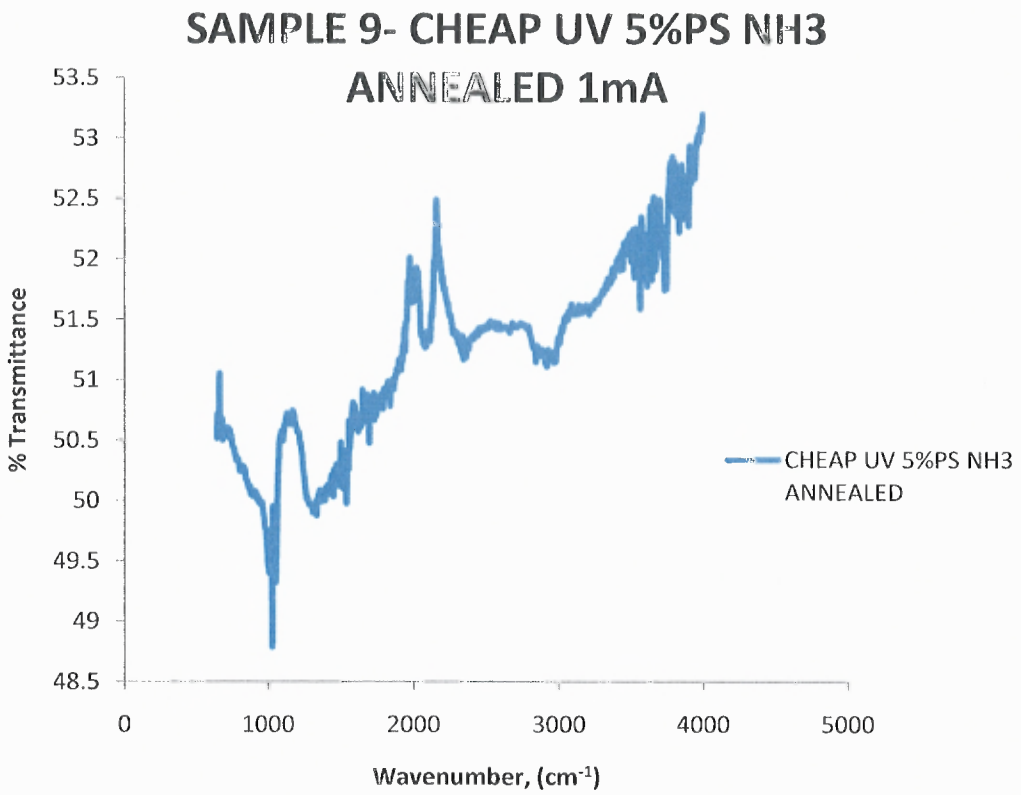


**Figure C.9** Sample number 9 - CHEAP SWNT ammonia annealed with 5%polystyrene , electrochem reaction at 1mA current.

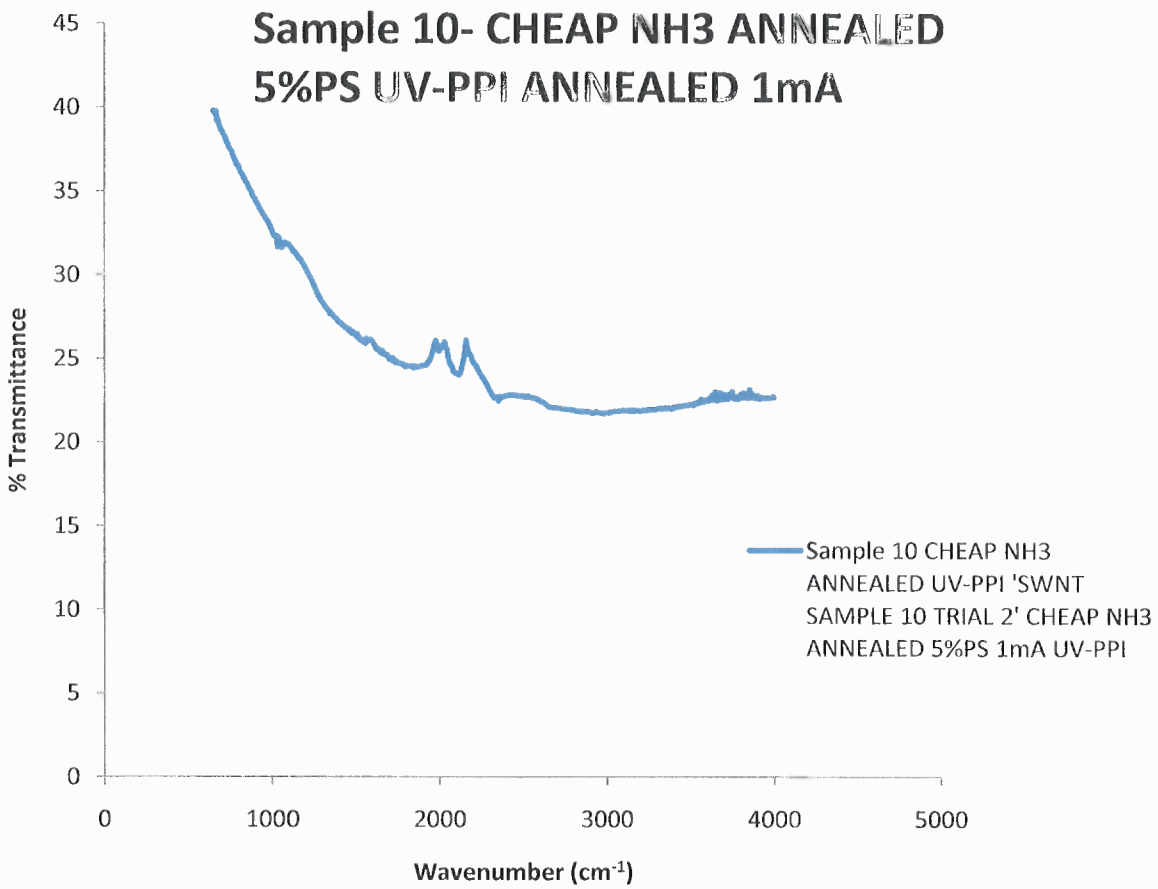


**Figure C.10** Sample number 10 - CHEAP SWNT ammonia annealed , 5%polystyrene, UVduring electrochem reaction at 1mA current.

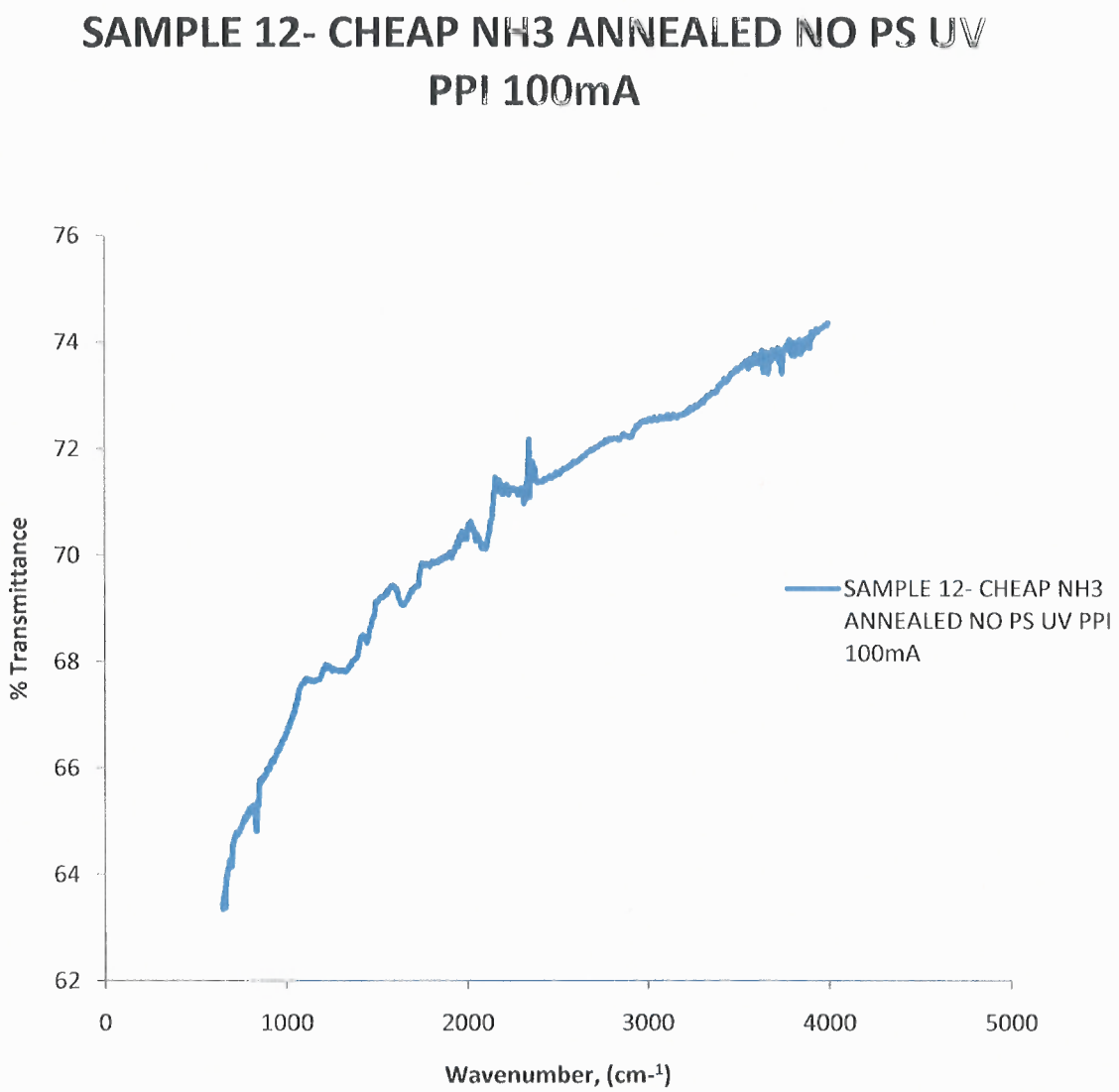


**Figure C.11** Sample number 12 – CHEAP SWNT ammonia annealed, no polystyrene, UV electrochem with 100mA current.

## APPENDIX D

## FTIR-ATR DATA FOR PE-CVD SAMPLES

Figure D.1 to D.11 show the FTIR- ATR analysis of PECVD Cheap SWNT annealed and not annealed substrates.

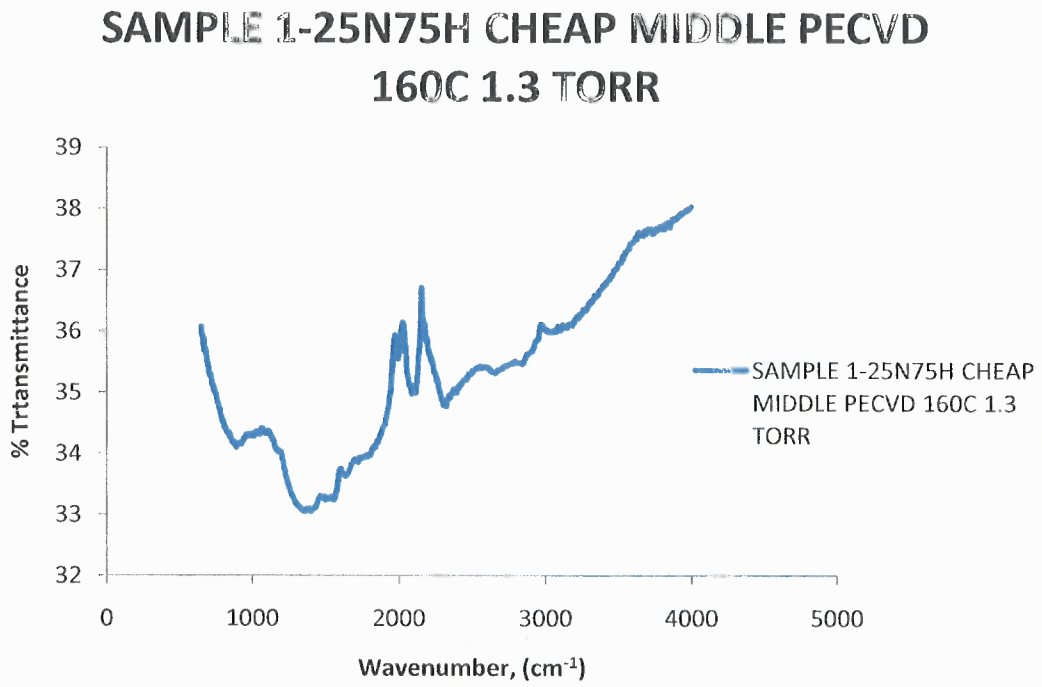


**Figure D.1** Sample 1 for 25N75H annealed Cheap SWNT Middle boat from the plasma.

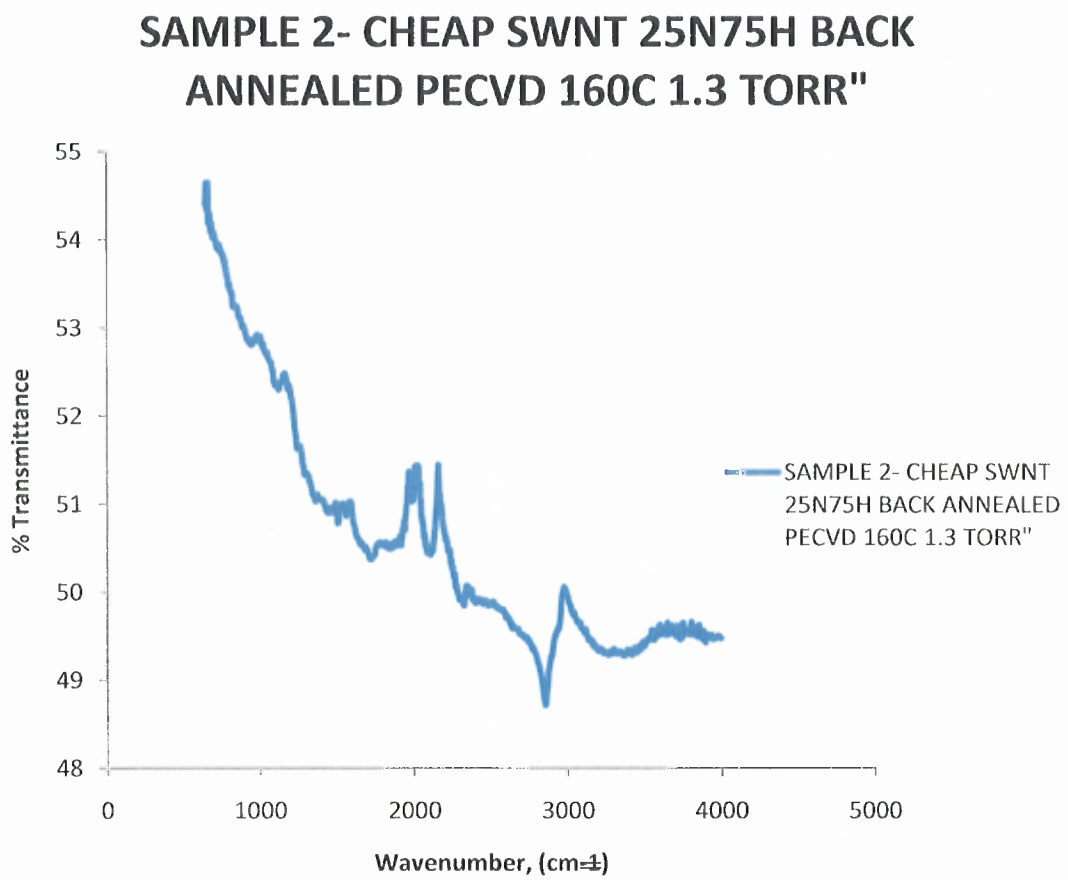


**Figure D.2** Sample 2 for 25N75H annealed Cheap SWNT Back boat from the plasma.

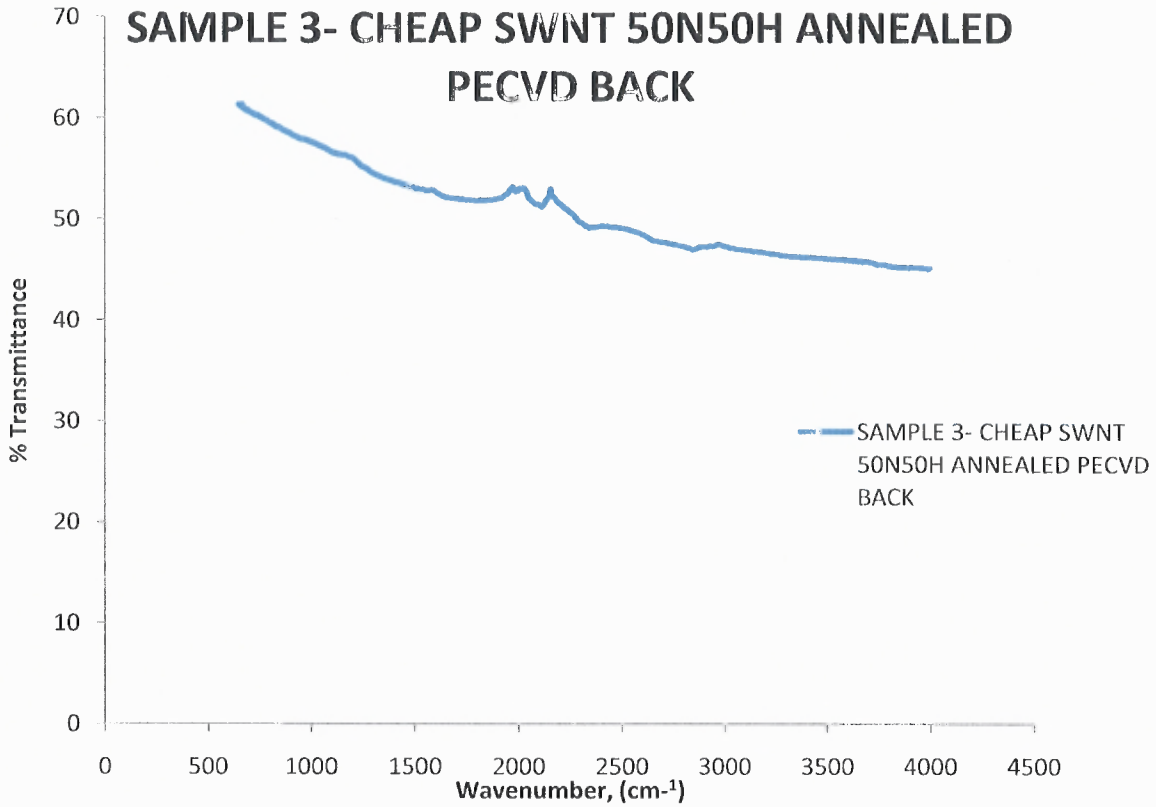


**Figure D.3** Sample 3 for 25N75H annealed Cheap SWNT Back boat from the plasma.

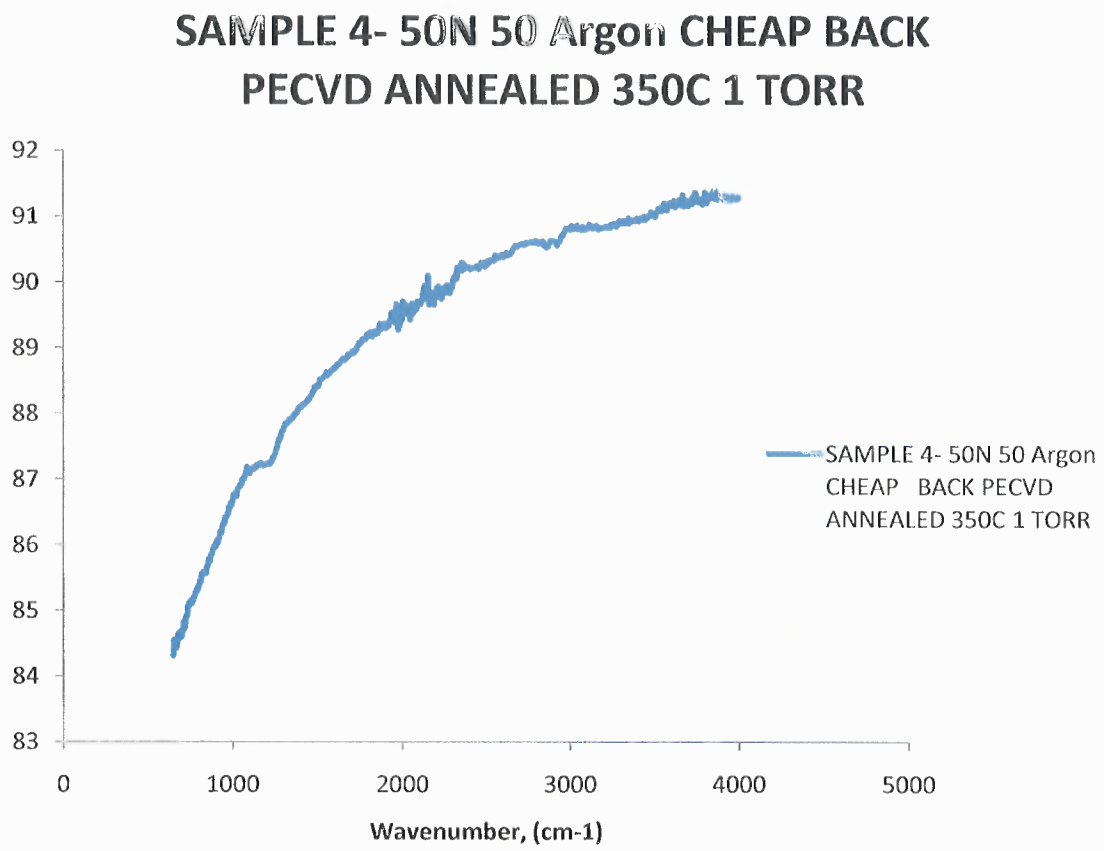


**Figure D.4** Sample 4 for 25N75H annealed Cheap SWNT Back boat from the plasma.

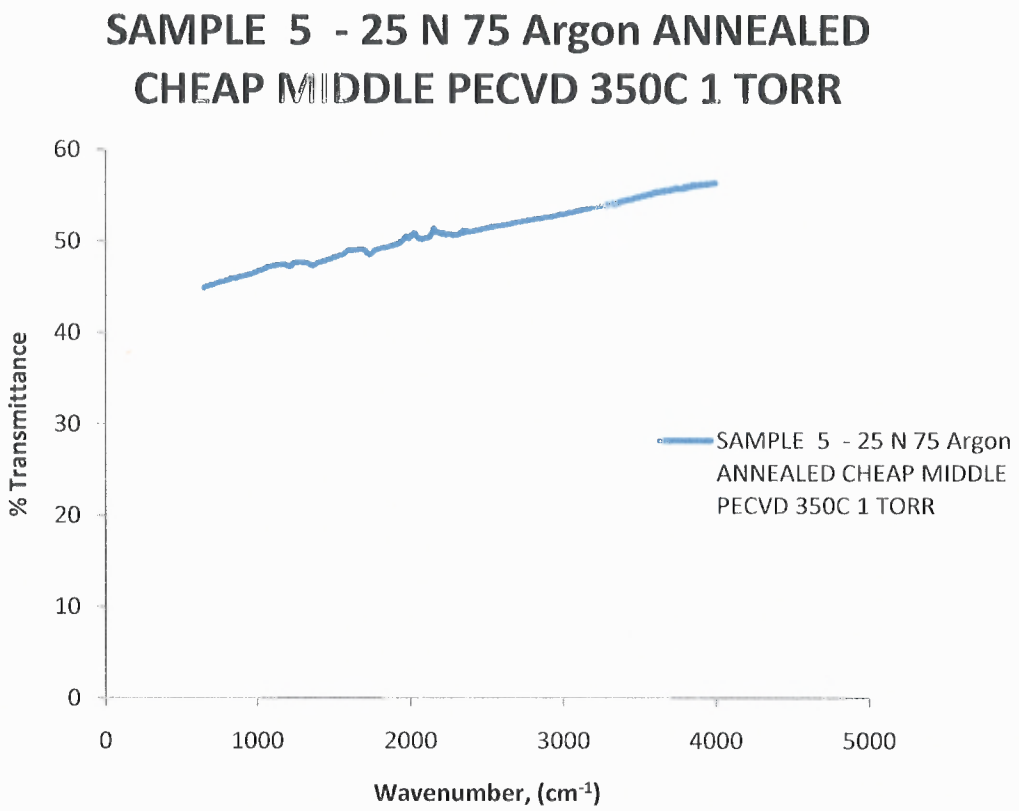


**Figure D.5** Sample 5 for 25N75H annealed Cheap SWNT Middle boat from the plasma.

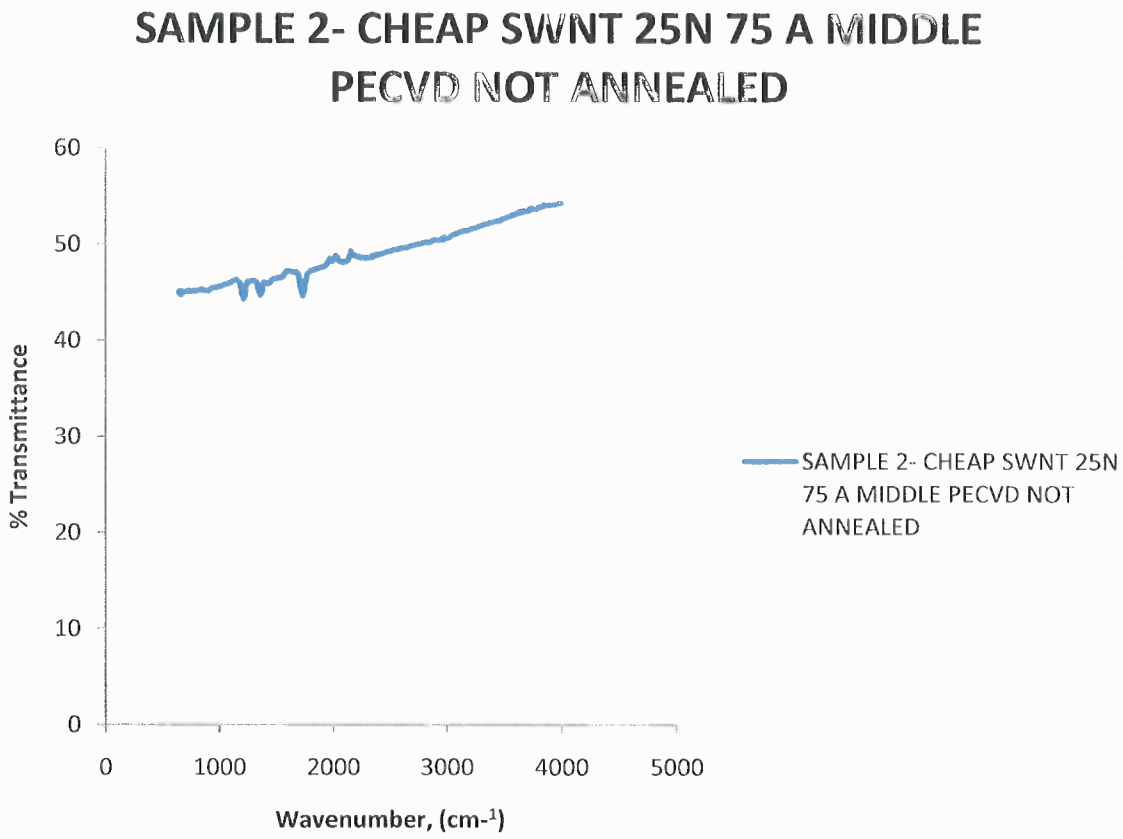


**Figure D.6** Sample 2 for 25N75A unannealed Cheap SWNT Middle boat from the plasma.

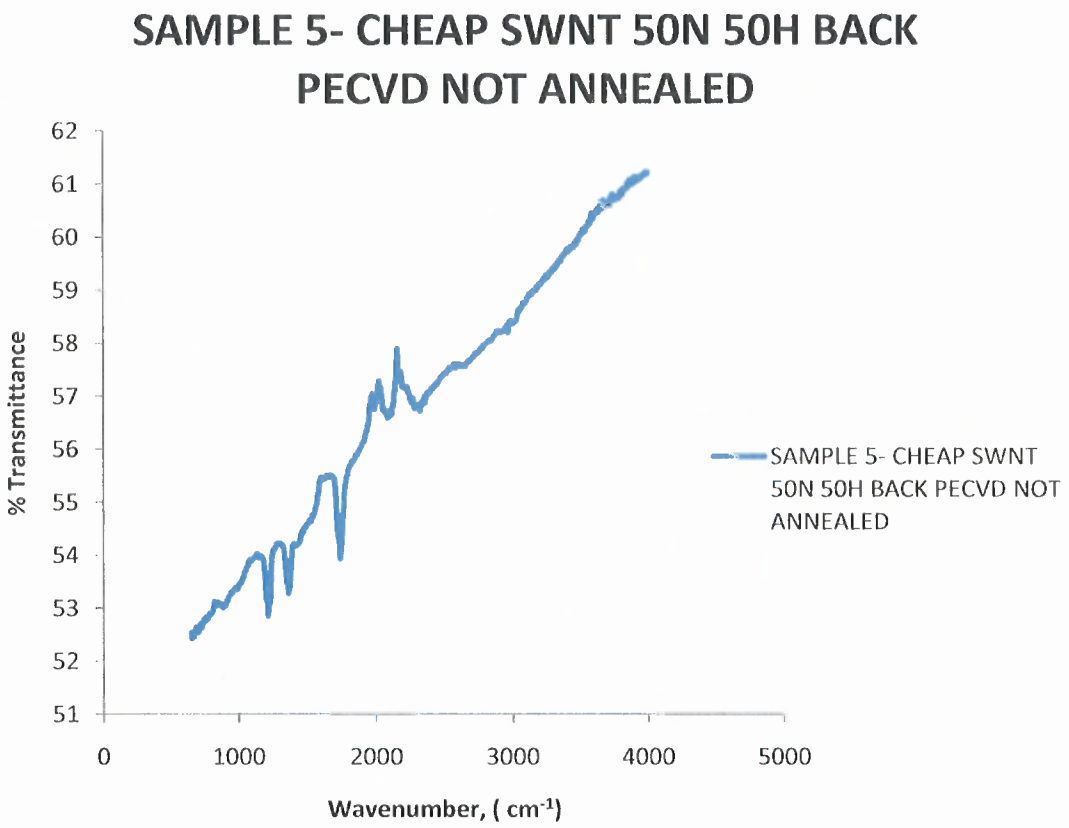


**Figure D.7** Sample 5 for 50N50H unannealed Cheap SWNT Back boat from the plasma.

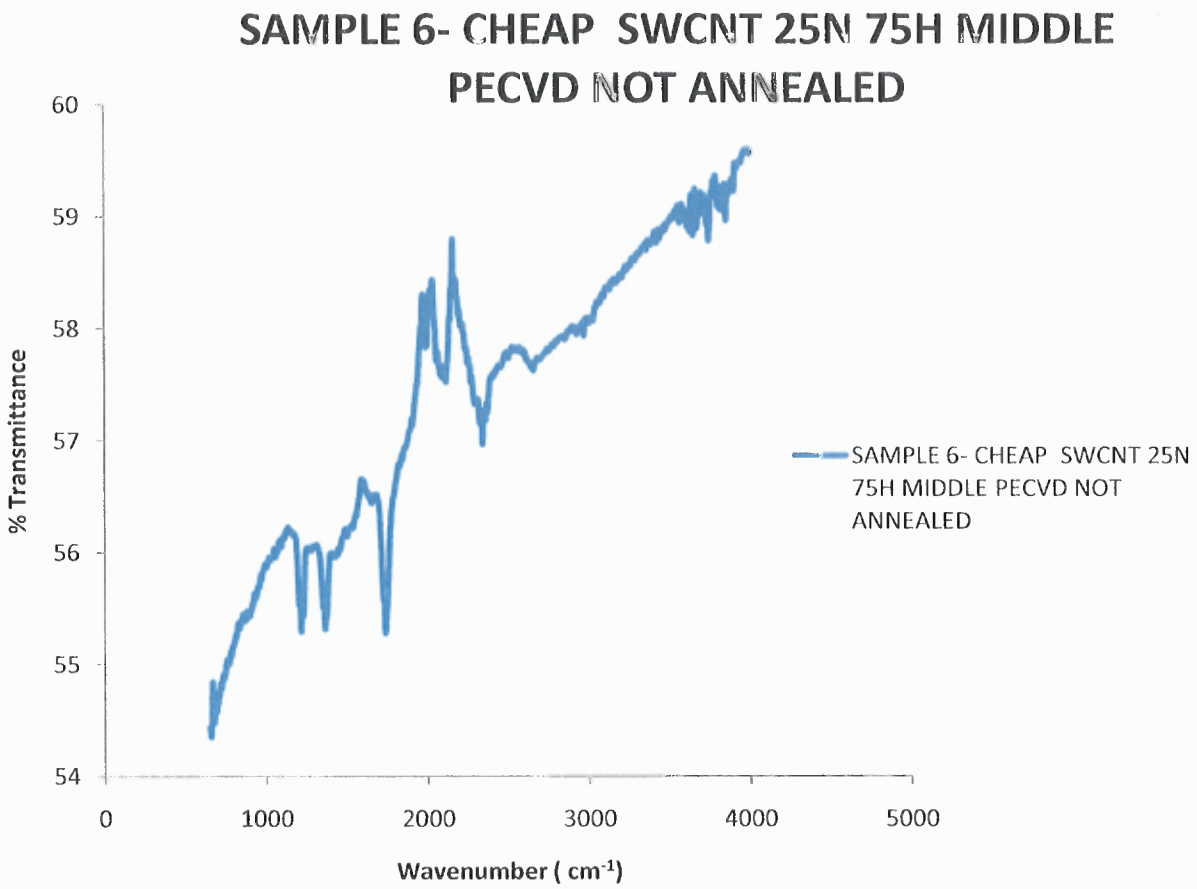


**Figure D.8** Sample 6 for 25N75H unannealed Cheap SWNT Middle boat from the plasma.

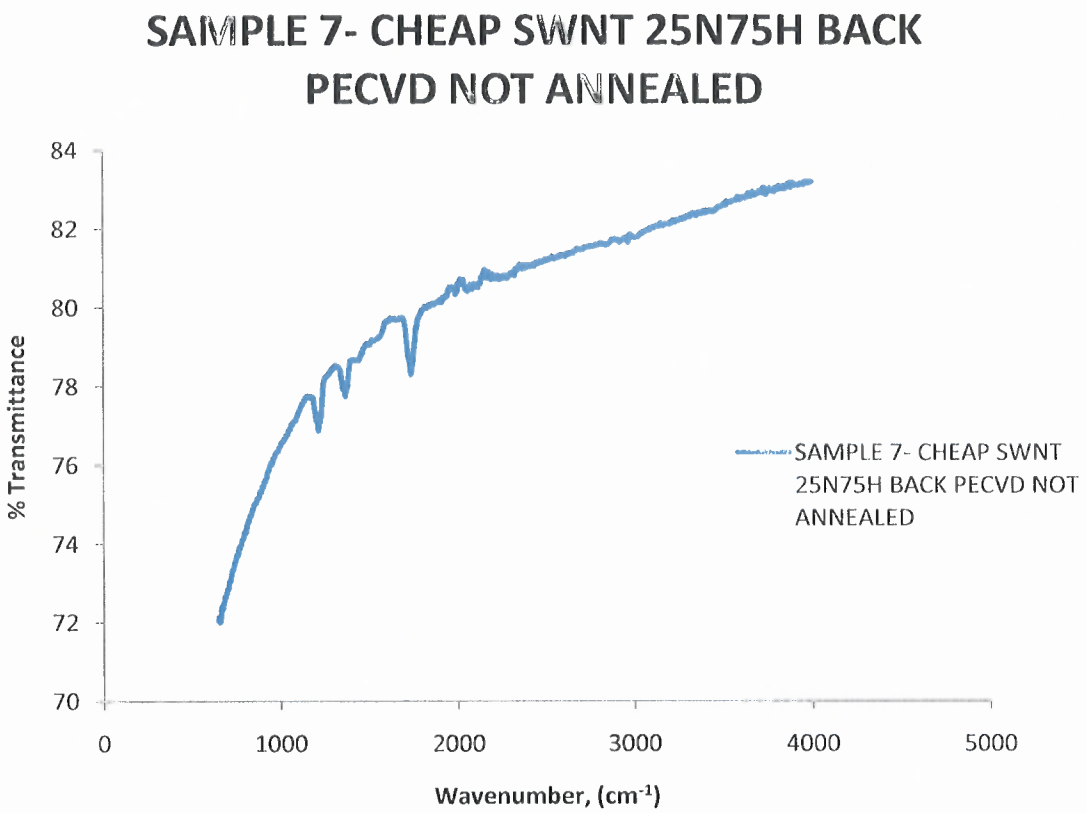


**Figure D.9** Sample 7 for 25N75H unannealed Cheap SWNT Back boat from the plasma.

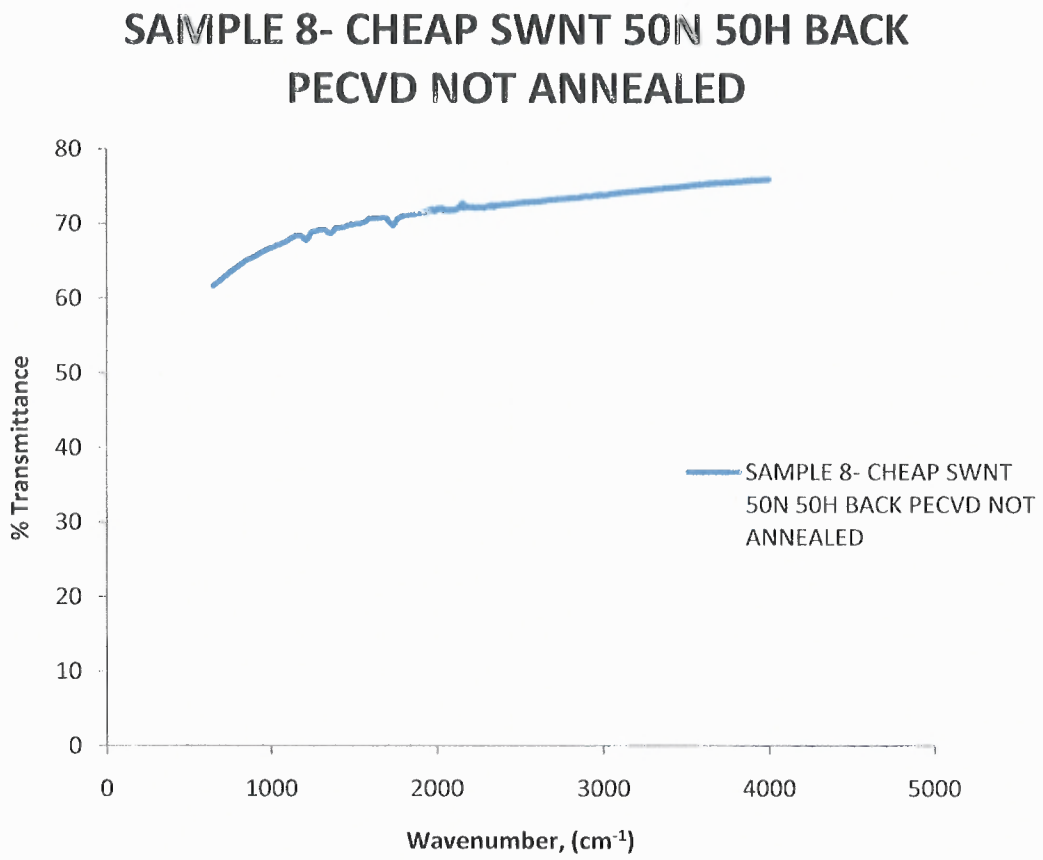


**Figure D.10** Sample 8 for 50N50H unannealed Cheap SWNT Back boat from the plasma.

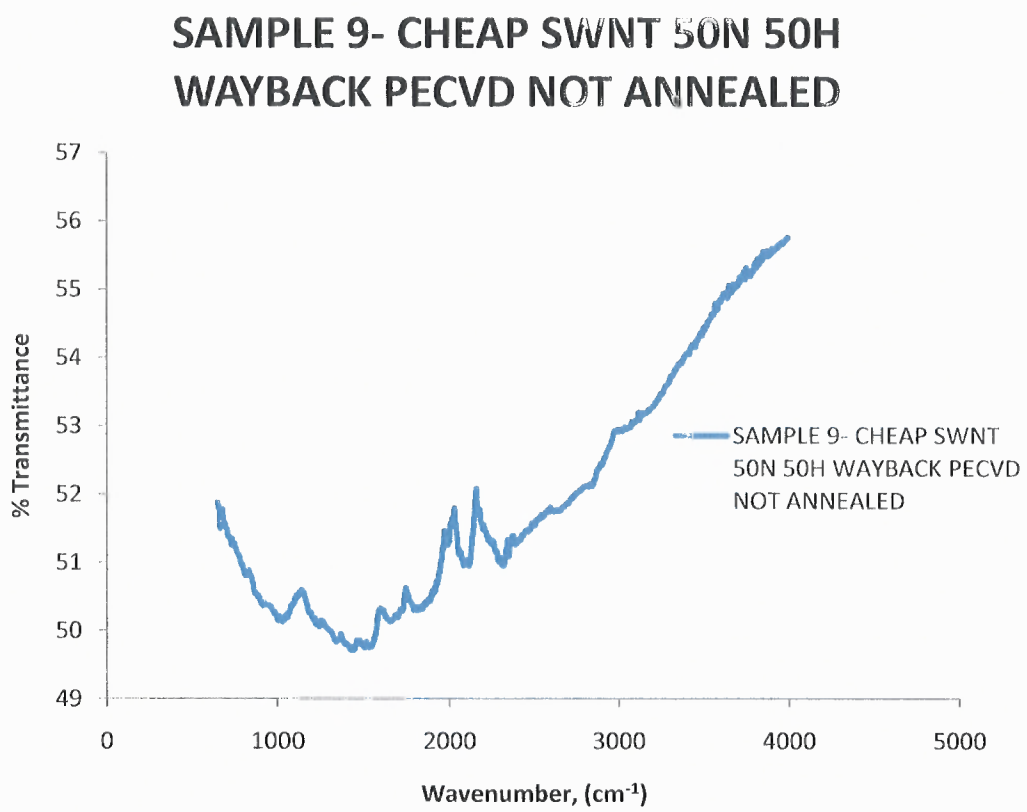


**Figure D.11** Sample 9 for 50N50H unannealed Cheap SWNT WayBack boat from the plasma.

## REFERENCES


[1] V. Ponec and W. Van Braneveld, "The Role of Chemisorption in Fischer-Tropsch Synthesis", *Journal of Industrial Engineering Chemical Product Research and Development*, Vol. 18, No. 4, 1979.

[2] C. Leveritt, P. Conroy and A. Johson, "Characterization of the Erosivity of Advanced Solid Gun Propellants", Proceedings of the 37th JANNAF Combustion Subcommittee Meeting, Monterey, CA, November 2000.

[3] Walsh, C. and Knott, C., "Gun Propellant Formulations with High Nitrogen Modifiers", Proceedings of the 31st JANNAF Propellant Development and Characterization Subcommittee Meeting, Charlottesville, VA, March 2003.

[4] P.J.Cote, C. Richard, "Gas-Metal Reaction Products in the Erosion of Chromium-Plated Gun Bores." *Wear* **24** 1(2000) 17-25.

[5] S. Sopok, C. Rickard, G. Pflegl, P. Vottis, P. O'Hara, S. Dunn, and D. Coats, "Erosion Predictions for the Final Configuration of the M829E3 Round, Technical Report ARAEW-TR-04001, U.S. Army ARDEC, Armaments Engineering & Technology Center, Weapon Systems & Technology, Benet Laboratories, Jan 2004.

[6] S. Sopok, P. Vottis, P. O'Hara, G, Pflegl and C. Rickard, " Comprehensive Erosion Model for the 120-mm M256/M829A2 Gun System, Technical Report ARCCB-TR-98018, U.S. Army ARDEC, Armaments Engineering & Technology Center, Weapon Systems & Technology, Benet Laboratories, Oct 1998.

[7] S. Sopok, C. Rickard, S. Dunn, Thermal-chemical-mechanical gun bore erosion of an advanced artillery system part one: theories and mechanisms, *Wear,* 258(2005)659-670.

[8] P. Conroy, P. Weinacht and M. Nusca, "Extended Range 5" Navy Gun, Theoretical Thermal and Erosion Investigations", Proceeding of the 35th JANNAF Combustion Subcommittee Meeting, Tucson, AZ, December 1998 P.J.Cote, C. Richard, "Gas-metal reaction products in the erosion of chromium-plated gun bores." *Wear* 24 1(2000) 17-25.

[9] P.J.Cote, S.L. Lee, M.E. Todaro, G.Kendall, "Application of Laser Pulse Heating to Simulate Thermo mechanical Damage at Gun Bore Surface", *Journal of Pressure Vessel Technology*, Vol. 125, p.335-341, August 2003.

[10] P.J.Conroy, C.S. Leveritt, J.K. Hirvonen, and J.D. Demaree, The Role of Nitrogen in Gun Tube Wear and Erosion, 24th Army Science Conference Proceedings, Nov 2004.

[11] H. Underwood, A.P. Parker, P.J. Cote, S. Sopok, *Trans. ASME*, 121(1999), 116-120.

[12] T.G. Manning, D. Chiu and D. Park, Characterization and Ballistic Properties of High Energy High Performance ETPE Gun Propellant for Future Large Caliber Applications" , Proceedings of the 2005 JANNAF 40th Combustion Sub-Committee/28th APS/22nd PSHS/ 4th MSS Joint Meeting at Charleston Convention Center & Charleston AFB, Charleston, S.Carolina, 13-17 Jun 2005.

[13] Ken Kuo, Lee Harris and Thelma Manning, "Development and Characterization of High Performance Solid Propellants Containing Nano-sized Energetic Ingredients", 31st International Symposium, Proceedings of the Combustion Institute, Vol. 31, Apr 2006.

[14] Mench, M.M., Yeh, C.L., Kuo, K.K., "Propellant Burning Rate Enhancement and Thermal Behavior of Ultra-Fine Aluminum Powders (ALEX)" Energetic Materials Production, Processing and Characterization, 29th International ICT Conference, June 30 – July 3, 1998, pp3-01-3-05. .

[15] Ulas, A., Kuo, K.K., Gotzmer, C., "Ignition and Combustion of Boron Particles in Fluorine-Containing Environments," *Combustion and Flame*, Vol 127, pp. 1935-1957, 2001.

[16] G. Verhaegen and J. Drowart, Mass Spectrometric Determination of the Heat of Sublimation of Boron and of the Dissociation Energy of B, *J. Chem. Phys.*, 37, 6,(1962).

[17] Eremets, M.I., Gavriliuk, A.G., Trojan, I.A., Dzivenko, D.A., Boehler, R., Single bonded form of nitrogen, *Nature Materials*, **3** (2004) 558); (b) M. I. Eremets, A. G. Gavriliuk, I. A. Trojan, Single-Crystalline Polymeric Nitrogen, *Appl. Phys. Lett.* **90**, 171904 (2007); (c) Y. Ma, A. R. Oganov, Z. Li, Y. Xie, J. Kotakoski,

Novel High Pressure Structures of Polymeric Nitrogen, *Phys. Rev. Lett.* **102**, 065501 (2009).

[18] Eremets, M.I., Yu, M., Popov, I.A., Denisov, V.N., Boehler, R., Hemley, R.J., Polymerization of nitrogen in sodium azide, *J. Chem. Phys.* 120 (2004) 10618.

[19] Abou-Rachid, H., Hu, A., Arato, D. Sun, X., Desilets, S., Novel Nanoscale High Energetic Materials: Nanostructured Polymeric Nitrogen and Polynitrogen, *Proc. 7th International Symposium on Special Topics in Chemical Propellants*, Kyoto, Japan (2007).

[20] Caracas, R., Raman Spectra and Lattice Dynamics of Cubic Gauche Nitrogen, *J. Chem. Phys.* **127**, 144510 _2007.

[21] Kuhl, A. L., Ullrich, G.W., Gurtman, G., McFarland, C., "Disruptive Energetics", 4th Advanced Energetics Technical Exchange, Jan 22-25, 2008, Fort Belvoir, VA

[22] Kuhl, A.L., Fried, L.E. Howard, Micahel W. and Seisew, M.R., et al, Detonation of Meta-stable Clusters, 39th ICT Conference on Energetic Materials, 24-27, 2008, Karlsruhe, Germany

[23] Abou-Rachid, H., Hu, A., Timoshevskii, V., Song, Y., Lussier, L-S., Nanoscale High Energetic Materials: A Polymeric Nitrogen Chain N8 Confined inside a Carbon Nanotube *Phys. Rev. Lett.* 100 (2008)196401.

[24] Peiris, S. M., Russell, T.P., Photolysis of Compressed Sodium Azide ($NaN_3$) as a Synthetic Pathway to Nitrogen Materials, *J. Phys. Chem.*, A107 (2003) 944.

[25] Abou-Rachid, H. et al, "Novel Nanoscale High Energetic Materials :Nanostructured Polymeric Nitrogen and Polynitrogen, 7th International Symposium on Special Topics in Chemical Propulsion, 17-21 Sep 02, Kyoto, Japan.

[26] Abou-Rachid, H., Hu, A., Arato, D. Sun, X., Desilets, S., Novel Nanoscale High Energetic Materials: Nanostructured Polymeric Nitrogen and Polynitrogen, Proc. 7th International Symposium on Special Topics in Chemical Propellants, Kyoto, Japan (2007).

[27] Abou-Rachid, H., Hu, A., Timoshevskii, V., Song, Y., Lussier, L-S., Nanoscale High Energetic Materials: A Polymeric Nitrogen Chain N8 Confined inside a Carbon Nanotube *Phys. Rev. Lett.* 100 (2008)196401.

[28] J. Kunstmann and A. Quandt, Broad Boron Sheets and Boron Nanotubes: Ab initio Study of Structural, Electronic, and Mechanical Properties, *Physical Review* B 74, 035413 (2006).

[29] C.C.Tang, M. Lamy de la Chapelle, P.Li, Y.M. Liu, H.Y. Dang, S.SW. Fan, Catalytic Growth of Nanotube and Nanobamboo Structures of Boron Nitride, *Chemical Physics Letters*, 342 (2001), 492-496.

[30] D. Ciuparu, R.F. Klie, Y. Zhu, and L. Pfefferle, Synthesis of Pure Boron Single-Wall Nanotubes, *J. Physics Chemistry*, B, 2004, 108, 3967-3969, Feb 27, 2004

[31] A. W. Searcy and C. E. Myers, The Heat of Sublimation of Boron and The Gaseous Species of the Boric Oxide System, *Journal of Physical Chemistry*, Vol.61(7), 957-960, Jul. 1957.

[32] I. Bousteni, A. Quandt, E. Hernandez, and A. Rubio, New Boron Based Nanostructured Material, *Journal of American Physics,* Vol. 110, No. 6, 3176-3185.

[33] Cheetah version 5, Fried, L.E., Howard, Michael W., Souers, Clark P., Vitello, Peter A., Lawrence Livermore National Laboratory.

[34] Anderson, Ronald D.; Fickie, Kurt D.," IBHVG2 (Interior Ballistics of High Velocity Guns, Version 2) A User's Guide", ADB117104, Technical Report. Jan 1983-Jan 1987, US Army Ballistic Research Laboratory, Aberdeen Proving Ground, Maryland.

[35] Alan B. Dalton, Edgar Munoz, Steve Collins, Bog G. Kim, Joselito Razal, Miles Selvidge, Jonathan N. Colemana, and Werner J. Blau, "Improving the Mechanical Properties of Single-Walled Carbon Nanotube Sheets by Intercalation of Polymeric Adhesives", *Applied Physics Letters,* Volume 82, Number 11, 17 March 2003.

[36] J. Biercuk, M. C. Llaguno, M. Radosavljevic, J. K. Hyun, and A. T. Johnson, *Appl. Phys. Lett.* **80**, 2767, 2002.

[37] J.J. Ghou, Z. Liang, and B. Wang, Experimental Design and Optimization of Dispersion Process For Single Walled Carbon Nanotube Bucky Paper, *International Journal of Nanoscience,* Vol. 3, No. 3 (2004) 293{307}, World Scientific Publishing Company.

[38] U. D. Venkateswaran, A. M. Rao, E. Richter, M. Menon, A. Rinzler, R. E., Smalley, and P. C. Eklund, *Phys. Rev.* B **59**, 10928 ~2000.

[39] R.H. Baughman, C. Cui, A.A.Zakhidov, Z. Iqbal, J.N. Barisci, G.M.Spinks, G.G.Wallace, A.Mazzoldi, D. De Rossi, A.G.Rinzler, O.Jaschinski, S. Roth, A.M. Kertesz, Carbon Nanotube Actuators, *Science,* 284, 1340 (1999).

[40] M. Cadek, J. N. Coleman, V. Barron, K. Hedrick, and W. J. Blau, *Appl. Phys. Lett.* **81**, 5123 ~2002.

[41] B. P. Grady, F. Pompeo, R. L. Shambaugh, and D. E. Resasco, *J. Phys. Chem.,* B 106, 5852 ~2002.

[42] S. M. Smith, S. A. Voight, H. Tompkins, A. Hooper, A. Alec Talin, J. Vella, "Nitrogen-doped Plasma Enhanced Chemical Vapor Deposited (PECVD) amorphous carbon: processes and properties", *Thin Solid Films*, **398 –399**, 163 (2001).

[43] T. Kato, G.-H.Jeong, T.Hirata, R.Hatakeyama, "Structure Control of Carbon Nanotubes Using Radio-Frequency Plasma Enhanced Chemical Vapor Deposition", *Thin Solid Films*, **457**, 2 (2004).

[44] C. Yu, S. C. Wang, M. Sosnowski, Z. Iqbal, *Synthetic Metals 158*, 425 (2008).

[45] T. Nozaki, T. Karatsu, K. Ohnishi, K. Okazaki, "A Pressure-Dependent Selective Growth of Single-Walled and Multi-Walled Carbon Nanotubes Using Plasma Enhanced Chemical Vapor Deposition", *Carbon*, 48, 232 (2010).

[46] Y. Show, Y. Yabe, T. Izumi, H. Yamauchi, "Development of Triode Type RF Plasma Enhanced CVD Equipment for Low Temperature Growth of Carbon Nanotube", *Diamond & Related Materials,* 14(2005)1848.

[49]S. Veprek, Z. Iqbal, J. Brunner, M. Scharli, Preparation and Properties of Amorphous Phosphorus Nitride Prepared in a Low-Pressure Plasma, *Phil. Mag. B*, 43 (1981)527.

[49] Y. Abdi, S. Mohajerzadeh, J. Koohshorkhi, M.D. Robertson, C.M. Andrei, "A plasma Enhanced Chemical Vapor Deposition Process to Achieve Branched Carbon Nanotubes", *Carbon,* **46**, 1611 (2008).

[50] Y. Chai, Q. F. Zhang, J.L. Wu, "A Simple Way to CNx/Carbon Nanotube Intramolecular Junctions and Branches", *Carbon* **44**, 687 (2006).

[51] A. Suzuki, T. A. Ivandini, A. Kamiya, S. Nomura, M. Yamanuki, K. Matsumoto, A. Fujishima, Y. Einaga, "Direct Electrochemical Detection of Sodium Azide in Physiological Saline Buffers Using Highly Boron-Doped Diamond Electrodes", *Sensors and Actuators B*, **120**, 500 (2007).

[52] K. Gong, F. Du, Z. Xia, M. Durstock, L. Dai, "Nitrogen-Doped Carbon Nanotube Arrays with High Electrocatalytic Activity for Oxygen Reduction", *Science* **323**, 760 (2009).

[53] H.Liu, F.Y. Zhang, R.Li, X. Sun, S. Desilets, H.A.Rachid, M.Jaidan, L.S.Lussier, "Structural and Morphological Control of Aligned Nitrogen Doped Carbon Nanotubes", *Carbon* (2010).

[54] J. Kim, H. Xiong, M. Hofmann, J. Kong, S. Amemiya, "Scanning Electrochemical Microscopy of Individual Single-Walled Carbon Nanotube", *Anal. Chem.*, **82**, 1605 (2010).

[55] A. S. Claye, J. E. Fischer, C. B. Huffman, A. G. Rinzler, R. E. Smalley, "Solid-State Electrochemistry of the Li Single Wall Carbon Nanotube System", *J. The Electrochem. Soc.,* **147**, 2845 (2000).

[56] H. Wolfschmidt, R. Bussar, U. Stimming, "Charge Transfer Reactions at Nanostructured Au(111) Surfaces: Influence of the Substrate Material on Electrocatalytic Activity", *J. Phys.: Condens. Mat.,* **20**, 374127 (2008).

[57] L. Pfefferle and D. Ciuparu, "Growth of Boron Nanostructures with Controlled Diameter", US Patent 20050256006 (2005).

[58] Rao, A.M., Richter, E. Bandow, S. Eklund, P.C., Williams, K.A., Fang, S., Subbaswamy, K.R., Menon, M., Thess, A., Smalley, R.E., Dresselhaus, G., Dresselhaus, M.S. (1997). Diameter-selective Raman scattering from vibrational modes in carbon nanotubes, *Science*, 275,187-191.

[59] http://las.perkinelmer.com/content/TechnicalInfo/TCH_FTIRATR.pdf, February 28, 2010.

[60] J. N. Coleman, W. J. Blaue, A.B. Dalton, E. Munoz, S. Collins, B.G. Kim, J. Razal, M. Selvidge, G. Vierito, R.H. Baughman, Improving the Mechanical Properties of Single-Walled Carbon Nanotube Sheets by Intercalation of Polymeric Adhesives, *Appl. Phys. Lett.* **82**, 1682 (2003).

[61] P. Ayala, R. Arenal, M. Rummeli, A. Rubio, T. Pichler, "The Doping of Carbon Nanotubes with Nitrogen and Their Potential Applications", *Carbon* **48**, 575 (2010).

[62] A. C. Ferrari, J. C. Meyer, V. Scardaci, C. Casiraghi, M. Lazzeri, F. Mauri, S. Piscanec, D. Jiang, K. S. Novoselov, S. Roth, A. K. Geim, *Phys. Rev. Lett.* **97,** 187401 (2006)

[63] M. E. Kooi, L. Ulivi, and J. A. Schouten, Vibrational Spectra of Nitrogen in Simple Mixtures at High Pressures, *International Journal of Thermophysics*, **20**, 867 (1999).

[64] W.J. Lauderdale, J.F. Stanton, R.J. Bartlett, Stability and Energetics of Metastable Molecules: Tetraazatetrahedrane ($N_4$), Hexaazabenzene ($N_6$), and Otaazacubane ($N_8$), *J. Phys. Chem.*, **96**, 1173 (1992).

[65] F.J. Owens, Density Functional Calculation of Structure and Stability of Nitrogen Clusters $N_{10}$, $N_{12}$, and $N_{20}$, *Journal Molecular Structure (Theochem)* **623,** 197 (2003).

[66] H. Abou-Rachid, A. Hu, V. Timoshevskii, Y. Song, L-S. Lussier, *Phys. Rev. Lett.* **100**, 196401 (2008).

[67] J. N. Coleman, W. J. Blau, A.B. Dalton, E. Munoz, S. Collins, B.G. Kim, J. Razal, M.Selvidge, G. Vierito, R.H. Baughman, *Appl. Phys. Lett.* **82**, 1682 (2003).

[68] Y. Wang, Z. Iqbal, S. Mitra, *Carbon*, 44, 2804 (2006).

[69] M. Larhed, A. Hallberg, *Drug Discovery Today*, 6, 406 F2001).

[70] J.-J. Shie and J.-M. Fang, *J. Org. Chem.*, 72, 3141 (2007).

[71] C. Haensch, T. Erdmenger, M. W. M. Fijten, S. Hoeppener, U. S. Schubert, *Langmuir*, 25, 8019, (2009).

[72] H. Liu, Y. Zhang, R. Li, X. Sun, S. Désilets, H. A.-Rachid, M. Jaidann, L.-S. Lussier, "Structural and Morphological Control of Aligned Nitrogen Doped Carbon Nanotubes", *Carbon* **48**, 1498 (2010).

[73] P. B. Amama, O. Ogebule, M. R. Maschmann, T. D. Sandsa, T. S. Fisher, "Dendrimer-Assisted Low-Temperature Growth of Carbon Nanotubes by Plasma-Enhanced Chemical Vapor Deposition", *Chem. Commun.,* 2899 (2006).

[74] Y. Li, D. Mann, M. Rolandi, W. Kim, A. Ural, S. Hung, A. Javey, J. Cao, D. Wang, E. Yenilmez, Q. Wang, J. F. Gibbons, Y. Nishi, H. Dai, "Preferential Growth of Semiconducting Single-Walled Carbon Nanotubes by a Plasma Enhanced CVD Method", *Nano Lett.,* **4**, 317 (2004).

[75] M. E. Kooi, L. Ulivi, and J. A. Schouten, Vibrational Spectra of Nitrogen in Simple Mixtures at High Pressures, *International Journal of Thermophysics*, **20**, 867 (1999).

[76] D. S Wavhal, S. Goyal, R. B Timmons, "Synthesis of Electrically Conducting Tin Films by Low-Temperature, Plasma-Enhanced CVD", *Chem. Mater.,* **21**, 4442 (2009).

[77] H. Kinoshita, R. Ikuta, K. Sakurai, "Sputter-Assisted Plasma CVD of Polymer-like Amorphous CNx-H Films Using Supermagnetron Plasma", *Thin Solid Films,* **515**, 4121 (2007).

[78] S. Veprek, Z. Iqbal, J. Brunner, M. Scharli, Preparation and Properties of Amorphous Phosphorus Nitride Prepared in a Low-Pressure Plasma, *Phil Mag. B*, **43**, 527 (1981).

[79] C. Cantalini , L. Valentini, I. Armentano, L. Lozzi, J.M. Kenny, S. Santucci, "Sensitivity to $NO_2$ and Cross-Sensitivity Analysis to $NH_3$, Ethanol and Humidity of Carbon Nanotubes Thin Film Prepared by PECVD", *Sensors and Actuators B*, **95**,195 (2003).

[80] D. Lin-Vien, N.B. Colthup, W.G. Fateley, J.G. Grasselli, Handbook of Infrared and Raman Characteristic Frequencies of Organic Molecules, Academic Press, San Diego (1991).

[81] Propellants, Explosives, Pyrotechnics 33, No. 1(2008) F 2008

[82] North Atlantic Treaty Organization (NATO) STANAG 4147, Chemical Compatibility of Ammunition Components with Explosives (Non-Nuclear Applications), June 5, 2001.

[83] Y. Wang, S.V. Malhotra, F.J. Owens, Z. Iqbal, Chem. Phys. Lett. 407 (2005) 68.

[84] Y. Zhong, M. Jaidann, Y. Zhang, G. Zhang, H. Liu, M. I. Ionescu, R. Li, X. Sun, H. A.-Rachid, L.-S. Lussier, "Synthesis of High Nitrogen Doping of Carbon Nanotubes and Modeling the Stabilization of Filled DAATO@CNTs (10,10) for Nanoenergetic Materials", *J. Phys. Chem. Solid*, **71**, 134 (2010).

[85] K. R. V. Szarmes and J. M. Ramaradhya, Can. Patent, 879,586, 31 August, 1971.

[86] P. G. Hall, J. Chem. Soc. Faraday Trans, Part 2, 67, 556 (1971).

[87] A. E. Oberth, U.S. Patent, 5,071,630, December, 1991.

[88] T. Ozawa, *J. Therm. Anal.,* 2, 301 (1970).

[89] H. E. Kissinger, Anal. Chem., 29, 1702 (1957).

[90] A. Suzuki, T. A. Ivandini, A. Kamiya, S. Nomura, M. Yamanuki, K. Matsumoto, A. Fujishima, Y. Einaga, "Direct Electrochemical Detection of Sodium Azide in Physiological Saline Buffers Using Highly Boron-Doped Diamond Electrodes", *Sensors and Actuators B*, **120**, 500 (2007).

[91] Y. Wang, S.V. Malhotra, F.J. Owens, Z. Iqbal, *Chem. Phys. Lett.* 407 (2005) 68.

[92] Y. Wang, M. S. Malhotra, and Z. Iqbal, "Nanoscale Energetics with Carbon Nanotubes", *Mat. Res. Soc. Symp. Proc.*, **800**, 351 (2004).

[93] S. Li, Zhi Jiang, and S.Yu, Thermal Decomposition of HMX Influenced by Nano-Metal Powders in High Energy Fuel, *Fuel Chemistry Division Preprints **20 02**, 47(2),* 596.

[94] Ball P., Garwin L., Nature 1992, 355, 761.

[95] Kuo K. K., Summerfield M., Fundamental of Solid Propellant Combustion, AIAA. Inc, New York, 1984.

[96] Zhou Min F., Andrews L., *J. Phys. Chem.* A 2000, 104, 2618-2625.

[97] S. Mathew, K. Krishnan, and K. N. Ninan, A DSC Study on the Effect of RDX and HMX on the Thermal Decomposition of Phase Stabilized Ammonium Nitrate, *Propellants, Explosives, Pyrotechnics,* 23, 150-154 (1998).

[98] M. Herrmann, W. Engel, and N. Eisenreich, *Propellants, Explos Pyrotech.* 17, 190 (1992).

[99] W. Engel, Propellants, Explos., Pyrotech. 10, 84 (1985).

[100] P. M. Madhusudanan, K. Krishnan, and K. N. Ninan, *Thermochem. Pyrotech.* 17, 190 (1992).

[101] C. Spyckerelle, Genevie`ve Eck, EURENCO France, Sorgues Plant 1928 route dAvignon, BP 311, 84706 Sorgues Cedex (France), Per Sjçberg, Anna-Maria Amne'us EURENCO Sweden, SE-69186 Karlskoga (Sweden), Reduced Sensitivity RDX Obtained From Bachmann RDX, *Propellants, Explosives, Pyrotechnics* 33, No. 1(2008) F 2008

[102] Risha, G.A., "Enhancement of Hybrid Rocket Combustion Performance Using Nano-Sized Energetic Particles," Ph.D Dissertation, The Pennsylvania State University, 2003.

[103] D. Ciuparu, R.F. Kile, Y.Zhu, and L. Pfefferle, Synthesis of Pure Boron Single-Wall Nanotubes, *J. Phys. Chem.* B 2004, 108, 3967-3969.